Models for Non-Isothermal Compositional Gas-Liquid Flow and Transport in Porous Media

Der
Fakultät für Bau- und Umweltingenieurwissenschaften
der Universität Stuttgart

vorgelegte

Habilitationsschrift

von
Dr.-Ing. Holger Class

Stuttgart, im Oktober 2007

Contents

List of Figures

List of Tables

Nomenclature

Symbol	Meaning	Dimension/Unit
A	free energy	[J]
B	general quantity transported with flow	
C	number of components	
Cr	Courant number	[-]
D	diffusion coefficient	[m^2/s]
E	energy	[J]
F	degrees of freedom	
$\mathbf{F}$	Faraday's constant ($\mathbf{F}$=96484.56)	[C/mol]
$\mathbf{F}$	vector of external forces	[N]
Gr_{lin}	gravity number	[-]
H	enthalpy	[J]
H	Henry coefficient	[Pa]
J	diffusive and dispersive fluxes	[mol/(m^2 s)]
$\mathbf{K}$	intrinsic permeability	[m^2]
$\mathbf{K}$	Jacobian matrix	
M	molecular weight	[kg/mol]
M_{ij}	mass matrix	
N	amount of substance	[mol/(m^2)]
P	number of fluid phases	
Pe	Peclet number	[-]
Q	thermal energy	[J]
R	individual gas constant	[J/(kg K)]
$\mathcal{R}$	universal gas constant ($\mathcal{R}$=8.314)	[J/(mol K)]
Re	Reynolds number	[-]
S	saturation	[-]
T	temperature	[°C, K]
U	internal energy	[J]
V	volume	[m^3]
W	work	[J]
X	mass fraction	[-]
$\mathbf{a}$	vector of acceleration	[m/s^2]
abs	convergence criterion of solvers	
b	characteristic width of the transient steam zone	[m]
b	mass-specific intensive quantity corresponding to B	
c	specific heat capacity	[J/(kg K)]
$\mathbf{g}$	vector of graviation $(0,0,-g)^T$	[m/s^2]
h	characteristic height of the transient steam zone	[m]
h	piezometric head	[m]
h	specific enthalpy	[J/kg]
i	current density	[A/m^2 = C/(m^2 s)]
$\mathbf{k}_f$	hydraulic conductivity tensor	[m/s]

k_r	relative permeability	[-]
l	length	[m]
m	mass	[kg]
n	number of moles	[mol]
$\mathbf{n}$	unit normal vector	
p	pressure	[Pa, bar]
q	flow rate, source/sink	[m^3/s, J/s, kg/s]
q_s	steam injection rate	[kg/s]
r	radius	[m]
t	time	[s]
$\mathbf{u}$	vector holding corrections of primary variables	
$\mathbf{v}$	Darcy velocity vector	[m/s]
x, y, z	coordinates	[m]
x	mole fraction	[-]
z	geodetic height	[m]
Γ	boundary of volume Ω	
Ψ	total potential	[Pa]
Ω	volume, model domain	
α	Van Genuchten parameter	[1/Pa]
β	compressibility/expansion coefficient	[-]
β	scaling parameter for capillary pressure	[-]
γ	surface tension	[J/m^2 = N/m]
ε	convergence criteria (defect reduction)	
η	damping factor	
θ	contact angle	[$^\circ$, rad]
λ	heat conductivity	[J/(m s K)]
λ	Brooks-Corey parameter	[-]
λ	mobility	[1/ (Pa s)]
μ	dynamic viscosity	[Pa s]
ν	kinematic viscosity	[m^2/s]
ρ	density	[kg/m^3, mol/m^3]
σ	surface	[m^2]
τ	tortuosity	[-]
ϕ	porosity	[-]

Indices:

b	boiling, brine
c	capillary
e	effective
f	fluid
g	gas
h	piezometric head
i, j, k	node
kin	kinetic
l	grid level

l	liquid
lin	linear
m	methane
mol	molar
n	NAPL
nl	non-linear
no	nodal points
p	pressure
pm	porous medium
r	residual
ref	reference
t	total liquid
s	solid
s	steam
sat	referring to saturation vapor pressure curve
T	temperature
t	time
upw	upwind node
vis	viscous
w	water
α	phase

Exponents:

C	Cauchy
D	Dirichlet
N	Neumann
R	reaction
a	air
c	contaminant
k	iteration
$lump$	lumping
n	time level
o	oxygen
w	water
κ	component

Chapter 1

Introduction

1.1 Motivation

1.1.1 General Overview

Multiphase flow systems in porous media occur in many different fields of applications. One may basically distinguish between natural porous media and technical porous media. A classical natural porous medium is the subsurface where many different kinds of multiphase flow problem classes occur, see Fig. 1.1. They deal primarily with the sustainable management and the protection of the natural resource groundwater and with the exploitation of other resources like oil or gas. Recently, also the usage of subsurface systems for the disposal of anthropogenic wastes or greenhouse gases came to the fore. The different fields of multiphase flow problems in the subsurface engage a strong interdisciplinary scientific community, for example, environmental engineers, reservoir engineers, (hydro-)geologists, mathematicians, physicists, chemists, etc.

Worldwide, groundwater is the main resource of drinking water and in many countries the only available fresh water. Groundwater is endangered by a variety of substances with different degrees of toxicity. A classical problem, for example, is the infiltration of nitrate from agriculture. Nitrate dissolves in water and is transported through the vadose zone into the aquifers. Other contaminants can also exist as separate non-miscible liquid phases. Many organic liquids like halogenated organic solvents or hydrocarbon fuels dissolve in water only very fractional. They are denoted as Non-Aqueous Phase Liquids (NAPL). Dependent on their density, whether they are denser or lighter than water, they are called DNAPL or LNAPL. It is estimated that in Germany alone there are more than 200.000 NAPL-contaminated sites [47]. Thus, there is a great need to develop strategies and technologies for the remediation of such sites. In the last decades, soil-air extraction combined with thermal enhancement by steam, steam/air, or thermal wells established as a state of the art technology for the remediation of the source zones of the contamination where distinct amounts of NAPLs in phase are present. Recently, on many such sites, the so-called natural attenuation strategy relies on the natural ability to degrade the contaminants outside of the source zone. Often, this is supplemented by optimizing the conditions (nutrients, oxygen) for the biodegrading bacteria.

Another important subsurface flow problem that gains increasing attention is the migration of

gases due to natural occurence or anthropogenic activities like mining, nuclear waste disposal, or CO_2 injection into gas and oil reservoirs or into other geological formations for the purpose of long-term storage (also illustrated in Fig. 1.1). A common issue of these problems is to prevent an uncontrolled release of the gases to the atmosphere which is a delicate job since buoyancy forces and heterogeneities or fault zones counteract. There is obviously also an economic interest concerning the exploitation of oil and gas reservoirs by enhanced methods that often apply gas (e.g. CO_2) injection into depleted reservoirs in order to increase the recovery rates.

While the subsurface topics are clearly in the main focus of this work, there is still a number of technical porous media where flow and transport plays an important role and for which the basic model concepts presented in this work can be applied or at least adapted. One such technical porous media flow problem is the water-gas management in cathodic gas diffusion layers of fuel cells (Fig. 1.4). There, the porous gas diffusion layer has the purpose of controlling the gas (oxygen) transport from the gas discharge channels to the reaction layer and concurrently, due its hydrophobic property, it supports the displacement of the liquid water that is produced by the reaction. Although the fuel-cells will be the only technical porous medium that is discussed in detail within the scope of this work, there are still many other technical applications. Just to name a few, we mention here gas and/or liquid flow processes through filters, the behavior of ink in paper, the transport of dissolved salt through concrete as a potential threat for the iron/reinforcement, the gas flow through catalytic converters in cars, the gas-liquid-solid interactions in baby diapers, etc. For most of these technical processes, the main issue for process engineers to model them is to optimize the systems. Thus, once the respective forward models are available, they are often used along with optimization algorithms and inverse modelling tools.

Generally, any (mathematical/numerical) model or model concept represents an abstraction of naturally or technically occuring phenomena or complex systems in economics. Models are aimed to comprehend the essential parameters of the phenomena and to assemble them into mathematical equations that can be solved analytically or numerically. Numerical flow and transport models allow an integrating consideration of complex physical systems. Such models have proven to be indispensable tools in many engineering problems, for example, for improving process understanding and identification, optimization, pre-experimental predictions, planning of protection and remediation measures, interpretation of measurement data, etc. A model can help explaining situations, for example, the appearance or distribution of a contamination in a groundwater system, or the origin/leakage path of CO_2 that is detected somewhere at the ground surface. Models can also simulate interventions into systems and predict their effects. Furthermore, analyses of parameter sensitivities are an important purpose of model applications.

In the frame of this thesis, we will focus on models for isothermal and non-isothermal compositional gas-liquid processes. This headline comprises the aforementioned fields of applications. We will show that these systems have many features in common and we will also point out their characteristic differences and explain the specifically required model adoptions.

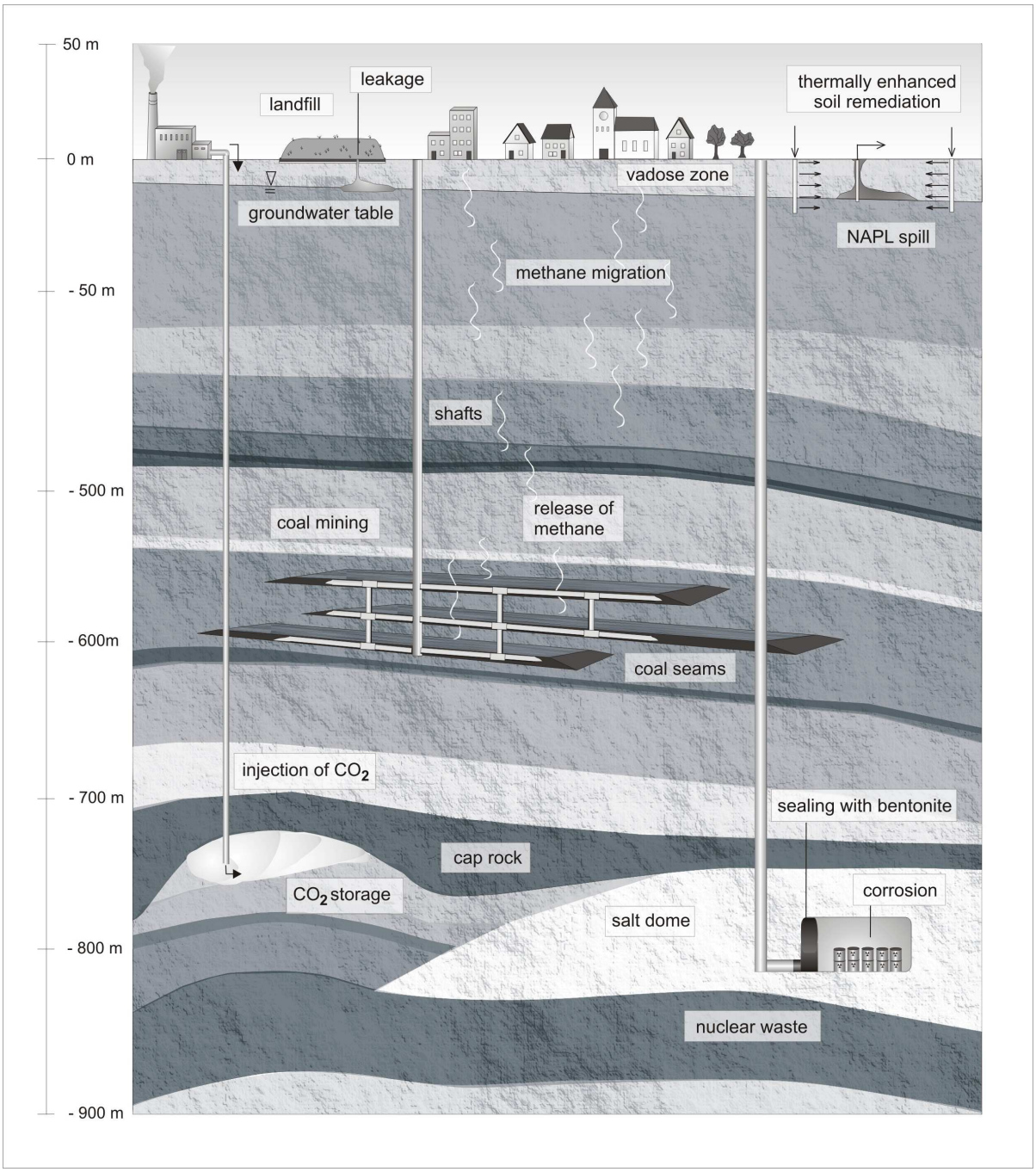

Figure 1.1: Schematic view on selected gas-liquid flow problems in the subsurface.

1.1.2 Distinctiveness of Gas-Liquid Systems

Gas-liquid multiphase systems are in the main focus of this work. Although they can occur in many different porous media flow applications, most of them can be characterized by some distinct features which are discussed below. Some of these features can also occur in certain liquid-liquid multiphase systems, nevertheless their distinctiveness for gas-liquid systems appears to be significant.

Fluids, Liquids, and Gases

Within this thesis, the terms fluids, liquids, and gases are used as follows:

- The term **fluid** is a generic name that embraces both gases and liquids. A fluid continually deforms under an applied shear stress while solids can at least to some degree resist. One can generally distinguish between *Newtonian fluids* and *non-Newtonian fluids* according to their reaction under applied stress. For *Newtonian fluids*, the stress is proportional to the strain.

- A **liquid** is a fluid that can form a free surface, for example, in open channels or vessels.

- A **gas** does not form a free surface. Gases tend to fill the available space of a container.

Differences in Fluid Properties

Typically, the density of a substance in its liquid state of aggregation is higher than in the gaseous state. For example, liquid water at atmospheric pressure and ambient temperatures, say 20 $^{\circ}$C, has a density of roughly 1000 kg/m^3. In contrast to that, the same substance water in its vapor form (steam), has a density of approximately 0.6 kg/m^3 which is lower by three orders of magnitude than the liquid. The density of air at the same conditions is approximately 1.2 kg/m^3 and thus comparable with the steam density.
The simple conclusion, which we have to draw from these strong density differences, is that gravity effects like buoyancy experienced by a lighter gas in a surrounding heavier liquid must play a dominant role in many gas-liquid systems. This will be discussed later in detail, for example, in Sec. 2.3 for the injection of steam in the saturated zone or in Sec. 2.4 for the hydrodynamic trapping of sequestered CO_2 in geological formations. Buoyancy effects are also illustrated in the corresponding sample problems given in Secs. 6.3 and 6.4.

In most cases, also the viscosities of gases and liquids differ by some orders of magnitudes. Taking again the example of liquid water and steam at 1 bar, we find that liquid water at 20 $^{\circ}$C has a dynamic viscosity of $1.0 \cdot 10^{-3}$ Pa s while steam at the same temperature has $1.2 \cdot 10^{-5}$ Pa s. Note that the influence of pressure on the viscosity is a lot less than that of temperature (see also Sec. 3.1.3.2).
Viscosity is a fluid property that directly influences the *mobility* of a fluid. Assuming constant relative permeability (see Sec. 3.1.5.2) one can state that the higher the viscosity of a fluid, the lower is its mobility. This is of particular interest in cases where a fluid is displaced by another fluid of different viscosity. If the displacing fluid has a lower viscosity than the resident one, the

displacement front is very stable - except for heterogeneous porous media, where the permeability distribution affects the shape of the displacement front, but this is a different topic.

When a more viscous fluid is displaced by a less viscous one, the shape of the displacement front can be unstable and often characterized by *fingers* of the displacing less viscous fluid protruding into the more viscous resident fluid. It depends on the viscosity ratio $\mu_{displacing}/\mu_{resident}$ whether viscous fingering occurs or not. More precisely, in porous media flow systems the mobility ratio $\lambda_{displacing}/\lambda_{resident}$ determines the susceptibility of a displacement front to viscous fingers. Here, the mobility λ, defined as the ratio of relative permeability k_r and dynamic viscosity μ takes furthermore the influence of the phase saturations into account since they influence the relative permeabilities. Mobility ratios are mostly substantially smaller than viscosity ratios which is a hint that hydrodynamic flow instabilities are weaker in porous media than in 'free' space [68].
Viscous fingering can occur, for example, in enhanced oil recovery (EOR), where CO_2 is injected to enhance the production of oil in depleting reservoirs. Since the viscosity of the oil is much higher than the one of the injected CO_2, the CO_2 tends to protrude in fingers into the oil, thus parts of the oil which is aimed to be displaced by the CO_2 remain behind the front and the efficiency of the EOR technology is reduced. Another application where viscous fingering can occur is the displacement of a NAPL by water or a solvent which are injected, for example, in a pump-and-treat remediation of a contaminated site. A process where the viscous fingering is strongly supported by a huge density difference is the so-called air-sparging, where air is injected into polluted groundwater zones in order to stimulate the natural activities of bacteria by the supply of oxygen. The air bubbles are strongly affected by both buoyancy and the viscosity ratio so that the ascension of the air occurs by distinct fingers in preferential flow paths. Modelling this requires either a very high resolution of the grid which is general rather inefficient, or other approaches, like a double continuum model as suggested, for example, by *Falta* (2000) [58].
Influence on the length and width of triggered fingers has the miscibility of the two fluids. If the displacement occurs miscible, for example, a water/alcohol-mixture displacing a NAPL-contamination - some alcohols dissolve both NAPL and water -, then the mixing process counteracts the growth of developing fingers. Another stabilizing effect on the displacement is given, for example, if the displacement is accompanied by a simultaneously propagating condensation front as in the case of steam injection into the subsurface for a thermally enhanced remediation of NAPL-contaminated soils. This will be explained in detail in Sec. 2.2.
As discussed, for example, by *Garcia & Pruess* (2003) [68], also capillarity has a stabilizing influence on displacement fronts.
Within this work, we will not further elaborate on viscous fingering effects and leave it at this short discussion. The topics and applications that are addressed in the following are not significantly influenced by viscous fingers. Instead, we refer to the literature where both experimental and theoretical or numerical investigations can be found, cf., e.g. [88, 101, 68, 97].

Vapors, Condensate, Heat Exchange

The saturation vapor pressure curve (see Sec. 3.2.1.2) describes the equilibrium partitioning between a liquid substance with its corresponding vapor in the gaseous phase. Therefore, it is characteristic for many gas-liquid systems that a change of the ambient conditions like pressure and/or temperature brings about a shifting of the liquid-vapor equilibria of the involved sub-

stances in a system. Accordingly, depending on the direction of the shifting, a transition of mass from the liquid phase to the gaseous one or vice versa occurs. This goes along with an exchange of the latent heat of vaporization. Consequently, a full description of the overall process requires a balance of the thermal energy in the system in addition to the mass balances of the involved substances (or: *components*). Under certain conditions, the exchange of thermal energy may be neglected and the system is assumed to be isothermal. But it will be shown in the following chapters that the gas-liquid systems addressed by this thesis are often strongly influenced by non-isothermal processes.

Influence of Composition on Fluid Properties

Gaseous phases can strongly vary in their composition, for example, during non-isothermal processes if one or several liquids are present which produce vapors. For example, cold air in an air-water system contains only a very small fraction of steam while the steam fraction in the gas phase approaches one when the system is near or at the boiling point of water. As a consequence of changing composition also the fluid properties of the gas phase vary.

If the gas phase is a mixture of several gaseous components, this mixture is always homogeneous since the gases are mixed on the molecular scale. In contrast to that, mixtures of liquids are often immiscible or only partly miscible so that these mixtures are denoted as heterogeneous (multiphasic) mixtures. In other words, while there can be several liquid phases present simultaneously, the gaseous components involved in a system are always comprised within a single gas phase. The most well-known example of a gas mixture is air which consists of 21% oxygen, 78% nitrogen, and 1% other gases of which the most prominent one is CO_2 with 0.04%. The fluid properties of air are determined by the fractions of the components and their respective individual properties. The air properties can be estimated with good accuracy by linearly interpolating the properties of the components. The same holds for other gas mixtures if they behave approximately like ideal gases (see Sec. 3.1.3.1).

The properties of liquid phases can also be strongly influenced by their composition. Yet, in most cases the relation between liquid fluid properties and composition is rather non-linear, and it requires often complex constitutive equations to describe this properly.

Compressibility of the Gas Phase and the Liquid Phases

According to the law of *Boyle-Marriote* the volume of an ideal gas at isothermal conditions is inversely proportional to the pressure. For non-isothermal conditions, the influence of temperature on the gas volume superimposes the dependence on pressure which is expressed by the *ideal gas law* (see Sec. 3.1.3.1).

Liquid phases are much less compressible than gases. For a long time, they were assumed to be even incompressible until the English physicist *John Canton* proved their compressibility in 1761. Thus, in liquid-liquid multiphase systems it is a common simplifying assumption to neglect the compressibility. This will be discussed shortly in the context of the mathematical solution

procedure of the governing equations in Sec. 5.1.1.3.

All topics addressed in this thesis require a consideration of the gas compressibility and therefore produce rather complex systems of governing partial differential equations, for which simplifying assumptions, for example, in order to develop analytical solutions, cannot be made.

1.1.3 A Natural Porous Medium: The Subsurface

The subsurface is the place where the majority of those porous media flow problems occurs, which are in the focus of environmental engineers. Therefore, one should attach importance to the structure and porous media properties of the subsurface being of relevance for the flow and transport processes. Basically two main factors influence the behavior of multiphase flow systems in the subsurface:

- The *structure (and its heterogeneity)* affect the resistance of the porous medium to fluid flow. Depending on the scale of consideration (see Sec. 3.1.1) this can be expressed, for example, on a scale that allows some volume averaging by the distribution of permeability and porosity (see Sec. 3.1.2).

- The *wettability* determines which of the phases in a multiphase system is the wetting phase and therefore covers the surface of the porous matrix preferentially. Typically, subsurface systems are water-wet. This means, the preference of a solid is to be in contact with a water phase rather than, for example, an oil or gas phase. Water-wet rocks, for example, sandstones or carbonates preferentially imbibe water. Nevertheles it may occur, for example, in oil reservoirs that components of the crude oil alter the surfaces of the rocks to become partially oil-wet, or in coal where the wettability can depend on the composition, pressure conditions, etc.

  The wettability influences the hydraulic behavior strongly. This is reflecetd via the relationships between phase saturations, relative permeabilities, and capillary pressure.

Figure 1.1 shows that the depth in which the different multiphase flow problems are located in the subsurface extends from the shallow soil zone down to more than 1 km. The examples shown in this cartoon start in the vadose zone which is spoiled by leachates from landfills or NAPL spills. These contaminations pose a potential threat to the groundwater and therefore to drinking water resources. The other subsurface flow problems shown here are located in greater depth. The depth of coal mines, which may release methane from unmined seams, depends on the local depth of the carbon layers and can be in several hundred or a few thousand meters. Also the depth of CO_2 injection or nuclear waste disposals can vary according to the location of appropriate target formations. Yet, for CO_2, experts aim at achieving supercritical conditions which requires a minimum depth of typically 700 m.

Over this depth, there are typically a large number of geological layers involved so that a standard characterization of subsurface properties is impossible. However, what most geological layers have in common is that the description of their properties depends on the spatial scale on which they are viewed. For a description of the properties in flow models it is in general necessary to average over some volume. Figures 1.2, and 1.3 prove this scale-dependence impressively.

Fig. 1.2 shows a photograph of the soil structure in a quarry in the south of Germany from a rather distant perspective. One can identify a more or less horizontal layering, yet the layers themself are seemingly homogeneous. This layered structure is the result of the sedimentation process and is responsible for the anisotropy of the permeability in sediment rocks. Typically, the vertical permeability is much lower than the horizontal one.
Zooming in, as shown in Fig. 1.3, the structure reveals a heterogeneity on a far smaller scale. Here, the grain size distribution appears to be locally distinctive. Gravel inclusions in sandy or silty layers can be observed.

1.1.4 Technical Porous Media

Porous media are often found in technical fluid flow systems. Within this work, we will particularly focus on the gas diffusion layer of a PEM (*proton exchange membrane* or *polymer electrolyte*) fuel-cell.

Fig. 1.4 shows micrograph pictures of a commercial electrode material as it is used in PEM cells. Compared to the dimensions, in which typical subsurface flow problems are considered, the fuel-cell systems are orders of magnitude smaller. The thickness of a gas diffusion layer - also denoted as: electrode, backing - is less than 1 mm, in the order of some tens to several hundred μm. This through-plane dimension determines the oxygen diffusion rate. Thinner layers offer less resistance to the gas flow in so-called interdigitated flow fields (see Sec. 2.6). However, the gas diffusion layer has also the function of a backing material and therefore to protect the membrane. From the cross section shown at the bottom of Fig. 1.4 one can recognize a fibrous structure of the electrode. In this case the material is carbon paper containing only a small number of fibres in the through-plane direction.
Compared to the subsurface structure, the structure of the electrodes in PEM fuel-cells is mostly more regular. Due to the fibrous structure, the electrode reveals a distinct anisotropy with higher permeability in the direction of the fibres (in-plane directions).

A similar structure is also found in paper as shown by the micrographs in Fig. 1.5. The fibers can be easily detected in the surface graph (top). The cross-section (bottom) shows the complex porous structure with a clear in-plane orientation of the fibers and void spaces (pores). This raises the suspicion of anisotropic behavior. A multiphase flow problem in paper, particularly dominated by capillarity, is given, for example, when ink is applied to the surface in an offset printing technique. During the offset print process, the ink is applied in the regions of the images while water is applied in the surroundings. The velocity of the water-uptake and drying has influence on the quality of successive color prints and on the deformation behavior. A comprehensive study of this is given by the thesis of *Middendorf* (2000) [117].

Another technical porous media flow problem is the transport of moisture, heat, and salt in concrete or other building materials. For building physics, the thermal and hygric processes in concrete are of great importance and therefore also a field of application for numerical models. This is described, for example, by *Grunewald* (1997) [73, 46]. These materials are often very low permeable, thus capillarity and diffusive transport strongly affect the transport rates.

The reactive gas flow through catalytic converters in cars is a further technical porous media flow problem as well as the gas-liquid processes in baby diapers, where the latter is particularly coupled with strong deformation by a swelling material. There are obviously many other technical porous media flow problems which are not mentioned here. Yet, we can conclude that the kind of models that are described and explained in this thesis can be adopted to widespread fields of application.

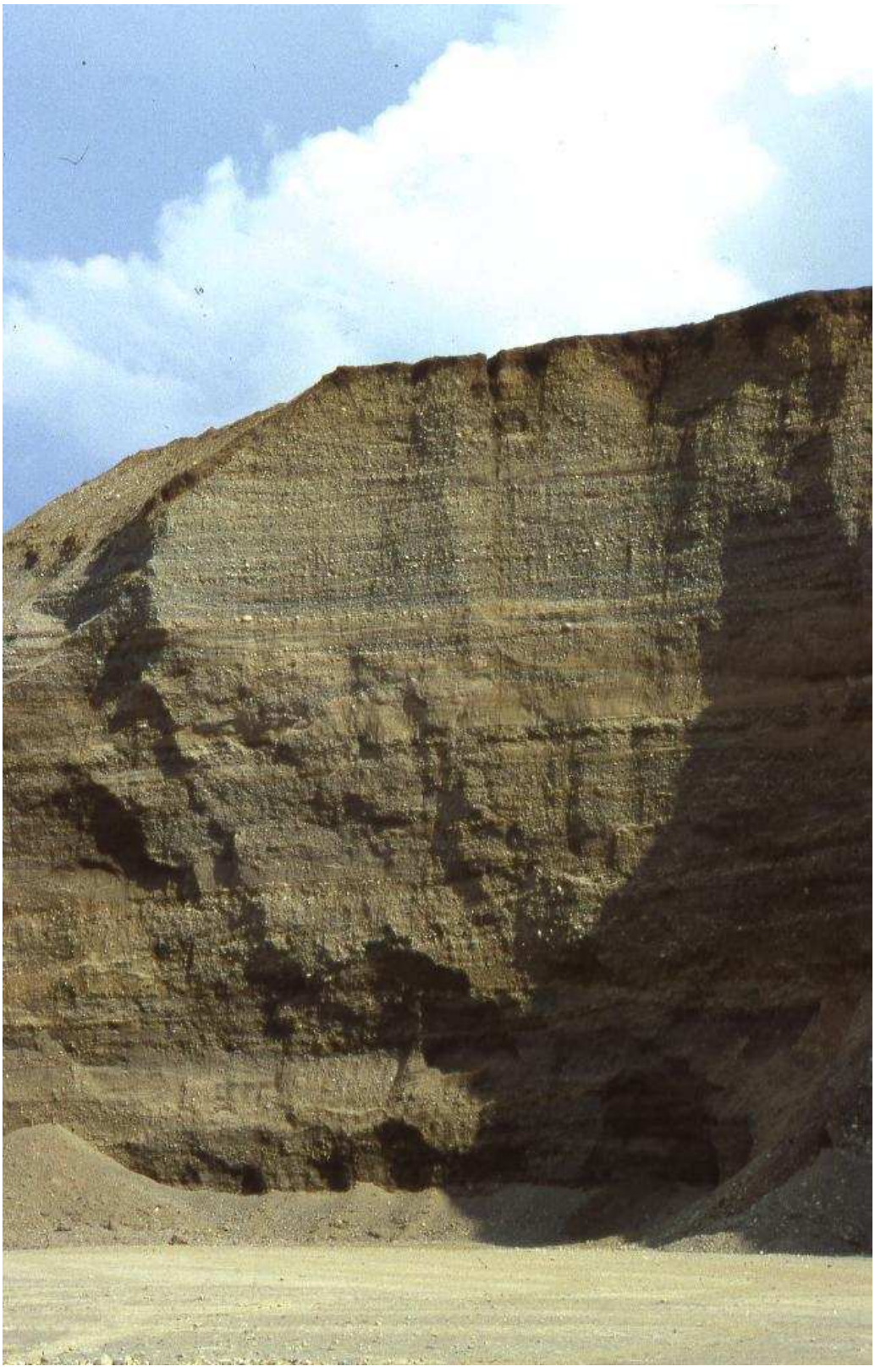

Figure 1.2: Soil structures from different perspectives. Photographs taken in a quarry (permission from *A. Färber*, Universität Stuttgart.

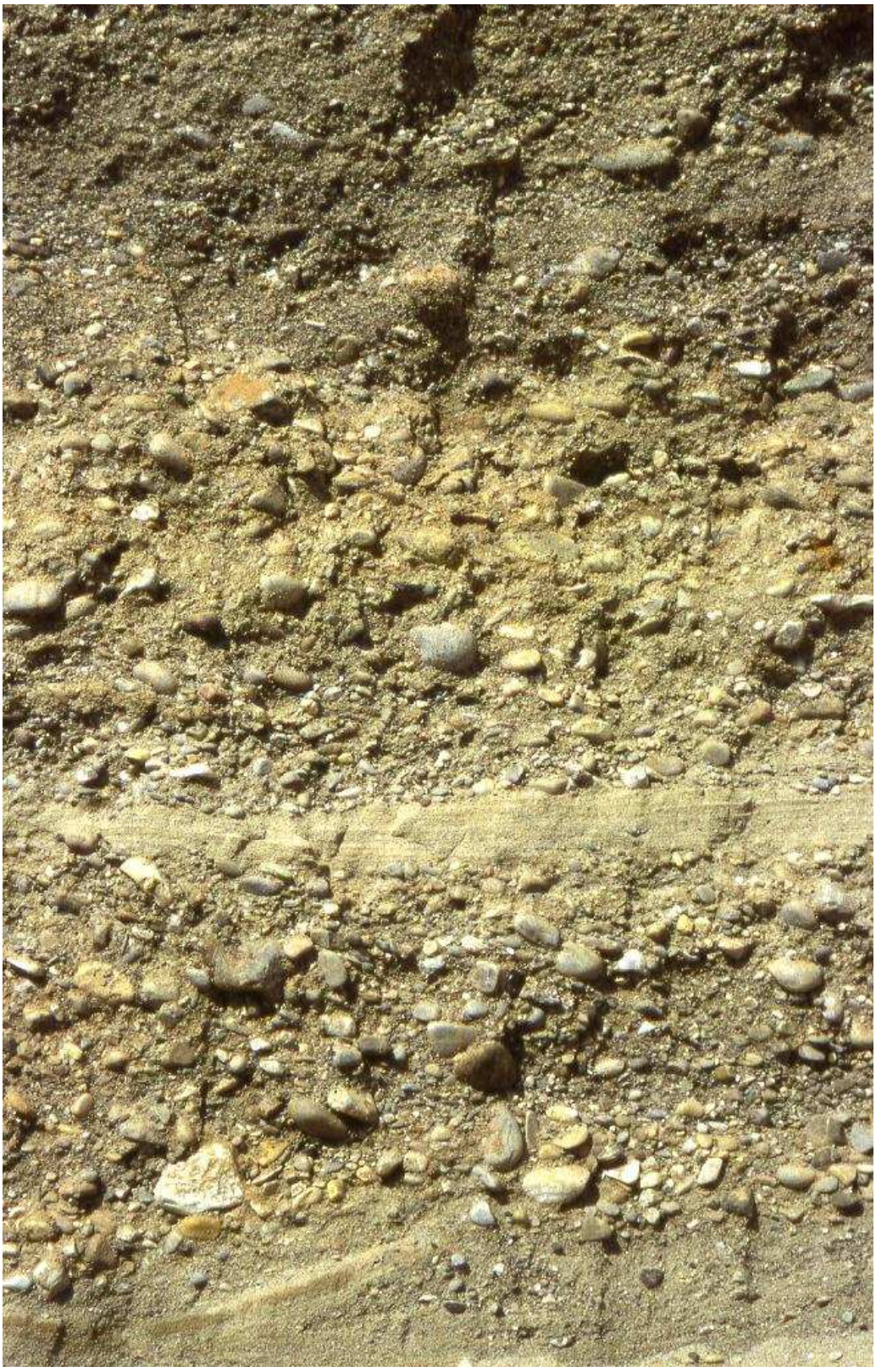

Figure 1.3: Soil structures from different perspectives. Photographs taken in a quarry (permission from *A. Färber*, Universität Stuttgart).

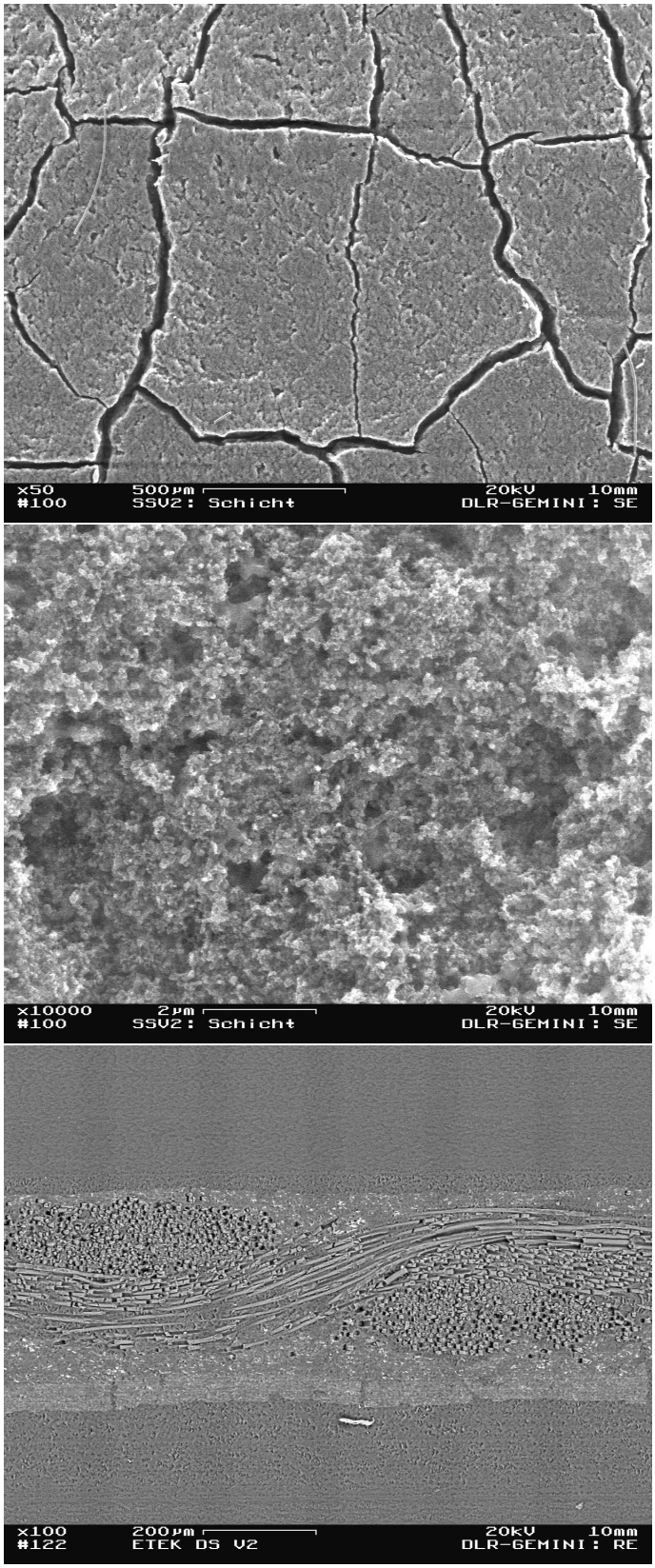

Figure 1.4: *SEM* micrographs: Top views with different zooms on a commercial electrode material for fuel cells (top and middle); cross section of the same material (bottom); from *Acosta et al.* (2006) [2].

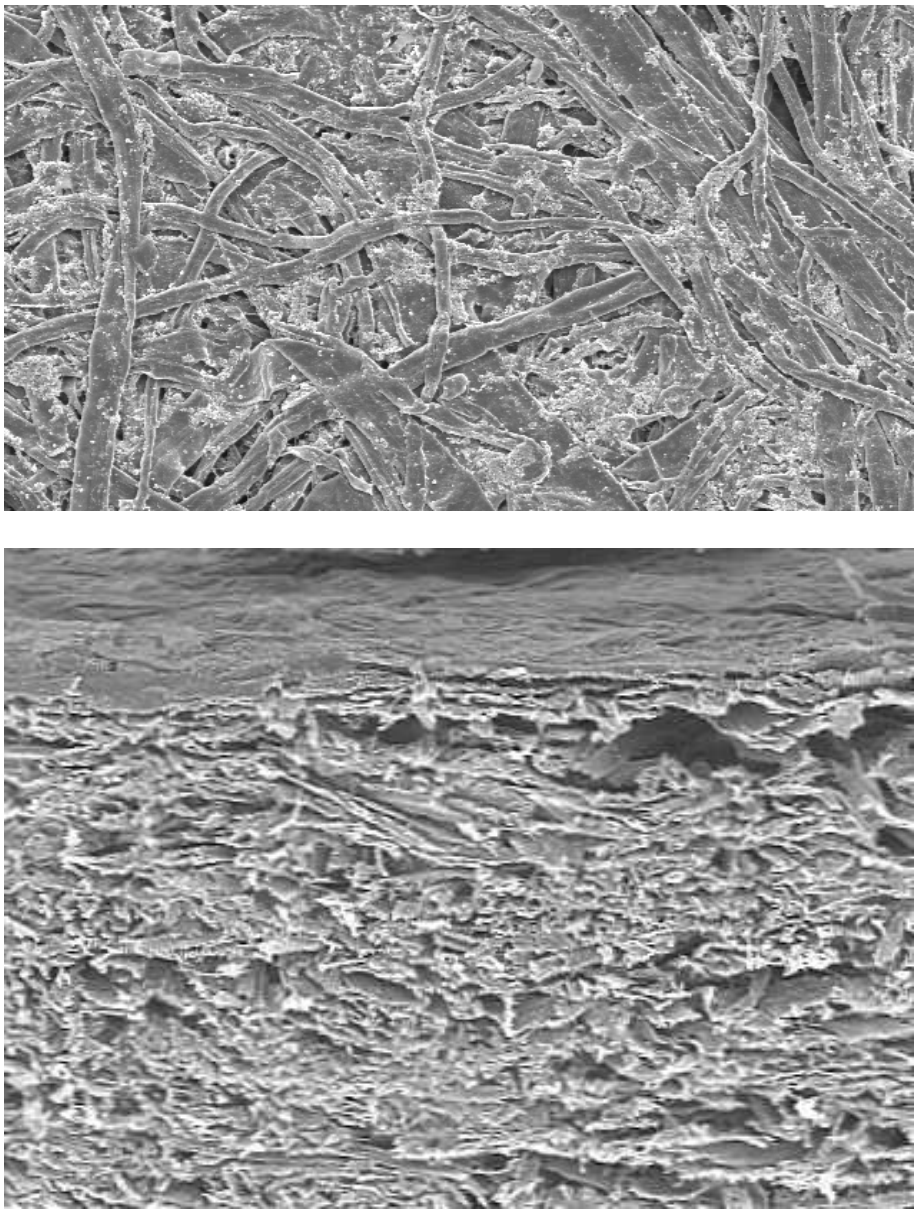

Figure 1.5: *SEM* micrographs of paper from *Middendorf* (2000) [117]. Top: in-plane structure (surface); bottom: through-plane structure (cross-section, obtained from a cut of the frozen material), in the upper region a part of the surface is visible.

1.2 Timeline of Literature and Research

The description of flow processes in porous media has already a long tradition. Undoubtedly the most fundamental contribution to the research on porous media flow until today is described by *Henry Darcy* (1856) [43]. He found out that the advective flow rate through a porous material is in good approximation linearly dependent on the pressure gradient and on the hydraulic conductivity. A first multiphase flow concept was proposed by *Buckingham* (1907) [21] which also influenced the scientific community in this field strongly. He introduced that the hydraulic conductivity of an unsaturated soil depends on the water content. *Richards* (1931) [147] extended this and formulated a partial differential equation for water flow in the unsaturated zone which is commonly known as *Richards equation*. Another basic early work is documented by *Leverett* (1941) who explains the fundamentals of capillarity in porous solids.
One of the most-cited textbooks on fluid dynamics in porous media was written by *Bear* (1972) [15] and gives a comprehensive introduction into the fundamental physical processes and their mathematical description. Also *Scheidegger* (1974) [150] describes the physics of flow and transport through porous media. A great interest in porous media flow was forced by the petroleum industry aiming at an efficient exploitation of oil and gas reservoirs. *Aziz & Settari* (1979) [7] and *Chavent & Jaffre* (1978) [29] focus on methods to model the flow processes in petroleum reservoirs with numerical simulators, and *Lake* (1989) discusses in detail the techniques for *Enhanced Oil Recovery* (EOR). Another more general textbook on the modelling of transport phenomena in porous media is the book of *Bear & Bachmat* (1990) [16]. The book of *Looney & Falta* (2000) [112] deals in great detail with the flow and transport processes in the vadose zone having also a strong focus on forward and inverse modelling techniques.

The model capabilities improved significantly in the last few decades and many models consider complex coupled and non-linear multiphase processes including mass transfer between the fluid phases. On the one hand, this puts high demands on accurate quantitative approaches for fluid properties, hydraulic properties, and mass transfer processes. And on the other hand, there is a need for sophisticated algorithms and discretization methods in order to solve the arising systems of non-linear partial differential equations fast and efficiently.
Comprehensive tables and constitutive equations for gas and liquid fluid properties are provided by, for example, *Hirschfelder et al.* (1954) [86], *Vargaftik* (1975) [168], *Reid et al.* (1987) [146], or *Poling et al.* (2001) [141]. Issues of computational methods in subsurface flow were addressed by *Huyakorn & Pinder* (1983) [92]. An excellent overview of numerical methods and discretization schemes for multiphase subsurface flow models is given by *Helmig* (1997).

Classical fields of application for porous media multiphase flow and transport models are still (i) in reservoir engineering for improving and optimizing the production of oil and gas and (ii) in environmental engineering for addressing issues like groundwater management, protection, and remediation. These topics are covered by the aforementioned textbooks and an additional huge number of other books and more specific publications in scientific journals. Many of them are cited in this thesis in the specific context.
Recently, petroleum engineers and environmental engineers started joint efforts on developing models for the simulation of CO_2 injection into deep geological formations. A detailed overview of the general issues of *Carbon Dioxide Capture and Storage* (CCS) is given by the Special

Report of the *Intergovernmental Panel on Climate Change* (IPCC) [95]. Regarding specifically the aspects of modelling related processes in these geological formations, we refer, for example, to the publication of *Pruess* (2006) [38].
Model concepts for multiphase flow in porous media have been transfered also to other fields of application. Within this thesis, we discuss particularly the processes in the cathode diffusion layer of PEM fuel-cells, cf., e.g. [139, 2, 48] which occur on a distinctively smaller scale than typical subsurface problems.

The majority of models that focus mainly on the flow and transport processes in a porous medium neglects a potential deformation of the porous matrix. At least, they do not consider local deformations by a Lagrangian view on the local material points, but potentially accounts for structural alterations somehow phenomenologically, for example, by constitutive functions of porosity or permeability dependent on pressure. The *Theory of Porous Media* as, for example, introduced by *de Boer* (2000) [45] or *Ehlers* (1996) [55] applies a fully coupled consideration of flow and matrix deformation. It allows with additional balance equations (momentum balance for the solid) an explicit consideration of the matrix material properties.

As already mentioned, this literature survey provides only an outcrop of the existing literature related to the broad bandwith of topics that are addressed by this thesis. There exist also many commercial software packages and research codes for the simulation of multiphase flow in porous media which are also not named here. As mentioned earlier, references to further and more recent publications and advances in the different fields are given later associated with the particular context.

1.3 Structure of the Thesis

Following these introductory comments, Chapter 2 spans the range of gas-liquid problems that are addressed in this work. It provides the motivation for considering these topics as gas-liquid flow and transport problems in porous media. The basic characteristics are explained and the key issues of current research and open questions are raised. Chapter 3 first gives a derivation of the model concept and the governing equations for the mathematical description of multiphase systems. This is then step by step extended to take into account compositional and non-isothermal effects. In Chapter 4 the specific adaptations that are required for the different fields of application are explained. Chapter 5 discusses the basic mathematical treatment of the systems of partial differential equations and auxiliary algebraic equations. Furthermore, the spatial and temporal discretization methods, the linearization and solution strategies, and the process adaptive switching of primary variables are accounted in the context of the different topics that this thesis covers. Chapter 6 provides a couple of example applications that illustrate the behavior of the different multiphase multicomponent gas-liquid systems. At that point, we also discuss for the respective study in detail the assignment of appropriate boundary conditions and the possibly occuring difficulties. Finally, Chapter 7 summarizes the scope of this thesis and provides some perspectives for further research on these different topics.
The structure of this work was chosen according to criteria that consider the consecutive procedure of modelling, starting from the awareness of a flow and transport problem and ending in

the evaluation of simulation results. The total procedure of modelling could be summarized as follows:

- The motive to develop and apply a numerical model is the awareness and cognition of a physical problem which is given, for example, by complex interacting processes that are aimed to be described and simulated. The scope of the problem has to be defined, i.e. which processes are relevant on which time- and length-scale.
  → Chapter 2

- The processes that had been identified before to be relevant must be parameterized by mathematical equations. This leads in general to a set of governing equations (e.g. balance equations for mass and heat) and in many cases to additional constitutive relations (e.g. to evaluate the fluid properties as functions of the state variables pressure, temperature, etc.) that are needed for the closure of the system.
  → Chapter 3 and Chapter 4.

- The system of partial differential equations that has arisen from the previous step needs to be solved. In cases where this is not possible analytically - which is typically the case for the problems that are addressed in this work - the continuous problem has to be transfered to a discrete one by discretizing the equations in space and time. Also potentially occuring non-linearities in the equations require a treatment to generate linear systems of algebraic equations that can then be solved by appropriate solvers.
  → Chapter 5

- For the individual problem the model domain, the mesh, the initial and boundary conditions, the time-step size, the convergence criteria, etc. must be defined in order to perform the actual simulation run. The produced output files can then be visualized or evaluated and analyzed otherwise.
  → Chapter 6

Since we address different topics in this work, it might be that a reader is interested only in one or two of them. Figure 1.6 provides an illustrative overview of the contents and structure of this thesis. The different topics that are addressed could be subsumed by

- Contaminant spreading and thermally enhanced soil remediation of contaminated sites.

- CO_2 storage in geological formations including the combination with the recovery of gas and oil.

- Water-gas systems in cathodic diffusion layers of PEM fuel-cells.

- Methane migration in abandoned coal mines.

- The influence of matrix deformation or structural alterations on flow and transport processes, for example, in cohesive soils or in diapers.

The latter two are not illustrated by applications in Chapter 6.

For example, a reader who is interested in modelling CO_2 sequestration processes could read Chapter 1 (Introduction) as well as Secs. 2.4 and 4.3. Chapter 5 is more general and not specific to one of the topics. In Secs. 6.4 and 6.5 one finds some illustrative examples dealing with CO_2 storage. The final Chapter 7 (Summary and Future Perspectives) is again not topic-specific.

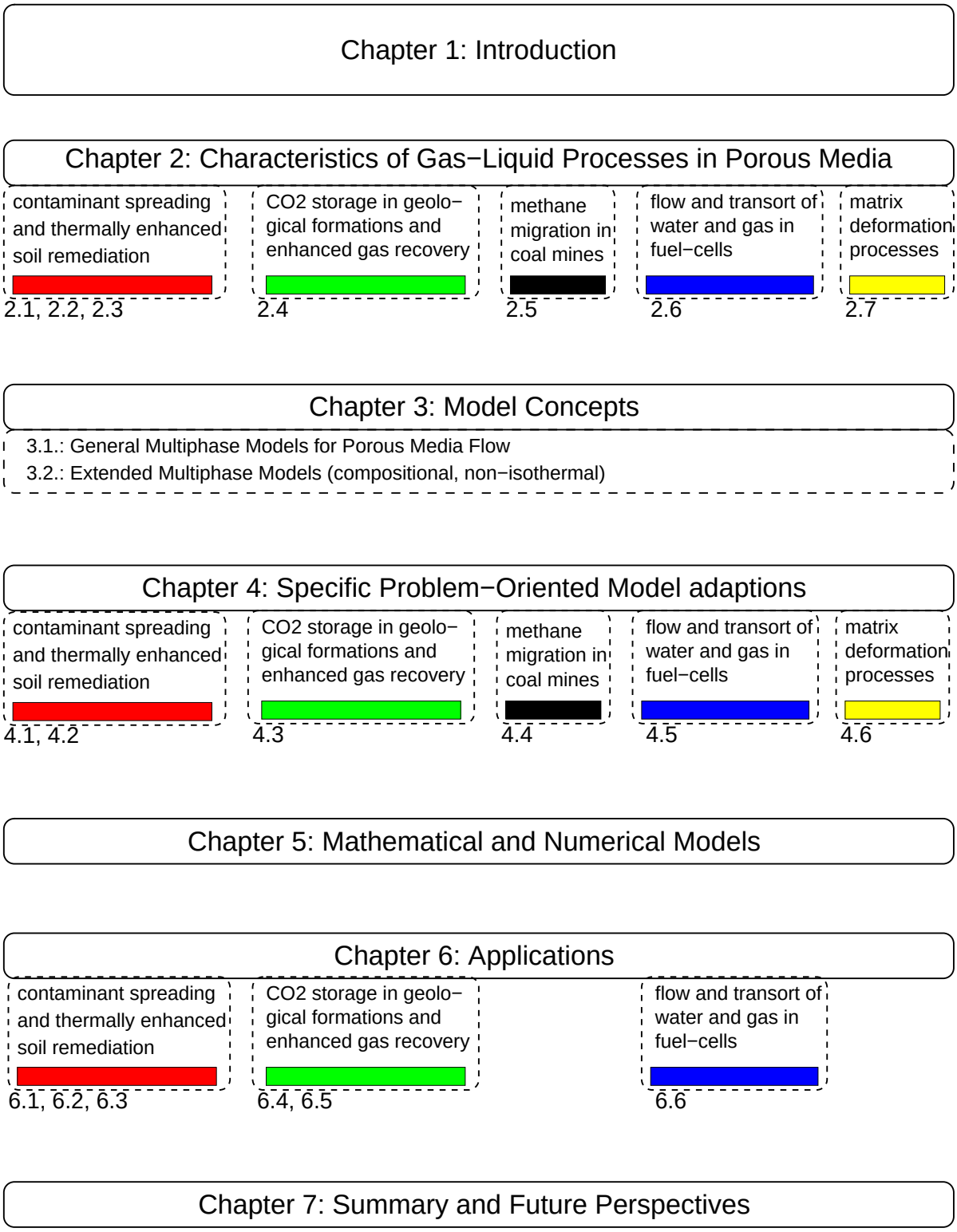

Figure 1.6: Structure and topics of the thesis.

Chapter 2

Characteristics of Gas-Liquid Systems in Porous Media

In this section, we explain the characteristic behavior of different gas-liquid multiphase flow problems in the subsurface and in porous diffusion layers of fuel-cells. We further outline the respective issues and specific problems to be addressed by numerical simulations. This gives us the motivation for the development of model concepts (see Chapter 3) that are adapted to the specific problem-related degree of complexity.

2.1 Contaminant Spreading in the Unsaturated Zone

The unsaturated zone (vadose zone) is a region in the subsurface that represents the interface between the saturated groundwater zone and the atmospheric environment. The unsaturated zone is very important for agriculture since it provides the water for the growth of the plants and is in strong interaction with the local climate and water cycle. The moisture content of a soil depends on several factors, obviously on the climate, but also on the water retention capacity and on the depth of the groundwater table below the ground surface. Generally, fine materials reveal better water retention capacities than coarser soils which is an effect of capillarity. Also the capillary fringes are higher in finer materials. Characteristic for the unsaturated zone is that the gas phase (soil air) is normally at atmospheric pressure. The presence of soil air in the unsaturated zone is due to its high mobility often of only minor influence on the flow of liquid phases like water or liquid contaminants. Thus, some models apply an equation, that is named after *Richards* (1931) [147] and assumes an infinite mobility of the soil air.

All potential contaminants that endanger the groundwater quality normally have to pass the unsaturated zone. Many contaminants reside there for a long time since they become trapped due to different mechanisms. They pose therefore a serious threat to the aquifers below since they may be washed out by the natural groundwater recharge due to precipitation and in this way they can be shifted into the saturated zone. Dependent on whether the contaminant exists in a separate liquid phase or is dissolved in the water phase or in the soil air, several basic trapping mechanisms for contaminants in the unsaturated zone can be distinguished.

- Contaminants existing in an own liquid phase, for example, NAPLs:

  - Typically, liquid contaminants leave a trace of an immobile residual saturation on their way through the unsaturated zone. How much liquid phase can be trapped depends on several factors, mainly on the magnitude of capillary forces and thus on the soil type, the interaction between the liquid, gaseous, and solid phases, etc. (see Sec. 3.1.4). Another important parameter for the residual trapping of contaminants is the viscosity. The more viscous a liquid phase is the more pressure gradient is required to keep it flowing.
  - If the unsaturated zone is strongly heterogeneous, it may occur that the downward flowing liquid pools on low-permeable lenses. It is a characteristic feature of multi-phase systems in porous media that low permeable zones filled with a wetting fluid (mostly water) can pose a capillary barrier for a non-wetting phase. Thus, there is a certain overpressure required for the non-wetting phase to penetrate through such lenses (see Sec. 3.1.4.1).

- Dissolved contaminants in the water phase, for example, NAPLs, nitrate, pesticides:
  - Soils have generally a capacity to adsorb dissolved components in the water. Adsorption is a complex physical and/or chemical process and is commonly described by isotherms as a function of the components partial pressures (see Sec. 4.1.4). Varying pressures, temperatures, or concentrations can cause an adsorption or desorption of contaminants in the soil. Generally, soils with high contents of carbon tend to have higher sorption capacities.
  - Dissolved contaminants can also be simply trapped in residual (immobile) water. These can then be easily remobilized if the water saturation increases, for example, by precipitation.

- Evaporated contaminants in the gas phase, for example, NAPLs:
  Actually, evaporated contaminants in the unsaturated soil air are not really trapped there since the soil air is in general a rather mobile phase. However, these vapors may dissolve into the soil water and then underly the trapping mechanisms as described above.

In this work, we focus on contaminants that are able to form a separate liquid phase (NAPLs). However, they can also to some degree dissolve into the water phase and therefore contaminate, for example, drinking water resources. From the point of view of a modeler it will make a big difference if compositional effects are of importance for the spreading of a contaminant in the subsurface or not, cf., e.g. [36]. This will be an aspect that we will have a closer look on later in Secs. 5.4 and 6.2. Accordingly, one could distinguish the governing processes during the spreading of a contaminant liquid phase by means of their miscibility with the ambient water or the soil air. An *immiscible displacement* is given if the infiltrating liquid contaminant phase displaces the ambient water or air without mixing by dissolution or evaporation. On the other hand, if the latter processes play a role, this could be denoted as *miscible displacement* and requires a more sophisticated model concept as will be explained in the following chapters.

At this point we should also mention another important aspect concerning the spreading of NAPLs in the subsurface, although this actually affects more the saturated groundwater zone and less the unsaturated zone. NAPLs can have a density higher or lower than that of the

groundwater. NAPLs that are denser than water are called *DNAPLs* (dense non-aqueous phase liquids), the lighter ones are *LNAPLs* (light NAPLs). While LNAPLs usually pool upon the groundwater table, DNAPLs are able to penetrate into the saturated zone and the vertical propagation is not constrained by the water table. Thus, DNAPLs are even more feared than LNAPLs since this characteristic behavior makes the choice of the remediation method for a contaminated site rather difficult [62]. This discussion will be continued in the next two sections dealing with thermally enhanced remediation techniques in the unsaturated (Sec. 2.2 and in the saturated zone (Sec. 2.3).

2.2 Thermally Enhanced Soil Vapor Extraction in the Unsaturated Zone

Since the 1980s, the remediation of contaminated soils became an increasingly important topic for environmental engineers in the industrialized countries worldwide. A huge number of contaminated sites endanger the drinking water resources. Estimates assume that in Germany alone more than 200.000 sites with NAPL-contaminations exist [47]. Thus, it is a huge ecological and economical challenge to develop efficient remediation techniques. In this section, we focus on soil vapor extraction in the unsaturated zone which is meanwhile a state-of-the-art on-site in-situ technique for NAPL-contaminations in the unsaturated zone [60, 17, 112]. The idea is simply to extract the contaminants with the soil air which requires the transition from the liquid phase into the gas phase. The fact that many NAPLs have relatively low vapor pressures, i.e., their evaporation rate is rather small at ambient temperatures, makes conventional soil air extraction a lengthy and inefficient technique. This holds particularly if the unsaturated zone is strongly heterogeneous so that the soil air flows along paths of low resistance and does not even reach entrapped contaminations in low-permeable regions. The logical consequence is that thermal energy is required to heat up the soil and increase the evaporation rate of the NAPLs. This can be done on various ways, for example, by injecting steam or a hot steam/air mixture, or also with fixed heat sources (thermal wells).

Figure 2.1 illustrates the basic assembly for a soil air extraction thermally enhanced by an injection of steam. An extraction well is placed into the source zone of the NAPL contamination. This is surrounded by injection wells (in the 2D-figure one well on each side).
Then, steam can be injected into these wells and deliver its thermal energy to the soil. When the hot steam comes into contact with the cooler soil, it transfers its latent heat of vaporization. Thus, the steam condenses and liquid water accumulates while at the same time the local soil temperature increases. Upon reaching the temperature which is required for preventing further condensation, the steam/condensation front can move on. The propagation of this front is very stable since potentially developing fingers are quickly smoothed out by heat conduction. Obviously, this behavior depends on the degree of heterogeneity. Given large low-permeable lenses, they can cause a local retardation of the temperature increase while the steam/condensation front can move on in the higher permeable zones. For the heating of the low-permeable heterogeneities heat conduction becomes an important process since it allows that also these regions can be heated up. The contaminants evaporate and thus become mobile within the gas phase with which they can be extracted.

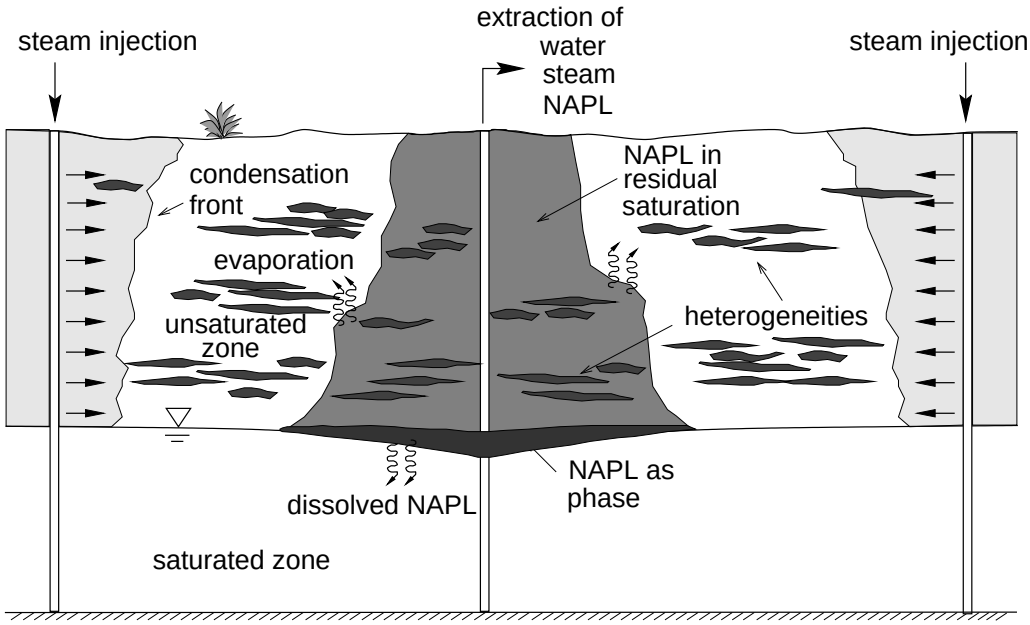

Figure 2.1: Thermally enhanced soil vapor extraction [57].

A process of particular interest concerning the remediation of low-permeable heterogeneities is diffusion. Since the advective flow of air or steam occurs more or less around the regions of low permeability, it is the diffusion of evaporated contaminants in the gas phase that determines the success of a remediation. If low-permeable lenses can be heated up, mainly by heat conduction, then the local concentration of contaminant vapor in the gas phase increases and thus also the concentration gradient and the diffusive flux out of the lenses.

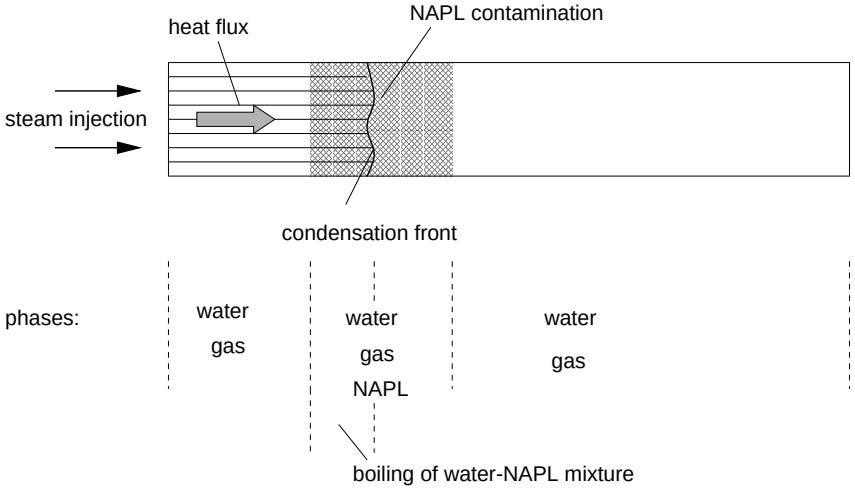

Figure 2.2: Sketch of steam injection for the remediation of a NAPL-contaminated unsaturated porous medium.

Figure 2.2 gives schematically a 1D situation of a steam injection into a NAPL contaminated soil. Typically, different combinations of fluid phases are present in the domain of interest. Within the

NAPL contamination we have three phases (water, gas, NAPL) while there are only two (water and gas) elsewhere.
Behind the front, the gaseous steam flow represents an efficient heat flux to the front since the hot steam has a comparably huge specific enthalpy (see also Fig. 3.19). According to Fig. 2.2, there are two distinct zones within the NAPL contamination. The zone which is ahead of the front is still in its original state. In that zone, where the steam already arrived, the mixture of liquid phases (here: NAPL and water) boils together. This boiling process of two immiscible liquid phases is the reason for a characteristic behavior of the temperature as illustrated in Fig. 2.3. The temperature profile between the injection well and the extraction well reveals distinct segments. Ahead of the front, the temperature is still at its initial value, then the front is characterized by its steepness and the jump to a plateau temperature in that part of the steam zone where liquid NAPL still exists. There, the mixture of liquid NAPL and liquid water boils which reduces the boiling temperature unto a value that is determined by the saturation vapor pressure curves of both liquids (see Sec. 4.1.1). After all liquid NAPL has evaporated, the temperature can increase to the boiling temperature of pure steam.

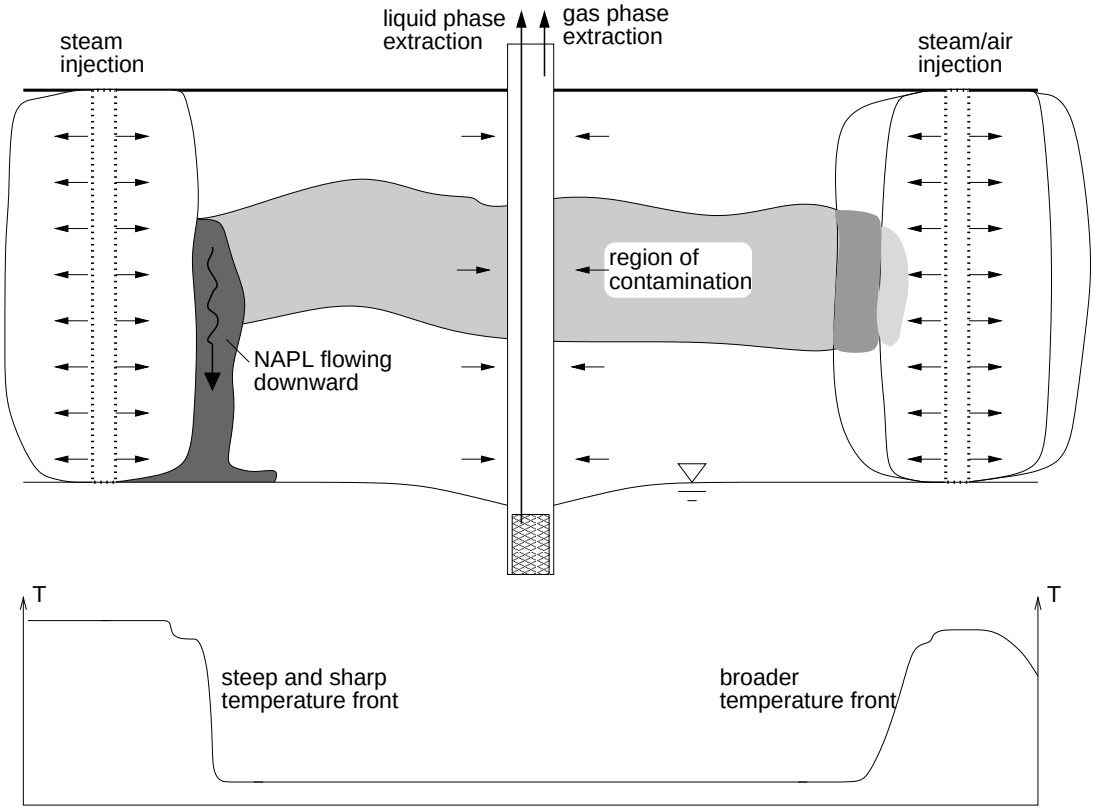

Figure 2.3: System behavior and temperature profile for an injection of steam or steam/air into an unsaturated NAPL-contaminated zone.

Figure 2.3 also shows another characteristic behavior of this system. At the steam front, (re-)-condensing NAPL accumulates which can lead to high saturations so that liquid NAPL becomes mobile. In the unsaturated zone, this leads typically to a downward flow of the NAPL towards the groundwater table (see Fig. 2.3 left). In case of an LNAPL, this leads to a pool on the water table.

For a DNAPL the situation is worse. Since the density of a DNAPL is higher than that of water, the DNAPL can penetrate into the saturated zone and move into deep regions of an aquifer where its recovery becomes very difficult or even impossible. Thus, for DNAPLs, steam injection is a technique which implies serious risks. Therefore, one tries to prevent this downward-sinking of DNAPLs by limiting the saturation of the accumulating condensates at the front. This can be achieved by adding air to the injected steam. Air is not condensible and can therefore transport the evaporated contaminants beyond the condensation front. But, since the heat capacity of air is rather low compared to steam, this transport beyond the steam front does not reach very far, however far enough to broaden the zone of (re-)condensation. Furthermore, the temperature front becomes flatter (see Fig. 2.3 right). Both effects act towards limiting the liquid NAPL saturation. By controlling the ration of steam and air during the injection, the remobilization of liquid DNAPLs can be prevented. However, it should be clear that this holds theoretically. In practice, it is hardly feasible to optimize the steam/air ratio since the situation in the subsurface can not be monitored sufficiently.

One should further mention here that an increased temperature has two other minor effects that also increase the mobility of residually trapped NAPLs. First, the capillary effects that are responsible for the liquid retention capacity of the soil are reduced by decreasing surface tensions. Second, the viscosity of NAPLs decreases with increasing temperatures.

2.3 Steam-Injection in the Saturated Zone

For contaminations with DNAPLs, the injection of steam into the saturated zone is a relevant remediation option. Although the physical processes are essentially similar to an injection into the unsaturated zone, there is a major difference concerning the influence of buoyancy. In the unsaturated zone, the density difference between air and steam is negligible for the spreading of the steam. However, in the saturated zone, the density difference between steam and the ambient liquid water is three orders of magnitude. This has enormous consequences for the shape of the propagating steam zone. Upward-acting buoyancy forces compete with radially-acting gradients of the injection pressure (viscous forces). Depending on their ratio, the steam zone develops rather radially (viscous forces dominate over buoyancy) or it overrides the saturated region and escapes vertically (buoyancy dominates).

Figure 2.4 shows this basically different behavior of spreading steam zones in the unsaturated zone (left) and in the saturated zone (lower). A special case would be given if there is a confining impermeable barrier above the injection horizon. Then, the steam zone is forced into horizontal direction, however it can gravitationally override the saturated zone. This phenomenon is well-known in the petroleum industry where steam injection is applied for a long time as a means to enhance the recovery of oil from the reservoirs. In the remediation business, it is important to reach a distance as far as possible with an injection well in order to minimize the required number of wells for a given contamination. Thus, the radius of influence of an injection well is very important for the design and planning of a remediation scenario.

Ochs (2007) [131, 132] derived an expression to predict the shape of the propagating steam front

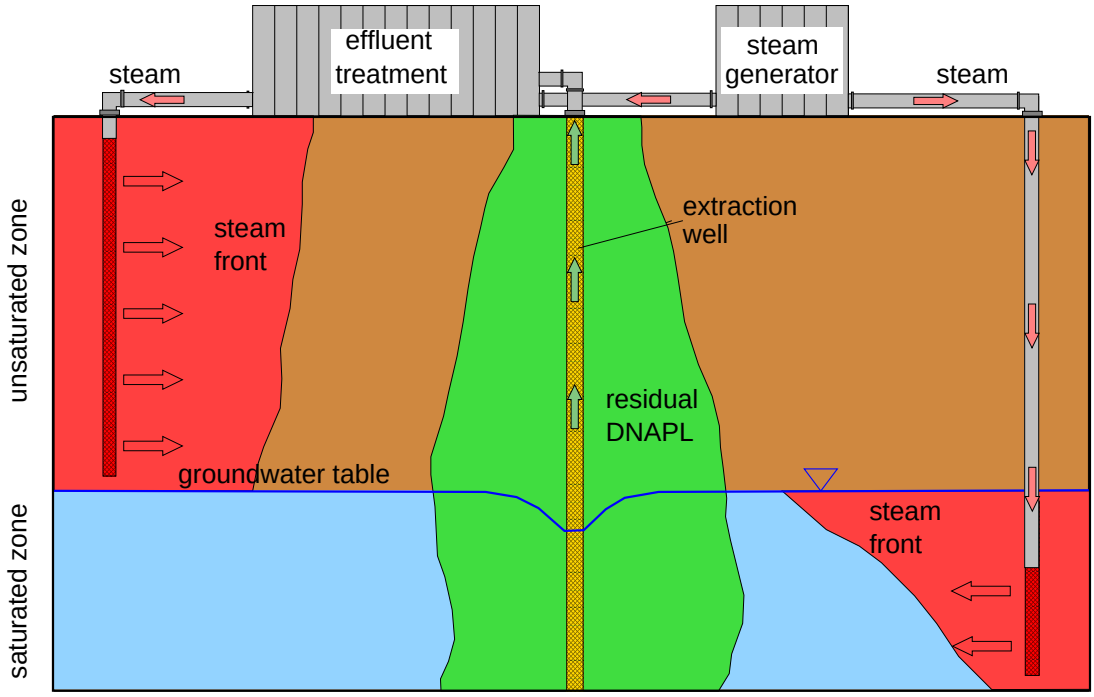

Figure 2.4: Steam front evolution during steam-injection in the unsaturated and in the saturated zone.

in the saturated zone. He based his considerations on the work of *Van Lookeren* (1983) [167] who was interested in the propagation of the steam in an oil reservoir confined by an overlying impermeable caprock. *Van Lookeren* states that the shape (inclination) of the steam front is a function of a dimensionless gravity number which is a measure of the ratio between viscous forces and buoyant forces. According to the definition of *Van Lookeren* and the extension for an unconfined spreading of steam in a two-dimensional water-saturated medium made by *Ochs*, the gravity number is given as

$$\mathrm{Gr}_{\mathrm{lin}} = \frac{\mu_s\, q_s}{b\, K_s\, \rho_s\, h\, (\rho_w - \rho_s)} = \frac{\text{viscous forces}}{\text{buoyant forces}}. \tag{2.1}$$

The dynamic viscosity μ_s of the steam and the densities ρ_s and ρ_w are fluid properties. K_s represents the permeability to steam, q_s is the steam injection rate and h and b are characteristic lengths of the transient steam zone. b stands in this case for the thickness of the quasi-2D flume which *Ochs* used for his investigations. h can be identified as the height of the steam zone. While in *Van Lookeren's* theory, this height was given by the height of the reservoir confined by the caprock, *Ochs* defined h to be the timely variable height of the steam zone. Since h appears in the denominator of Eq. (2.1), we can reckognize that at later times (increasing h), the gravity number $\mathrm{Gr}_{\mathrm{lin}}$ becomes smaller. Thus, buoyancy effects gain influence with increasing steam zones.

Ochs could prove in a series of numerical simulations and laboratory experiments that the gravity number of Eq. (2.1) is useful for the prediction of the steam front propagation. The ratio of the injection rate q_s versus the permeability K is the effective parameter that determines the thermal radius of influence of an injection well.

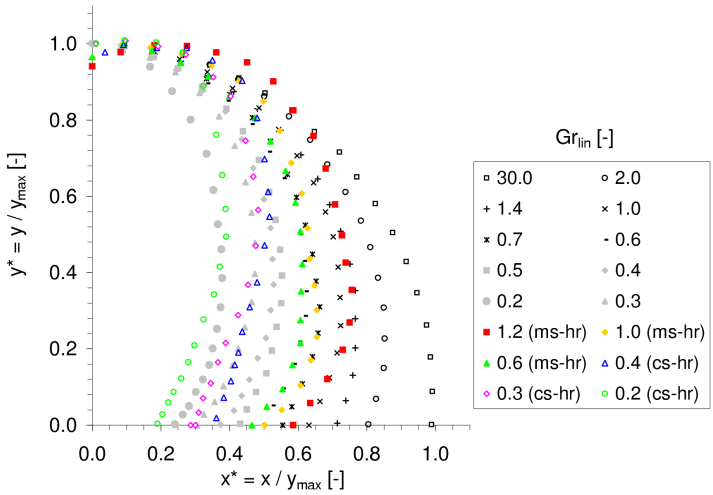

Figure 2.5: Dimensionless diagram with characteristic type curves and experimental data as a function of Gr; ms/cs indicates results of experiments with a medium/coarse sand, hr indicates that a comparatively high steam injection rate of 3.6 kg/h is used [132].

In Fig. 2.5, a set of characteristic type curves is assembled that was obtained from performing a series of numerical simulations for different gravity numbers. Thereby, q_s and K were varied. Since the results used for the plots in Fig. 2.5 are taken for a constant q_s, these plots are based on a variation of the permeability K. The type curves are compared with experiments in different sands. One can see, that the results of the experiments fit well into the type curves of the medium sands, while there are obvious discrepancies between experimental and simulated type curves. The reasons therefore are (i) that some boundary effects in the experiment are not sufficiently taken into account by the model, and (ii) that the approach for the calculation of the effective permeability K_s is simplified too much. This is discussed in detail, also for a three-dimensional radial steam zone, by *Ochs* (2007) [130] and would be beyond the scope of the discussion here.

2.4 CO_2 Storage in Geological Formations

The storage of CO_2 in geological formations is currently intensively discussed by science, politics, and industry as an option to reduce the emissions of this greenhouse gas into the atmosphere. The *Carbon Capture and Storage (CCS)* technology aims at separating carbon dioxide from the flue gases of power plants (fossil-fuelled or other CO_2 emitting ones) with a subsequent transport to a site where it can be injected for storage into a deep geological formation, cf., for example, the special report of the *Intergovernmental Panel on Climate Change (IPCC)* [95], from which also Figs. 2.6 and 2.8 are taken. Capturing CO_2 from power plants increases the costs of the produced energy significantly since it consumes much energy. Thus, it also increases the

needs of fossile resources. *IPCC* (2005) [95] gives estimated figures of 10-40% increase of fuel needs and 30-60% increase of energy production costs depending on the specific circumstances of the applied CCS technique.

2.4.1 Available Target Formations

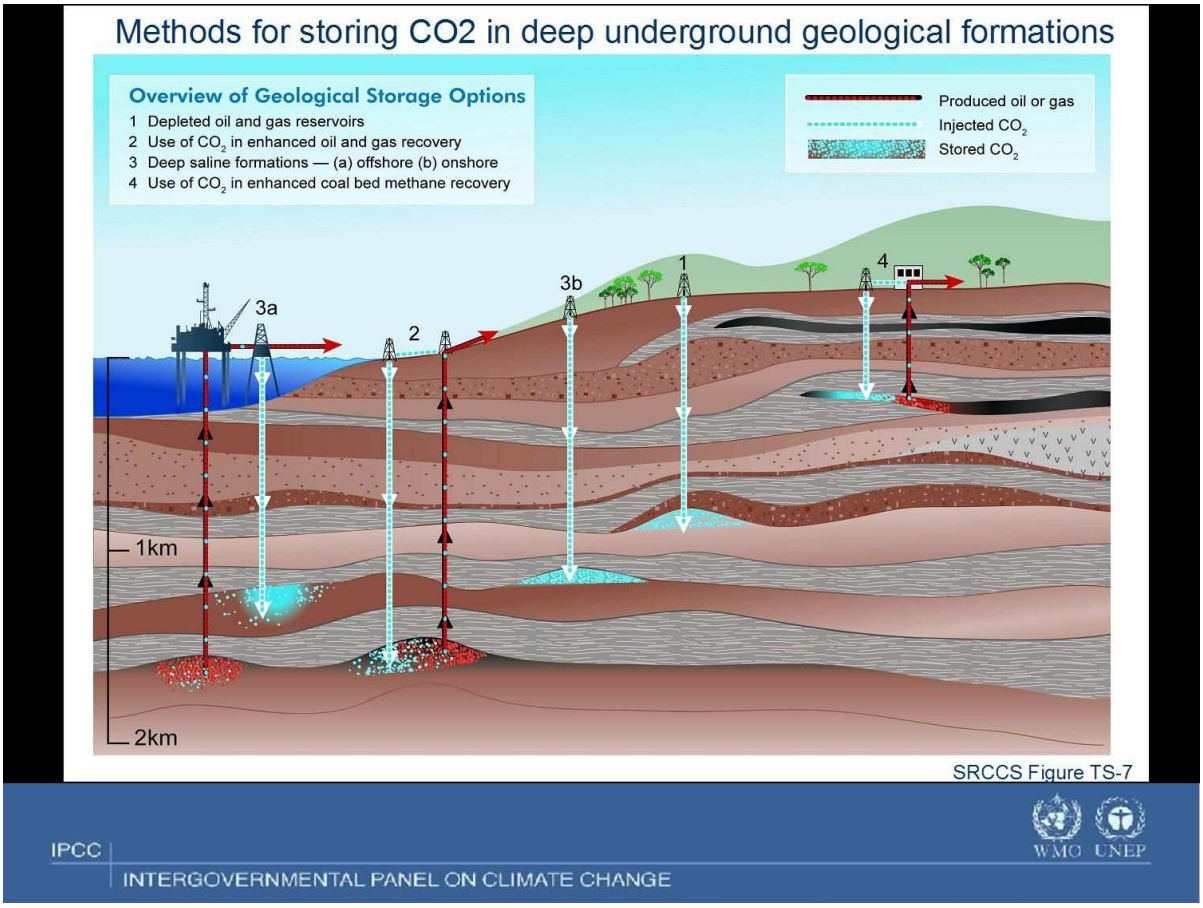

Figure 2.6: Overview of CO_2 storage options, courtesy of *IPCC*.

Different target formations are available for an underground storage of CO_2. They are illustrated in Fig. 2.6. We will discuss them in the following in the order in which they are numbered in Fig. 2.6, although later on we will particularly focus on saline aquifers. All of the target formations are located in sedimentary rocks since only those are porous enough to have storage capacity of interest.

Depleted oil and gas reservoirs represent somehow natural storage options since they have already proven their ability to prevent fluids from leaving the reservoir over long periods of time. The existence of an effective overlying impermeable caprock is in such cases given. CO_2 can also be used to enhance the recovery of oil and gas from the reservoirs. This can be achieved by injecting compressed CO_2 into the reservoir where it expands and displaces more oil or gas towards a production well. Furthermore, CO_2 dissolves in the oil and lowers its viscosity which

increases the flow rate of the oil. **Enhanced oil and gas recovery** (EOR) - sometimes also called **improved oil recovery** (IOR) - and **enhanced gas recovery** (EGR) is already applied for some decades by the petroleum industry. This option of CO_2 storage has the advantage that the costs are offset by the sale of additionally recovered oil or gas. However, the capacities of declining oil and gas fields are limited. They are also geographically distributed which sets up the problem of transport infrastructure. One should note that the combustion of the extra oil/gas obtained from EOR/EGR releases typically more CO_2 to the atmosphere than can be removed during the injection.

Deep **saline aquifers** are considered to have large underground storage capacities for CO_2. Preferably, these aquifers should be deeper than 800 m below ground surface. Then, the CO_2 is in supercritical state (see Fig. 4.9) and has a typical density between 600 and 800 kg/m^3. A high CO_2 density allows a more efficient usage of available storage capacities and reduces buoyancy on the CO_2 phase. Nevertheless, this means that CO_2 is still buoyant and tends to move upwards. Saline aquifers as target formations for CO_2 storage need to have reasonably high porosities and a low porous/low permeable overlying caprock preventing upward migration. Over time, the CO_2 plume beneath the caprock will dissolve in the brine. CO_2-rich brine is heavier than 'fresh brine' and tends to sink down to the bottom of the saline aquifer. Aquifers that contain silicates rich in calcium, magnesium, and iron are likely to react with the CO_2 to form carbonates. This processes will make the storage very permanent. On the other hand, geochemical reactions may also affect the permeability of the aquifer and thus reduce the injectivity.

Among the geological formations with a potential suitability for CO_2 storage is **coal**. It is an especially attractive target since CO_2 can be used to **enhance** the recovery of **coal-bed methane** (ECBM), cf. [140]. The processes that govern the storage of CO_2 in the coal and the simultaneous enhanced release of methane from the coal are manifold and complex. Commonly, the coal and adjacent strata are dewatered in order to lower the reservoir pressure, therby causing gas (methane) to desorb. Coal has typically open fissure and fracture networks which are important since they allow an improved access to large surface areas of coal which is necessary for a rapid sorption of the CO_2 to the coal in its micropores. The sorption capacity of coal is sensitive to pressure and temperature. Competitive sorption of the components CO_2 and CH_4 to goal tends towards a higher sorption capacity for CO_2. Some experimental investigations under high pressures have been carried out, for example, by *Busch et al.* (2006) [23], however there is still a great need for further research in this field since the exact mechanisms dominating the adsorption/desorption behavior are poorly understood.

2.4.2 Trapping and Potential Leakage Mechanisms

Effective geological storage of CO_2 can occur by different interacting physical and geochemical processes and trapping mechanisms. This is illustrated schematically in Fig. 2.7 which is modified after the *IPCC Special Report on Carbon dioxide Capture and Storage* (2005) [95]. The dominating processes and trapping mechanisms are in the following discussed particularly with regard to storage in saline aquifers. However, this discussion can easily be extended to the other potential target formations mentioned in Sec. 2.4.1.

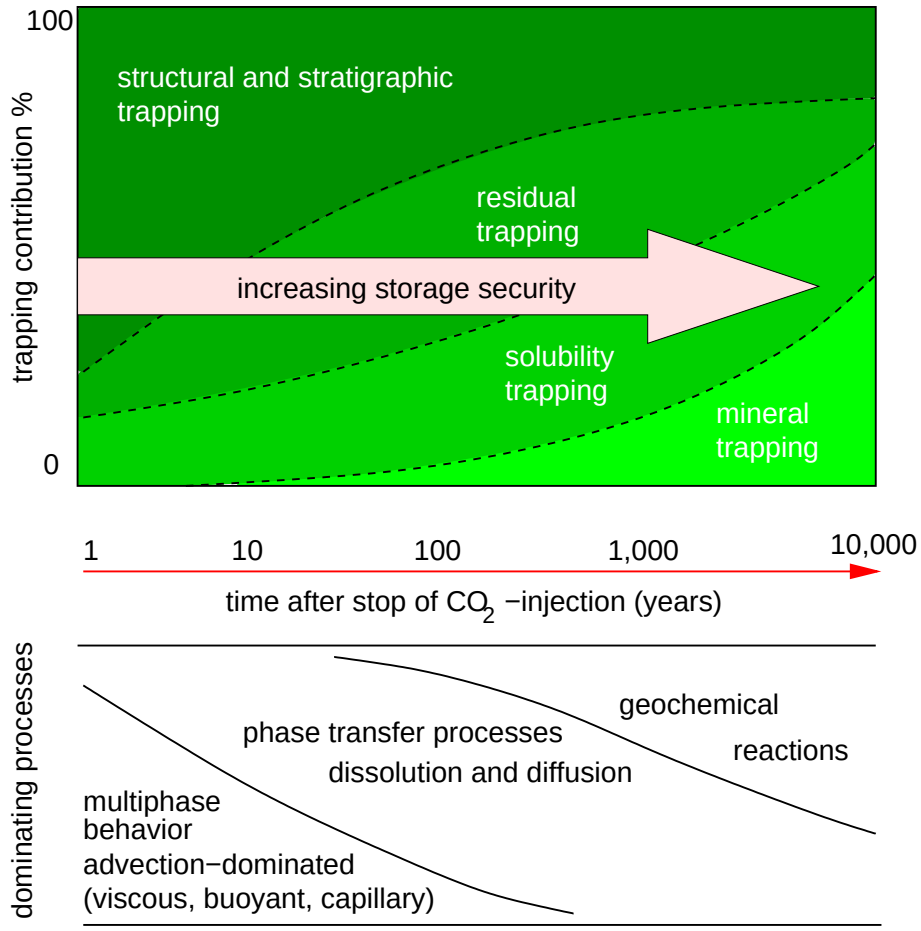

Figure 2.7: Variation of the trapping mechanisms and the dominating processes on different time-scales (modified after [95]).

When CO_2 is injected into a formation it forms a discrete phase around the injection well. The ambient water (brine) is displaced and the CO_2 moves both laterally due to the pressure gradient induced by the injection and vertically due to buoyancy. This advection-dominated multiphase flow behavior can also be affected by capillary effects depending on the properties of the rock formation. As long as the discrete CO_2 phase is mobile, it requires **structural and stratigraphic trapping** by seals (caprocks) to prevent an escape from the target reservoir towards more shallower depths or eventually back to the atmosphere. Such seals are, for example, very low permeable shales or salt beds. Also faults by folded or fractured rocks can serve as structural barriers although, under certain circumstances, they can also represent preferential pathways for escaping CO_2. One might have the suspicion that the displacement of brine in the saline aquifer by the injected less viscous CO_2 is subject to viscous fingering. But *Garcia & Pruess* (2003) [68] concluded from their study on flow instabilities during injection of CO_2 into saline aquifers that potentially occuring unfavorable mobility ratios are counteracted by capillarity and dissolution of CO_2 in the aqueous phase, and thus the distribution of permeability rather than hydrodynamic instability dominates the multiphase fluid displacement.

CO_2 migration will stop either upon reaching structural/stratigraphic barriers or if the mobility of

the discrete phase becomes zero. This occurs when the CO_2 saturation decreases until the residual saturation which is a strong function of the capillary pressure–saturation relationship (see also Sec. 3.1.4). In Fig. 2.7, this mechanism is denoted as **residual trapping**. The mobility of the CO_2 in the multiphase system CO_2-brine is affected by effects hysteresis. CO_2 is the non-wetting phase in the reservoir. While the injection of CO_2 into the brine-filled reservoir represents a drainage process, a stop of the injection causes a reversal from drainage to an imbibition process. Thereby, parts of the CO_2 become trapped in the pores. The discontinous and immobile gas bubble lead to an increased residual saturation. On the macroscopic scale, on which we commonly develop our model concepts, this can be expressed by hysteretic relative permeability functions [98].

In the long term, increasing quantities of CO_2 dissolve in the formation water and are then subject to the movement of the groundwater and the diffusion/dispersion processes therein. The above-mentioned *IPCC* report refers to this as **solubility trapping**. The great advantage of solubility trapping concerning the storage safety is that the buoyancy effects vanish once that the CO_2 is dissolved. The water that is rich of dissolved CO_2 becomes even heavier and tends to sink towards the bottom of the reservoir. Indeed, this process is rather slow and occurs only on a larger time-scale than the advection-dominated multiphase spreading. Another term that is often used - and that comprises residual and solubility trapping - is **hydrodynamic** trapping.

Dissolution of CO_2 in the water (solubility trapping) also forms ionic species. This causes changes in the pH and initiates geochemical reactions. If some fraction of the CO_2 can be converted to stable carbonate minerals, this **mineral trapping (or geochemical trapping)** is expected to be the most permanent form of geological storage [75]. The geochemical processes themselves are comparatively slow taking in the range of thousands of years.

Figure 2.7 puts the estimated time-scales of the physical and geochemical processes that govern the trapping of CO_2 into a context. There is obviously a gradual change of the dominating processes and it is difficult to really separate the time-scales. Nevertheless, this will be an important issue when thinking about the coupling of models of different complexity (see also Secs. 5.4 and 6.2).

As important as the understanding of the trapping mechanisms is the knowledge about potential leakage pathways. Figure 2.8 illustrates potential leakage mechanisms in saline formations and suggests remedial measures in case of an occurence of a leakage [95]. The basic pathways for an escape from a formation are accordingly either through the pore system or through fractures and faults in the caprock (Cases B, C, D in Fig. 2.8) which can also be antropomorphic such as poorly completed or abandoned wells (Case E in Fig. 2.8, see also Fig. 2.9). An escape through the pore system requires that the capillary entry pressure of the caprock has to be overcome (Case A in Fig. 2.8). The processes that lead to a leakage through fault zones are manifold and depend strongly on the conditions at the specific site. Cases F and G show that it is in principle also possible that dissolved CO_2 is transported with a groundwater flow towards the atmosphere or the ocean.

Formations that have been explored for oil and gas production appear to be attractive for the in-

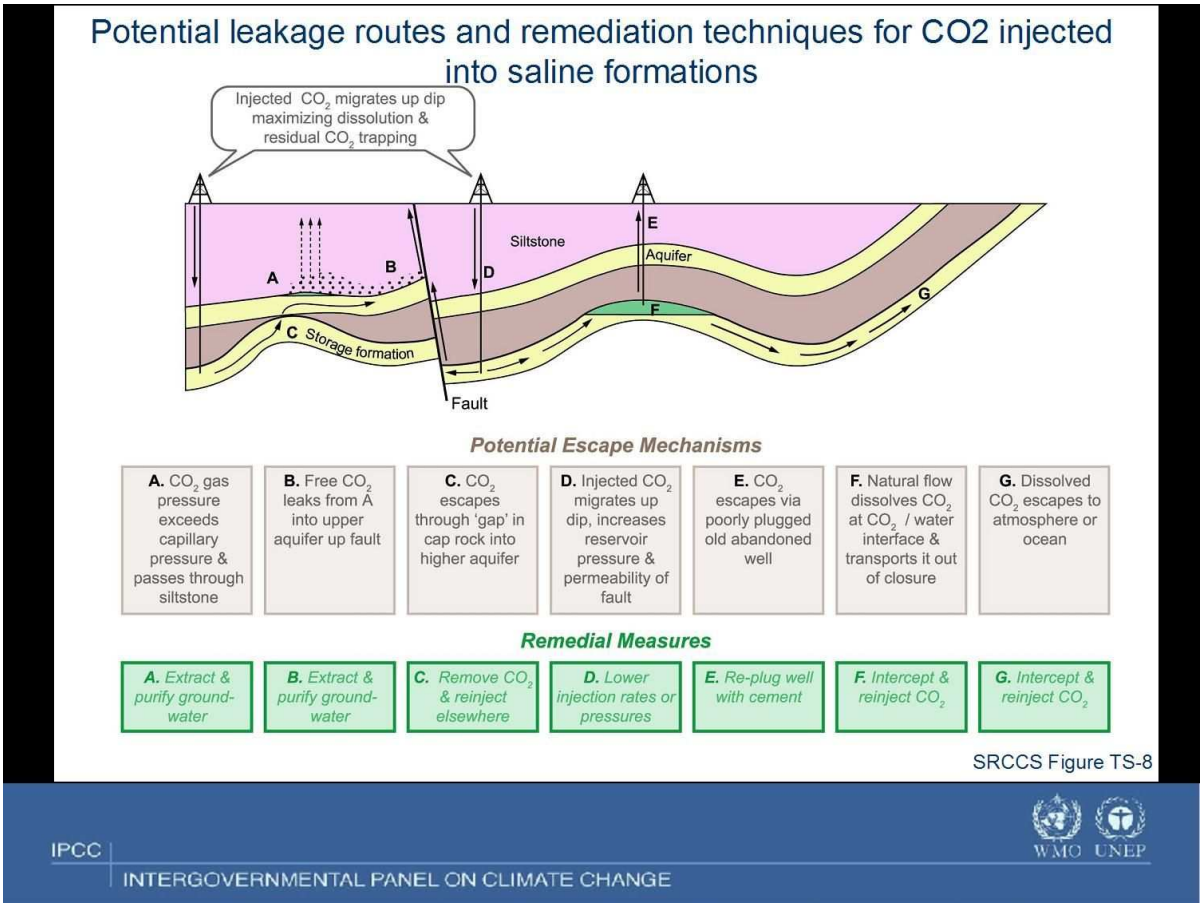

Figure 2.8: Overview of potential leakage mechanisms, courtesy of *IPCC*.

jection of CO_2 since they have an existing infrastructure of oil and gas wells. On the other hand, it is particularly typical for such formations that they are downright perforated by many wells, which implies an increased risk of escape (Fig. 2.9). *Gasda et al.* (2004) [69] address this problem in detail for a saline formation in the mature sedimentary Alberta Basin in Canada where the average well-density is about 0.3 wells per km^2. The escape pathways in old abandoned wells include, for example, fractures in the cement plugs, corroded casings, etc. Some authors also developed and applied mathematical and numerical models for this leakage scenario through abandoned wells, cf. [128, 54].

2.5 Methane Migration in Abandoned Coal Mines

Uncontrolled methane migration is a problem that is linked with the closure of coal mines and the stop of the ventilation. Recently, this has become a big topic in Germany since many coal mines in the Ruhr area and in the Saarland are currently shut down.

Coal mining requires in general a dewatering of the groundwater zone. This lowers the hydrostatic pressure on the coal seams and enhances the release of adsorptive-bound methane from the coal. The amount of methane that can be adsorbed to the coal depends on its ambient par-

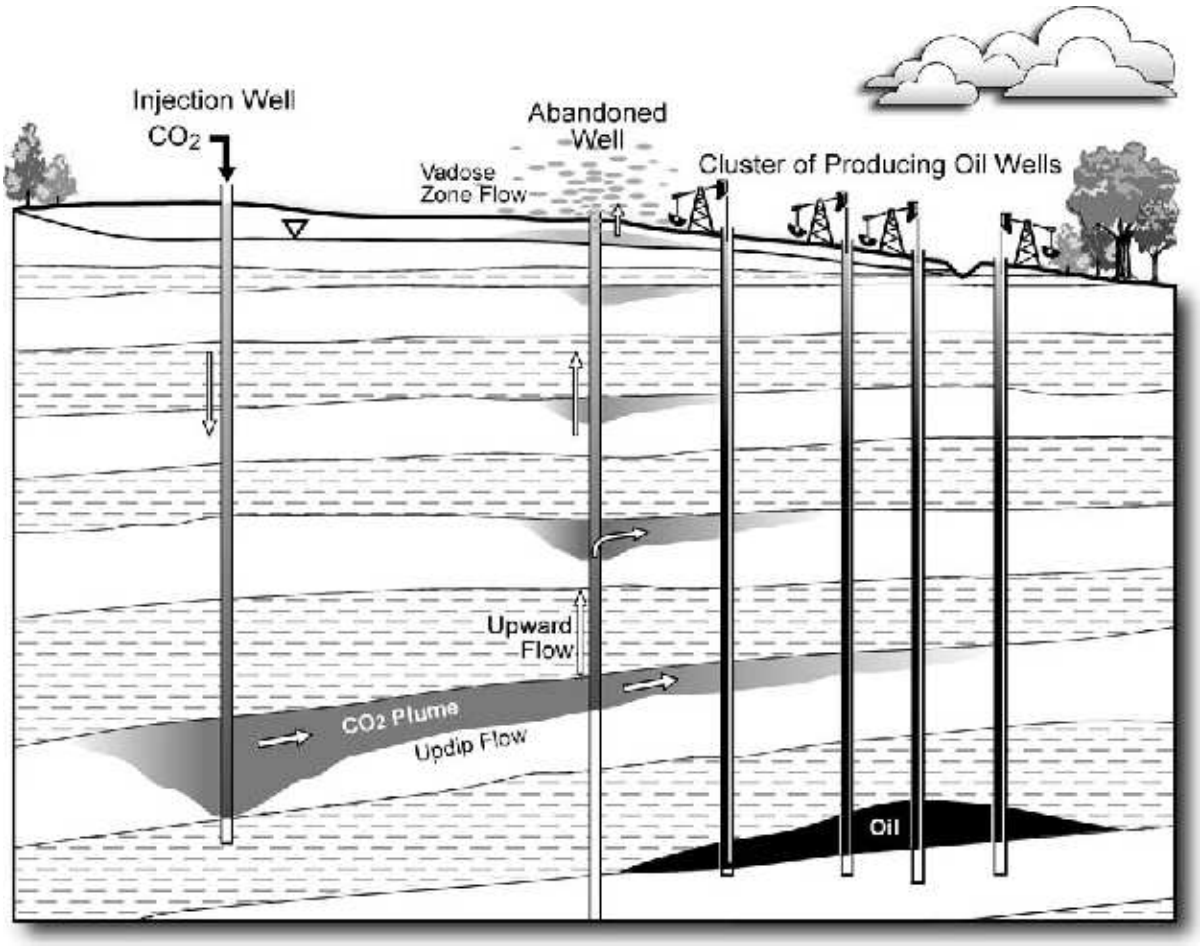

Figure 2.9: Typical situation of a possible injection scenario in a saline aquifer: CO_2 injection wells and producing oil wells in direct vicinity. Figure from *Gasda et al.* (2004) [69].

tial pressure. Thus, a pressure lowering in the coal seams shifts the equilibrium towards lower adsorbed gas contents in the coal. This phenomenon is utilized for the methane production in the enhanced coal-bed methane (ECBM) technology (see also Sec. 2.4.1). This process of continuous release of methane is even accelerated in the mining region where the coal is cracked and its specific surface is enlarged. During the operation of a coal mine, the released methane is well-controlled by the installed ventilation systems which collect it in the roads and shafts of the mine and transport it in a diluted concentration to the atmosphere.

The shut-down of a coal mine includes the stop of the dewatering and the ventilation. Since the rise of the lowered groundwater level unto its orginial level can last for several years, it takes quite a while to stabilize the adsorption/desorption equilibrium and to stop the further release of methane. Thus, there remains a time-period between the shut-down of the ventilation and the re-establishment of the original groundwater level in which the coal can emit further methane into the mine working. During this time, the migration of methane occurs uncontrolled. It depends on the release rates (methane source terms) and the local liquid and gas saturations whether methane is dissolved in the ambient water or forms a separate phase which experi-

ences strong buoyant forces towards the ground surface. It is likely that the major part of the desorbed methane gathers in the former roads and shafts of the coal mine and it is relatively easily accessible by gas extractions there [81]. However, a potential threat for above-lying residential areas will arise if the methane can gather in fault zones, migrate uncontrolled into shallower regions, and eventually escape somewhere into the atmosphere. Figure 2.10 (left) shows bubbles of methane appearing in a pond, the principle situation is also delineated in Fig. 1.1. Accumulations of methane, for example, in buildings or excavation pits represent particular risks for fire and explosions. This has been frequently observed in the German Ruhr area.

Once the dewatering is stopped, the increasing water level further enhances the buoyancy upon the methane. Potentially trapped accumulations of gaseous methane become also compressed by the re-increase of the hydrostatic pressure and tend to escape in upward direction through fractures and fault zones.

Figure 2.10: Methane bubbles in a pond (left picture), gas extraction system at the ground surface (right).

Measures, like concerted gas extraction wells (Fig. 2.10 (right)), that can be taken to reduce the risks of explosions and fire due to methane at the ground surface require a thorough understanding of the gas migration processes. As described above, these can be very complex single-phase or multiphase processes with compositional effects (dissolution/ degassing) and adsorption/desorption. Heterogeneities, fractures, and other fault zones play an important role since they determine the preferential pathways of the methane. In principle, the methane migration problems show great similarity with the problem of CO_2 storage in geological formations and the investigation of potential leakage pathways (see Sec. 2.4). The major differences are the

slightly different thermodynamic properties of methane and carbon dioxide (methane is lighter, less viscous, and less soluble in water) and the distribution of the source in the subsurface. The release of methane occurs widespread over large areas from the coal seams, while the carbon dioxide is injected punctually and spreads from the injection wells towards a more diluted concentration/saturation.

The aims of modelling and numerically simulating methane migration include (i) the prediction of potential accumulations of gas in the subsurface so that methane production wells (gas extractions, see Fig. 2.10 (right)) can be drilled, and (ii) the determination of release rates (source terms) since these can affect both the amounts of methane that reach the ground surface and the pathways that the gas takes.

For further details concerning the principle processes of methane migration from abandoned coal mines and the numerical simulation of these processes we refer, for example, to *Helmig et al.* (2006) [81] or *Hinkelmann et al.* (2004) [84].

2.6 Transport of Water and Oxygen in Fuel-Cells

Fuel-cells recently gained much attention as a promising source of power supply in electrical vehicles or portable devices. One of the different types of cells is represented by the polymer electrolyte membrane (PEM) fuell-cell which can be operated with hydrogen or methanol. It has the advantage that it can be operated in the range from ambient temperatures up to roughly 100 C. In order to turn fuel-cells into a really competitive alternative to fossil-fuelled engines, there is still a great demand for research concerning the cell performance and cost reduction. As will be explained in the following, a key role for the performance is due to the gas-liquid multiphase multicomponent system on the cathode side of the membrane-electrode assembly (MEA) (Fig. 2.11), cf., for example, *Acosta et al.* (2006) [2], *Pasaogullari & Wang* (2004) [139].

The PEM fuel-cell consists of a proton conducting polymer membrane between two porous catalytic electrodes. Both electrodes consist of a porous gas diffusion layer (backing) and a reactive layer containing a catalyst. This MEA as sketched in Fig. 2.11 is arranged between two cell plates that provide electrical connection and have flow fields (not shown in Fig. 2.11, see for this Fig. 2.12) that deliver the reactants to the surface of the reactive layer and allow the removal of the reaction products from the cell. Particularly in the cathode diffusion layer, this results in a complex gas-liquid system including the components oxygen (O_2), nitrogen (N_2), and water vapor (H_2O). It is in particular the cathode that potentially limits the overall cell performance. Reasons for this are the slower kinetics of the oxygen reduction reaction compared to the hydrogen oxidation and the transport limitations for oxygen. If the cell is operated with air instead of pure oxygen, which is preferred in order to keep operational costs low, the stagnant nitrogen hinders the oxygen transport. The water that is produced by the reaction at the catalyst layer further limits the oxygen transport towards the reaction layer which has a negative effect on the performance of a fuel-cell. This is caused by two different processes. First, depending on the temperature, a certain amount of the produced water forms water vapor which counter-diffuses in opposite direction to the oxygen. Furthermore, the other part of the water forms a liquid phase

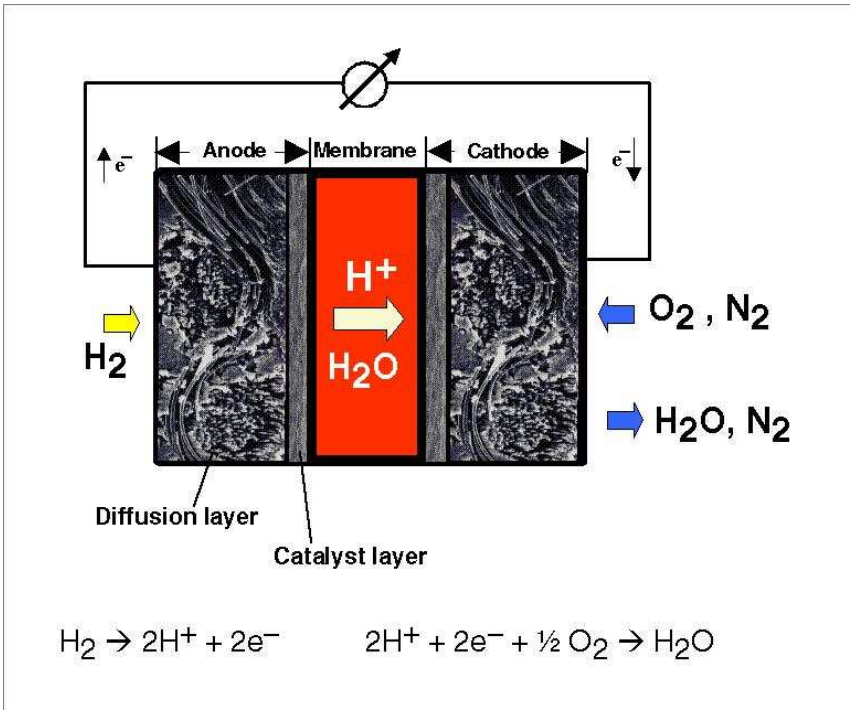

Figure 2.11: Membrane-electrode assembly (MEA) and overall reaction in a fuel-cell.

which can accumulate and thus reduce the mobility of the gaseous components including the oxygen. The accumulation of liquid water in the cathode diffusion layer is further enhanced by the electro-osmotic drag of water through the membrane.

What makes the water management in the cathode diffusion layer very difficult in practice is, that on the one hand the membrane has to be humidified to enable the transport of protons, but on the other hand, at high current densities, accumulating liquid water (produced by the reaction and electro-osmotic drag) hinders the gas/oxygen transport to the catalyst reaction layer. Liquid water in the catalyst layer also affects the oxygen reduction reaction. In practice, the diffusion layer is made of a teflonized conducting carbon material that has hydrophobic properties and advances the liquid water removal.

The thickness of the diffusion layers in a fuel-cell is typically less than one millimeter. That is why measuring the concentration profiles of the reactants, the products thereof, and the saturation profiles is hardly feasible. Mathematical and numerical models promise to help improving the understanding of the overall interaction of the different physical, thermodynamical, and electro-chemical processes involved in the fuel-cell. A special focus of recent model developments has been on the cathode.

The conditions in the cathode diffusion layer are strongly affected by the gas flow in the gas distribution channels whose primary task is the oxygen supply but they also have to take up and transport away the water produced by the reaction. Basically, two different types of flow fields are distinguished as illustrated in Fig. 2.12. The so-called *conventional flow field* consists of overall

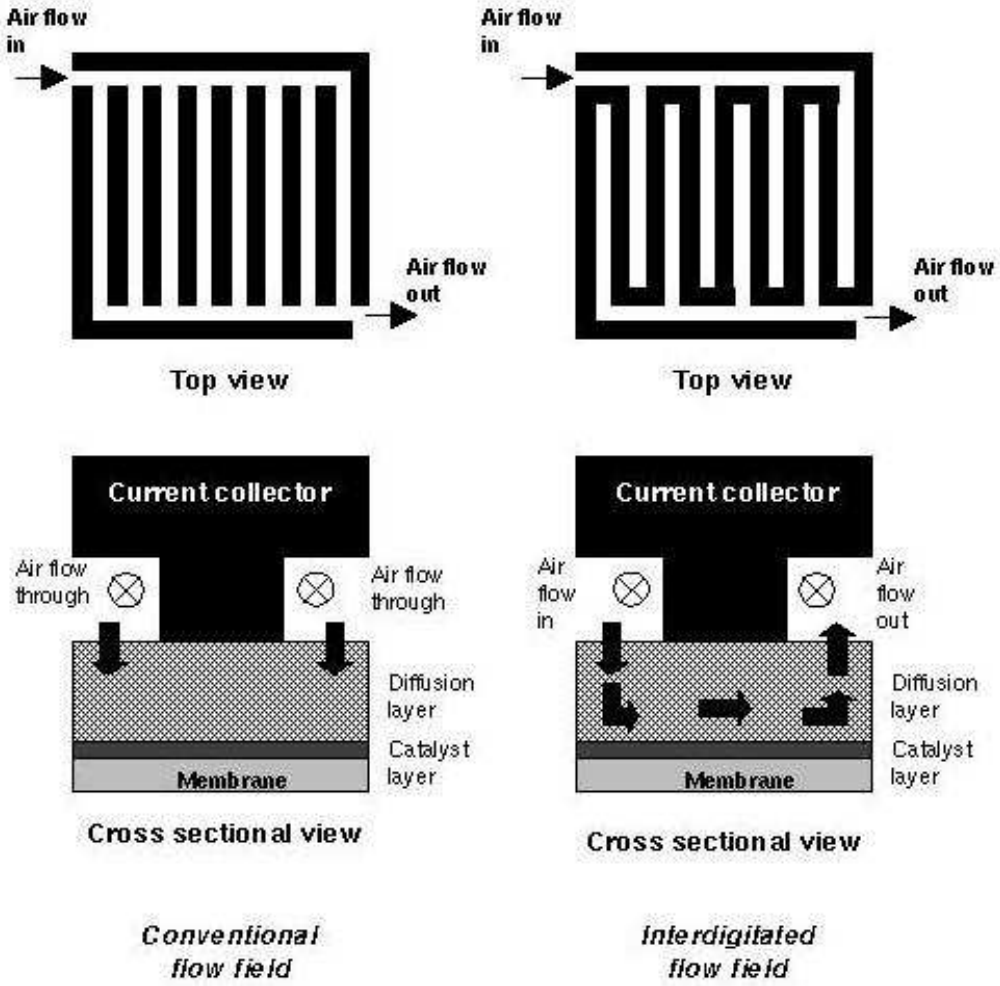

Figure 2.12: The difference of the principles of an interdigitated and a conventional flow field in the gas distribution channels.

connected channels which are in contact with the porous diffusion layer. The contact surface between channel and diffusion layer is periodically interrupted by the shoulders which serve as current collectors. The characteristic feature of the conventional flow field is that the pressure in the gas channels on both sides of the shoulder is approximately equal. There is only a slight pressure drop between in-flow and out-flow of the entire gas distribution plate. The transport of oxygen to the reaction layer through the diffusion layer occurs predominantly by diffusion. In contrast to that, the *interdigitated flow field* consists of channels that are connected with the in-flow and others connected to the out-flow. They are arranged such that the gas flow is forced under the shoulders through the porous diffusion layer. The pressure difference between in-flow and out-flow channels generates a pressure gradient within the diffusion layer, thus producing an advectively enhanced transport of oxygen into the diffusion layer.

From the viewpoint of the diffusion layer, the conditions in the gas channels represent the bound-

ary conditions for the gas-liquid multicomponent system in the porous medium. The dominating parameter for the hydraulic behavior is the pressure on both sides of the shoulders which depends crucially on the type of flow field. Yet, an important role falls to the detailed processes at the interface between the diffusion layer and the gas channels. The water that is produced by the reaction and transport through the diffusion layer has to be taken up by the gas flow. Along the channels, this reduces the capacity of the gas to take up water vapor. How far the water transport in the gas channels occurs as vapor or as liquid is an important issue for the boundary condition of the diffusion layer. If less water can be taken up in the gas channels, this increases the risk of liquid water accumulations in the diffusion layer. A fully coupled model for both the diffusion layer and the gas channels requires different but interacting model concepts, multiphase multicomponent porous media flow in the diffusion layer and multicomponent gas flow in the gas channels where even the influence of liquid water droplets may influence the flow. Currently existing models do not have the capability to consider these complex and coupled threedimensional effects.

The problem of boundary conditions and the interaction between diffusion layer and gas channels will be discussed for a 2D example problem in Sec. 6.6.

2.7 Matrix Deformation in Porous Media Flow Systems

Many porous media flow systems show negligible influences of matrix deformation on the hydraulic behavior. If at all, then deformation affects mainly the porosity of the matrix, for example, due to pressure changes or chemical processes between fluids and matrix like precipitation or dissolution. The focus of interest in those systems is then typically on the hydraulic behavior and the flow and transport processes of the fluids and their constituents. This holds for the majority of groundwater related flow and transport systems. If necessary, the influences of porosity changes can be taken into account phenomenologically by constitutive relationships, for example, as a function of pressure. A gas-liquid flow problem that can be affected by porosity changes is the injection of CO_2 into saline aquifers or other geological formations (see Sec. 2.4). In the near-field of the injection wells, large pressure differences may cause mechanical deformations. Yet, exactly this should be avoided by controlling the pressure increase that the reservoir can bear without damaging the barrier of the caprock. Porosity can also change by precipitation of salt if CO_2 displaces the ambient brine so that the region adjacent to the injection well can dry out.

In contrast to that, there are applications of porous media systems involving fluid flow that show characteristic structural alterations. Many of those belong to the field of civil engineering or geotechnics, for example, hydraulic base failure, instabilities of slopes, embankments, dikes, crack formation in cohesive materials like sealing materials under landfills, etc. The focus in these applications is predominantly on the deformations, yet influenced by fluid flow. The modeling of strong structural alterations requires an explicit formulation of material laws for elastic, plastic, or visco-plastic deformations. This is beyond the scope of this work and we refer therefore to the literature, e.g. [45, 55, 100].

2.8 Overview of Gas-Liquid Problems and Dominant Processes

Table 2.8 is an attempt to summarize the explanations given in this chapter concerning the characteristics of the different gas-liquid multiphase multicomponent problems. The table is aimed at reflecting the relative importance of the different processes (advection, diffusion, dissolution, vaporization/condensation, heat conduction, heat convection, and reaction). This is expressed by the number of '+' that are assigned to the processes for the different gas-liquid problems. One must be aware that the rating which is given by Tab. 2.8 can not fulfill a claim of absoluteness. The diversity of questions, boundary conditions, and parameters is large; thus the relative importance of certain processes may strongly differ from the weight assigned to it in this table. Some explanatory comments are given in the table. For example, in case of advective processes, one can distinguish different driving forces (viscous, buoyant) or other factors of influence (e.g., soil structure) on the advective flow behavior.

Table 2.1: Overview of gas-liquid multiphase systems and dominant processes. Dependent on the specific problem, the relative importance of the different physical and chemical processes can strongly vary.

	Dominant Processes						
Gas-Liquid Problem	advection	diffusion	dissolution	vaporization/ condensation	heat conduction	heat convection	reaction
contaminant spreading	++++ soil structure, fluid properties(density, viscosity)	+++	++	++			+ adsorption, natural attenuation
steam injection in unsaturated zone	+++ mainly viscous	++	++	++++	++	+++	
steam injection in saturated zone	++++ buoyant and viscous			+++	++	++	
CO_2-storage in geological formations	++++ (early time-scale) viscous and buoyant	++ (medium time-scale)	+++ (medium time-scale)	+	+	+	++ (large time-scale) geochemical
methane migration	++ soil structure	++	++				+++ sorption
fuel-cells	++ boundary conditions	++ boundary conditions		+	+	+	+++ electrochemical

Chapter 3

Model Concepts

A basic and essential step towards the numerical simulation of any physical process is always the development of an appropriate model concept which is capable of describing the relevant characteristics of the respective system. The term *system* demands to be clarified in this context. It comprehends a thermodynamic system that is defined above the continuum scale within a certain domain. Outside of the domain - separated by clearly defined boundaries - is the environment of the system. The accuracy of a model concept with respect to the real physical processes depends obviously on the degree of abstraction which in turn is related to the scale at which the processes are examined. This poses one of the major challenges to the modelers. A good compromise between necessary assumptions for the reduction of complexity and the preservation of the essential characteristic system properties has to be found. We will show in this work, for example in Sec. 5.4 that the relevance of certain system properties to a problem may depend on the issues that are addressed by a numerical simulation. The structure of this chapter follows this statement and introduces the model concepts for gas-liquid multiphase flow problems in the order of their complexity. Section 3.1 gives a review of general multiphase model concepts for flow in porous media. Based on that, the following sections deal with the details of more complex models for coupled flow and transport systems including also phase transition of components and non-isothermal effects.

The terms *phases* and *components* are already used above. Their usage maybe commonly comprehensible. Anyway, we regard it as indispensable to define their meaning in the explanations below. We further give some basic definitions and assumptions that are required for this chapter.

Phases and components:
With the term *phase* we denote matter that has a homogeneous chemical composition and physical state. At normal conditions (moderate/low pressures and temperatures - depends on the chemical species) solid, liquid, and gaseous phases can be distinguished. While there can coexist several liquid phases separated by sharp interfaces, it is characteristic for gaseous species that they completely mix up in a single gas phase. In the region of the critical point, which is defined by the critical pressure and the critical temperature (see Fig. 4.9), the differences between the liquid and gaseous phases become indistinct. This phenomenon will be discussed in more detail in Chapter 4.

The *components* are the constituents of the phases. In general, they can be associated with a unique chemical species. But many models also comprise for the sake of simplification multiple chemical species with similar properties. An example for such a pseudo-component is air.

Multiphase systems and multiphase multicomponent systems:
According to the scale of abstraction in the conceptual model one can distinguish between multiphase models and multiphase multicomponent models. The latter can inherently take compositional effects into account. Processes like diffusion of components within phases or mass transfer of components between phases can be modeled by multiphase multicomponent models. A decoupled consideration of flow and component transport is also possible using multiphase models. However, the solution process then is sequential, first the flow and then the transport on the given flow field.

Thermal, chemical, and mechanical equilibrium:
The thermodynamical systems that we investigate in this work underly certain equilibrium assumptions.
The *thermal equilibrium* is an equivalent to the assumption that the local temperature is identical in all existing phases. This holds for processes with a local dominance of conduction over convection. In other words, the thermal equilibrium is violated if the convection gains influence compared to conduction. Thus, one can state that low flow velocities of the phases and small soil grains with low heat capacities are favorable for the thermal equilibrium assumption.
The *chemical equilibrium* means that the chemical activity of a species (component) is equal in all fluid phases. The number of existing phases is not relevant. Consequently, the mole fractions in a multiphase multicomponent system are constant if pressure and temperature are constant.
Mechanical equilibrium is fulfilled, if all forces acting on a body sum up to zero. In a porous multiphase system, beside the phase pressures the capillary pressure plays a role. Thus, mechanical equilibrium results from the definition of the capillary pressure on the macro scale (see Sec. 3.1.4).

Extensive, intensive, specific state variables:
The thermodynamic state of a system is uniquely characterized by distinct values of physical properties like, for example, pressure, temperature, density, or others. In other words, state functions, that describe the thermodynamic state as a function of state variables, are not dependent on the path the variables took to achieve a respective state. The number of independent state variables corresponds to the systems number of degrees of freedom, see also Sec. 5.3.1. We can distinguish different types of state variables. The values of *extensive state variables* depend proportionally on the magnitude of a system. Examples for extensive quantities are mass, volume, (total) internal energy, etc. On the other hand, *intensive state variables* are independent of the system size. Thus, pressure and temperature are intensive quantities. The third type is given by the so-called *specific state variables*. One obtains specific quantities when extensive quantities are divided by the size (typically the mass) of the system. The specific enthalpy or the specific volume are examples for them. Specific quantities behave similar as intensive ones, however they are in general different for each phase.

3.1 General Multiphase Models for Porous Media Flow

3.1.1 Scales

Any multiphase system in a porous medium requires the presence of fluid phases and a porous matrix. The fluid phases with their components exist within the void space (pores) of the porous matrix. There, they interact with each other driven by pressure gradients, gravity, concentration gradients, temperature gradients etc. These interactions are commonly denoted as multiphase multicomponent processes. However, the scale on which they are considered can be important for the mathematical description and even for the significance of a physical process in a porous medium. A process may dominate on a small scale but be neglible for the system behavior on a larger scale. For example, capillarity (see Sec. 3.1.4) can dominate the phase spreading on a scale that is in the range of centimeters whereas it has in general no significance in comparison to the influence of gravity on a larger scale in the range of kilometers.

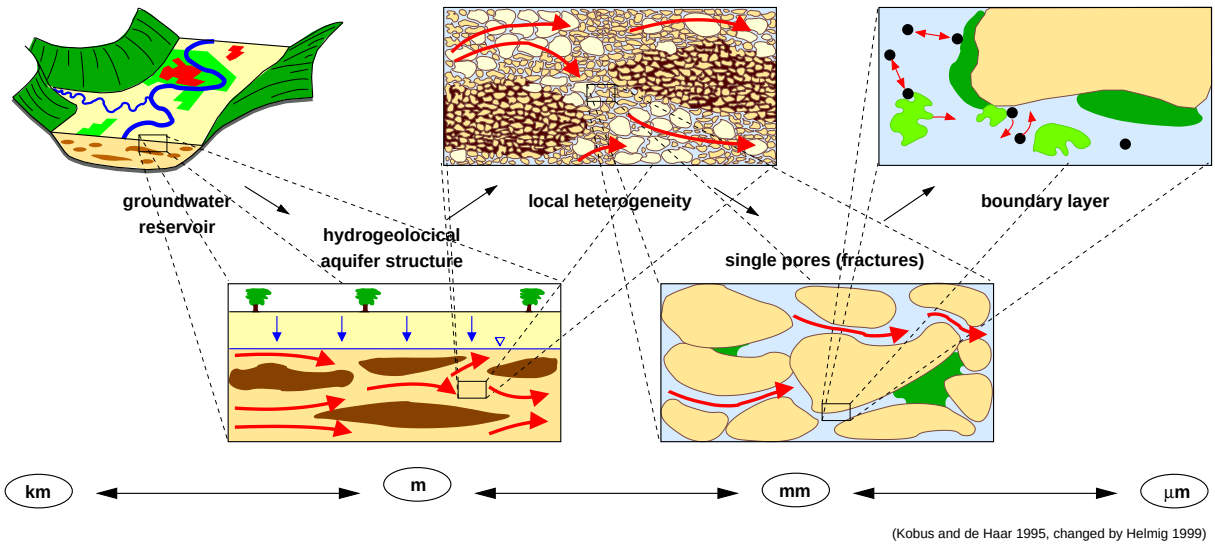

Figure 3.1: Different consideration scales for fluid flow in porous media according to [99].

The scale dependence of multiphase processes is mainly a consequence of the heterogeneous structure of the porous medium. Figure 3.1 illustrates that heterogeneities can be identified on every scale. It shows a recursive sequence of zooms into an aquifer system. Generally, one can associate the different zoom levels with respective consideration scales. This is obviously arbitrary and so the definition of length scales is not unique in literature. The transition from on scale to another occurs gradually. However, we outline the identification of different length scales in the following:

- The *molecular scale*, on which molecules are considered.
- The *continuum scale*. On this scale, one considers an amount of molecules that is large enough to obtain averaged fluid properties like, for example, the density (see Fig. 3.3). The consideration of the fluids as continua is a prerequisite for this work.

- The *micro scale* (or: *pore scale*), which is small enough to resolve individual pore spaces. The fluid movement on the micro scale can be described, for example, by the *Navier-Stokes* equations. Further, pore network models are developed for describing micro scale processes [83].

- The *local scale*, on which the description of individual pores is not practical. Instead, an averaged flow description on the basis of a *representative elementary volume* (REV, see Sec. 3.1.2) is applied. This scale is often also denoted as *REV scale*.

- The scales above the local scale (or: REV scale) are more or less arbitrary in their definition. They may be classified according to the structure of the porous medium, the influence of heterogeneities, etc. In general, we define the *field scale* to be the highest scale. But still, it depends on the problem which extension the field scale actually has. For example, we expect that a CO_2 injection scenario in a geological formation occurs on a larger problem domain than a steam-injection for the remediation of a contaminated site. Intermediate scales inbetween are denoted, for example, as *meso scale* or *macro scale*.

Any model concept for multiphase flow in porous media is based on a consideration of the physics on a certain scale. This requires that all effects that occur due to heterogeneities on smaller scales must be taken into account on the considered scale by effective parameters. On the other hand, it is in general no problem to include heterogeneities on scales larger than the considered one. This can easily be done by varying the different parameters spatially inside the model domain. Parameters may vary gradually (e.g., fluid densities, viscosities) or discontinuously (permeability, porosity, capillarity). A fracture or a fault zone is always an apparent discontinuity in a porous medium. If the number of fractures is small enough, they can be described discretely. However, a periodical appearance of fractures or block-heterogeneities may be not possible to resolve although their presence may dominate the flow processes. This is the motivation for a field of research dealing with upscaling and homogenization methods, cf. [124, 56, 118, 82]. Presently, upscaling and homogenization are rather academic disciplines and a significant knowledge transfer for the simulation of large practical real-life problems is still ahead.

For multiphase porous media flow, the influence of different spatial scales affects the model concept as explained above. The definition and size of scales is dependent on the structure of the porous medium. The distinction of different time scales is at first sight not that obvious. But if we, for example, look in detail on the equilibrium assumptions made above, then it becomes clear that this assumption is only valid on a time scale large enough to neglect that time required for a system to equilibrate. We will also discuss later in Sec. 5.4 how processes on different temporal scales affect the choice of the model concept for a numerical simulation.

3.1.2 The Representative Elementary Volume

As already explained, the definition of a representative elementary volume requires the consideration of the physical processes on a scale that allows an averaging of system properties yielding unique values. Figure 3.2 (left) illustrates this. It requires a minimum size V_0 of a control volume for obtaining a unique non-oscillating value for the ratio ϕ of pore volume V_{po} to total volume V.

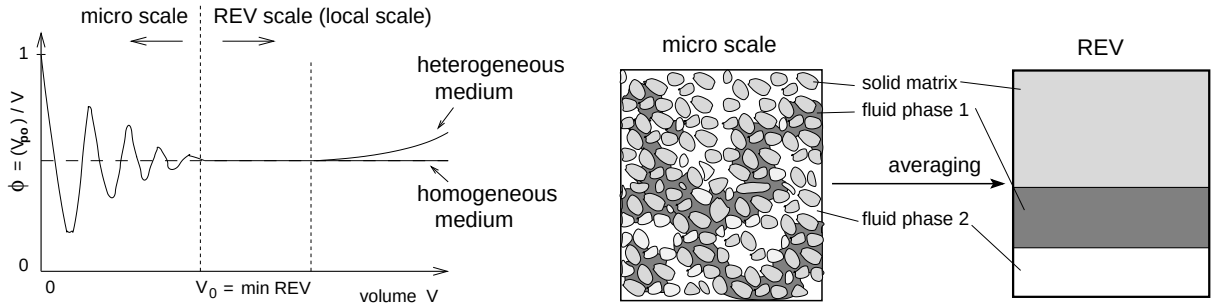

Figure 3.2: Averaging: definition of the minimum size of a representative elementary volume after *Bear* (1972) [15] (left). Transition between micro scale and REV scale (right).

This can be used for the definition of the porosity ϕ:

$$\phi = \frac{\text{volume of pore space in REV}}{\text{total volume of REV}} \tag{3.1}$$

Equation (3.1) is a basic example for upscaling. The porosity ϕ represents an effective parameter of the porous medium that does not exist below the scale of the REV. On smaller scales, the pore space must be described discretely. The fact that the porosity is chosen for the definition of a minimum REV size does not mean that this holds equally for other parameters of the porous medium. Theoretically, the choice of a REV size requires evidence for all relevant parameters analogously to Fig. 3.2 (left).

Once the REV is chosen and the porosity is defined according to Eq. (3.1) we can introduce a further effective parameter, namely the saturation of a phase α:

$$S_\alpha = \frac{\text{volume of phase } \alpha \text{ in REV}}{\text{volume of pore space in REV}} \tag{3.2}$$

Figure 3.2 (right) shows the transition from the real distribution of solid matrix, pore space, and fluid phases within the pore space to the schematic model of the REV. It can be easily recognized that the following supplementary constraint holds for the saturations of all phases within a REV:

$$\sum_\alpha S_\alpha = 1 \tag{3.3}$$

3.1.3 Fluid Properties

Following the explanations in Sec. 3.1.1, we consider the fluids as continua, which means that after averaging over a volume $V > V_0$ (see Fig. 3.3) one can assign them properties like *density* and *viscosity* that characterize their hydraulic behavior. Obviously, the required V_0 in Fig. 3.3 is by far smaller than that in Fig. 3.2 (left) for the definition of the porosity.

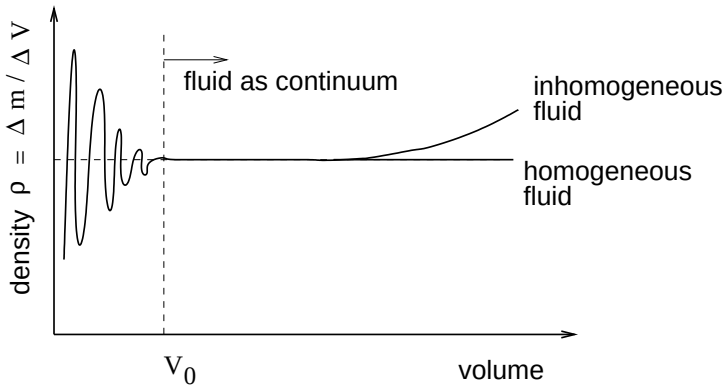

Figure 3.3: Density of a fluid when considered above the continuum scale after [15].

3.1.3.1 Density

Above the continuum scale, the density ρ of a fluid is a thermodynamic state variable dependent on temperature and pressure. Its total differential can be written as

$$d\rho = \frac{\partial \rho}{\partial p} dp + \frac{\partial \rho}{\partial T} dT = \rho \beta_p dp + \rho \beta_T dT \tag{3.4}$$

with

$$\beta_p = \frac{1}{\rho} \frac{\partial \rho}{\partial p} \qquad \text{and} \qquad \beta_T = \frac{1}{\rho} \frac{\partial \rho}{\partial T} \, . \tag{3.5}$$

The relation between different state variables can be described by equations of state. A very well-known equation of state (EOS) is the *ideal gas law*, which is given by

$$pV = n \mathcal{R} \, T \, , \tag{3.6}$$

where n represents the number of moles and $\mathcal{R} = 8.314$ J/(mol K) the universal gas constant. T is the absolute temperature in [K]. Dividing by the volume V and replacing n/V by the molar density ρ_{mol} yields

$$p = \rho_{\text{mol}} \mathcal{R} \, T \, . \tag{3.7}$$

Equation (3.7) can be further modified by considering the molecular weight M in [kg/mol]. After dividing $\mathcal{R}$ by M and multiplying ρ_{mol} by M we obtain

$$p = \rho_{\text{mass}} R T \, . \tag{3.8}$$

R is the individual gas constant in [J/(kg K)] for a chemical species and ρ_{mass} is the mass density. Presuming that ρ in Eqs. (3.4) and (3.5) stands for the mass density, we can use Eq. (3.8) to express β_p and β_T for an ideal gas as follows:

$$\beta_p = \frac{1}{\rho} \frac{1}{RT} \qquad \text{and} \qquad \beta_T = \frac{1}{\rho} \frac{p}{RT^2} \qquad \text{(for ideal gases)} \tag{3.9}$$

The assumption of a gas to be an ideal gas is only reasonable for pressures far below the critical pressure. Thus, for atmospheric conditions, this holds for many gases or vapors. Intermolecular

forces can cause a deviation from the ideal gas behavior. Mutual repulsion of molecules favors the expansion of gases during a pressure lowering or a temperature increase, whereas mutual attraction causes a better compression in case of a pressure increase or temperature decrease. The distance between the molecules determines whether repulsion or attraction becomes significant. While for moderate pressures intermolecular attraction dominates, the repulsion forces gain influence with further increasing pressure. If thermodynamic conditions exist for which these effects can not be neglected, we need further equations of state to account for the density. In Sec. 4.3, we present a concept for the description of CO_2 properties at high pressures.

Also, the description of densities for liquids like water, NAPLs, etc. requires equations of state. For water, the equations of state of the *IAPWS* formulations [94] can be used to calculate the thermodynamic properties of water and steam. The *International Association for the Properties of Water and Steam* (*IAPWS*, see *http://www.iapws.org*) provides new calculation standards. These formulations replace the equations of the *International Formulation Committee* (IFC) [93], they are also faster and more accurate.

For the estimation of the density of NAPLs or other liquids, there is a variety of methods available in the literature, cf. [146, 111, 1] etc. Many of the available methods refer to analogies in the behavior of different substances for reference values of T/T_{crit} or p/p_{crit}. For example, *Lide & Kehiaian* (1994) [111] describe a formulation of the *Rackett* equation applicable to calculate the molar densities of organic liquids, given by

$$\rho_{\text{mol},n} = \left(A_2 \cdot A_1^{1+(1-T/T_{\text{crit}})^{2/7}} \right)^{-1} \tag{3.10}$$

where A_1 and A_2 are empirical fluid-specific parameters. The respective parameter values, for example, to calculate the molar density of m-xylene are $A_1 = 0.25919$, $A_2 = 0.0014569$, and $T_{\text{crit}} = 617.1$ K. Another modified formulation of the *Rackett* equation is presented by *Reid et al.* (1987) [146]:

$$\rho_{\text{mol},n} = \left(10^{-5} \cdot \mathcal{R} \cdot \frac{T_{\text{crit}}}{p_{\text{crit}}} \cdot Z_{RA}^{1+(1-T/T_{\text{crit}})^{2/7}} \right)^{-1} \tag{3.11}$$

The parameter values of Z_{RA}, T_{crit} and p_{crit} are given exemplary in the following table for the LNAPL (NAPL lighter than water) mesitylene and the DNAPL (denser than water) TCE (trichloroethylene).

Table 3.1: Parameter values for the modified *Rackett* technique after [146].

	Z_{RA}	T_{crit}	p_{crit}
mesitylene (LNAPL)	0.2556	637.3 K	31.3 bar
TCE (DNAPL)	0.272	572.0 K	50.5 bar

Another method for estimating saturated liquid densities, the so-called *Hankinson-Brobst-Thomson* method is proposed by *Thomson et al.* (1982) [165]. Its extension to near-critical compressed liquids is discussed by *Aalto & Keskinen* (1999) [1].

The particular importance of equations of state for the estimation of fluid densities for gas-liquid flow processes should be emphasized. They are required as closure relations for the system of partial differential equations (PDE). If the assumption of incompressible fluids can be made for a flow problem, one can significantly reduce the complexity of the PDE. This holds both for the Navier-Stokes equations and the multiphase flow equations on the REV scale. For example, the *Buckley–Leverett* equation (Eq. 5.17) is based on the assumption of incompressibility. However, the multiphase systems in this work are characterized by effects of compressibility (or thermal expansion) particularly of the gaseous phases. Thus, it is a major problem for the model verification that there is practically no analytical solution of compressible flow problems available against which the numerical models could be tested.

3.1.3.2 Viscosity

Viscosity is a measure of the resistance of a fluid to deformation under shear stress [172].

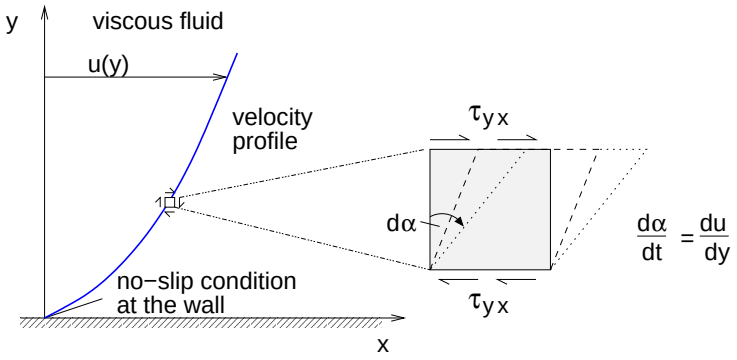

Figure 3.4: Shear stress τ and velocity gradient.

Figure 3.4 illustrates a velocity profile which could typically occur inside a pore but also near to the boundary of a pipe or open channel flow. The viscosity of the fluid is a measure for the velocity of the angular deformation $\frac{d\alpha}{dt}$. According to *Newton's* theory for the behavior of *Newtonian* fluids, the dynamic viscosity is a proportionality factor between shear stress τ and velocity gradient du/dy:

$$\tau = \mu \frac{du}{dy} \quad \text{(see Fig. 3.4)} \tag{3.12}$$

One can distinguish between the dynamic viscosity μ (in Pa·s; old unit P - Poise - can be transfered by 1 P = 0.1 Pa·s) which is used in Eq. (3.12) and the kinematic viscosity ν (in m^2/s). ν represents the denominator of the *Reynolds* number which quantifies the influence of inertia versus viscous forces in order to classify turbulent, laminar, and creeping flow. Dynamic and kinematic viscosity are related via the density by

$$\nu = \frac{\mu}{\rho} \, . \tag{3.13}$$

Viscosity is in general a function of temperature while its pressure dependence is often negligible. The viscosity of gases increases as temperature increases, but the viscosity of liquids decreases at higher temperatures.

Table 3.2: Some selected values of dynamic viscosities (Pa · s); data mainly from [110]

Gases at 0 °C		Liquids at 25 °C	
air	$1.74 \cdot 10^{-5}$	water	$0.89 \cdot 10^{-3}$
methane	$1.027 \cdot 10^{-5}$	benzene	$0.604 \cdot 10^{-3}$
carbon dioxide	$1.372 \cdot 10^{-5}$	methanol	$0.544 \cdot 10^{-3}$

Temperature-dependent tables or functions for the calculation of dynamic viscosities can be found in the literature for all common species. The viscosities of water and steam can be taken from *IAPWS* [94]. Computation methods for organic liquid and their vapors can be found in *Reid et al.* (1987) [146] and others. A semi-empirical formula is, for example, the following:

$$\mu_{\mathrm{NAPL}} = exp(A + B/T + C \cdot T + D \cdot T^2) \tag{3.14}$$

A, B, C, and D are empirical constants specific for each substance.
The dynamic viscosity of gaseous phases requires particular attention. In case of a gaseous mixture, the viscosity is a strong function of the composition, see also Sec. 3.2.1. A simple approach just weights the individual dynamic viscosities of the gaseous componentes with their mole fraction:

$$\mu_g = \sum_{\kappa} \mu_g^{\kappa} x_g^{\kappa} \tag{3.15}$$

More precise but restricted to binary gaseous mixtures is the method proposed by *Wilke* which is described by [146]. The *Wilke* method is applicable for low pressures and represents a simplification of the kinetic theory of gases. According to *Wilke*, the dynamic viscosity of a gas phase composed of two substances I and II is

$$\mu_g = \frac{x_g^I \cdot \mu^I}{x_g^I + x_g^{II} \cdot \phi_{I,II}} + \frac{x_g^{II} \cdot \mu^{II}}{x_g^{II} + x_g^I \cdot \phi_{II,I}} \tag{3.16}$$

$\phi_{I,II}$ and $\phi_{II,I}$ are parameters for describing the interaction of the binary components in the mixture. $\phi_{II,I}$ is defined as:

$$\phi_{II,I} = \frac{\left(1 + \sqrt{\frac{\mu^{II}}{\mu^I}} \cdot \left(\frac{M^I}{M^{II}}\right)^{1/4}\right)^2}{\sqrt{8 \cdot \left(1 + \frac{M^{II}}{M^I}\right)}} \tag{3.17}$$

with M^I und M^{II} representing the respective molecular weights. $\phi_{I,II}$ can be obtained analogously by exchanging the indices/exponents.

3.1.4 Capillary Pressure

Liquids tend to minimize their surface since this means a state of minimized free energy. Textbooks of physical chemistry, for example *Atkins* (1996) [6], formulate a relation between the change of a liquid's free energy A (in J) and the change of its surface σ (in m^2).

$$dA = \gamma d\sigma \tag{3.18}$$

According to Eq. (3.18), the surface tension γ has the dimension [Jm^{-2}] which is equal to [Nm^{-1}]. A reduction of the free energy occurs spontaneous and requires also a reduction of the surface. Thus, it is in the nature of liquids that their surface is in general curved. This can result in bubbles, cavities or drops when liquids are in equilibrium with their vapors or other fluids. An essential observation is that the pressure on the concave side of an interface is always larger than on the convex side. This is expressed by the *Laplace* equation

$$p_{in} = p_{ex} + \frac{2\gamma}{r} , \tag{3.19}$$

where r is the radius of a spherical cavity inside of a liquid. The curvature of a liquid has direct influence of the corresponding vapor pressure as will be explained later and expressed by Eq. (3.77).

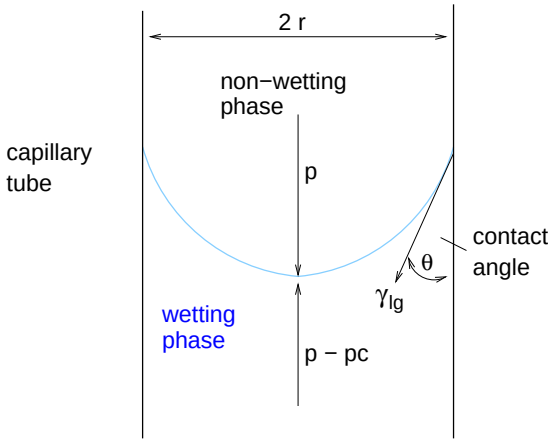

Figure 3.5: Equilibrium in a capillary tube after [6].

In porous media, these properties of surfaces in contact with each other and with the solid phase (porous matrix) cause a phenomenon denoted as capillarity. Let us consider the capillary tube in Fig. 3.5. The energy of adhesion between solid wall and liquid is the higher the more wall surface is wetted by the liquid. By wetting the walls, the surface of the liquid inside the tube has to be curved which in turn leads to a pressure difference between the wetting liquid, for example water, and the surrounding atmosphere according to Eq. (3.19). Thus, the higher pressure of the surrounding atmosphere pushes the column of wetting liquid inside the capillary tube upwards until an equilibrium between the pressure of the liquid column and the capillary pressure p_c is achieved:

$$p_c = \rho g h , \tag{3.20}$$

where h is the increased height of the liquid inside the tube. Taking into account Eq. (3.19), this leads to

$$h = \frac{2\gamma}{\rho g r} . \tag{3.21}$$

Figure 3.5 shows further that the contact angle between the meniscus interface and the wall is not necessarily equal to zero, although this is valid approximately for a water-air system in a

capillary glas tube. The value of the contact angle depends on the equilibrium of forces at the interface between liquid and solid wall. It can be shown [6] that

$$\cos\theta = \frac{\gamma_{sg} - \gamma_{sl}}{\gamma_{lg}}\,, \tag{3.22}$$

where γ_{sg}, γ_{sl}, and γ_{lg} represent the surface tensions solid/gas, solid/liquid, and liquid/gas. In order to take the effect of the contact angle into account, we multiply the right-hand side of Eq. (3.21) with $\cos\theta$.

3.1.4.1 The Influence of Saturation

The main difference between a capillary tube and a porous medium regarding the effects of capillarity is the typical irregularity of porous media. Therefore, following the discussion about scales in Sec. 3.1.1 and Sec. 3.1.2, it is not appropriate to resolve the phenomenon of capillarity on the basis of individual pores if the relevant scale is above the micro scale. Thus, on the local scale and above it is common to use constitutive relationships which express the capillary pressure in the REV as a function of other parameters. The saturation of the wetting phase has obviously the strongest influence. Due to its higher affinity to the solid matrix, the wetting phase will always tend to maximize its contact with the solid. Thus, if the saturation of the wetting phase is low, it dominantly occupies the narrow pores due to their high ratio of contact surface to volume. In other words, the non-wetting phase always prefers the larger pores for the same reason. In a state of low wetting phase saturation, the average radius of the meniscus is comparatively small. Thus, the capillary pressure is accordingly high.

The most well-known parametrizations for capillary pressure on the local scale dependent on the wetting phase saturation are the functions of *van Genuchten* (1980) [166] and *Brooks & Corey* (1964) [20]. The *van Genuchten* approach is

$$p_c = \frac{1}{\alpha}\left(S_e^{-1/m} - 1\right)^{1/n} \tag{3.23}$$

with the effective saturation

$$S_e = \frac{S_w - S_{wr}}{1 - S_{wr}}\,. \tag{3.24}$$

The parameters α [1/Pa] and n are empirical parameters of the porous material. While α is a scaling parameter for the magnitude of the capillary pressure, the parameter n characterizes the uniformity or non-uniformity of the porous medium (see Fig. 3.6). A large n expresses a comparatively uniform soil which means that the size of the pores does not strongly vary. On the other hand, a non-uniform pore size distribution can be described by small values of n. Commonly, the parameter m is expressed in terms of n by

$$m = 1 - \frac{1}{n}\,. \tag{3.25}$$

The *van Genuchten* relationship assumes that the capillary pressure tends to zero for fully-saturated conditions ($S_w = 1$). According to Eq. (3.19), this corresponds to the assumption of an infinitely large pore radius of the largest pore. As Fig. 3.6 illustrates, the capillary pressure tends

asymptotically to infinity for $S_w \rightarrow S_{wr}$. This means, that a further reduction of the saturation by increasing the capillary pressure is not possible. The saturation is then too small to form a coherent phase that can be continously driven by a pressure gradient. S_{wr} is the residual saturation of the wetting phase. In other words, S_{wr} expresses the retention capacity of the porous medium with respect to the wetting phase. This is why the $p_c - S$ relationship is also denoted as the soil moisture retention curve.

The *Brooks & Corey* function behaves quite similar as the *van Genuchten* approach with the only but important difference that it assumes a finite non-zero value of the capillary pressure for fully-saturated conditions (see Fig. 3.6). This value is called the entry pressure p_d [Pa] of the porous medium and it corresponds to the size of the largest pore according to Eq. (3.19). The entry pressure must be overcome by the non-wetting phase to penetrate into the largest pore. The *Brooks & Corey* approach can be written as

$$p_c = p_d S_e^{-1/\lambda} . \tag{3.26}$$

While p_d is directly related to the α parameter of *van Genuchten*, the parameter λ corresponds to *van Genuchten's n* representing the uniformity of the pore size distribution. *Lenhard et al.* (1989) [105] describe the correspondence between the two models of *van Genuchten* and *Brooks & Corey* in detail.

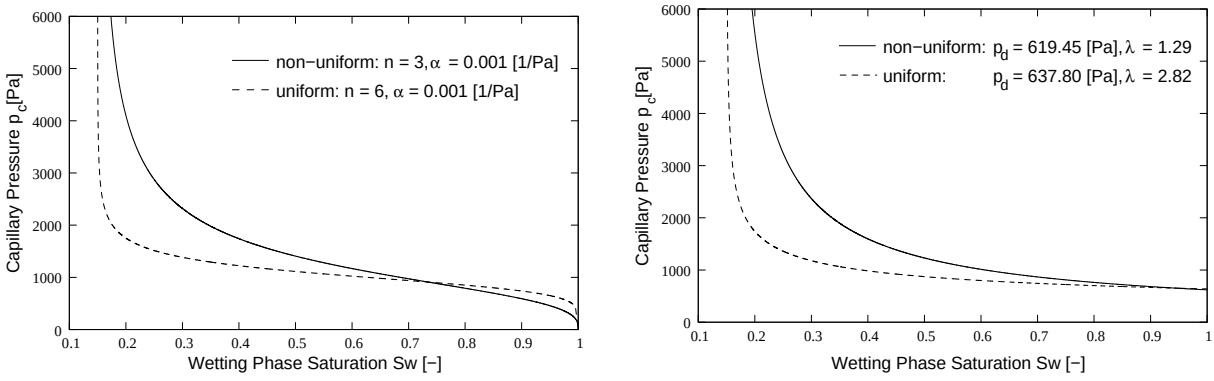

Figure 3.6: Capillary pressure as a function of the wetting phase saturation according to the approaches of *van Genuchten* (left) and *Brooks & Corey* (right).

3.1.4.2 Other Parameters and Processes Influencing Capillarity

As explained, the value of the capillary pressure in a porous medium is a strong function of the phase saturations. However, there are other parameters and processes that may become significant. We will discuss them only shortly, although for each of the following topics, comprehensive work can be found in the literature.

The influence of *temperature* on capillarity results from the temperature-dependence of the surface tension. The approach of *Leverett* (1941) [108] applies directly to this. He suggests a

scaling of p_c with respect to a reference value p_0 according to the variation of the surface tension:

$$p_c = p_0 \cdot \gamma(T) \cdot 1.417(1-S_e) - 2.120(1-S_e)^2 + 1.263(1-S_e)^3 \tag{3.27}$$

Other authors report also experimentally strengthened results of decreasing capillary pressures with increasing temperatures, cf. [154, 173].

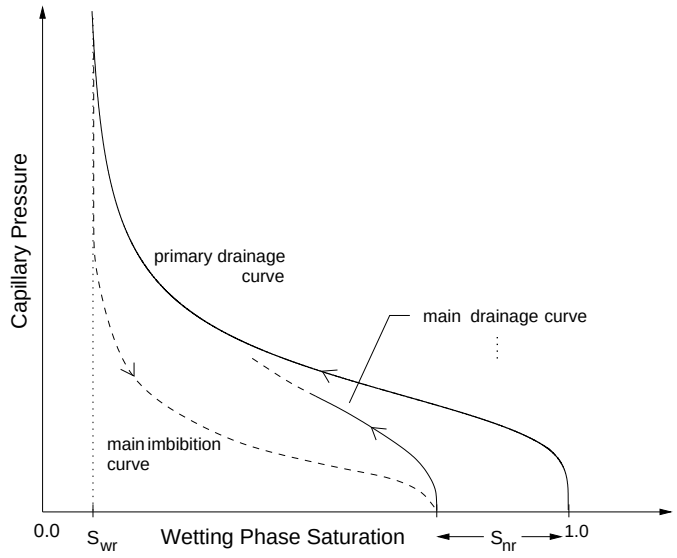

Figure 3.7: Principle of the hysteretic behavior of the capillary pressure–saturation relationship.

Typically, due to different physical processes, transient multiphase flow systems show changes of the wetting phase saturation. This means that the value of capillary pressure moves along the respective curves shown in Fig. 3.6. The bad news is that these curves is actually valid for only a certain direction of the process which is indicated by the sign of $\partial S_w/\partial t$. A positive $\partial S_w/\partial t$ means a local increase of the wetting phase saturation called imbibition whereas the opposite direction is called drainage. For each direction, the $p_c(S_w)$ relationship differs in general. This behavior is denoted as *hysteresis*. The principle of the hysteretic behavior of the capillary pressure is schematically illustrated in Fig. 3.7. Let us assume a fully-saturated system ($S_w = 1$). A drainage of this system driven by a gradually increasing capillary pressure yields the primary drainage curve (see Fig. 3.7). For $S_w \to S_{wr}$, the capillary pressure tends to infinity since - as explained above - a further reduction of S_w is not possible.
The following infiltration process starting at $S_w = S_{wr}$ is described by the main imbibition curve. It is characteristic that the main imbibition curve ends at a saturation value smaller than 1. This occurs due to entrapment of the non-wetting phase which is a result of processes on the pore scale, cf. [28, 155]. The amount of non-wetting phase entrapment is described by the respective residual saturation S_{nr}. Another change of the direction at $S_w = 1 - S_{nr}$ yields the main drainage curve such that the hysteresis cycle becomes closed. The difference between the capillary pressures of the drainage and imbibition curves for given saturations is due dynamic pore scale processes like, e.g., direction- and velocity-dependent contact angle phenomena, c.f. [114, 113], or the ink-bottle effect, c.f. [119]. If a change from imbibition to drainage or vice versa occurs inbetween the end points of the main curves, the thereby arising curves are denoted commonly

as secondary drainage/imbibition scanning curves.

As already indicated, the function $p_c(S_w)$ is not unique if *dynamic effects* play a role which is the general case. *Hassanizadeh et al.* (2002) [77] describe this phenomenon in detail. They formulate a relation between the dynamic capillary pressure p_c^d and the equilibrium capillary pressure p_c^e as a function of the parameter τ multiplied with the rate of change of saturation:

$$p_c^d - p_c^e = -\tau \frac{\partial S_w}{\partial t} \tag{3.28}$$

p_c^e is a function of saturation only. Eq. (3.28) was already proposed by *Stauffer* (1977, 1978) [161, 162] who observed the respective effects in his experiments. However, the determination of the parameter τ is a rather delicate problem. *Manthey* (2006) [113, 114] worked on numerical simulations of drainage experiments developing a strategy to estimate τ and the impact of dynamic effects based on a dimensional analysis of the contributing dynamic, viscous, gravitational, and equilibrium capillary forces.

3.1.4.3 More than Two Fluid Phases

If more than two fluids exist locally in a porous medium it will become rather difficult to distinguish the fluids with respect to their wettability. Let us consider a system of three fluid phases. Assuming firstly that all three phases are coherent and have a non-zero saturation, one could then idealize the distribution of the fluids in a pore according to their wettability as shown in Fig. 3.8.

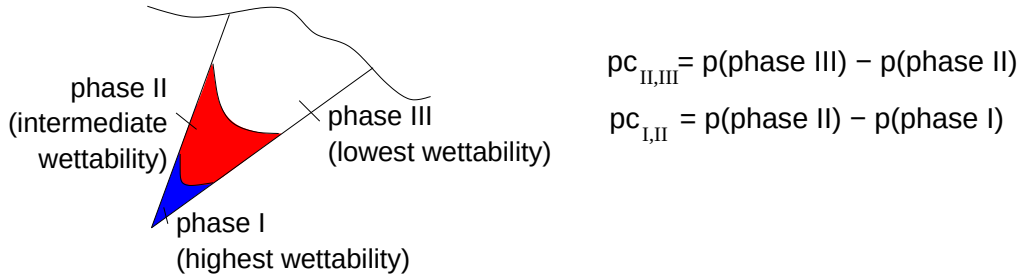

Figure 3.8: Schematic idea of fluid distribution and capillary pressures in a pore when more than two fluids exist.

Based on that assumption, we introduce in the following an approach proposed by *Parker & Lenhard* (1987) [137]. Exemplary, we therefore use a three-phase system consisting of water as the most wetting phase (corresponding to phase I in Fig. 3.8), a NAPL phase which is intermediate wetting (phase II), and a gaseous phase representing the non-wetting phase (phase III), see also Sec. 4.1. It should be noted that this approach can not account for the influence of contact angle effects with impact on the spreading of the NAPL phase inbetween of the interface water/gas. Below a critical saturation, NAPLs with a negative spreading coefficient [3] tend due to their high internal cohesion to form discontinuous droplets.

Using the approach following *Parker & Lenhard*, the phase pressures can be calculated by

$$\begin{aligned} p_n &= p_g - \Theta p_{c_{\mathrm{gn}}}(S_t) - (1-\Theta)\left[p_{c_{\mathrm{gw}}}(S_w) - p_{c_{\mathrm{nw}}}(S_w = 1)\right] \\ p_w &= p_n - \Theta p_{c_{\mathrm{nw}}}(S_w) - (1-\Theta)\left[p_{c_{\mathrm{nw}}}(S_w = 1)\right] . \end{aligned} \tag{3.29}$$

Basically, the total pressure difference between the water (most wetting) and the gas phase (non-wetting) is the sum of the two-phase capillary pressures between water/NAPL $p_{c_{\mathrm{nw}}}$ and NAPL/gas $p_{c_{\mathrm{gn}}}$. As Fig. 3.9 shows, the sum of both is in general not equal to the two-phase capillary pressure $p_{c_{\mathrm{gw}}}$ between gas and water. Thus, there occurs a problem for disappearing NAPL saturations since the transition from the three-phase system to the two-phase system must be continuous. This can be accomplished by introducing the parameter

$$\Theta = min(1, \frac{S_n}{S_{nr}}) . \tag{3.30}$$

The task is now to quantify the capillary pressure curves for $p_{c_{\mathrm{nw}}}$ and $p_{c_{\mathrm{gn}}}$. *Leverett* (1941) [108] suggests a scaling according to the respective ratios of the surface tensions. According to *Lenhard* (1994) [103], the scaling parameters β_{nw} and β_{gn} are calculated as follows:

$$\beta_{\mathrm{nw}} = \frac{\gamma_{\mathrm{gn}} + \gamma_{\mathrm{nw}}}{\gamma_{\mathrm{nw}}} \qquad \beta_{\mathrm{gn}} = \frac{\gamma_{\mathrm{gn}} + \gamma_{\mathrm{nw}}}{\gamma_{\mathrm{gn}}} \tag{3.31}$$

Then, $p_{c_{\mathrm{nw}}}$ and $p_{c_{\mathrm{gn}}}$ are obtained by

$$p_{c_{\mathrm{nw}}}(S_w) = \frac{1}{\beta_{\mathrm{nw}}} p_{c_{\mathrm{gw}}} \tag{3.32}$$

and

$$p_{c_{\mathrm{gn}}}(S_t) = \frac{1}{\beta_{\mathrm{gn}}} p_{c_{\mathrm{gw}}} . \tag{3.33}$$

Since water is the most wetting liquid, this approach assumes that the ratio of NAPL saturation to gas saturation has no influence on $p_{c_{\mathrm{nw}}}$. Thus, $p_{c_{\mathrm{nw}}}$ is a function of S_w. Analogously, $p_{c_{\mathrm{gn}}}$ is not dependent on the ratio of S_w to S_n since gas is always the non-wetting phase and $p_{c_{\mathrm{gn}}}$ is a function of $S_t = S_w + S_n = 1 - S_g$. S_t is denoted as the total liquid saturation.
The value of the scaling parameter β requires knowledge of the respective surface tension values. Tab. 3.3 lists some selected values of surface tensions for water/NAPL and NAPL/air systems. With these surface tensions and Eq. (3.31), one obtains $\beta_{\mathrm{nw}} \approx 1.7$ to 2.0 and $\beta_{\mathrm{gn}} \approx 2.0$ to 2.4.
The capillary pressure functions for $p_{c_{\mathrm{gn}}}$ and $p_{c_{\mathrm{nw}}}$ are plotted in Fig. 3.9. For a fixed value of $S_n = 0.3$ the curves of $p_{c_{\mathrm{gn}}}(S_t)$ and $p_{c_{\mathrm{nw}}}(S_w)$ are calculated based on the *van Genuchten* model scaled with the β-parameters as indicated in the figure. The range of S_w is between 0 and 0.7 accordingly. In comparison to that, the solid line represents the *van Genuchten* curve for a water/gas system. The dotted line shows that the sum of the capillary pressures $p_{c_{\mathrm{gn}}}$ and $p_{c_{\mathrm{nw}}}$ is smaller than the pure two-phase water/gas capillary pressure. While $p_{c_{\mathrm{nw}}}$ and $p_{c_{\mathrm{gw}}}$ reveal the typical asymptotic behavior towards infinity for S_w approaching the residual saturation value of $S_{wr} = 0.15$, this can not be seen for $p_{c_{\mathrm{gn}}}$. The reason therefor is that the NAPL saturation is constant at 0.3 such that the steep increase of p_c near to the residual saturation (here: total liquid residual saturation $S_{tr} = 0.25$) is not possible within the given range.

Table 3.3: Experimentally determined surface tensions after *Schmidt* (1999) [151].

NAPL	γ_{gn} NAPL/air	γ_{nw} NAPL/water
Mesitylen	0.02633	0.0390
Xylol	0.02790	0.0336
TCE	0.03091	0.0313

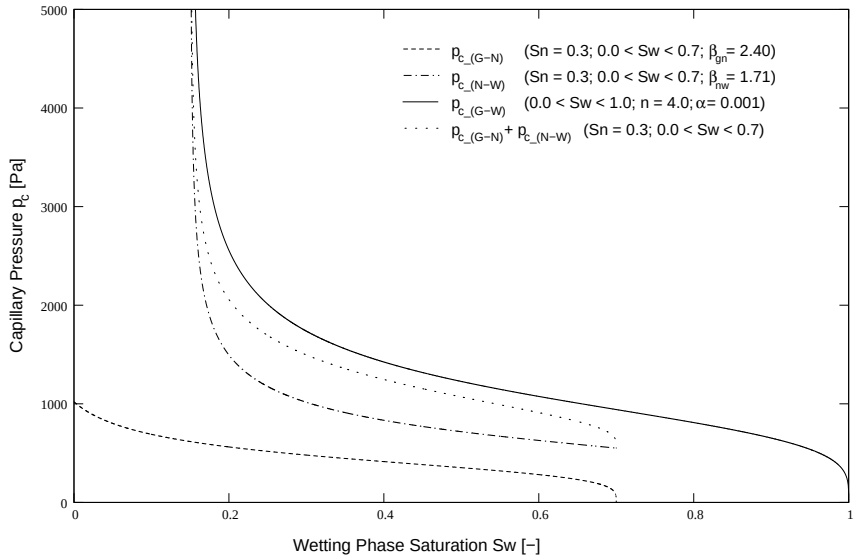

Figure 3.9: Plot of the capillary pressure functions in a three-phase water-NAPL-gas system for a fixed NAPL saturation of 0.3 according to the scaling approach of *Lenhard* (1994) [103].

3.1.4.4 Capillary Pressure Influences the Behavior of the Conservation Equations

In general, multiphase processes without capillary pressures are governed by the mutual displacement of fluids. Mathematically, this is described by hyperbolic conservation equations. Physically interpreted this means, that the flow has locally a unique direction. For the numerical treatment of hyperbolic systems, we refer to the literature, e.g. *LeVeque* (1992) [107]. If, however, a system is influenced by capillary pressure, then the phase flow is locally multidirectional since *capillary diffusion* acts in all directions with non-zero dp_c/dS (elliptic behavior). The mathematical behavior of the conservation equations is then mixed hyperbolic/parabolic where the parabolic behavior becomes more significant with increasing capillary pressure.

3.1.5 Permeability (Hydraulic Conductivity)

The permeability (or: hydraulic conductivity) of a porous medium is undoubtedly the most important parameter to characterize the hydraulic behavior. The concept of mathematically describing porous media flow by means of the permeability as a measure of the resistance that is exerted by the porous matrix goes back to *Henry Darcy* and is explained below. However, the so-called *Darcy law* holds only for single-phase flow (groundwater flow, flow of oil in reservoirs) and has to be extended for multiphase flow. Therefore, a further parameter specific for multiphase systems

is introduced and denoted as relative permeability, see Sec. 3.1.5.2.

3.1.5.1 Permeability/Hydraulic conductivity after *Darcy* for Single-Phase Flow

In 1856, the French hydraulic engineer *Henry Darcy* investigated the flow of water through gravel beddings and found that the flow rate q (in cm^3/s) through the material over a length l (cm) with the flow area A (cm^2) driven by the pressure difference Δp (atm) is proportional to the hydraulic conductivity k (in D - Darcy) [43]. Formally, this is expressed by

$$k = \frac{q\,\mu\,l}{\Delta p A}\,, \tag{3.34}$$

where the dynamic viscosity μ is given in cP. Obviously, Eq. (3.34) has uncomfortable units and should be transfered to SI units. First of all, the unit D - Darcy - (often used as mD since 1 D is a relatively high permeability) is still common for characterizing geological formations or gas/oil reservoirs. The conversion to SI units is

$$1D \approx 1 \cdot 10^{-12}\text{m}^2 \qquad \text{(more precise: } 1D = 9.86923 \cdot 10^{-13}\text{m}^2\text{)}\,. \tag{3.35}$$

Usually, the general *Darcy* equation is written as

$$\mathbf{v} = -\mathbf{k}_f \nabla h\,, \tag{3.36}$$

where $\mathbf{v}$ is the *Darcy* velocity vector (in m/s), $\mathbf{k}_f$ is the hydraulic conductivity tensor (m/s), and

$$h = \frac{p}{\rho g} + z \tag{3.37}$$

represents the piezometric head (m). In the form of Eq. (3.36), the hydraulic conductivity still depends on the fluid and is not a characteristic parameter of the porous matrix alone. The influence of the fluid and the resistance of the porous matrix to the flowing fluid can be described if the hydraulic conductivity is expressed by

$$\mathbf{k}_f = \mathbf{K}\frac{\rho \mathbf{g}}{\mu}\,, \tag{3.38}$$

where the intrinsic permeability $\mathbf{K}$ (in m^2) is now a property of the porous medium corresponding to k in Eq. (3.34).

The validity of *Darcy's law* is commented by *Bear* (1972) [15] as follows: "In practically all cases, *Darcy's law* is valid as long as the *Reynolds number* based on average grain diameter does not exceed some value between 1 and 10."Thereby, Re is defined by

$$\text{Re} = \frac{|\mathbf{v}|\,l\,\rho}{\mu} \tag{3.39}$$

with the characteristic length scale l representing the average grain diameter of the porous medium.

3.1.5.2 Relative Permeability and Extended Darcy's Law for Multiphase Flow

If several fluids co-exist locally within the pore space, they mutually hinder their mobility. Thus, there is additional resistance to the movement of the fluid phases which can be expressed by a reduction of the permeability in *Darcy's law*. The relative permeability $k_{r\alpha}$ of a fluid phase α accounts for this by being multiplied with the intrinsic permeability of the porous medium. The product of relative permeability and intrinsic permeability is often denoted as effective permeability. Accordingly, for multiphase flow in porous media, an extended version of *Darcy's law* is used, given by

$$\mathbf{v}_\alpha = -\frac{k_{r\alpha}}{\mu_\alpha}\mathbf{K}\cdot(\nabla p_\alpha - \rho_\alpha \mathbf{g}) \,, \tag{3.40}$$

where $k_{r\alpha}/\mu_\alpha$ is called the mobility λ_α of the phase. $k_{r\alpha}$ takes values between zero and one dependent on the phase saturation. $k_{r\alpha} = 1$ corresponds to fully-saturated single-phase flow conditions, while $k_{r\alpha} = 0$ is valid for all phase saturations below the residual saturation (see above Sec. 3.1.4.1).

For two fluid phases, there are a number of approaches in the literature that quantify the relative permeability–saturation relationship. As done in Sec. 3.1.4 for the capillary pressure–saturation relationship, we select here again only the famous functions of *van Genuchten* [166] and *Brooks & Corey* [20]. Both models are developed on the basis of a bundle of capillary tubes model. *Burdine* (1953) [22] presumed in his approach that the bundle of parallel capillary tubes, which represent the porous medium, can vary their radii only perpendicular to the direction of the flow. The $p_c(S)$ functions of *Brooks & Corey* are associated with the model of *Burdine*. The obtained $k_r(S)$ functions are given by

$$k_{rw} = S_e^{\frac{2+3\lambda}{\lambda}} \qquad \text{for the wetting phase and} \tag{3.41}$$

$$k_{rn} = (1-S_e)^2\left(1-S_e^{\frac{2+\lambda}{\lambda}}\right) \qquad \text{for the non-wetting phase} \tag{3.42}$$

in a two-phase system.

A further development of the bundle of capillary tubes model is presented by *Mualem* (1976) [121]. This model allows also a variation of the pore/tube radii in the direction of the flow. The application of the *van Genuchten* $p_c(S)$ relationship to the *Mualem* bundle of tubes approach yields then

$$k_{rw} = \sqrt{S_e}\left[1-\left(1-S_e^{1/m}\right)^m\right]^2 \tag{3.43}$$

$$k_{rn} = (1-S_e)^{\frac{1}{3}}\left[1-S_e^{1/m}\right]^{2m} \,. \tag{3.44}$$

The *Brooks & Corey* and the *van Genuchten* relative permeability–saturation relatioships are plotted in Fig. 3.10 for the same set of parameters λ and n as in Fig. 3.6.

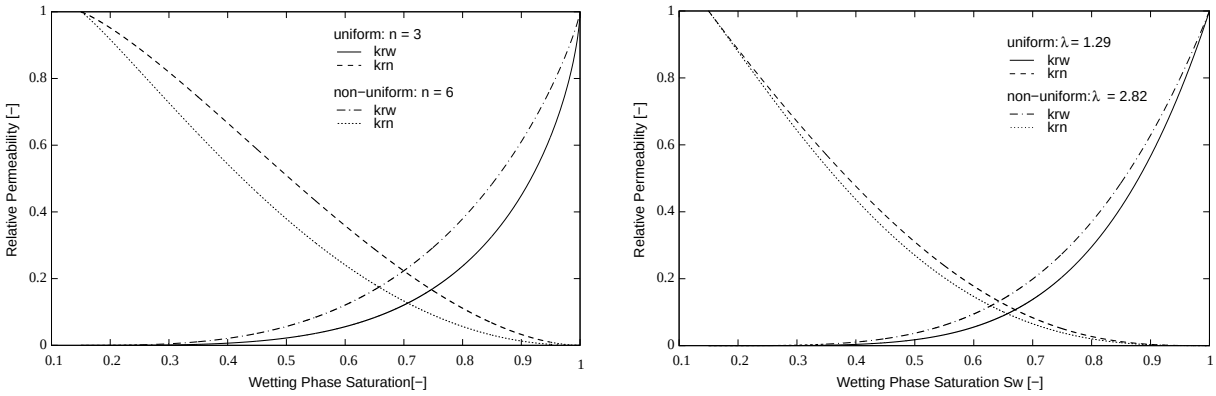

Figure 3.10: Relative permeability of both non-wetting and wetting phase as a function of the wetting phase saturation according to the approaches of *van Genuchten* (left) and *Brooks & Corey* (right).

One can clearly see that the increase of the non-wetting phase relative permeability for increasing but small S_n occurs much faster than the corresponding increase of k_{rw} for increasing but small S_w. The reason for this is that the non-wetting phase occupies predominantly the larger pores when entering the porous medium. Since larger pore have typically a higher permeability (less resistance), k_{rn} reaches quickly larger values. On the other hand, if the wetting phase enters into a porous medium that is initially filled with a non-wetting phase (imbibition), the wetting phase first occupies the smaller pores and the non-wetting phase will draw back into the larger pores.

3.1.5.3 Relative Permeabilities in a Three-Phase Water-NAPL-Gas System

For three-phase systems, we should again take into account the order of wettability as done before in Sec. 3.1.4.3. This helps us to define the influence of the different phase saturations on the respective relative permeabilities. Due to its highest affinity to the soil grains, the water phase always fills the smallest pores. Thus, it has no significant influence on the relative permeability k_{rw} how the remaining pore space is shared by the two other fluids (NAPL and gas). Analogously, the gaseous phase has the lowest affinity and fills the largest pores predominantly. Accordingly, the relative permeability k_{rg} depends only on the gas-phase saturation. Consequently, we can apply the two-phase relative permeability–saturation relationships in order to calculate k_{rw} and k_{rg}. A difficulty occurs for the computation of the NAPL phase relative permeability since NAPL is the intermediate wetting phase, and it depends on the ratio of the gas and water saturations how the NAPL phase is distributed within larger or smaller pores. The approach of *Parker et al.* (1987) [138] accounts for that. It is based on the *van Genuchten* parameterization and given by:

$$k_{rn} = \sqrt{\frac{S_n}{1-S_{wr}}} \cdot \left\{ \left(1 - \bar{S}_w^{\frac{n}{n-1}}\right)^{\frac{n-1}{n}} - \left(1 - \bar{S}_t^{\frac{n}{n-1}}\right)^{\frac{n-1}{n}} \right\}^2 \tag{3.45}$$

with

$$\bar{S}_w = \frac{S_w - S_{wr}}{1-S_{wr}} \qquad \text{and} \qquad \bar{S}_t = \frac{S_w + S_n - S_{wr}}{1-S_{wr}} \; . \tag{3.46}$$

Equation (3.45) does not explicitly account for a residual NAPL saturation. This means that NAPL is mobile already at very small saturations presuming that enough water is locally present. This is expressed in the formula by the total liquid saturation $S_t = S_w + S_n$. Following the discussion of the wettability above, this appears to be reasonable. A modification of Eq. (3.45) assigns a specific residual saturation S_{nr} also to the NAPL phase. Thus, S_{nr} has to be overcome before the NAPL phase becomes mobile.

$$k_{rn} = \sqrt{\frac{S_n - S_{nr}}{1 - S_{wr}}} \cdot \left\{ \left(1 - \bar{S}_w^{\frac{n}{n-1}}\right)^{\frac{n-1}{n}} - \left(1 - \bar{S}_t^{\frac{n}{n-1}}\right)^{\frac{n-1}{n}} \right\}^2 \tag{3.47}$$

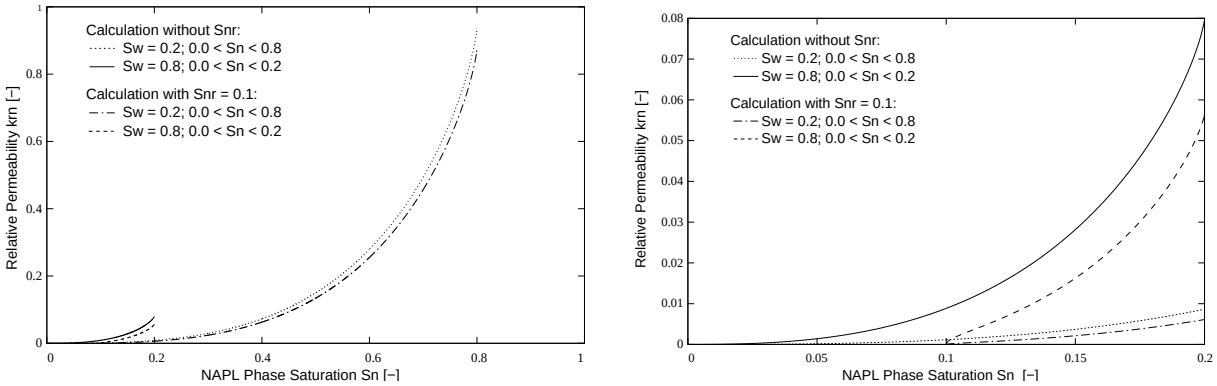

Figure 3.11: Relative permeability of the NAPL phase according to Eq. (3.45) with explicit consideration of a residual NAPL saturation and Eq. (3.47) without. The right picture shows the details for the range $0 \leq S_w \leq 0.2$.

In Fig. 3.11, we plotted the relative permeability of the NAPL phase according to Eqs. (3.45) and (3.47) for two different constant values of the water saturation. For $S_w = 0.2$ the difference between both equations is less significant than for $S_w = 0.8$. As already explained, in the latter case the total liquid saturation is higher and the NAPL phase becomes rapidly mobile according to Eq. (3.45), whereas if a residual NAPL saturation of $S_{nr} = 0.1$ is explicitly considered, this value is a threshold for the NAPL phase mobility.

3.1.5.4 Further Influences on Relative Permeabilities

We explained already that the direction of a multiphase displacement process, whether an imbibition or a drainage is given, affects the capillary pressure–saturation relationship. Since the relative permeabilities can be derived from the $p_c(S)$ relationships, for example by using the bundle of capillary tubes models of *Mualem* or *Burdine*, one should also expect an influence of the $p_c(S)$ hysteresis in the relative permeability behavior.

Another important aspect is the value of the residual saturations, particularly those of the liquid phases. If the systems are not in a state of thermodynamic equilibrium, for example due to ongoing evaporation, there is no unique value of the corresponding residual saturation. However, although *Coats et al.* (1974) [41] and *Coats* (1976) [40] report on the temperature dependence of relative permeabilities, the author does not know of functions that quantitatively describe this

influence.

Verma (1986) [169] describes the influence of phase transition on the relative permeabilities of water and steam. While for non-condensing gaseous phases like air the liquid water within the pores represents an obstacle, condensing gas components like steam can partly compensate this. If steam is hindered in its flow by liquid water in the pore, it can condense, transfer its latent heat of vaporization to the water and the surrounding porous matrix, and eventually pick up part of this latent heat of vaporization further downstream by evaporating additional water. This results in an apparently increased relative permeability for steam.

Relative permeabilities are also subject to effects of hysteresis. As for the capillary pressure-saturation hysteresis, this results from changes between drainage and imbibition processes. For example, *Juanes et al.* (2006) [98] describe the modelling of capillary trapping effects by taking this into account via a hysteretic relative permeability model using the *Land* model [102].

3.1.6 Balance Equations

In general, the flow of fluids can be described by balance equations for mass, momentum, and energy. On the basis of an *Eulerian* view on a finite control volume, the balance equations can be derivated from the transport theorem after *Reynolds*.

3.1.6.1 The Reynolds Transport Theorem

Let B be an arbitrary property (e.g., energy, momentum) of a flow and $b = dB/dm$ the corresponding mass-specific intensive quantity. The total amount of B within a subdomain (or: control volume) Ω is then

$$B = \int_{\Omega} b\rho \, d\Omega \qquad \text{with } b = \frac{dB}{dm} \, . \tag{3.48}$$

For the change of B in Ω over the time-interval dt, the following contributions have to be considered:

- the local change of B within Ω.
- the fluxes of B across the boundaries of Ω.

This is formulated in the *Reynolds transport theorem* for a fixed control volume with constant boundaries as follows:

$$\frac{d}{dt}B = \int_{\Omega} \frac{\partial}{\partial t}(b\rho) \, d\Omega + \int_{\Gamma} b\rho(\mathbf{v}\cdot\mathbf{n}) \, d\Gamma \tag{3.49}$$

with $\mathbf{n}$ representing the unit normal vector of the boundary.

3.1.6.2 Mass Balance - Continuity Equation

The general mass balance equation for a fixed *Eulerian* control volume can be derivated from the *Reynolds transport theorem* with the continuity condition

$$\left(\frac{dm}{dt}\right)_{\text{system}} = 0\,, \tag{3.50}$$

which says that the change of the mass m within a closed system is zero. Setting $B = m$ und $b = dm/dm = 1$ in Eq. (3.49) one obtains

$$\left(\frac{dm}{dt}\right)_{\text{system}} = 0 = \int_{\Omega} \frac{\partial}{\partial t}\rho \; d\Omega + \int_{\Gamma} \rho(\mathbf{v}\cdot\mathbf{n}) \; d\Gamma\,. \tag{3.51}$$

With the *Gaussian integral theorem*

$$\int_{\Omega} \nabla\cdot\mathbf{F} \; d\Omega = \int_{\Gamma} \mathbf{F}\cdot\mathbf{n} \; d\Gamma \tag{3.52}$$

we could write the mass balance within a single integral

$$\int_{\Omega} \left(\frac{\partial}{\partial t}\rho + \nabla\cdot(\rho\mathbf{v})\right) \; d\Omega = 0 \tag{3.53}$$

and then transform it into differential form by assuming Ω to be infinitesimally small:

$$\frac{\partial}{\partial t}\rho + \nabla\cdot(\rho\mathbf{v}) = 0 \tag{3.54}$$

What is now particular for multiphase porous media flow?
At first, the flow through a porous medium occurs only within the pore space; thus, the porosity ϕ has to be considered in the balance equation. Secondly, the mass balance is valid for each fluid phase α. We can then formulate the continuity equation for each α as

$$\frac{\partial(\phi S_\alpha \rho_\alpha)}{\partial t} + \nabla\cdot(\rho_\alpha \mathbf{v}_\alpha) = 0 \tag{3.55}$$

respectively by including *Darcy's law* in its extended form, this yields

$$\frac{\partial(\phi S_\alpha \rho_\alpha)}{\partial t} - \nabla\cdot\left(\rho_\alpha \frac{k_{r\alpha}}{\mu_\alpha}\mathbf{K}\cdot(\nabla p_\alpha - \rho_\alpha \mathbf{g})\right) = 0\,. \tag{3.56}$$

3.1.6.3 Momentum Balance versus Darcy's Law

Preliminary, we can remark that porous media flow behaves very special concerning the balance of momentum due to the very small *Reynolds* numbers that typically occur such that inertia terms can be neglected. We stated already above that small Re are a necessary precondition for the validity of *Darcy's law*.

In general, the momentum balance can be formulated with the *Reynolds transport theorem* and the *second Newtonian axiom*

$$\sum \mathbf{F} = m\mathbf{a} = m\frac{d\mathbf{v}}{dt} = \frac{d}{dt}m\mathbf{v} \,. \tag{3.57}$$

Applying $B = m\mathbf{v}$ and $b = dB/dm = \mathbf{v}$, we obtain

$$\sum \mathbf{F} = \int_{\Omega} \frac{\partial(\mathbf{v}\rho)}{\partial t}\, d\Omega + \int_{\Gamma} \mathbf{v}\rho(\mathbf{v}\cdot\mathbf{n})\, d\Gamma \tag{3.58}$$

Here, $\mathbf{F}$ is the vector of external forces acting on the control volume Ω either as body forces (gravity) or as surface forces (pressure, viscous shear stress). With an analogous procedure as before and by taking into account gravity, pressure and shear stress as external forces we can transform the momentum balance into a general differential form given by:

$$\rho\mathbf{g} - \nabla p + \nabla\cdot\tau_{ij} = \rho\frac{d\mathbf{v}}{dt} \tag{3.59}$$

For *Newtonian fluids*, the relation between shear stress and viscosity can be used to formulate the *Navier–Stokes equation*:

$$\rho\mathbf{g} - \nabla p + \mu\nabla^2\mathbf{v} = \rho\frac{d\mathbf{v}}{dt} \tag{3.60}$$

With this equation (plus continuity equation, of course), the flow can be described on the pore scale. Nevertheless, as discussed in Sec. 3.1.1, the solution of the *Navier–Stokes equation* on the pore scale is not practical for most multiphase porous media problems.

On the local scale (REV scale), *Darcy's law* represents kind of an upscaled, effective equation, cf., e.g. *Whitaker* (1999) [171]. The influence of the porous medium is included by the permeability which is also an effective parameter. Then, *Darcy's law* can substitute the *Navier–Stokes equation* with the significant benefit that it is now possible to decouple the computation of the velocity from the continuity equation. We should note, that with some effort it is also possible to derive *Darcy's law* formally from the *Navier–Stokes equation*.

Finally, we can conclude that on the local scale where *Darcy's law* can be applied, there is no further momentum balance required in addition to the mass balance given by Eq. (3.56).

3.1.6.4 The General Equations for Isothermal Multiphase Flow

As explained before, it depends on which scale a multiphase porous media flow is described, whether the *Navier–Stokes equation* (on the pore scale) or *Darcy's law* (on the local/REV scale) is applied. Presuming a local scale consideration, Eq. (3.56), applied for each phase α, together with some closing relations sufficiently describes the system. For example, the closing relations for the system of partial differential equations in an isothermal two-phase system without phase transitions are the following algebraic equations:

- the difference between the pressures of the non-wetting and the wetting phase is the capillary pressure:

$$p_n - p_w = p_c \tag{3.61}$$

- the sum of both saturations equals one (see Eq. 3.3).
- constitutive relationships for the density, viscosity, relative permeability, and capillary pressure.

The system of equations is strongly coupled and behaves non-linear which is mainly caused by the relationships of relative permeability and capillary pressure as a function of saturation.

3.2 Extended Multiphase Models

In this section, we focus on extensions of the model concept for isothermal two-phase porous media flow which was explained above. Of special interest will be compositional systems of multiple fluid phases including a gaseous phase (see Sec. 3.2.1). Since many applications require the consideration of non-isothermal effects, we will also present the necessary model parameters and constitutive relations for the assembly of the thermal energy equation (Sec. 3.2.2). Finally, Chapter 4 provides the specific model adaptions for the different application problems that will be investigated and simulated later on in Chapter 6.

3.2.1 Compositional Models

The basic definition of phases and components was already given in the beginning of this chapter. In a multiphase system without the consideration of compositional effects it does not play a role whether the phases consist of a single component or are a composition of several species. Physical effects that are caused by the composition of the phases and their spatial variability occur if components can be transferred between fluid phases, for example due to dissolution, or if different ratios of the components in the phases (concentrations) lead to diffusive flow. Figure 3.12 illustrates schematically the concept of two fluid phases including two components. In this case, each phase can be associated with a main component (the solvent) in which a limited amount of the other component (solute) can be dissolved. An example for such a system would be a NAPL infiltration into the groundwater (saturated zone). Both phases are only miscible to a very limited amount. Obviously, there exist also other multiphase multicomponent systems where the local physical processes can determine which component is dominant in a fluid phase. For example, the gas phase in the unsaturated zone consists normally mainly of air, but if the soil is heated up to the boiling temperature of water, the steam displaces the air and becomes locally the main component in the gaseous phase.

In general, the composition of the phases can be mathematically expressed by mole fractions x_α^κ or mass fractions X_α^κ of the components κ in the phases α, both with the constraint that their sum over the components in a phase must equal one:

$$\sum_\kappa x_\alpha^\kappa = \sum_\kappa X_\alpha^\kappa = 1 \tag{3.62}$$

The transformation between mole fractions and mass fractions requires knowledge of the molecular weights M^κ. Then, the mass fraction X_α^κ can be calculated from

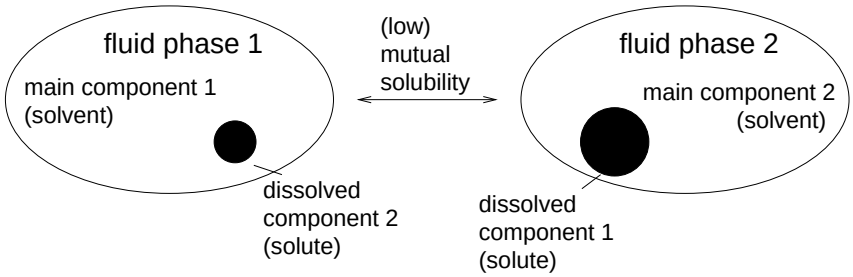

Figure 3.12: Principal model of two low-miscible fluid phases, each consisting of a main component and a limited dissolved amount of the other fluid. An example for such two low-miscible fluids is a water-NAPL system.

$$X_\alpha^\kappa = \frac{x_\alpha^\kappa M^\kappa}{\sum_\kappa x_\alpha^\kappa M^\kappa} \,. \tag{3.63}$$

The physical processes that produce phase transitions of components are manifold. We will discuss in the following particularly dissolution of gaseous components in liquids. After that, we will concentrate on mass transfer due to evaporation and condensation, thereby bridging the gap to non-isothermal systems. Before that, we introduce diffusive/dispersive transport of components within the fluid phases and the corresponding consideration in the model concept.

3.2.1.1 Diffusion/Dispersion

Diffusion and dispersion are processes that tend to equilibrate spatial concentration gradients. Accordingly, diffusive and dispersive fluxes J are generally expressed by the *Fickian* approach

$$J = -D\nabla C \,, \tag{3.64}$$

where C represents the concentration of the transported substance and D is the diffusion (dispersion) coefficient. Depending on the processes, D can be a scalar or a tensor (see below).
Similar to the influence of capillary pressure on the mathematical behavior of the partial differential equations, also diffusion/dispersion shifts its character towards parabolic. The relation between advective and diffusive/dispersive fluxes can be measured by the *Peclét* number, which is given by

$$\mathrm{Pe} = \frac{\mathbf{v}\Delta l}{D} \,. \tag{3.65}$$

Δl is a characteristic length scale. The *Peclét* number is of special interest for the choice of the discretization method [78]. Diffusive processes lead to parabolic equations which are rather good-natured with respect to the stability of the numerical solution. However, systems with hyperbolic dominance require special stabilization techniques like, for example upwinding methods [107, 78, 9].

Diffusion and dispersion can be distinguished physically. Both processes are commonly covered by the term *hydrodynamic dispersion* in porous media flow [149]. Molecular diffusion describes the net fluxes of components due to the motion of molecules and given concentration gradients.

The net fluxes can be explained by the random movement of molecules according to the kinetic theory of gases. In regions with higher concentrations of a certain component statistically more molecules move away compared to those that come in. In contrast to that, mechanical dispersion describes the spreading of components due to fluctuations of magnitude and direction of the flow velocities. This is principally illustrated in Fig. 3.13. As shown there, most flow systems show a spatial variability of the velocity. In many cases, the velocity distribution changes perpendicular to the flow direction due to the non-slip condition at the porous matrix. Transverse mixing enhances the dispersive spreading of some initial concentration that is transported by advection (e.g., in turbulent flow or, like here, due to pore space tortuosity in porous media flow). Mathematically, hydrodynamic dispersion is described by Eq. (3.64) and a dispersion tensor, which is given by

$$\mathbf{D} = \frac{\mathbf{v}\mathbf{v}^T}{||\mathbf{v}||}(\alpha_l - \alpha_t) + \mathbf{I}(D_{\mathrm{pm}} + \alpha_t||\mathbf{v}||) \; . \tag{3.66}$$

Here α_l and α_t are the longitudinal and transversal dispersion coefficients (in m) which are in practice rather difficult to determine since their values depend strongly on the scale of consideration and the discretization length of the numerical grid. D_{pm} is an effective molecular diffusion coefficient in the porous medium. The parameters and processes influencing the value of D_{pm} are discussed below.

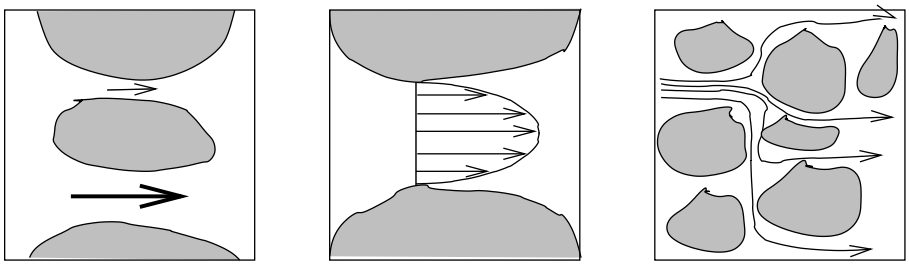

Figure 3.13: Dispersion mechanisms in single-phase porous media flow.

The effective molecular diffusion coefficient in porous media is always smaller than the literature values for given mixtures. Firstly, the tortuosity of the pore connections (pathlines) reduces diffusion significantly. Secondly, since we consider diffusion within fluid phases in a multiphase context, this effect is enhanced by the distribution of the phases which is dependent on the saturation and the wettabilities. This phenomenon is taken into account, for example, by the approach of *Millington & Quirk* (1961) [120] who suggest to calculate the effective tortuosity by

$$\tau = \frac{(\phi S_\alpha)^{7/3}}{\phi^2} \; . \tag{3.67}$$

With this, the effective molecular diffusion coefficient is commonly estimated using

$$D^\kappa_{\mathrm{pm}} = \tau\phi S_\alpha D^\kappa_\alpha \; . \tag{3.68}$$

Here, D^κ_α is the 'real' diffusion coefficient of component κ in phase α.

As it can be easily concluded from Eq. (3.66), the influence of molecular diffusion increases with decreasing velocities. Flow velocities in subsurface flow are characteristically in the order of m/day or 10^{-7} ... 10^{-8} m/s. A typical molecular diffusion coefficient is in the order of 10^{-6} m^2/s in the gas phase and 10^{-9} m^2/s in the water phase. According to these numbers and under consideration of the great uncertainty of α_l and α_t, the modeler has to outweigh carefully whether it can be reasonable to neglect dispersivity if the precondition of low velocities is given. In practice, a common way to determine α_l and α_t is to use them as fitting parameters to measurement data, for example, in modelling the transport of nitrate in a regional aquifer.

3.2.1.2 Vapor Pressure and the Laws of *Dalton, Henry,* and *Raoult*

The computation of the mole fractions of the components in the phases is in general a sophisticated thermodynamic problem. However, there are systems that allow a reasonable simplification by applying the laws of *Henry, Raoult,* and *Dalton*. Note, that in the following we restrict this discussion to mole fractions since the computation of mass fractions can be done in simple analogy.

The mole fractions in the fluid phases of gas-liquid systems are typically closely related with each other in cases where both a gas phase and one or several liquid phases co-exist. In other words, the mole fraction of a component in the gas phases influences its corresponding fraction in the liquid phase (and vice versa). The key parameter for this is the vapor pressure.

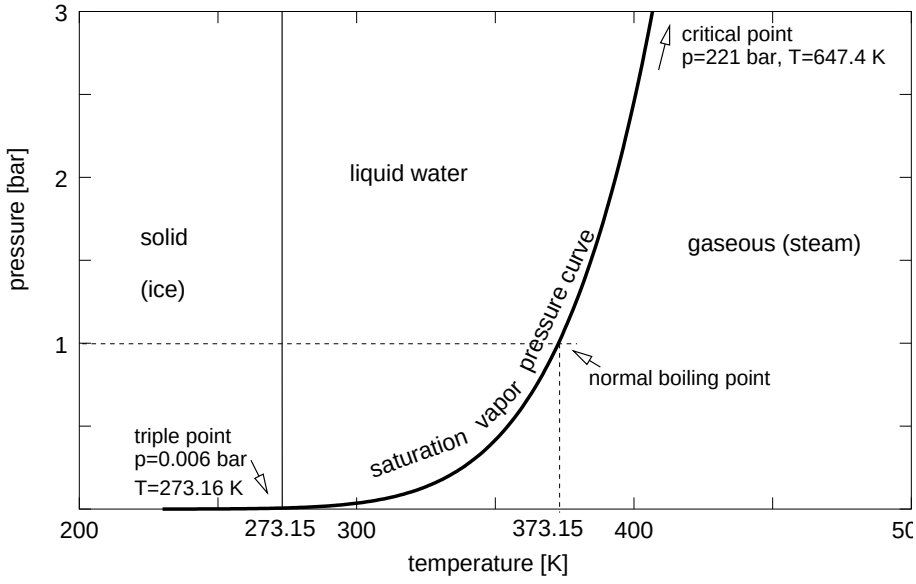

Figure 3.14: Phase diagram of water including the saturation vapor pressure curve.

Figure 3.14 shows the phase diagram of water in a range of low pressures and moderate temperatures, thus still far below the critical point which is for water at 221 bar and 647 K (374 C). The saturation vapor pressure curve represents therein the separation of the liquid water and steam regions. The curve continues until the critical point. Above that, steam and vapor can no longer be distinguished. This will be of detailed interest in Sec. 4.3 where the properties of sub-

and supercritical CO_2 are required for the modelling of CO_2 injection into deep geological formations. The saturation vapor pressure is a strong function of temperature. The curve describes the change of the equilibrium state between the molecules leaving the liquid into the gas phase (vapor) and those returning from the vapor back to the liquid. Since the mutual attraction and repulsion of molecules is individual, each species has its own saturation vapor pressure curve. The more volatile a species, the higher is its vapor pressure for a given temperature. This will be an important aspect later in Sec. 4.1 for the discussion of thermally enhanced remediation of NAPL contaminated soils. The curves are plotted for water and some selected NAPLs in Fig. 3.15 using the *Antoine* equation which is given by

$$\log_{10}\left(\frac{p^{\mathrm{w}}_{\mathrm{sat}}}{\mathrm{mbar}}\right) = A - \frac{B}{C + T/^{\circ}C}\,, \tag{3.69}$$

where A, B, and C are empirical parameter (cf, for example, *Reid et al.* (1987) [146]. Tab. 3.4 lists them for the curves of Fig. 3.15.

Table 3.4: *Antoine* constants for water and selected organic liquids

	A	B	C
water	8.19621	1730.63	233.426
trichloroethylene (TCE)	6.51827	1018.603	192.731
m-xylene	7.00909	1462.266	215.11
1,3,5-trimethylebenzene (mesitylene)	7.07638	1571.005	209.728

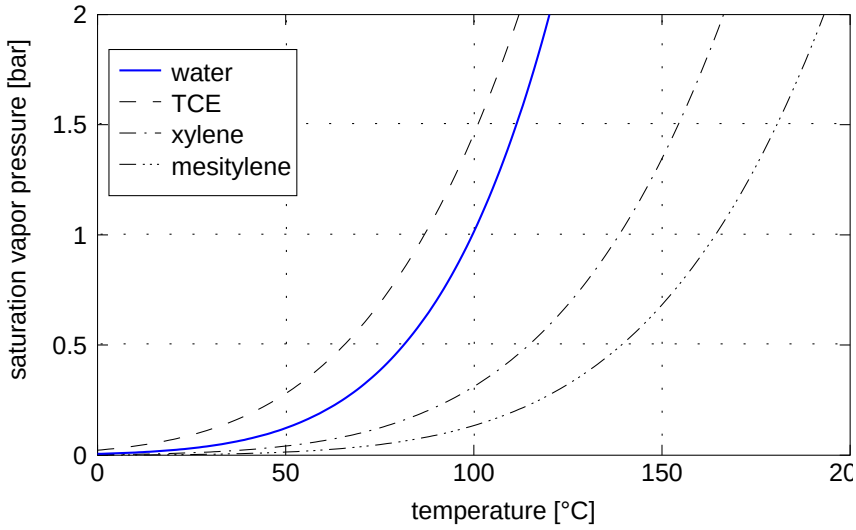

Figure 3.15: Saturation vapor pressures of water and some selected NAPLs.

Often, there can be found more precise formulas or tables in the literature like the *IAPWS* formulations [94] for water or *Span & Flacke* (2004) [157] for CO_2.

In general, the gas phase consists not only of a single vapor but of a mixture of gaseous components. Under the assumption of only ideal gas components obeying all Eq. (3.6), we state that this equation is also valid for a mixture of ideal gases. Then, the total pressure of the gas phase equals the sum of the partial pressures p_g^κ of the gaseous components. This relation is commonly denoted as *Dalton's* law for ideal gas mixtures:

$$p_g = \sum_\kappa p_g^\kappa \tag{3.70}$$

Assuming the gas phase is a binary mixture of vapors in an equilibrium state with their liquids, then, according to Eq. (3.70), the total gas phase pressure corresponds to the total vapor pressure. Figure 3.16 (left) illustrates that the total vapor pressure of a binary mixture depends on the composition of the mixture. If the mixture behaves ideally as depicted (left figure), there will be a linear relationship between the mole fractions and the vapor pressures of the pure components:

$$p_g = p_g^1 + p_g^2 = x^1 p_{\text{sat}}^1 + x^2 p_{\text{sat}}^2 \tag{3.71}$$

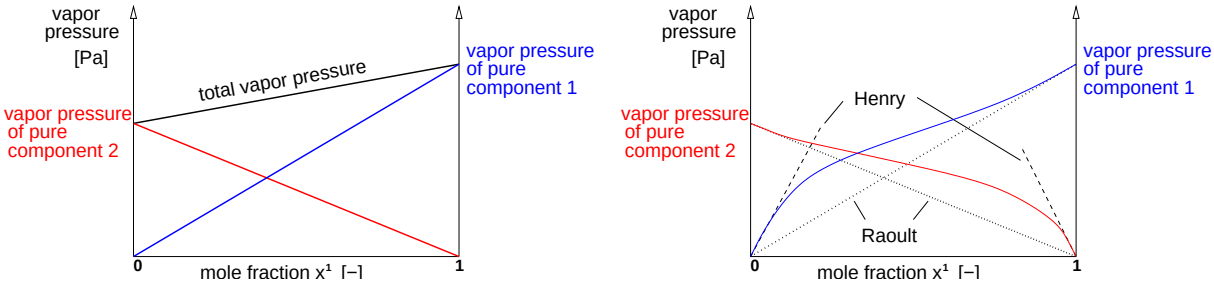

Figure 3.16: Vapor pressure of a binary liquid mixture: ideal behavior (left) and real behavior with the tangents illustrating *Raoult's law* and *Henry's law* (right).

Real mixtures, however, typically show a deviation from the ideal behavior as principally indicated in Fig. 3.16 (right). For mixture compositions with a great surplus of one component (very small amount of the other component in the mixture), the partial pressure of the predominating component (the solvent) still changes linearly with its mole fraction.

$$p_g^\kappa = x^\kappa p_{\text{sat}}^\kappa \tag{3.72}$$

This is known as *Raoult's* law and holds in most cases only for the solvent. For increasing fraction of the solute, the function is no longer linear. In cases where the mutual solubilities are very low, it is also justified to neglect even the reduction of the vapor pressure of a solvent according to Eq. (3.72) and to assume instead the partial pressure of the respective gaseous component equal to the saturation vapor pressure of the pure component. An example for such a mixture is the water-NAPL system discussed in Sec. 4.1.

As Fig. 3.16 (right) indicates, the difference between the ideal and the real behavior is very significant for the solute which is present in very low concentrations. However, it appears to follow also a straight line below a certain mole fraction. This is expressed by *Henry's* law

$$p_g^\kappa = x^\kappa H_\alpha^\kappa \tag{3.73}$$

where H_α^κ is the *Henry* coefficient for the dissolution of component κ in phase α.

Summarizing, we can conclude that for diluted solutions there are equations available for a good approximation of the vapor pressure depending on the mole fractions. This holds both for the solvent (*Raoult's* law) and for the solute (*Henry's* law).

Practically, *Dalton's* law and *Henry's* law can be used for the computation of the mole fractions in the gas phase and in the liquid phases. Presuming ideal gases and applying *Dalton's* law, the mole fractions in the gas phase are given by

$$x_g^\kappa = \frac{p_g^\kappa}{p_g} \,. \tag{3.74}$$

If liquid phases exist, then they are assumed to be in equilibrium with their corresponding vapors. Thus, p_g^κ equals p_{sat}^κ. A vapor in the gas phase without its locally existing corresponding liquid phase is undersaturated and can thus not be derived from p_{sat}^κ. As explained later in Sec. 5.3, this has consequences for the choice of the primary variables.

If *Henry's* law can be applied, then the mole fractions in the liquid phases are

$$x_\alpha^\kappa = \frac{p_g^\kappa}{H_\alpha^\kappa} \tag{3.75}$$

with α being restricted to represent liquid phases here. H_α^κ are to be determined experimentally or taken from the literature. It is known, for example, that the solubility of air in water decreases with increasing temperature while the solubility of organic components then often increases.

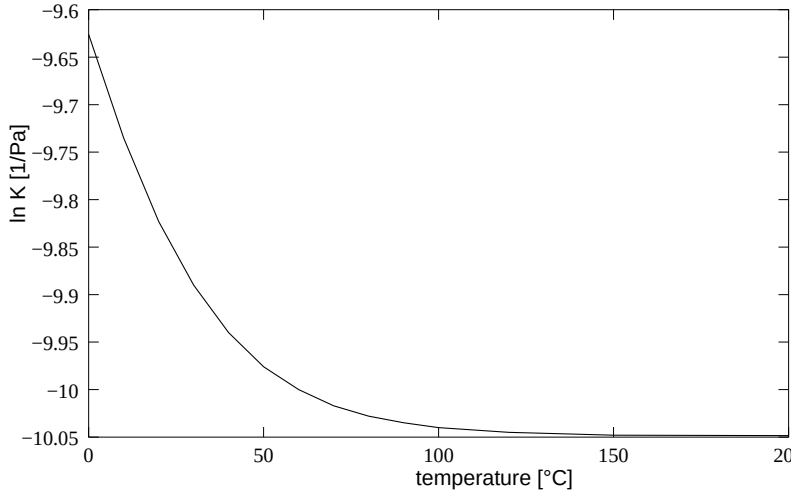

Figure 3.17: Logarithm of the *Henry* coefficient of air in water dependent on temperature.

Figure 3.17 shows the temperature dependence of the *Henry* coefficient of air in water where

$$(H_w^a)^{-1} = \left(0.8942 + 1.47 \cdot e^{-0.04394\,T}\right) \cdot 10^{-10} \qquad [\text{Pa}^{-1}] \tag{3.76}$$

is used as suggested, for example, by [78].

If the number of components in a fluid phase is n, then $n-1$ relations are needed to compute the respective mole fractions. The last one is then obtained from the constraint of Eq. (3.62).

3.2.1.3 Vapor Pressure Lowering at High Capillary Pressures

The vapor pressure requires particular attention in porous media where due to capillarity the interfaces between liquid water and its vapor respectively the air is curved. It is a known thermodynamic phenomenon that the vapor pressure above a curved surface of a water droplet (on the convex side of the liquid-vapor interface) is increased relative to the vapor pressure at a plane surface (see also Sec. 3.1.4). This effect is due to the increased surface tension of the droplets against which work has to be performed by the condensing molecules.

In the porous medium, this effect is also relevant, however for water as the mostly wetting fluid, it occurs with a different sign. The wetting liquid water occupies the pores with the liquid phase being on the concave side of the interface. Thus, the vapor pressure in the pore is lowered relative the value on a plane surface (Fig. 3.18).

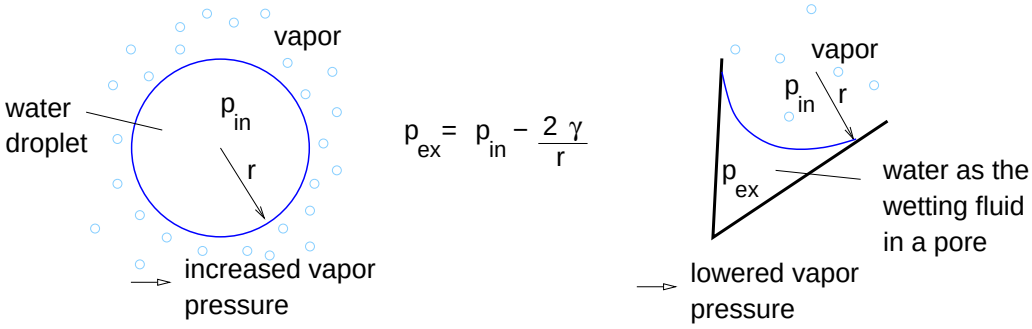

Figure 3.18: Effect of curved surfaces on the vapor pressure.

The *Kelvin* equation takes the effect of curved surfaces on the vapor pressure into account. In a porous medium with the capillary pressure representing the pressure difference at the vapor-liquid interface, the equation can be formulated as

$$p^w_{\text{sat,curved}} = p^w_{\text{sat}} \cdot \exp\left[-\frac{p_c}{\rho_w R_w T}\right] \tag{3.77}$$

with $R_w = 461.6$ J/(kg K) representing the gas constant, for example, for water vapor.

3.2.1.4 Evaporation and Condensation

In the previous sections, we already discussed the saturation vapor pressure curve as a function of temperature. The curve describes the change of the equilibrium between molecules leaving and returning to the liquid state of aggregation. In case of more molecules leaving an evaporation occurs. Evaporation is forced, according to Eq. (3.74),

- by increasing temperature (x^κ_g increases since $p^\kappa_g = p^\kappa_{\text{sat}}$ increases with temperature)

- or by decreasing ambient pressure (x_g^κ increases since the total gas phase pressure p_g is lowered).

The process in the opposite direction is condensation and the reasoning above can be used analogously.

Beside the transfer of mass components between the gaseous and the liquid phases, it is characteristic that evaporation and condensation are strongly coupled with an exchange of thermal energy. The latent heat of vaporization (see Fig. 3.19) is the difference between the specific enthalpy of the gaseous component and that one of its corresponding liquid at the same temperature and pressure. This will be in the focus of the next section where non-isothermal systems are discussed in detail.

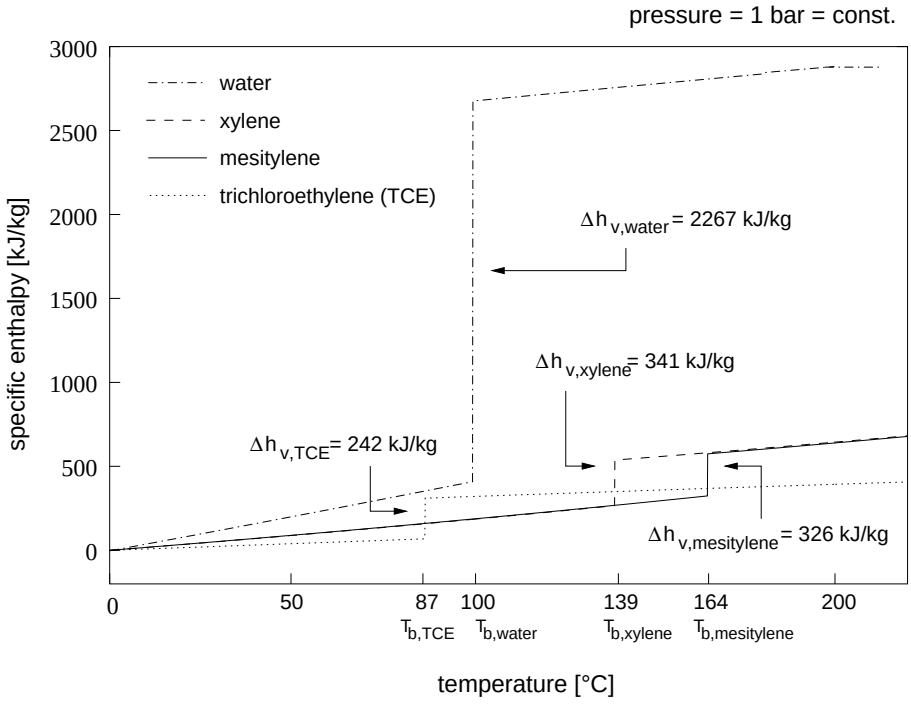

Figure 3.19: Specific enthalpy and latent heat of vaporization at atmospheric pressure conditions (1 bar): water and selected NAPLs.

3.2.2 Non-Isothermal Systems

3.2.2.1 Equations of State, State Variables, and the Phase Rule of Gibbs

The description of non-isothermal effects by an appropriate model concept requires knowledge of the thermodynamic background. A thermodynamic system consisting of several gaseous, liquid, or solid phases can be uniquely determined by a certain number of state variables if it is in a state of equilibrium. The state variables are then related with each other via equations of state. We introduced such an equation of state already with Eq. (3.6) representing the ideal gas law. Also, for example, the vapor pressure (see Sec. 3.2.1.2) is related via an equation

of state with the state variable temperature. The literature distinguishes different equations of state. The thermal equation of state describes the relation between the state variables pressure p, volume V, temperature T, and the number of moles n (e.g. ideal gas law). The properties of a thermodynamic system are not completely determined with a thermal equation of state alone. This requires additionally a caloric equation of state for a relation between pressure, volume, temperature, number of moles and the internal energy U or the enthalpy H (see below). The caloric equation of state is indispensable for the energy balance (first law of thermodynamics) since it determines the relevant state variables for the quantification of thermal energy exchange processes.

Not all state variables are independent of each other. The number of independent state variables F (degrees of freedom) depends on the number of components C and the number of fluid phases P. In general, the *phase rule* according to *Gibbs* formulates for a system in thermodynamic (thermal, chemical, and mechanical) equilibrium

$$\mathrm{F} = \mathrm{C} - \mathrm{P} + 2 \; . \tag{3.78}$$

For the description of multiphase multicomponent systems in porous media, this approach requires some modification. For porous media systems above the scale of a REV the phase saturations which sum up to one increase the number of degrees of freedom by P-1. Thus, we end up with

$$\mathrm{F} = \mathrm{C} - \mathrm{P} + 2 + (\mathrm{P} - 1) = \mathrm{C} + 1 \; . \tag{3.79}$$

For a thorough thermodynamic derivation of Eq. (3.78) and the equations used below to introduce the caloric state variables, we refer to the literature, e.g. [6] or other textbooks of thermodynamics. The details would be beyond the scope of this work.

3.2.2.2 The Caloric State Variables Internal Energy, Heat Capacity, and Enthalpy

In general, the internal energy U, the enthalpy H, and the heat capacities at constant volume and constant pressure respectively are the caloric state variables. Divided by the mass m of a system or a fluid/solid phase, they are the called the specific state variables denoted accordingly by lower case letters.
Thus, the specific internal energy u [J/kg] of a system or a phase accounts for the energy per kilogram of the molecules. The partial derivative of u with respect to temperature at constant specific volume yields the specific heat capacity at constant volume c_v:

$$c_v = \frac{\partial u}{\partial T} \tag{3.80}$$

c_v is the required amount of energy for increasing the temperature of 1 kg of a phase by 1 K while keeping its volume constant. If the volume is allowed to change during the heating (or cooling analogously), the amount of energy delivered does not equal the change of the internal energy. The difference corresponds to the volume changing work (p V). The sum of the internal energy and the volume changing work gives another state variable denoted as enthalpy H with

$$H = U + pV \tag{3.81}$$

or after division by m the specific enthalpy h

$$h = u + pv = u + \frac{p}{\rho}. \tag{3.82}$$

While the contribution of the volume changing work is often negligible for dense fluids, it is in general significant for gaseous phases at low or moderate pressures. Also the specific enthalpy is dependent on temperature. The respective partial derivative at constant pressure gives the specific heat capacity at constant pressure c_p:

$$c_p = \frac{\partial h}{\partial T} \tag{3.83}$$

For ideal gases, c_v and c_p are related via

$$c_p - c_v = \frac{R}{M}\,. \tag{3.84}$$

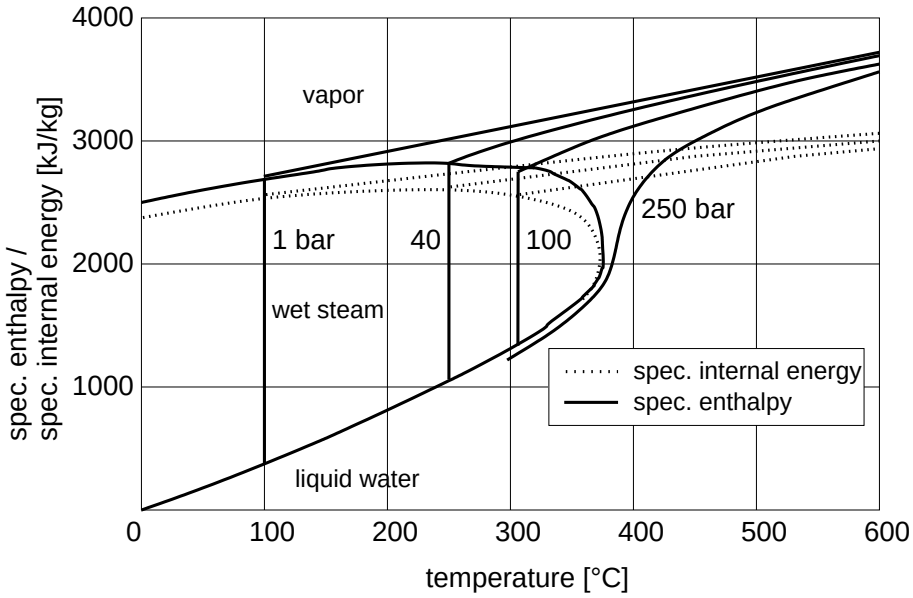

Figure 3.20: Specific enthalpy and specific internal energy of water as a function of temperature at different pressures.

Figures 3.20 and 3.21 illustrate the specific enthalpy of water as a function of pressure and temperature. In Fig. 3.20, we further see the specific internal energy which deviates from the specific enthalpy only for the vapor significantly whereas the curves for liquid water lay more or less on top of each other. In both illustrations, four characteristic regions can be distinguished. These are firstly the region of liquid water with relatively low enthalpies and secondly the region of water vapor with high enthalpies. Both are separated by the wet steam region which is characterized by a vertical section of the curves representing the latent heat of vaporization. If the specific enthalpy changes within the wet steam region, this results at isobaric conditions not in a change of the temperature (see Fig. 3.20). Instead, the ratio of vapor to condensate is shifted.

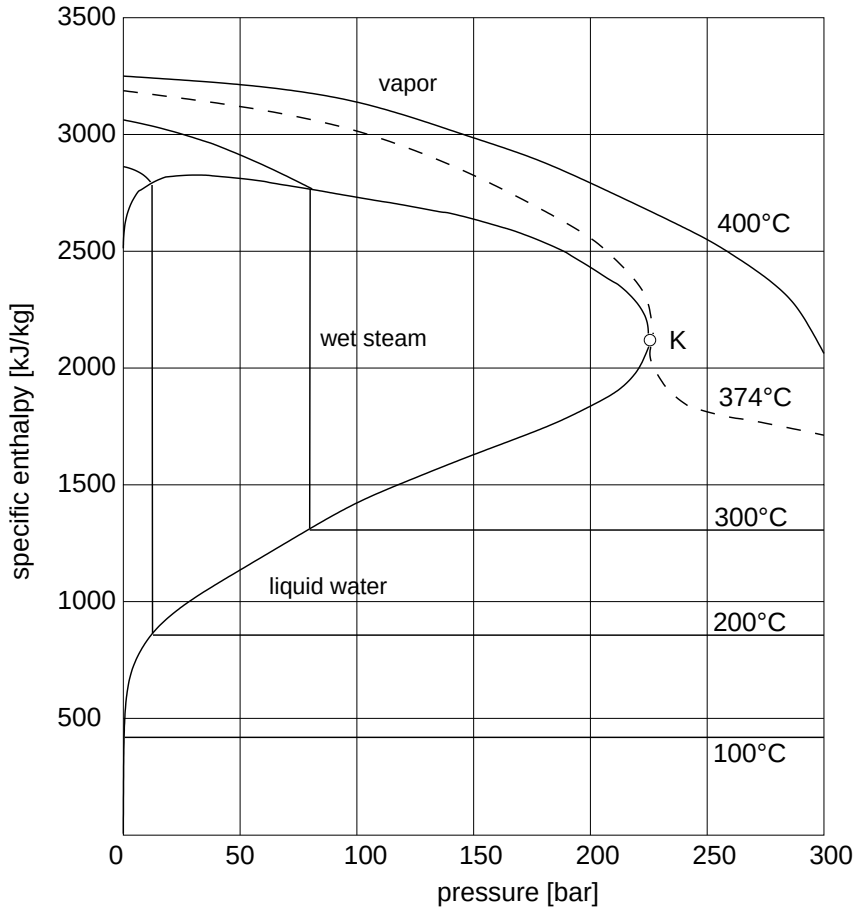

Figure 3.21: Specific enthalpy of water as a function of pressure at different temperatures.

The temperature does not change until all condensate (liquid) has evaporated or all vapor has condensed. The same holds analogously for isothermal conditions in Fig. 3.21. The specific enthalpy difference between the vapor and the liquid region is denoted as the latent heat of vaporization which was already introduced before. From Fig. 3.19, one can see that the latent heat of vaporization is significantly higher for water than for the organic liquids considered here. The fourth region in these graphs is that of the supercritical fluid at high pressures (> 221 bar) and temperatures ($> 374^{\circ}$C). There, vapor and liquid can not be distinguished and thus there is not latent heat of vaporization. The supercritical region will be of specific interest in Sec. 4.3 where the modelling of CO_2 storage in deep geological formations is discussed.

For the computation of the specific enthalpies of water and water vapor, it is recommended to use the data of *IAPWS* [94] or other tables which are manifold in the thermodynamic literature. Practically all the multiphase systems with liquid water involved which are considered in this work have only very small amounts of dissolved components in the water. This is typically very different in the gas phase. Its composition can vary strongly, for example, in a water-air system depending on temperature from almost pure air (low temperatures) to pure water vapor (boiling). Thus, for the computation of the specific enthalpy of the gas phase we determine the sum of the specific enthalpies of the gaseous components multiplied with their respective mass fractions:

$$h_g = \sum_\kappa h_g^\kappa X_g^\kappa \tag{3.85}$$

We calculate the specific enthalpy of air, for example, by the following relation between h_g^a and the specific heat capacity at constant volume c_v^a obtained from Eqs. (3.83) and (3.84):

$$h_g^a = c_v^a \cdot (T - 273.15) + \frac{R(T - 273.15)}{M^a} \tag{3.86}$$

T stands here for the absolute temperature in K. c_v^a may be assumed as a constant value of 733 J/(kg K) [57].

3.2.2.3 Heat Conductivity

Heat conduction is the molecular transport of thermal energy due to a temperature gradient. This heat transport mechanism is predominantly significant for solids while it is in general superposed by convective heat flow in liquids and gases. Generally, heat conduction is influenced by the intermolecular distances. Therefore, solids and liquids show typically better heat conduction properties than gases. It is well known that the low heat conductivity of gases is technically utilized for insulation materials with a high amount of gas pores.

Fourier's law of heat conduction describes the conductive heat flux proportional to the temperature gradient:

$$J^E = -\lambda \nabla T \tag{3.87}$$

λ is the heat conductivity of the material. Depending on the material, λ can be a scalar or a tensor. Equation (3.87) is a diffusion equation like the *Fickian* diffusion equation (3.64).

In (multi-)fluid-filled porous media, heat conduction is a rather complex process. Heat fluxes occur through conduction within the solid skeleton but also within the fluid phases, although heat conduction in gaseous phases may be neglected in general. For considering this in the model concept, it requires to decide whether the assumption of local thermal equilibrium can be maintained or not. Based on that, it is necessary to formulate the balance equations for thermal energy, see Sec. 3.2.3.1. If an energy balance is applied for each phase (including the solid phase), the heat conductivity is a material parameter. In case of a local thermal equilibrium assumption, we do not distinguish the temperatures in the locally existing phases. Thus, heat conduction can be described by averaging over the fluid-filled porous medium.

A simple approach is the weighting of the heat conductivities according to the volume ratios of the fluid phases, given by

$$\lambda_{\text{pm}} = \lambda_s(1 - \phi) + \sum_\alpha \lambda_\alpha \phi S_\alpha \tag{3.88}$$

where λ_{pm} is the averaged heat conductivity, λ_s that of the solid and λ_α the heat conductivity of the fluid phases α.

Eq. (3.88) neglects that the wettability of the fluids affects their contribution to the averaged heat conductivity. This can be easily explained for a water-air system with water representing the

wetting phase. The heat conductivity is obviously higher at high water saturations. However, the increase of λ_{pm} with increasing S_w is over-proportional for low water saturations since water fills predominantly the small pore angles due to its wettability. Thus, the contact areas between the soil grains which are necessary for the heat conduction are supported by the water. This increase of energy exchange area is less significant at higher water saturations. *Somerton* (1974) [156] suggests a root function to take this effect into account:

$$\lambda_{pm} = \lambda_{pm}^{S_w=0} + \sqrt{S_w}(\lambda_{pm}^{S_w=1} - \lambda_{pm}^{S_w=0}) \tag{3.89}$$

Equation (3.89) is formulated here for a water-air system. It can be easily extended to other multiphase systems.

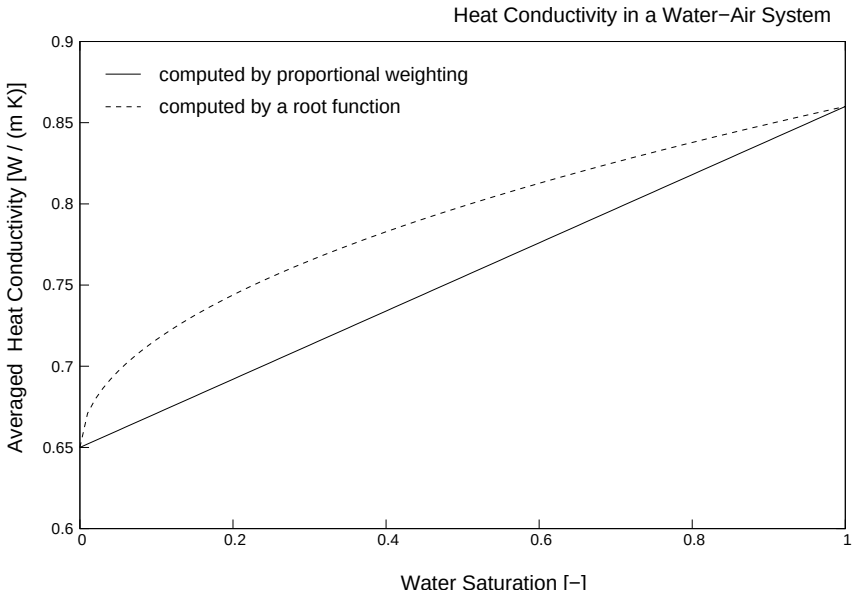

Figure 3.22: Averaged heat conductivity of the fluid-filled porous medium according to Eqs. (3.88) and (3.89) for a water-air system.

3.2.3 Balance Equations for Non-Isothermal Compositional Models

3.2.3.1 Energy Balance

The balance of energy can be formulated based on the first law of thermodynamics which says that there is no change of the energy in a closed system. In other words, if there is a change of a system's energy, this must be caused by heat fluxes across the system boundary and/or work which is performed by or to the system. We can express this in terms of

$$\left(\frac{\partial Q}{\partial t} - \frac{\partial W}{\partial t}\right)_{\text{system}} = \left(\frac{dE}{dt}\right)_{\text{system}}, \tag{3.90}$$

where

- $\partial Q/\partial t$ is the heat flow due to conduction and radiation. Since radiation is normally not significant in porous media flow, we neglect this and formulate

$$\frac{\partial Q}{\partial t} = \int_\Gamma \lambda \nabla T \, d\Gamma = \int_\Omega \nabla \cdot (\lambda \nabla T) \, d\Omega \,. \tag{3.91}$$

  Here, λ is the heat conductivity of the porous medium (see Sec. 3.2.2.3), and T the temperature.

- $\partial W/\partial t$ is the work performed within the time interval dt. There are contributions of the volume changing work (pressure work on surfaces)

$$\frac{\partial W_p}{\partial t} = \int_\Gamma p \, (\mathbf{v} \cdot \mathbf{n}) \, d\Gamma = \int_\Omega \nabla \cdot (p\mathbf{v}) \, d\Omega \tag{3.92}$$

  and the viscous dissipation work $\partial W_{\text{vis}}/\partial t$ which is approximately zero due to very low flow velocities.

- E represents the energy of the system including a kinetic part

$$E_{\text{kin}} = \int_\Omega \frac{\rho}{2} v^2 \, d\Omega \tag{3.93}$$

  and a thermodynamic contribution of the internal energy

$$U = \int_\Omega \rho u \, d\Omega \,, \tag{3.94}$$

  where u is the specific internal energy (see Sec. 3.2.2.2). Typically, the flow velocities in a porous medium are so small that the kinetic energy is negligible compared with the internal energy. With the *Reynolds transport theorem*, the change of U within dt is

$$\begin{aligned} \frac{dU}{dt} &= \int_\Omega \frac{\partial}{\partial t} \rho u \, d\Omega + \int_\Gamma \rho u \, (\mathbf{v} \cdot \mathbf{n}) \, d\Gamma \\ &= \int_\Omega \left(\frac{\partial}{\partial t} \rho u + \nabla \cdot (\rho u \mathbf{v}) \right) d\Omega \,. \end{aligned} \tag{3.95}$$

Now, we are able to reformulate Eq. (3.90) and obtain

$$\int_\Omega \nabla \cdot (\lambda \nabla T) \, d\Omega - \int_\Omega \nabla \cdot (p\mathbf{v}) \, d\Omega = \int_\Omega \left(\frac{\partial}{\partial t} \rho u + \nabla \cdot (\rho u \mathbf{v}) \right) d\Omega \,. \tag{3.96}$$

With $h = u + p/\rho$ representing the specific enthalpy (see Sec. 3.2.2.2) this can be simplified and written in differential form as

$$\frac{\partial}{\partial t} \rho u + \nabla \cdot (\rho h \mathbf{v}) - \nabla \cdot (\lambda \nabla T) = 0 \,. \tag{3.97}$$

Equation (3.97) still does not consider the influence of the porous matrix and the presence of multiple fluids. The porous medium can store thermal energy according to its heat capacity and the total energy of the fluids equals the sum of the contributions of each fluids. Furthermore,

each fluid can flow separately and transport thermal energy. Thus, it is in general necessary to balance each fluid's thermal energy and the respective exchange with the other fluids and the porous matrix. But, as we explained already at the beginning of this chapter, it is for many cases (low velocities, small grains) reasonable to assume **local thermal equilibrium**. In this case, a single balance equation for thermal energy is sufficient and can be formulated as:

$$\frac{\partial}{\partial t}\left(\phi\sum_{\alpha}\rho_{\alpha}u_{\alpha}S_{\alpha}\right)+\frac{\partial}{\partial t}\left((1-\phi)\,\rho_{s}c_{s}T\right)$$
$$-\nabla\cdot(\lambda_{pm}\nabla T)-\sum_{\alpha}\nabla\cdot\left\{\frac{k_{r\alpha}}{\mu_{\alpha}}\rho_{\alpha}h_{\alpha}\mathbf{K}\left(\nabla p_{\alpha}-\rho_{\alpha}\mathbf{g}\right)\right\}=0\,,\qquad\forall\alpha \tag{3.98}$$

Here, c_s represents the specific heat capacity of the soil grains.

A non-isothermal multiphase model with **separate energy balance equations for the solid and the fluids** is presented by *Crone et al.* (2002) [42]. Their aim is to simulate steam injection operations for the heating of porous media as a common application in the field of chemical engineering. In the relatively coarse materials like, for example, lignite two basic differences occur compared with the fields of multiphase applications considered in this work. Firstly, the coarse porous structures with large grains and big pores allow high flow velocities. Secondly, heat conduction within the grains and heat transfer between fluids and solids are dominating processes. Both effects tend to violate the assumption of thermal equilibrium.
Crone et al. (2002) [42] formulate the 1D energy balance for the fluid mixture as

$$\frac{\partial(u\rho)}{\partial t}+\frac{\partial(\rho h v_{\mathrm{mix}})}{\partial x}=\frac{1}{\phi}\left[\frac{\partial}{\partial x}\left(\lambda_{\mathrm{pm}}\frac{\partial T_f}{\partial x}\right)+\alpha_{\mathrm{mix}}a_{\mathrm{mix}}(T_{s,0}-T_f)\right] \tag{3.99}$$

where v_{mix} is the effective flow velocity of the multiphase mixture defined by

$$v_{\mathrm{mix}}=\frac{1}{\phi\rho h}\sum_{\alpha}\rho_{\alpha}v_{\alpha}h_{\alpha} \tag{3.100}$$

with h representing the specific mixture enthalpy.

In Eq. (3.99), the heat transfer between fluids and solid phase is considered by the temperature of the fluid mixture T_f and the surface temperature of the solid phase $T_{s,0}$. Further parameters are the heat transfer coefficient α_{mix} and the specific surface area a_{mix}.
The energy balance for the solid phase is given by

$$\frac{\partial(\rho_s c_s T_s)}{\partial t}=\frac{1}{(1-\phi)}\left[\alpha_{\mathrm{mix}}a_{\mathrm{mix}}(T_f-T_{s,0})\right]\,. \tag{3.101}$$

In the formulation of Eq. (3.101), the heat conduction within the grains is neglected. Thus, $T_{s,0}$ should equal T_s as the uniform temperature of the whole particle. If heat conduction within the grains is relevant, Eq. (3.101) can be replaced by the following two equations. The first one accounts for the heat conduction within a sphere-shaped grain of radius r and can be written as

$$\frac{\partial T_s}{\partial t}=\frac{\lambda_s}{\rho_s c_s}\frac{1}{r^2}\frac{\partial}{\partial r}\left(r^2\frac{\partial T_s}{\partial r}\right)\,. \tag{3.102}$$

The second equation states that the transferred heat between fluid mixture and solid as well as the transport of energy into the grain via heat conduction should equal:

$$\alpha_{\text{mix}} a_{\text{mix}} (T_{s,0} - T_f) = \frac{\partial}{\partial r}(\lambda_s T_{s,0}) \tag{3.103}$$

3.2.3.2 Mass Balance per Component for Compositional Multiphase Models

We derived already in Sec. 3.1.6.2 the general mass balance equation for multiphase systems in porous media. Compositional flow systems include the same processes which are local storage, advection, and sources/sinks. Additionally, diffusion of components within the phases must be considered if relevant. It is convenient to formulate the mass balance equations for each component κ with the advantage that mass transfer of components between phases is implicitly encountered. In this case, the total balance of each component is obtained by considering the mass fractions (or molar fractions) of the components within the phases. The individual contributions of the phases - both in the local storage term and in the flux terms due to advection and diffusion - to the mass balance of a component are then summed up. Based on **mass fractions** X_α^κ, the mass balance equation can be formulated for each κ as

$$\begin{aligned} &\phi \frac{\partial (\sum_\alpha \rho_{\text{mass},\alpha} X_\alpha^\kappa S_\alpha)}{\partial t} - \sum_\alpha \nabla \cdot \left\{ \frac{k_{r\alpha}}{\mu_\alpha} \rho_{\text{mass},\alpha} X_\alpha^\kappa \mathbf{K} (\nabla p_\alpha - \rho_{\text{mass},\alpha} \mathbf{g}) \right\} \\ &- \sum_\alpha \nabla \cdot \left\{ D_{pm}^\kappa \rho_{\text{mass},\alpha} \nabla X_\alpha^\kappa \right\} - q^\kappa = 0 \qquad \forall \kappa,\ \forall \alpha\ . \end{aligned} \tag{3.104}$$

Analogously, this formulation can be modified to a molar balance where the molar densities and **mole fractions** are used to quantify the amounts of κ in the phases. This can be written as

$$\begin{aligned} &\phi \frac{\partial (\sum_\alpha \rho_{\text{mol},\alpha} x_\alpha^\kappa S_\alpha)}{\partial t} - \sum_\alpha \nabla \cdot \left\{ \frac{k_{r\alpha}}{\mu_\alpha} \rho_{\text{mol},\alpha} x_\alpha^\kappa \mathbf{K} (\nabla p_\alpha - \rho_{\text{mass},\alpha} \mathbf{g}) \right\} \\ &- \sum_\alpha \nabla \cdot \left\{ D_{pm}^\kappa \rho_{\text{mol},\alpha} \nabla x_\alpha^\kappa \right\} - q^\kappa = 0 \qquad \forall \kappa,\ \forall \alpha\ . \end{aligned} \tag{3.105}$$

Chapter 4

Specific Problem-Oriented Model Adaptions

Following Chapter 2, where different gas-liquid systems were characterized, we examine the adaption of the above-described model concepts for the specific problems more closely. We explain the necessary extensions of the concepts and discuss relevant assumptions and simplifications as well as additional processes and parameters in the models.

4.1 NAPL-Contamination and Thermally Enhanced Remediation

The necessary complexity of the model concept for water-NAPL-gas systems depends obviously on the specific problem. While the spreading of a NAPL in the subsurface after a spill may be described with a less complex model neglecting, for example, non-isothermal or even compositional effects, it requires a more sophisticated model for the simulation of thermally enhanced remediation scenarios, see also Sec. 5.4. Particularly, the boiling behavior of the NAPL-water mixture in the pore space requires specific attention and needs to be examined more closely. A detailed description of the model concept and solution methods as well as specific application examples for water-NAPL-air systems in the unsaturated zone are given by *Class et al.* (2002) [35] and *Class & Helmig* (2002) [34].

4.1.1 Boiling of Two Low-Miscible Liquids

The thermodynamic behavior of multicomponent mixtures depends strongly on the miscibility of the involved substances. Phase diagrams of multicomponent mixtures can therefore reveal very different characteristics. In the following, we restrict this discussion to a mixture of two liquid components. One can roughly distinguish three cases of different miscibility:

- The two components are fully miscible within a single liquid phase. In case that this mixture is ideal, the vapor pressure depends on the composition according to *Raoults* law, see Sec. 3.2.1.2.

- The two components are immiscible. The total vapor pressure is then equal to the sum of the vapor pressures of the components (compare with Fig. 4.2.
- The two components are miscible up to a certain degree. Dependent on the composition, only a single phase or two separate phases can form.

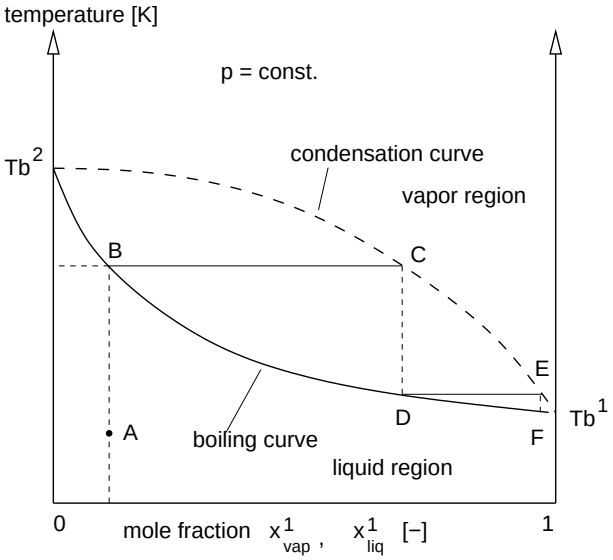

Figure 4.1: Boiling diagram of two fully miscible components.

Let us first consider the boiling behaviour of two fully miscible components within a single liquid phase. A corresponding boiling diagram is depicted in Fig. 4.1. There, component 1 is more volatile than component 2 which can be seen from the lower boiling temperature. Therefore, the contribution of component 1 to the total vapor pressure is larger than that of component two. From the boiling diagram of Fig. 4.1 one can follow up the temperature-dependent composition of the liquid and the gas phase in equilibrium. Below the boiling curve, only liquid exists, correspondingly above the condensation curve only vapor. Inbetween, the composition of both phases can be determined from the curves. In chemical engineering, such boiling diagrams are used, for example, to assess the efficiency of destillation processes. Exemplary, we illustrated a destillation procedure in the diagram following points A to E. Starting at point A, we have a certain composition of the binary liquid mixture. After heating up to point B, the mixture starts boiling. While the vapor phase is enriched with the more volatile component 1 (point C), the composition of the liquid phase is shifted towards smaller fractions of component 1. This comes along with an increase of the boiling temperature following the boiling curve to the left towards T_b^2. The vapor mixture at point C can be cooled down in the destillation set-up yielding an enriched fraction of component 1 in the condensate. This process can be repeated with the condensate until the desired composition is reached.

After this excursion to chemical engineering, we now concentrate on non-miscible liquids which are more relevant to our water-NAPL problem. If the two components are not miscible, the liquid mixture boils when the sum of both vapor pressures reaches the ambient pressure (*Dalton's* law). Thus, the basic difference to the fully miscible mixture is that the boiling temperature is

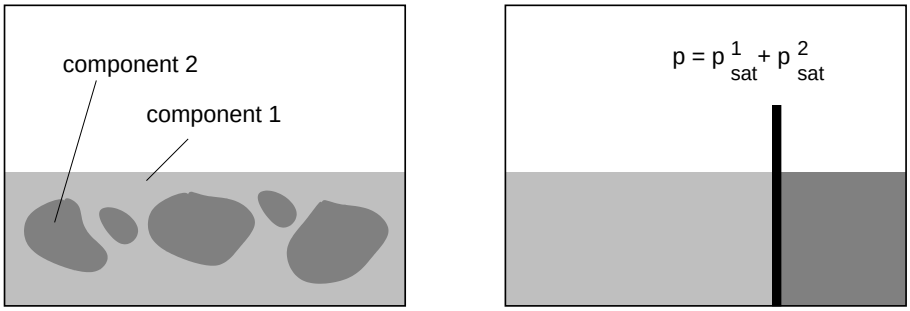

Figure 4.2: Conceptual model of two immiscible boiling liquids.

independent of the mixture composition. Correspondingly, the vapor produced during the boiling has a constant composition. Another characteristic feature is the reduced boiling temperature of two simultaneously boiling immiscible liquids compared with both boiling temperatures of the pure components (see Fig. 4.3).

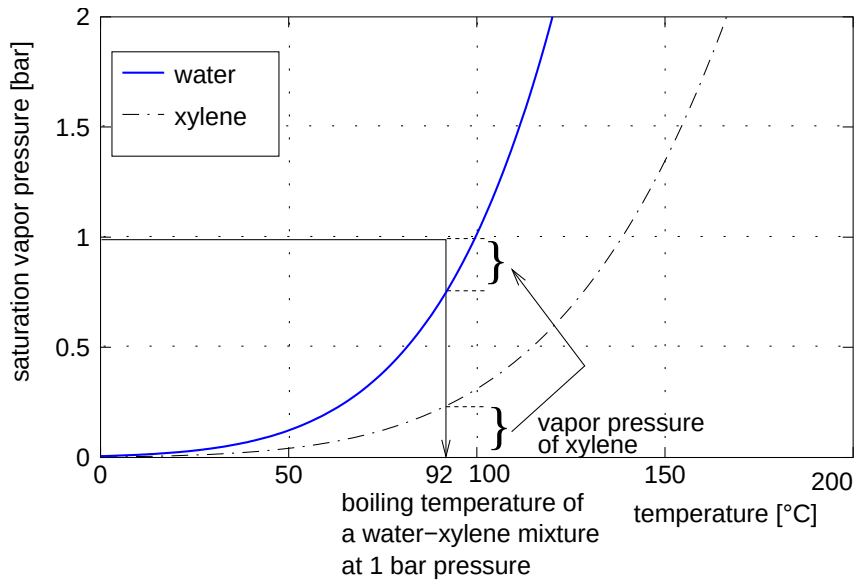

Figure 4.3: Vapor pressure curves of water and xylene illustrating the contributions of both components to the total vapor pressure during the boiling process at 1 bar ambient pressure.

Most NAPLs fulfill in combination with water the assumption of non-miscibility. Their mutual miscibility is very limited with a large mixing gap in the binary phase diagrams. A mixing gap occurs when an amount of a component B is added to another amount of a component A so that two separate liquid phases form. In such a case, the mutual solubility is exceeded. The mixing gaps of systems with limited mutual solubility is in general a function of temperature. They can be confined by upper or lower critical temperatures.

Figure 4.4 shows a boiling diagram of two components with limited mutual solubility in their liquid phases. The depicted system has no critical demixing temperature since the mixture starts

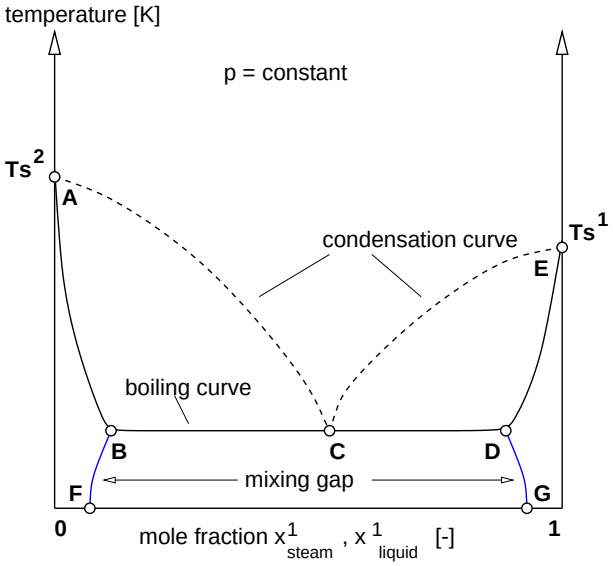

Figure 4.4: Boiling diagram of two liquids with limited mutual miscibility.

boiling before a status of liquid demixing can be reached. Let us follow the line given by points A to E. Starting at A, which represents the boiling temperature of the pure component 2 at a constant pressure p, the boiling temperature decreases with increasing fraction of component 1. Up to point B, this behavior corresponds to that of a fully miscible mixture as shown in Fig. 4.1. At point B, the solubility of component 1 in component 2 is exceeded and a second liquid phase appears. Thus, this point marks the lower boundary of the mixing gap. Point C is called the azeotrope. It marks the constant composition of the binary vapor mixture during the boiling of the liquid mixture for any liquid composition within the mixing gap. The vapor composition at the azeotrope is determined by the vapor pressure ratio as explained by Fig. 4.3. Points D and E correspond to B and A, however with component 1 as the solvent and component 2 as the therein fully dissolved component. The lines F-B and G-D shows that the critical composition for the appearance of a second liquid phase is temperature-dependent.

The solubility of many NAPLs in water is so low that the regions left of A-B-F and right of E-D-G can be neglected in the conceptual model. Their boiling behavior together with water can then by described with *Dalton's* law and the respective vapor pressure curves. Table 4.1 lists some selected water-NAPL mixtures with their boiling temperatures and vapor pressure ratios at atmospheric pressure.

4.1.2 Processes and Fluid Properties

The interaction between the involved phases and components in a non-isothermal water-NAPL-gas system with the components water w, NAPL (contaminant) c, and air a summarizes Fig. 4.5. It shows schematically the possibly occuring mass and energy transfer processes including also adsorption of dissolved organic contaminants to the solid porous matrix. Particularly evaporation and condensation are strongly coupled with the exchange of thermal energy. Further processes are advection/convection of phases as well as diffusion of the components within the gas phase.

Table 4.1: System parameters during the boiling of water-NAPL mixtures at $p = 1.013$ bar after *Betz* (1997) [17].

mixture	vapor pressures [bar]	boiling temperature [° C]	mole fraction in the vapor [-]
water	0.359	73.4	0.355
TCE	0.654		0.645
water	0.772	92.6	0.762
m-xylene	0.241		0.238
water	0.894	96.6	0.884
mesitylene	0.118		0.116

Typically, diffusion in water-NAPL-air systems in the unsaturated zone is only significant in the gas phase which is in the focus of Sec. 4.1.3 below.

The calculation of the fluid properties of NAPLs required for the balance equations is discussed in the following.

Density and Viscosity:
There exists a large number of approaches to estimate the densities and viscosities of organic liquids, many of them discussed by *Reid et al.* (1987) [146]. Some of those approaches and others were already given in Sec. 3.1.3.1 for the density and in Sec. 3.1.3.2 for the viscosity of the NAPLs. The individually required parameters and constants for the constitutive equations have to be taken from the literature anyway.

Enthalpy:
There exists a variety of approximations for estimating the enthalpies of organic liquids and vapors. Many of them, also those described below, are given in *Reid et al.* (1987) [146]. As Eq. (3.83) suggests, the specific enthalpy of liquid NAPLs can be obtained from an integration over the specific heat capacity at constant pressure:

$$h_n = \int_{T_{\text{ref}}}^{T} c_{p,\text{napl}}\, dT \tag{4.1}$$

Here, T_{ref} represents the reference temperature with $h_n(T_{\text{ref}}) = 0$, typically $T_{\text{ref}} = 0^{\circ}$C. The evaluation of the integral can be carried out numerically, for example, by a 2-point *Gauss* integration. The determination of $c_{p,n}$ requires in general further approximative methods. One is the *Missenard* group contribution method. This method simply assumes that the different groups in the structure of the molecules (–CH_3, C_6H_5–, –H, etc.) contribute with a certain value to the molar heat capacity. It is stated that this holds with satisfying accuracy for molecules without double bonds.
From Fig. 3.19 it becomes visible that the specific enthalpy curves have three distinct segments, (i) the liquid segment, (ii) the latent heat of vaporization, and (iii) the vapor segment. Thus, for the

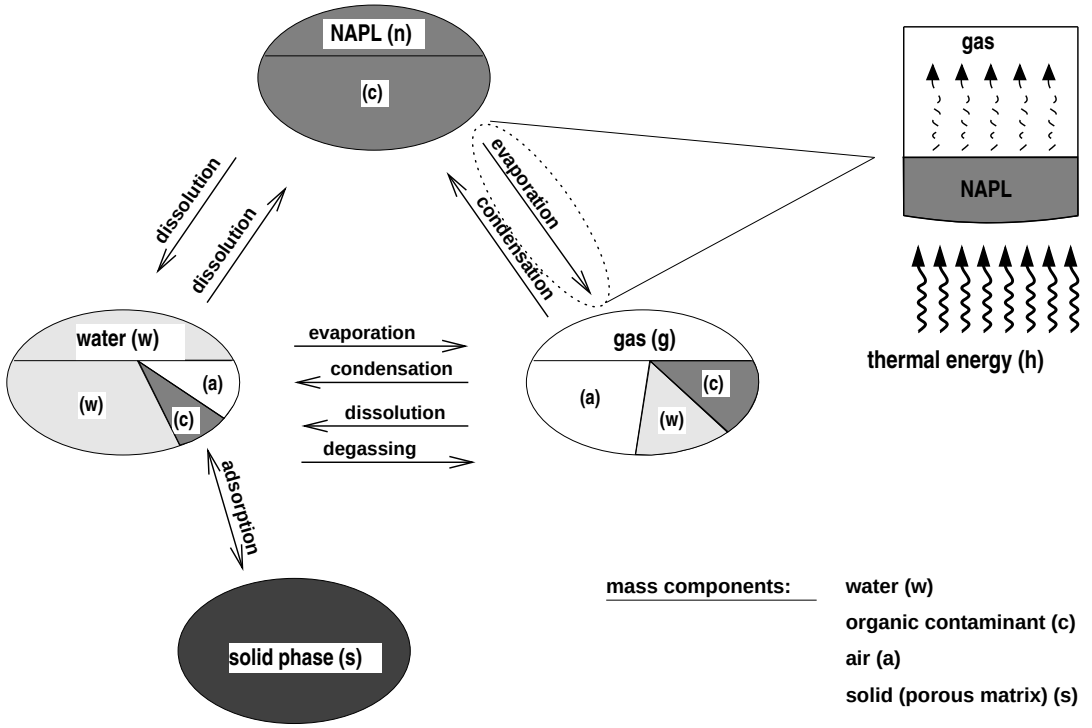

Figure 4.5: Mass and energy transfer between the phases in a water-NAPL-gas system [35].

approximation of the specific enthalpy of the organic vapors it is appropriate to consider these segments by

$$h_g^c = h_n + \Delta h_v^c + \int_{T_{\text{ref}}}^{T} c_{p,\text{vapor}}\, dT \tag{4.2}$$

with h_n, for example according to Eq. (4.1). Δh_v^c is the latent heat of vaporization which is estimated by the *Chen* method for the normal boiling point of NAPLs by

$$\Delta h_{v,b}^c = \frac{R\, T_{\text{crit}}\, T_{b,r}}{M^c} \left(\frac{3.978\, T_{b,r} - 3.958 + 1.555\, ln\, p_{\text{crit}}}{1.07 - T_{b,r}} \right) \tag{4.3}$$

where $T_{b,r}$ is the reduced normal boiling temperature ($T_{b,r} = T_b / T_{\text{crit}}$). Afterwards, the temperature-dependence of Δh_v^c can be taken into account by the *Watson* method, given by

$$\Delta h_v^c = \Delta h_{v,b}^c \left(\frac{1 - T_r}{1 - T_{b,r}} \right)^{0.375} \tag{4.4}$$

where $T_r = T / T_{crit}$ is the reduced temperature.

$c_{p,\text{vapor}}$ can be determined, for example, following the *Joback* method which is also a group contribution method.

4.1.3 Diffusion in a Three-Component System

The principal mechanisms of diffusion and dispersion are already discussed in Sec. 3.2.1.1. Practically, an effective molecular diffusion coefficient as given by Eq. 3.68 is used to compute diffusive fluxes through the porous medium. The difficulty in a three-component system is the determination of the diffusion coefficients from the mostly exclusively available binary diffusion coefficients. *Falta et al.* (1992) [59] suggest a calculation procedure which is in the following applied to determine the diffusivities for water vapor and the vapor of the contaminant from the binary diffusivities D_g^{aw}, D_g^{cw}, and D_g^{ac} in the gas phase.

$$D_g^w = \frac{1 - x_g^w}{\frac{x_g^a}{D_g^{aw}} + \frac{x_g^c}{D_g^{cw}}} \tag{4.5}$$

$$D_g^c = \frac{1 - x_g^c}{\frac{x_g^w}{D_g^{cw}} + \frac{x_g^a}{D_g^{ac}}} . \tag{4.6}$$

The sum of all molar fluxes due to binary diffusion (J_α^κ) is zero.

$$J_\alpha^a + J_\alpha^w + J_\alpha^c = 0 , \tag{4.7}$$

Thus, the diffusivity for the component air is not required since the diffusive air flux can be calculated via Eq. (4.7).
The diffusive mole flux of the components κ in a fluid phase is then given by

$$J_\alpha^\kappa = -\rho_{\mathrm{mol},\alpha} D_{\mathrm{pm}}^\kappa \nabla x_\alpha^\kappa , \tag{4.8}$$

where the computation of D_{pm}^κ follows Eq. (3.68).
Typically, molecular diffusion coefficients are several orders of magnitude larger in the gas phase ($\approx 10^{-5}$ m^2/s) than in the water phase ($\approx 10^{-9}$ m^2/s). For that reason, the diffusion in the water phase appears to be negligible for water-NAPL-air systems in the unsaturated zone and only diffusion in the gas phase is relevant.

4.1.4 Adsorption of Dissolved Contaminants to the Solid Matrix

Many liquid or gaseous components tend to accumulate at certain solid surfaces. This phenomenon is denoted as adsorption. Many industrial processes use adsorption techniques as cutting-off processes, for example, to separate organic dissolver vapors out of the air or to clean sewage waters. One can distinguish between polar (hydrophilic) and non-polar (hydrophobic) adsorbents. Hydrophilic adsorbents are suited to separate polar components, correspondingly hydrophobic adsorbents can be used for non-polar adsorptives (substances to be adsorbed). An important hydrophobic adsorbent is activated carbon. It has a very high inner surface and thus provides a high number of free adsorption positions. The adsorption of dissolved contaminants to the solid matrix depends on the amount of carbon in the soil since carbon provides the relevant surface to adsorb the non-polar molecules of the organic contaminants.

The adsorption processes depend on the state variables pressure and temperature and it is in general not possible to formulate an all-embracing equation of state. Adsorption equilibria are therefore preferraby described by isotherms. The *Freundlich* and *Langmuir* isotherms are the most common ones since they are relatively simple to understand.

Assuming that the surface of the adsorbent has a limited amount of free positions for the adsorptive to cover, the coverage θ represents the ratio of occupied to totally available positions. The amount of adsorbate (the adsorbed substance) depends on the totally available positions and on the concentration of the adsorptive in the circumfluent liquid (or on the partial pressure of the adsorptive in the circumfluent gas phase). At low concentration (or partial pressures), the adsorption isotherm of *Freundlich* can express this by

$$\theta = \alpha p^{\beta} , \tag{4.9}$$

where α and β are specific constants of the substance. β takes values between 0 and 1. p stands in this context for the concentration or the partial pressure. At higher concentrations of the adsorptives (or higher partial pressures), a saturation phenomenon can be observed since the available positions at the surface of the adsorbent are limited. This effect cannot be described by the *Freundlich* isotherm. The *Langmuir* isotherm accounts for that by

$$\theta = \frac{K p}{1 + K p} \tag{4.10}$$

with K representing here the adsorption equilibrium constant.
Equilibrium adsorption can be considered in the balance equations by simply adding the amount of adsorbate to the storage term in the balance equation of the respective component.

4.2 Steam Injection in the Saturated Zone

There exist some significant differences concerning the modelling of the steam front and the related processes between steam-injection in the unsaturated zone and an injection in the saturated zone. This is why here we dedicate a separate section to steam-injection in the saturated zone. The first special feature occuring is a non-physical oscillative behavior of the pressure during the steam-injection in the model domain. Thereby, one can observe an occasional appearance of spurious water back-fluxes into the steam zone followed by a collapse of the steam zone. This will be in the focus of Sec. 4.2.1. Another particularity is the practically complete disappearance of the air component in the steam zone which leads to severe numerical stability problems and requires a special treatment of the air-mass balance equation (Sec. 4.2.2). For further details on modelling steam-injection into saturated porous media we refer to the work of *Ochs* (2007) [131, 132, 130].

The basic difference between an injection in the saturated and in the unsaturated zone concerning the physical behavior due to the influence of gravity was already discussed in Sec. 2.3 and will not be further detailed here.

4.2.1 Pressure Fluctuations and Spurious Water Fluxes

A steam-injection into a water-saturated porous medium is in general correlated with a pressure increase according to the permeability (resistance) of the porous medium. This pressure increase is expected to occur gradually and smooth. However, numerical simulations of such a steam-injection into saturated porous media reveal a characteristic occurence of pressure fluctuations. Figure 4.6 shows the occuring pressure peaks in a quasi 1-dimensional domain with different mesh resolutions. In both cases, steam is injected from the left-hand boundary and the temporal development of the water pressure, the water saturation and the temperature at a discrete point near the left boundary are plotted.

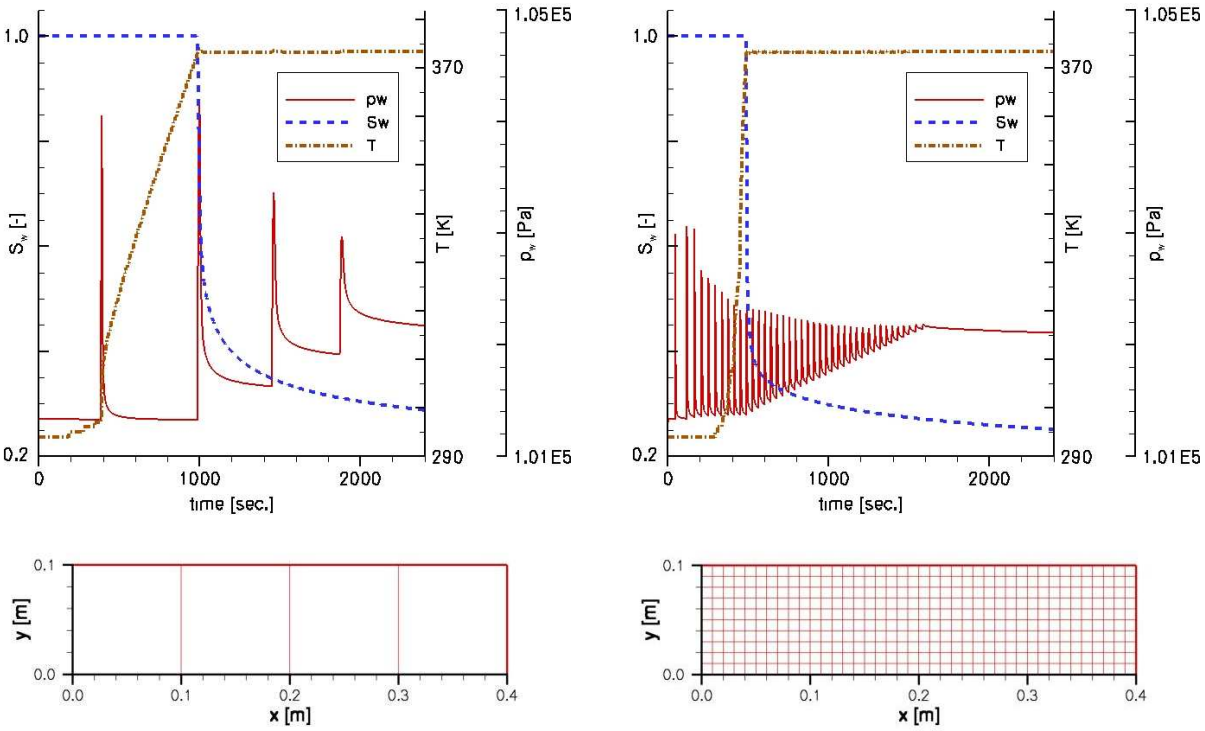

Figure 4.6: Pressure fluctuations for different mesh resolutions. The figures show the curves of p_w, S_w, and T at a discrete point near the left boundary. Figures taken from *Ochs* (2007) [130].

Obviously, both frequency and amplitude of the peaks depend on the mesh resolution. While the frequency increases for finer meshes, the amplitudes become smaller. An explanation for the arising pressure peaks is the transfer from the continuous physical system to the numerically discretized problem. Each time a control volume belonging to a certain discrete node is heated up to steam temperature, a pressure peak can be observed. During the heating of a control volume that is originally outside the steam zone, all steam entering the control volume during a certain time-step condenses until in another time-step the required enthalpy for the entire hot water-filled control volume to evaporate is reached. This evaporation occurs for the whole mass of water belonging to the control volume since each control volume is identified with unique node values of pressure, temperature, and saturation. Thus, the sudden volume expansion caused by the evaporation increases the pressure and produces the observed peaks. In Fig. 4.6 (left),

we observe that the second pressure peak coincides with the decrease of the water saturation and the reaching of steam temperature at the observation point. Thus, we conclude that this observation point belongs to the second control volume from the left-hand boundary.

There are also other parameters influencing the amplitudes of the peaks, for example, the q_s/K-ratio (steam rate versus permeability). The higher q_s/K the larger the amplitudes of the peaks.

Ochs (2007) [131] describes that the pressure fluctuations cause severe problems concerning the convergence of the non-linear solution process. Since mesh refinement causes apparently a dampening of this problem, the usage of h-adaptive refinement techniques to resolve the steam front can be promising. In order to avoid the pressure peaks entirely, it would be necessary to loosen the underlying model assumptions, for example, concerning the local thermodynamic equilibrium. Rate models that take into account the gradual process of phase transition between co-existing phases could be appropriate, however, they increase the model complexity severely and are thus expected to be not applicable for large problems.

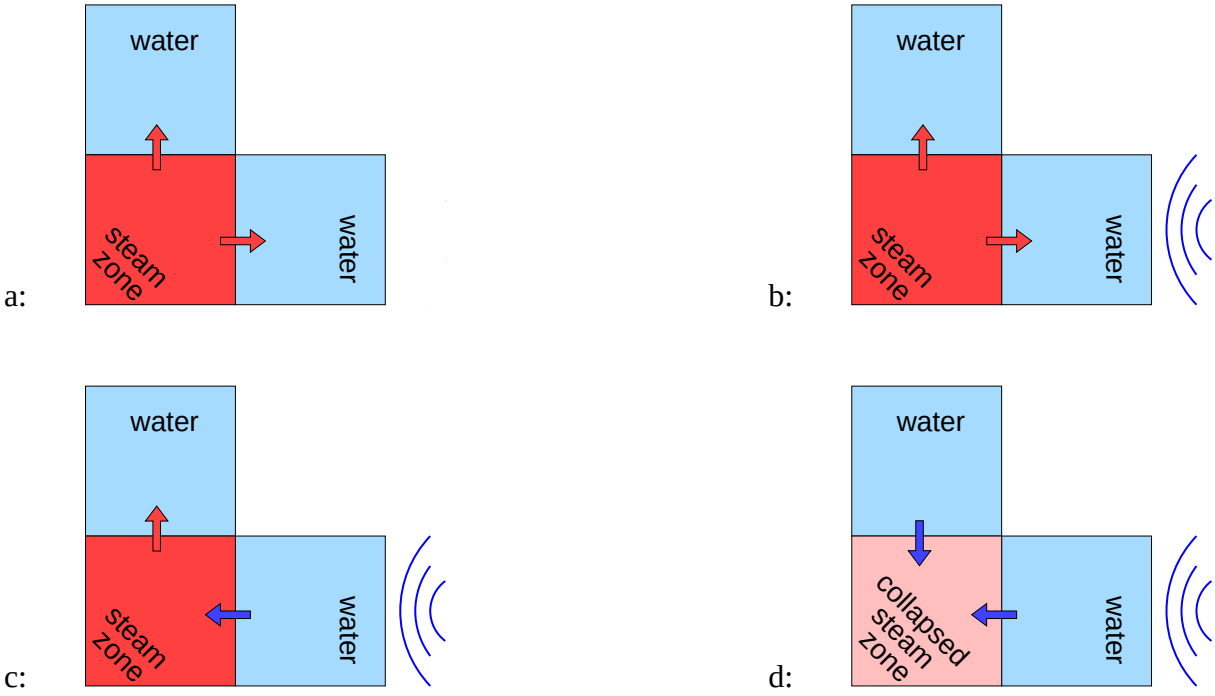

Figure 4.7: Spurious water back-flux phenomena during a steam-injection in the saturated zone: a) the normal (physically correct) situation near the steam front b) is suddenly changed after a pressure peak in the system, c) leads locally to a reversal of the flow direction d) causing steam to condense and eventually the steam front to collapse.

Figure 4.7 illustrates the mechanism of spurious water back-fluxes into the steam zone resulting from the non-physical pressure peaks. The physical process is monotonic with a continuous growth of the steam zone from the lower left corner towards the interior of the model domain. For the reasons explained above pressure peaks evolve at different locations inside domain (always there, where the steam front presently propagates). This can cause a local reversal of the

pressure gradient and thus a liquid water back-flux opposed to the steam front propagation. This water back-flux may even cause a collapse of the steam zone.

When a water back-flux into a control volume in the steam zone occurs it depends on the supply-rate of steam whether or not the required enthalpy to evaporate the back-flowing liquid water can be provided. If not, then a net amount of the inflowing steam condenses resulting in a locally decreasing pressure [131, 74]. This local pressure drop then drives further back-flowing water into the control volume so that the process becomes self-enhancing until the steam zone collapses and the simulation eventually fails.

A strategy to reduce spurious water fluxes as suggested by *Ochs* detects the local back-fluxes and reduces or completely blocks the back-fluxes. Based on an analysis of the processes as already suggested by *Gudbjerg et al.* (2004) [74], the criterion to fully block the spurious back-flux is the temperature difference between the steam inside the concerned control volume and the back-flowing water. In case of more than 10 K difference the back-flux is blocked, otherwise it is linearly reduced to zero between 0 K and 10 K.

4.2.2 A Two-Phase Single-Component Modeling Approach

When pure steam without air is injected in the saturated zone, the mole fraction of the air in the gas phase (and obviously also in the water phase) tends to zero. Air is displaced by steam and vanishes. This can cause severe numerical problems as also described by other authors [136, 64, 131]. Later Sec. 5.3, it will be stated that the set of primary variables has to be chosen in a way that they are all independent of each other, meaning that if one of the primary variables is changed the others will not be necessarily affected. For the moment, we are content with investigating the influence of the chosen primary variables on this specific problem in order to motivate the application of a two-phase single-component model.

For a non-isothermal two-phase two-component system of water and air as required for modelling the processes in the unsaturated zone, the primary variables are typically the gas pressure p_g, the water saturation S_w, and the temperature T (see Fig. 4.8). All secondary variables have to be computed as functions of the primary variables according to an algorithmic procedure. Let us exemplarily develop this algorithm for the computation of the air mole fraction in the gas phase:

$$
\begin{aligned}
\text{saturation constraint} \quad & S_g = 1 - S_w; \\
\text{capillary pressure constraint} \quad & p_w = p_g - p_c(S_w); \\
\text{saturation vapor pressure} \quad & p_g^w = p_{\text{sat}}^w(T); \\
\textit{Dalton's} \text{ law} \quad & p_g = \sum_\kappa p_g^\kappa; \\
\rightarrow \text{ ideal gas assumption} \quad & p_g^a = p_g - p_g^w; \\
& x_g^a = p_g^a / p_g;
\end{aligned}
$$

From this computation procedure it becomes obvious that, if the air mole fraction tends to zero,

this means that p_g tends towards p_g^w which is a function of temperature according to the saturation vapor pressure equilibrium. Thus, a change in p_g requires a change in T and vice versa. Both variables are not independent and are therefore a bad choice as primary variables to describe the system with no air existing.

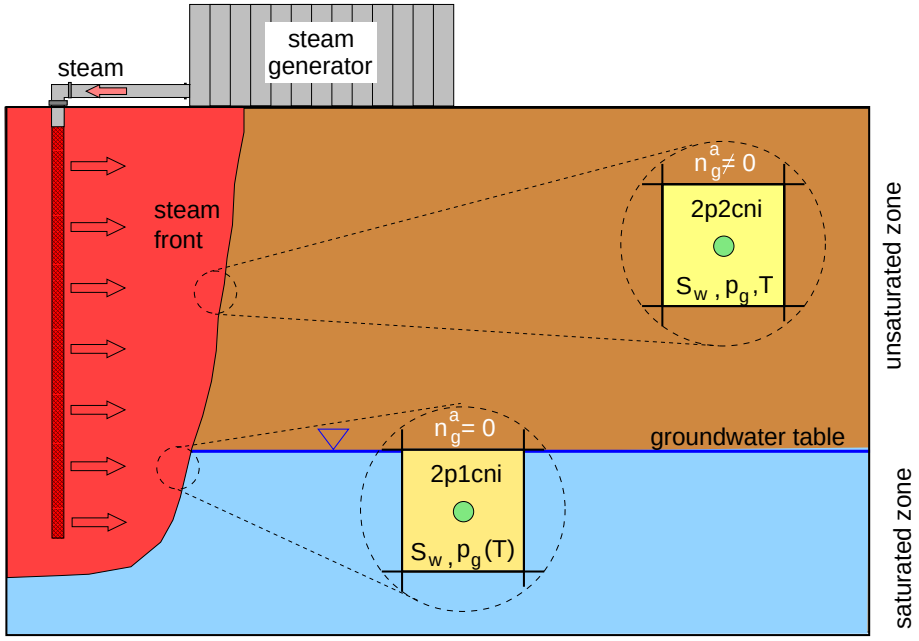

Figure 4.8: Different model concepts concerning the consideration of the air-component for steam-injection in the unsaturated zone and in the saturated zone.

To overcome this, steam-injection in the saturated zone can be modeled with a two-phase single-component concept by considering only water in its liquid and gaseous state of aggregation and by neglecting air completely (Fig. 4.8). This assumption is justified in the saturated zone since the amounts of dissolved or entrapped air have generally very low influence on the ongoing processes during an injection. Such a model can take advantage of the relation between the temperature and the steam pressure and use one of the two as a primary variable (see Tab. 5.2 in Sec. 5.3.4).

4.3 CO_2 Storage in Geological Formations

The injection of CO_2 into deep geological formations with the aim of storing this greenhouse gas for long time-periods causes complex multiphase multicomponent processes in the subsurface including also non-isothermal effects. Particularly the strongly varying fluid properties around the critical point of CO_2 require specific attention in the model concept. A detailed presentation of the recently developed model concept for simulating CO_2 injection and storage is given by *Bielinski* (2006) [18] and *Class et al.* (2006) [31]. Most of the figures in Sec. 4.3 are taken from the phD-thesis of *Bielinski*.

4.3.1 Phase Diagrams: CO_2 in Sub- and Supercritical State of Aggregation

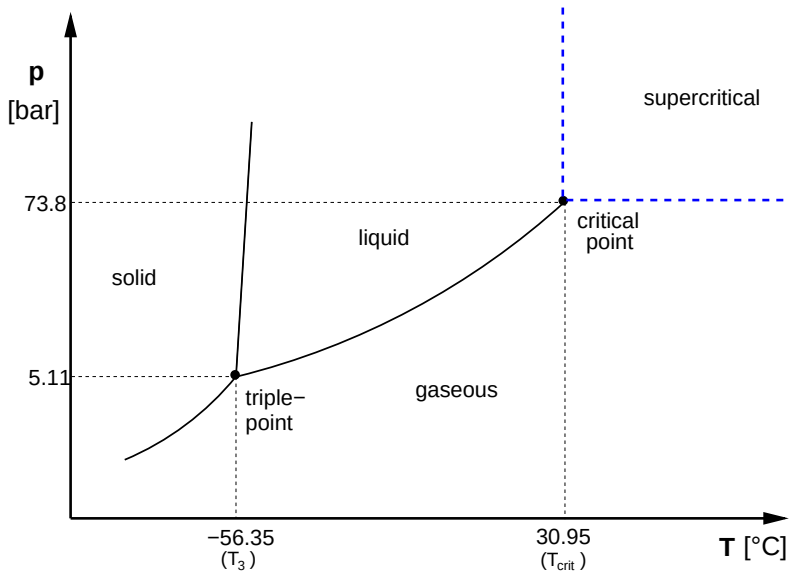

Figure 4.9: Phase diagram of CO_2.

Figure 4.9 shows the phase diagram of CO_2 with the critical point at 73.8 bar and 30.95 C. The supercritical state of aggregation requires pressure and temperature to be above the respective critical values. Then, a lowering of pressure or temperature can cause a transition from the supercritical to the gaseous or liquid state of aggregation without crossing the vapor pressure curve which represents a phase-coexistence line. The closer the pressure/temperature conditions are to the critical point, the stronger are the variations in the fluids properties like density, viscosity, and specific enthalpy.

Typically, the multiphase problem occuring after an injection of CO_2 into a geological formations is characterized by two fluid phases which may co-exist but not necessarily have to. One of them can be described as water-rich phase with water as the main component and a certain fraction of dissolved CO_2 (and potentially other components, for example, salt). The other phase is CO_2-rich which also may contain water in it.

Figure 4.10 depicts how the phase(s) exist at 25 C. The axis of the diagram are the total water mole fraction in the mixture and the system pressure. Note that the axis of the water mole fraction is interrupted and shows only the edges with values close to zero and close to one. There, single phases can occur with the whole amount of the other component dissolved. In the large region inbetween, both water-rich and CO_2-rich phase co-exist with their states of aggregation depending on the pressure conditions. There is obviously also a strong influence of temperature on the behavior of such a CO_2-water system. However, this cannot be seen from Fig. 4.10. It should further be noted that under certain p, T, x-conditions a small region with three fluid phases can occur, namely a gaseous CO_2-rich phase, a liquid CO_2-rich phase and a water-rich liquid phase. This is also neglected in Fig. 4.10.

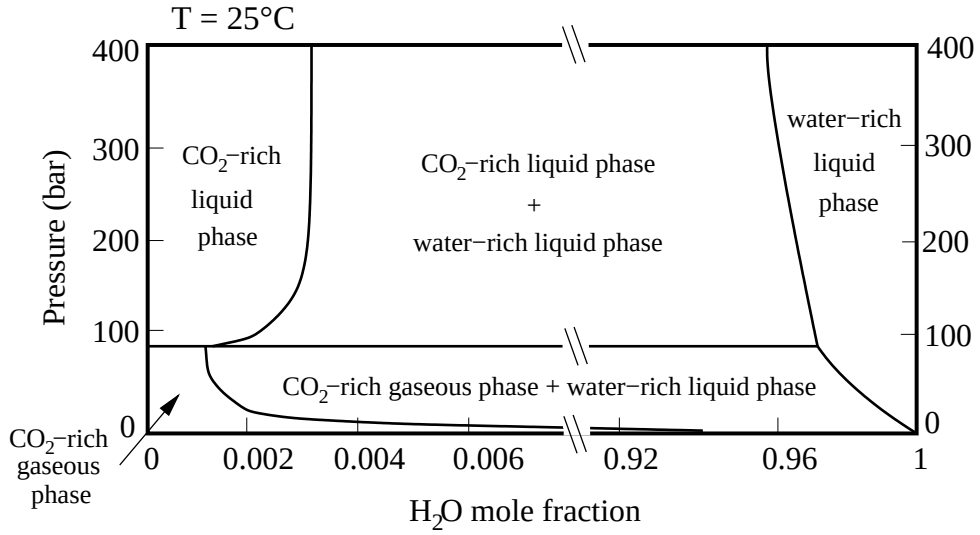

Figure 4.10: Phase diagram of a CO_2-water mixture at 25 C after *Spycher et al.* (2003) [159].

4.3.2 Processes, Fluid Properties and Characteristic System Parameters

A schematic illustration of the involved phases and components in analogy to Fig. 4.5 would comprise the two fluid phases as explained above including the two components water and CO_2 and, if necessary, also the component salt. The characteristic processes that dominate a typical CO_2 injection scenario and the storage mechanisms are discussed in the following:

- **Advective flow due to pressure gradients and buoyancy:**
  CO_2 is injected into a formation with a certain overpressure which is limited by the maximum pressure increase that the cap-rock can bear without fracturing. The induced pressure gradient causes a spreading of the CO_2 and - if CO_2 appears as a separate phase (see Fig. 4.10) - a displacement of the formation water (brine). This phase movement and displacement is commonly described by *Darcy's law* in the form of Eq. (3.40). The same holds for advective flow due to buoyancy. Since the CO_2 phase has a lower density than the surrounding brine, it tends to flow upwards and spread laterally at the top of the storage formation right below the cap-rock. Another gravitationally induced advection is the downward migration of water or brine containing high fractions of dissolved CO_2. As explained below, the density of water increases with the amount of dissolved CO_2 so that these waters tend to sink down to the bottom of the formations which is considered a very positive factor for a sustainable storage.

- **Thermal convection:**
  All advective flow goes along with the transport of enthalpy. Thus, thermal energy fluxes can be taken into account by multiplying the advective phase fluxes with the specific enthalpy of the phases, see Eq. (3.98).

- **Heat conduction:**
  Another heat transport process that is also included in Eq. (3.98) is heat conduction due to temperature gradients. For the calculation of the averaged heat conductivity, the approaches given by Eqs. (3.88) and (3.89) can be applied. Heat conduction may be an

important process at fault zones, fractures, or wells where a rapid local upward movement causes a cooling due to the expansion of the gas [53]. *Pruess* (2004) [143] describes that depending on the pressure and temperature conditions this cooling of the formation may allow local three-phase conditions to arise with an aquous, a liquid CO_2, and a gaseous CO_2 phase which mutually impede their movement. Heat conduction counteracts this cooling by transporting thermal energy from the ambient rock formation.

- **Mutual dissolution:**
  Water and CO_2 are partly miscible with each other (see Fig. 4.10) with mass fractions - particularly that one of CO_2 in water - significantly higher than the contaminant fractions in water dealed with in Sec. 4.1. The dissolution of CO_2 in water changes the pH-value which may also provoke chemical reactions with the formation minerals.

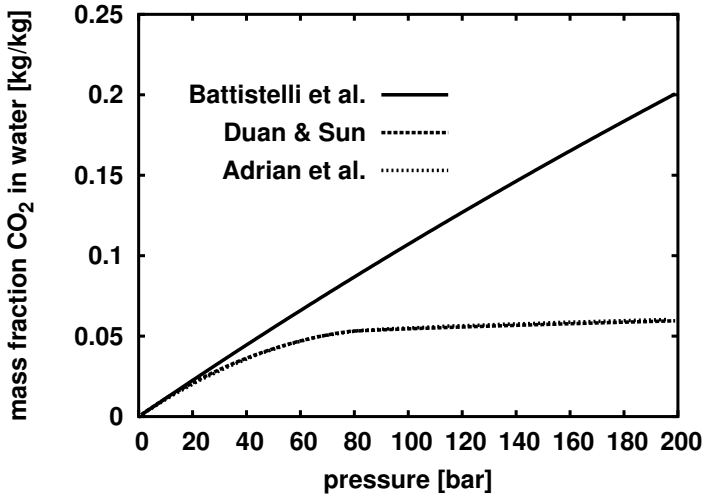

Figure 4.11: Comparison of different approaches (*Battistelli et al.* (1997) [13], *Duan & Sun* (2003) [52], and *Adrian et al.* (1998) [4] (EOS)) for the solubility of CO_2 in pure water at 34 C as a function of pressure.

The literature provides a number of approaches and equations of state (EOS) for the computation of dissolved fractions of CO_2 and water in the respective other phase. Some selected approaches are plotted in Figs. 4.11 and 4.12. Looking closer at Fig. 4.12, we can observe two basic things. First, there is a significant discrepancy between the two plotted approaches of *Duan & Sun* (2003) [52] and *Adrian et al.* (1998) [4] at high pressures above the critical point. There, the EOS proposed by *Adrian et al.* catches the real behavior in more detail. The second basic observation concerns the order of magnitude of the water mass fraction in CO_2 compared with the CO_2 mass fractions dissolved in water as shown in Fig. 4.11. The latter is significantly higher and for the sake of simplicitly, the dissolution (or evaporation) of water into the CO_2 phase is neglected by many models [18]. The approaches suggested by *Battistelli et al.* (1997) [13], *Duan & Sun* (2003) [52], and *Adrian et al.* (1998) [4] for the dissolution of CO_2 in water are shortly discussed in the following:

  - The adapted *Henry* approach suggested by *Battistelli et al.* (1997) [13].

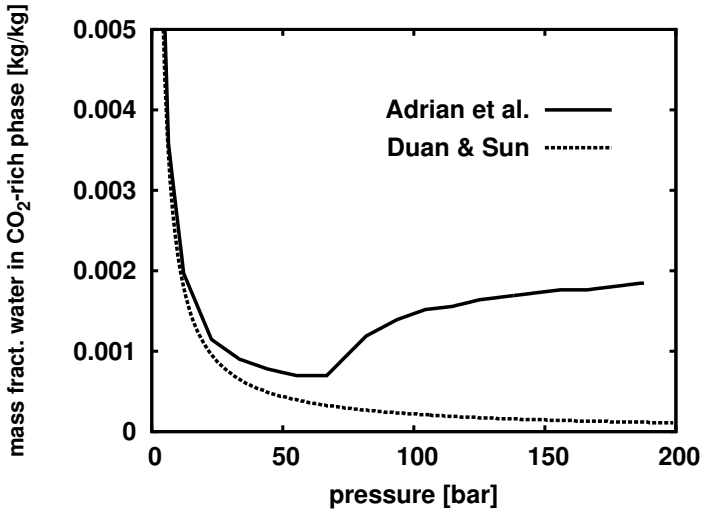

Figure 4.12: Comparison of different approaches for the solubility of water in CO_2 depending on pressure at 34 C (*Duan & Sun* (2003) [52] and *Adrian et al.* (1998) [4] (EOS)).

Henry's law holds for the dissolution of a gaseous component into a liquid phase (see Sec. 3.2.1.2) with its applicability limited to low solute fractions. That is obviously the reason why this approach overestimates the dissolved fraction at high pressures.

– The model of *Duan & Sun* (2003) [52].
Their equations are based on a specific particle interaction theory for the water and an equation of state for the CO_2 phase where they include salinity effects on the dissolution behavior. A large data set is used for the parameterization. The model is validated to these data at temperatures between 273 and 533 K, pressures of up to 2000 bar, and salinities of a molality of up to 4.3 mol/kg - corresponding to a salt mass fraction of approximately S = 0.2 kg/kg.

– The EOS proposed by *Adrian et al.* (1998) [4].
A modified Peng-Robinson equation of state after *Melhem et al.* (1989) [116] with the mixing rule of *Huron & Vidal* (1979) [91] is used. With this EOS one can describe phase equilibria and therefore the dissolution of CO_2 in pure water. This is considered to be a rather exact description of the solubility since the parameters required for the EOS are directly fitted to experimental data. Therefore, this EOS is considered here as the reference model for the solubilities.

As can be seen in Fig. 4.11, the curves obtained from the *Duan & Sun* model and the EOS of *Adrian et al.* lie more or less on top of each other. The *Duan & Sun* model is used in the following since it is able to include also the influence of salinity on the dissolution of CO_2 in the water phase.

Figures 4.13 and 4.14 show the mass fraction of dissolved CO_2 in the water phase (brine) at different temperatures, pressures, and salinities. The amount of dissolved CO_2 increases with increasing pressure and decreasing temperature and salinity. Note the strong influence of salinity on CO_2 dissolution. This effect has to be taken into account explicitly

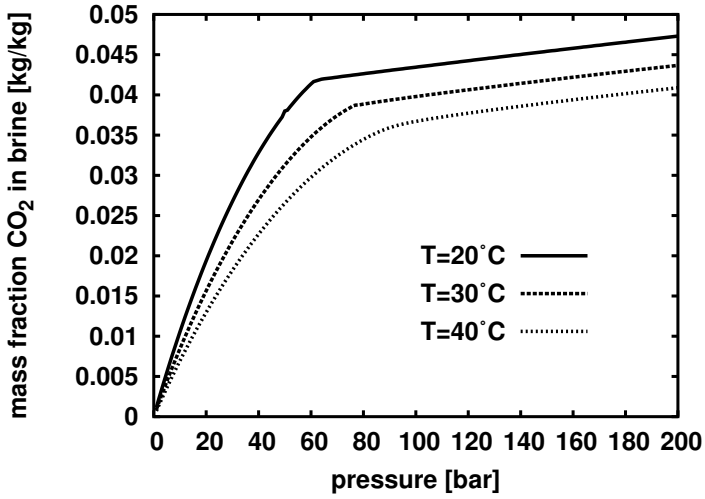

Figure 4.13: CO_2 solubility in brine as a function of pressure at different temperatures and constant salinity $S = 0.1$ kg/kg (*Duan & Sun* (2003) [52]).

as the formation fluids in deep aquifers are often highly saline.

Table 4.2 shows characteristic values of dissolved CO_2 in pure water and brine. These values are maximum concentrations at given pressure, temperature, and salinity provided that CO_2 availability is not limited.

- **Diffusion:**
  As the components mutually dissolve in the involved phases, the diffusive transport within the phases is an important process, particularly as an enhancing factor for the mechanism of solubility storage. Coupled with the density effect of CO_2 dissolution in the water which causes an advective downward sinking of such water, the diffusion further enhances the dissolution by transporting the water with already high CO_2 concentration away from the CO_2 plume. Diffusion (and also dispersion) can be considered in the model as explained above in Sec. 3.2.1.1.

- **Entry pressure - the cap-rock as a capillary barrier:**
  As already mentioned above, the CO_2 spreads below the cap-rock and accumulates there. The cap-rock prevents from a further rise into shallower regions due to its typically very low permeability but also by functioning as a capillary barrier for the non-wetting CO_2. The non-wetting fluid has to overcome the entry pressure (see Sec. 3.1.4.1) of the cap-rock before it can penetrate and move further. To account for this effect in the model, it is either necessary to resolve the mesh very fine at the cap-rock or to use an interface condition as, for example, suggested by *Niessner et al.* (2005) [127].

- **Adsorption:**
  Generally, it depends on the composition of the rock whether or not adsorption plays a role. In particular organic matter is required for physical sorption as explained before shortly in Sec. 4.1.4. Another phenomenon that is sometimes comprised within the term adsorption

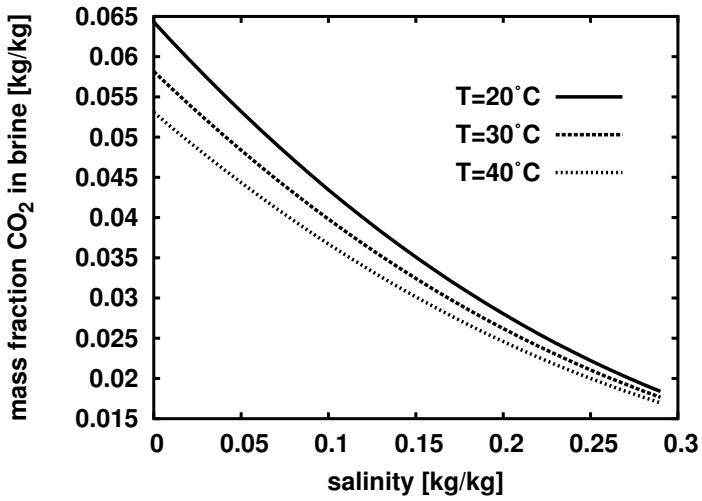

Figure 4.14: CO_2 solubility in brine as a function of salinity at different temperatures and constant pressure $p = 100$ bar (*Duan & Sun* (2003) [52]).

is chemical sorption due to mineral reactions, precipitation, and dissolution.
Concerning CO_2 injection and storage, desorption of methane and competitive adsorption of carbon dioxide is a relevant process for the enhanced coal bed methane (ECBM). Taking competitive binary sorption of two components i, j into account in the model requires an extension, for example, of the *Langmuir* approach:

$$\theta_i = \theta_{\max,i} \frac{K_i\, p_i}{1 + K_i\, p_i + K_j\, p_j} \tag{4.11}$$

- **Chemical reaction:**
  As mentioned before, chemical reactions under consumption or production of CO_2 are for the sake of simplification sometimes comprised within 'chemical sorption'. Basically, among the first reactions that take place when CO_2 gets into contact with the formation waters (brines) is the dissociation to carbonic acid:

$$CO_2 + H_2O \leftrightarrow H_2CO_3 \leftrightarrow H^+ + HCO_3^- \leftrightarrow 2H^+ + CO_3^{2-} \tag{4.12}$$

  After this, the dissolved CO_2 maybe minerally trapped by precipitating carbonates like calcite ($CaCO_3$)

$$HCO_3^- + Ca^{2+} \leftrightarrow CaCO_3 + H^+ \tag{4.13}$$

  or others (magnesite $MgCO_3$, siderite $FeCO_3$) analogously. In any case, this reaction produces acid and is consequently promoted if alkalinity can be provided, for example, by the weathering of feldspars. Mineral trapping and the relevant reactions are thoroughly studied in the frame of the CO_2-TRAP project [164]. There already exist some modelling approaches as, for example, implemented in the SHEMAT simulator [37], but presently still restricted to single-phase flow and transport excluding multiphase effects. Since mineral trapping occurs on a significantly larger time-scale than the relevant multiphase processes during the plume evolution takes place, it appears to be reasonable that a reaction model

like SHEMAT is applied subsequently to modelling the multiphase plume evolution after an injection with a simulator like MUFTE-UG [79, 5] (compare also with Sec. 5.4).

After this overview of the characteristic processes related to the injection and storage of carbon dioxide, a concise impression of the behavior of the **fluid properties** is given below. No specific details of calculational approaches and estimations will be discussed except for the references in the figure captions. Instead, the interested reader is referred to the work of *Bielinski* (2006) [18].

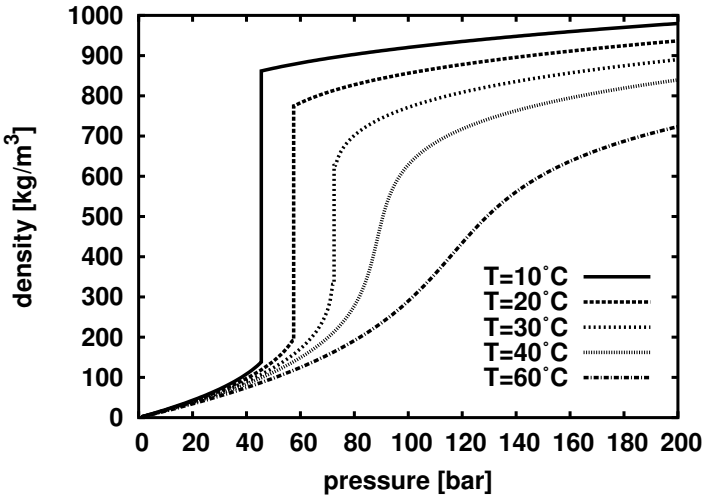

Figure 4.15: Density of CO_2 as a function of pressure at different temperatures (*Span & Wagner* (1996) [158]).

Figure 4.15 illustrates the **density of CO_2** as a function of pressure for various temperatures. We should remember the critical values of CO_2 at 73.8 bar pressure and 30.95 C temperature. For temperatures above the critical one, there is apparently a continuous smooth increase of the density with increasing pressure. These curves show the transition from sub-critical gaseous conditions to super-critical conditions without crossing the vapor pressure curve (see Fig. 4.9). In contrast to that, the lower temperature curves reveal a jump of the density when the vapor pressure curve is crossed. In any case, the density of CO_2 at high pressures shows a liquid-like behavior whereas the viscosity is at those conditions rather gas-like as can be seen in Fig. 4.16.

The typical S-shaped curves observed for the density can be observed also for the **dynamic viscosity of CO_2**. They show the same continuous variation from gaseous to super-critical conditions and the discontinuity from the gaseous to the liquid state of aggregation across the vapor pressure curve. While the viscosity of a gas increases with temperature, the opposite holds for liquid and supercritical conditions at the same pressures. Thus, the viscosity isotherms cross each other.

The **specific enthalpy of CO_2** is of interest in non-isothermal model concepts. Figure 4.17 shows the specific enthalpy dependent on pressure for different temperatures. The curves illustrate the enthalpy change relative to a reference state of h = 0 kJ/kg at p_{CO2} = 1.013 bar

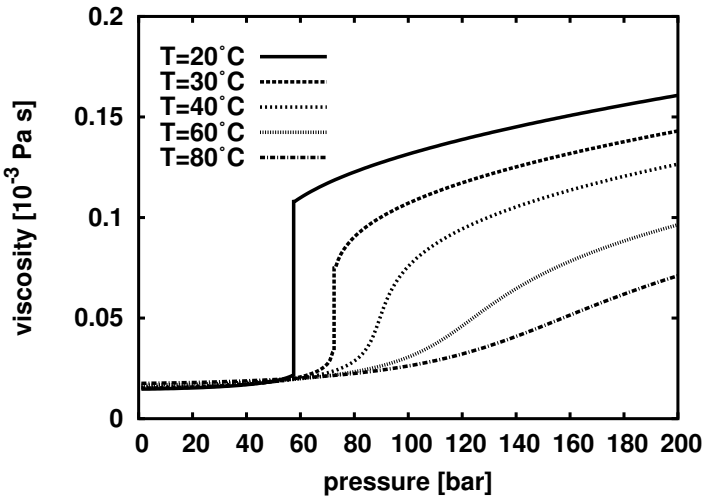

Figure 4.16: Viscosity of CO_2 as a function of pressure at different temperatures (*Fenghour et al.* (1998) [61]).

and T = 0 C. It is necessary to add 21.91 kJ/kg to the results of the SPAN & WAGNER equation since they use a different reference state. This causes a constant offset of the enthalpy curves; enthalpy differences are unaffected. The CO_2 reference state has to be the same as the one used for brine enthalpy, which is not shown here, in order to quantify the enthalpy change due to dissolved CO_2 correctly. The 10 C and 20 C curves show gaseous and liquid CO_2 for low and high pressures, respectively. As the volume change from gaseous to liquid is large, a jump in the specific enthalpy can be observed, which is the specific enthalpy of evaporation. The other curves are again above the critical temperature showing a smooth transition.

Concerning the **properties of the formation waters**, it is especially the influence of dissolved salt on the density that has to be taken into account. While for pure water the *IAPWS* formulations [94] are of excellent accuracy, there are a number of approaches that estimate brine densities dependent on salinity and dissolved fractions of CO_2 and other substances. Fig. 4.18 shows the density of water with different salinities and also one curve with dissolved CO_2, all three dependent on temperature at 100 bar pressure. The influence of the salinity is apparently as expected. Another very important aspect can be noted when comparing the two curves with same salinity $S = 0.25$ kg/kg. One of the curves represents the brine density with dissolved CO_2 ($X_b^{CO_2} = 0.02$ kg/kg). Dissolved CO_2 causes an increase of the water density. This phenomenon is of great interest for the long-term storage since it prevents the dissolved carbon dioxid from rising upwards. Thus, this effect is an important storage mechanism.

Table 4.2 gives an overview of characteristic conditions and corresponding system properties for some selected cases.

Although the details of the implementation were not discussed in this section, it became clear that the fluid properties require careful attention for the modeler due to their strong non-linear variations, in particular at the transitions between the states of aggregation and around the critical point. The simplifying assumption of constant fluid properties in the model is only possible

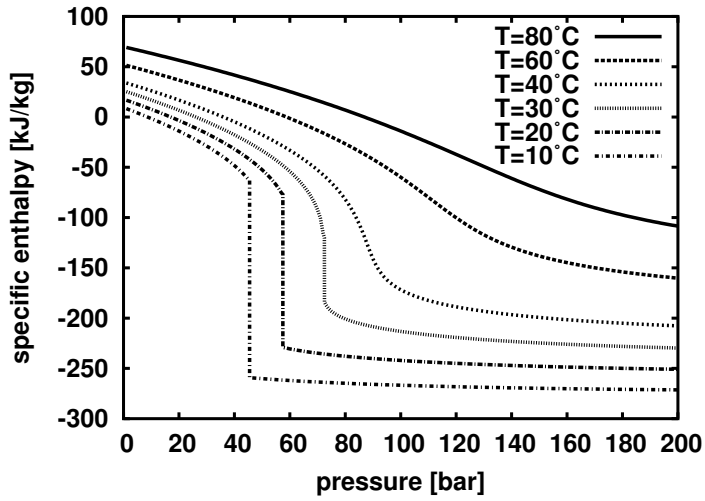

Figure 4.17: Specific enthalpy of CO_2 as a function of pressure at different temperatures (*Span & Wagner* (1996) [158]).

for very restricted cases where distinct vertical migrations do not occur so that pressure and temperature can be considered as constants in the domain of interest.

4.3.3 CO_2 and CH_4 Mixtures in EGR-Simulations

In the previous sections, the modelling of CO_2 migration and trapping in geological formations has been discussed where CO_2 was supposed to be the only non-aqueos component. The scenarios of *Enhanced Oil Recovery* (EOR) and *Enhanced Gas Recovery* (EGR) as explained in Sec. 2.4.1 require to include further components and potentially also phases into the conceptual model. Since the consideration of an additional oil phase is straightforward like the implementation of the NAPL component/phase, we focus here on the behavior of a CO_2/CH_4 mixture in EGR scenarios.

Let us restrict ourselves to the consideration of two phases (water and gas) with the three components water, methane, and carbon dioxide. The amount of water vapor can be calculated according to Eq. (3.74) by

$$x_g^w = \frac{p_{\text{sat}}^w}{p_g} \tag{4.14}$$

with p_{sat}^w being equal to the partial pressure of water vapor. For the typical gas reservoir conditions of interest, this yields rather small mole fractions of water vapor in the gas phase ($x_g^w|_{80\text{ bar},40\text{C}} = 9.2 \cdot 10^{-4}$). Thus, the influence of water vapor on the physical properties of the gas phase can be approximately considered as negligible. In order to determine the mole fractions of CO_2 and CH_4 it is necessary to choose one of both as primary variable. Once knowing the composition of the phases, the fluid properties must be calculated where a special interest is on the gas phase since their density, viscosity, and enthalpy depend strongly on its composition. Table 4.3 lists the critical conditions for CO_2 and CH_4. The densities of pure CH_4 and CO_2 are plotted over ranges of temperature and pressure in Fig. 4.19 calculated by using equations of

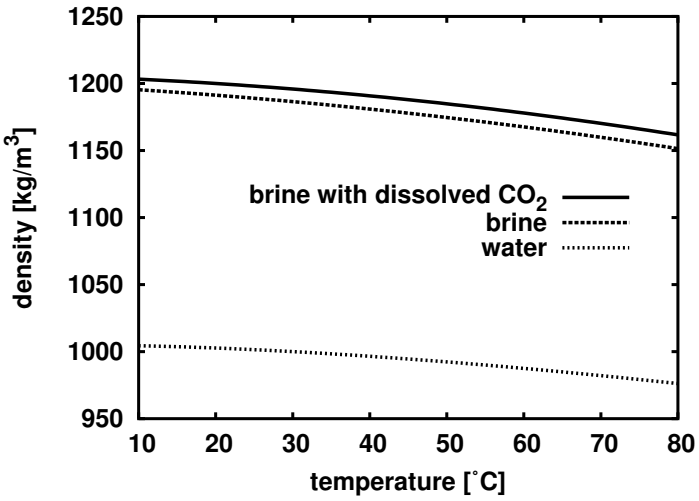

Figure 4.18: Pure water and brine density as a function of temperature at 100 bar pressure. Dotted line: pure water density (*IAPWS* (2003) [94]). Dashed line: brine density at a salinity of $S = 0.25$ kg/kg (*Batzle & Wang* (1992) [14]). Solid line: brine of same salinity with dissolved CO_2 (*Garcia* (2001) [67] ($X_b^{CO_2} = 0.02$ kg/kg)).

state proposed by *Duan et al.* (1992) [50]. While there is a disontinuity in the CO_2 density when crossing the vapor pressure curve, the density of CH_4 is continuous for the given pressures and temperatures since methane is in this entire range in a supercritical state. This characteristic feature can also be observed for viscosity and enthalpy. They are also smoother for CH_4.

With the equation of state by [51], the density of the gas phase as a mixture of CH_4 and CO_2 can be calculated. This is shown in Fig. 4.20 for 35C and 80 bar. On the right hand side of this figure, the viscosity of the mixture is plotted for the same pressure and temperature. The calculation is performed following the *Wilke*-method as given by Eq. (3.16). The viscosity of pure methane can be calculated, for example, using data from *Daubert & Danner* (1989) [44] and μ_c is given by *Fenghour et al.* (1998) [61].

At reservoir conditions, CO_2 is denser and more viscous than CH_4. Both of these properties increase the amount of CH_4 which can be recovered from the depleted reservoir and the amount of CO_2 which can be stored since the density difference between the two gases reduces mixing and the fact that the more viscous fluid displaces the less viscous one provides for a stable displacement.

The specific enthalpy of CH_4, h_m is calculated from its specific heat capacity with the ideal gas assumptions and the specific heat capacity is taken from [44]. Then, the specific enthalpy of the gas phase mixture can be calculated by Eq. (3.85).

An important feature of the CO_2/CH_4 system in an EGR-scenario is the diffusive/dispersive mixing of these two components since this is likely to affect the recovery rate of methane. A strong and fast mixing would cause a rapid breakthrough of injected CO_2 at the methane production well which is an unwanted effect concerning both the recovered gas and the storage effectivity for the CO_2.

Table 4.2: Characteristic values for CO_2 solubility and fluid properties of CO_2 and brine.

Case	T [C]	p [bar]	S [-]	X_w^{CO2} [kg/kg]	c_{CO2} [kg/m^3]	ρ_{CO2} [kg/m^3]	μ_{CO2} [Pa s]	ρ_b [kg/m^3]	μ_b [Pa s]
1	10	1	0	0.002	2.2	1.88	$1.42 \cdot 10^{-5}$	999.7	$1.31 \cdot 10^{-3}$
2	40	100	0.25	0.020	23.5	628.61	$7.58 \cdot 10^{-5}$	1180.9	$1.25 \cdot 10^{-3}$
3	70	100	0.25	0.016	19.2	247.77	$2.77 \cdot 10^{-5}$	1159.8	$0.77 \cdot 10^{-3}$
4	70	200	0.25	0.021	24.6	659.05	$8.30 \cdot 10^{-5}$	1162.9	$0.77 \cdot 10^{-3}$

Case 1: groundwater, close to surface,
Case 2: saline aquifer, depth of 1000 m,
Case 3: saline hot aquifer, depth of 1000 m,
Case 4: very deep injection, depth of 2000 m.

Table 4.3: Critical conditions for CH_4 and CO_2 from [51].

Fluid	Critical temperature [°C]	Critical pressure [bar]
CH_4	-82.55	46.41
CO_2	31.05	73.83

4.4 Methane Migration in the Subsurface

Modeling the release of methane from coal mines and its migration through shafts, roads, and rocks requires in general a reasonable compromise between computation time on the one hand and details both in the conceptual model and in the geometry description on the other hand [81, 84, 19]. There are a number of problems that make a detailed model of the methane migration through a coal mine rather complex. They will be briefly explained in the following.

- The release of methane from a coal seam can be modeled by adsorption and desorption approaches as explained above (Sec. 4.1.4). It depends on the composition of the ambient gas phase if the conceptual model has to account for compositional effects in the gas phase or if it can be assumed to consist of methane only. If the gas phase is pure methane, the p in Eqs. (4.10) and (4.9) represents the absolute gas (methane) pressure, whereas in case of a multicomponent gaseous phase (methane, air, vapor) p must be interpreted as the partial pressure of methane.

- In general, the geometry of a mine is characterized by a large number of structures like roads, shafts, coal seams, etc., which make this a very heterogeneous domain of interest. An accurate precise implementation in a model results quickly in a huge number of nodes so that for the sake of saving computation time a simplification of the conceptual model is necessary.

- Roads and shafts in the mines are typically hollow structures with a distinct extension in one direction so that flow within this structures can be considered as one-dimensional.

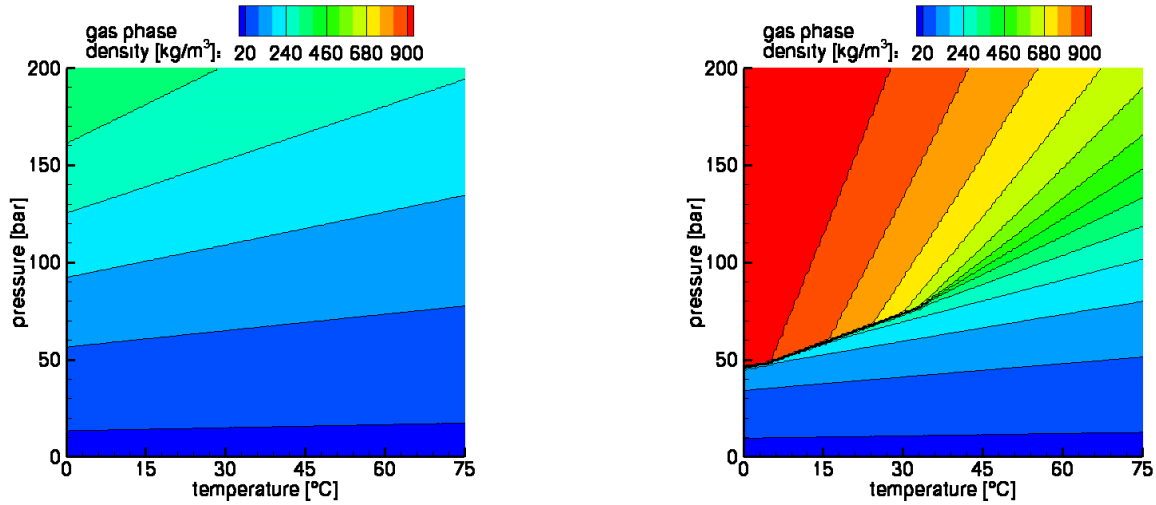

Figure 4.19: Densities of pure CH_4 (left) and CO_2 (right).

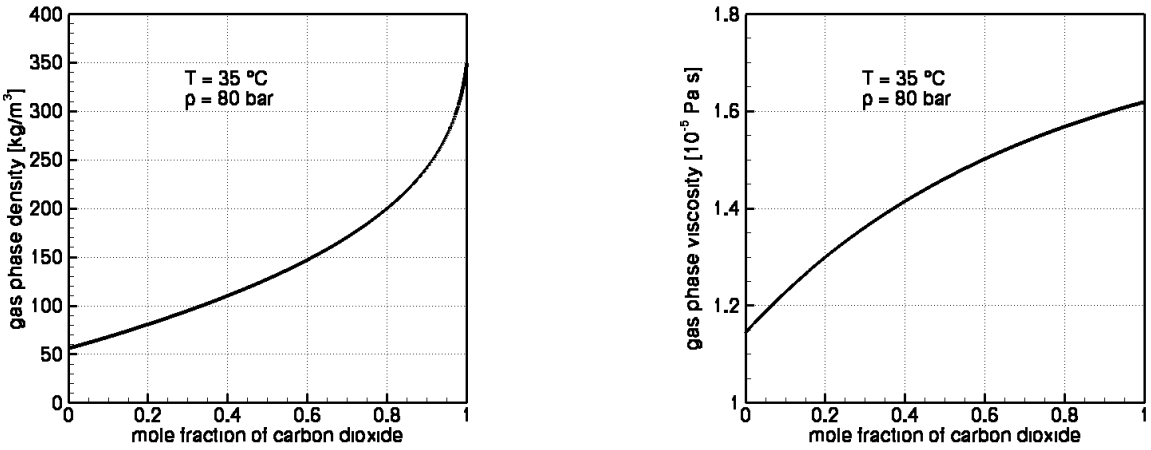

Figure 4.20: Density (left) and viscosity (right) of the gas phase as a mixture of CH_4 and CO_2.

The flow in such hollow tubes obeys in general not *Darcy's* law. This leaves the choice to disregard this fact and use *Darcy's* law with a very high permeability anyway or to model the flow in the hollow structures with pipe flow hydraulics [**?**] coupled to the surrounding multiphase porous media flow.

4.5 Multiphase Processes in Diffusion Layers of Fuel-Cells

After all these multiphase systems occuring in various depths of the subsurface, we now focus on a technical application of multiphase flow and transport through a porous medium. There are two major differences that characterize the processes in the diffusion layer of a fuel-cell in contrast to the environmental systems in the subsurface (see also Sec. 2.6):

- The first one is the scale on which the processes take place. While in the subsurface

typical REV sizes range from a few centimeter to several hundred meters, the entire thickness of a porous diffusion layer is about less than a millimeter. Since there are typically only a few fibres within that thickness, it leaves the definition of a REV size to be a matter of discussion. One may argue that the scale of interest is so small that we should use pore network models on the micro scale (see the discussion on scales in Sec. 3.1.1). However, we assume that the processes can still be considered as on a REV scale (local scale). Anyway, if a detailed spatial resolution of the discretized system is desired, this may produce element or volume sizes smaller than required for the definition of a REV.

- Second, the diffusion layers are in general rendered hydrophobic due to a treatment with water to enhance the liquid water removal. In environmental systems, the porous medium is practically always hydrophilic with water being the wetting phase.

In the following, we explain in Sec. 4.5.1 the multiphase multicomponent processes in the diffusion layer with a special focus on the oxygen diffusion and consumption by the overall reaction as well as the performance reduction if too much liquid water is present. Then, Sec. 4.5.2 gives some insight into the problem of the mixed hydrophobic/hydrophilic nature of the diffusion layer material.

4.5.1 Oxygen Diffusion and Consumption

Figure 6.31 illustrates in a cross-sectional view the cathodic diffusion layer of the membrane-electrode assembly (see also Fig 2.11) in contact with the gas distribution channels from Fig. 2.12. The multiphase processes which we want to simulate take place within the diffusion layer whereas the membrane and the gas channels are not considered in the simulations except for the appropriate description of the boundary conditions.

The oxygen transport mechanisms from the gas channels to the reaction layer through the diffusion layer depends on the operation mode of the gas channels, whether they are interdigitated or conventional (Fig. 2.12). The conventional set-up provides equal pressures in the half-channels on both sides of the shoulder of the current collector. Thus, there is no enforced advective gas flow towards the reaction layer and oxygen diffusion is the performance-limiting transport mechanism. In case of an interdigitated flow field in the gas distributors, both half channels have different pressures and an advective gas flow is superimposed on the diffusive transport influencing both the oxygen transport and that of the liquid water produced by the reaction.

As explained in Sec. 2.6 it is a key issue to optimize the liquid water distribution and its transport in the diffusion layer. While a minimum of water is required for the transport of protons, too much of it hinders the optimum supply of oxygen for the reaction, particularly at high current densities. For this reason, it is a major goal of the modelling efforts described here to investigate the dominating mechanisms and parameters for the oxygen transport.

Assuming that there is humidified air provided in the gas channels, we consider the gas phase to consist of three different components: oxygen, nitrogen, and water vapor (Fig. 4.21). We should note that in this case it is not appropriate to use air as a pseudo component since only oxygen

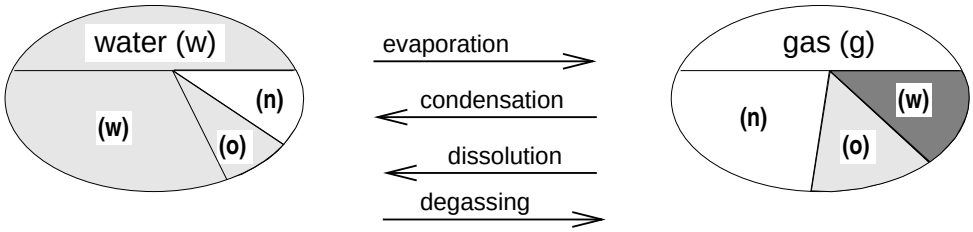

Figure 4.21: Phases, components, and processes in the two-phase three-component system for the description of the processes in the diffusion layer. Mass components: *w* (water), *o* (oxygen), *n* (nitrogen)

is consumed by the reaction and thus a concentration gradient of oxygen in the gas phase enhances the diffusion.

The consumption of oxygen and production of liquid water by the electro-chemical reaction can be modeled by a sink term for oxygen and a source term for water and heat at the left domain boundary taking into account the available concentration for the electro-chemical reaction and the local current density i. According to *Acosta et al.* (2006) [2] the current density i is a function of the oxygen partial pressure p_g^o and a number of other parameters. Knowing i, the oxygen consumption rate in the electro-chemical reaction is given by *Faraday's* law:

$$\frac{\partial N^{\mathrm{R}}_{\mathrm{O_2}}}{\partial t} = -\frac{i}{4\mathbf{F}} \tag{4.15}$$

Here, $\partial N^{\mathrm{R}}_{\mathrm{O_2}}/\partial t$ is the molar flux in [mol m^{-2} s^{-1}] due to the reaction (indicated by superscript R) having here a negative sign since oxygen is consumed. $\mathbf{F} = 96484.56$ C/mol represents *Faraday's* constant.
At the same time, the water production rate due to the reaction is given by:

$$\frac{\partial N^{\mathrm{R}}_{\mathrm{H_2O}}}{\partial t} = \frac{i}{2\mathbf{F}} \tag{4.16}$$

There is an additional water flux through the membrane due to electro-osmotic drag. The estimation of that water flux requires a value for the electro-osmotic drag coefficient $t_{\mathrm{H_2O}}$ which according to *Acosta et al.* (2006) [2] can be assumed for a fully hydrated membrane to be $t_{\mathrm{H_2O}} = 0.2327$. Then the electro-osmotic flux through the membrane (superscript M) is:

$$\frac{\partial N^{\mathrm{M}}_{\mathrm{H_2O}}}{\partial t} = t_{\mathrm{H_2O}} \frac{i}{\mathbf{F}} \tag{4.17}$$

The heat production by the reaction, considered as a heat source, is calculated as:

$$\frac{\partial q^{\mathrm{R}}}{\partial t} = (U_{\mathrm{th}} - U_{\mathrm{cell}})\, i \tag{4.18}$$

It is assumed that a part of the heat generated in the cathode reaction layer flows through the membrane to the anode side, depending on the thermal conductivity of the membrane.

4.5.2 Water and Gas in a Hydrophobic Porous Medium

The backing of a fuel-cell including the diffusion layer is typically made of a conducting carbon material, which is treated with teflon. Thus, the porous material becomes hydrophobic so that liquid water removal is enhanced. In a hydrophobic porous medium, the wetting fluid, i.e. the gas phase, will occupy the smaller pores, whereas the non-wetting fluid, i.e. the water phase, will occupy pores with a larger radius. This has obviously influence not only on the capillary pressure–saturation relation but also on the relative permeabilities of both water and gas phase. Since now the liquid water phase fills first the larger pores, it is expected to obtain a faster increase of the relative permeability of liquid water at low saturations compared with hydrophilic porous media.

For the implementation of the hydrophobic property into the model via the capillary pressure–saturation relationship, there are practically no measured data available in the literature. Some authors use some adapted scaling approaches like the *Leverett* approach to approximate the hydrophobic behavior [122, 139]. *Acosta et al.* present an indirect determination of the capillary pressure–saturation relationship for a carbon diffusion layer material. From the obtained $p_c(S)$–relation, they suggest to derive the relative permeabilities via a parallel capillary tubes model.

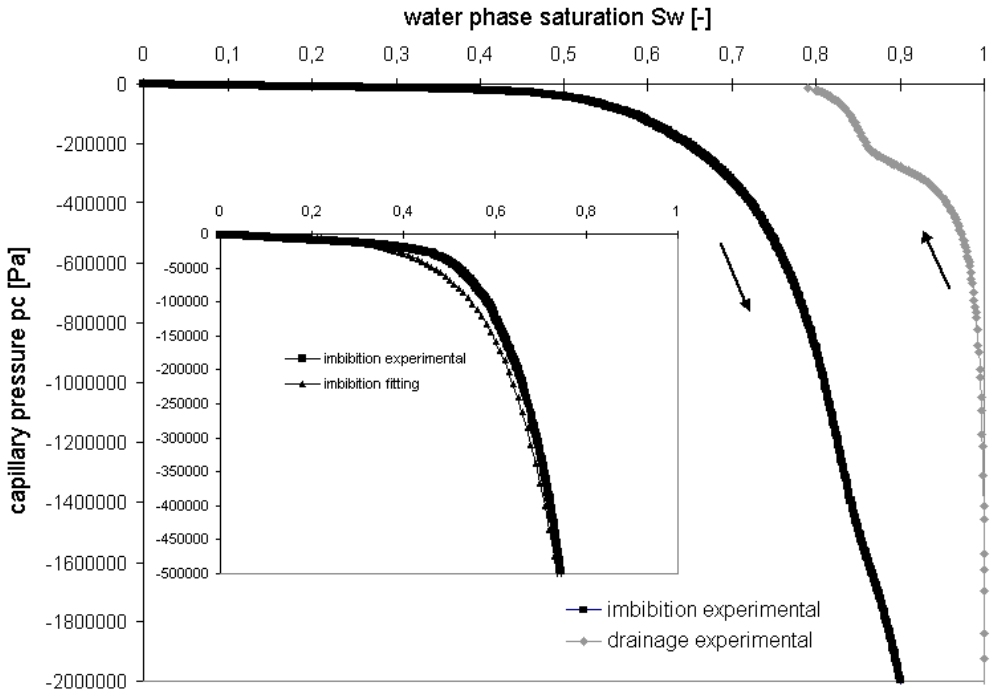

Figure 4.22: Capillary pressure–saturation data for a *DS-ELAT* electrode obtained by mercury injection and corrected for a water-air system by Eq. (4.19) [2]. The inserted zoom shows the relevant range of capillary pressure and a fitting for the imbibition curve.

Figure 4.22 shows the results they obtained from a mercury porosimetry method corrected for a water-air system. Mercury was forced under pressure into a core of the porous material and the saturation was determined from volumetric considerations. The correction of the obtained capillary pressure curve is done as proposed by [145, 152] taking into account the different surface tension and contact angle.

$$\frac{p_{c\ water-air}}{p_{c\ Hg-air}} = \frac{\gamma_{water}\cos\theta_{water}}{\gamma_{Hg}\cos\theta_{Hg}}\ . \tag{4.19}$$

It can be seen from Fig. 4.22 that there is a distinct hysteretic behavior for the drainage and imbibition process. Note, that in this context imbibition still stands for a process by which water displaces the gas phase although it is commonly referred to as denoting the displacement of a non-wetting phase by the wetting phase. The imbibition curve is in this case fully hydrophobic. Thus, at ambient pressure all liquid water should be expected to be expelled from the diffusion layer. However, it is a well-known phenomenon that once a high water saturation is reached in the diffusion there will be some residual water remaining indicating that the diffusion layer becomes partially hydrophilic. From Fig. 4.22, this residual water saturation at zero capillary pressure can not be identified reliably and thus *Acosta et al.* extended the drainage curve towards zero saturation with positive capillary pressures at small water saturations so that the partially hydrophilic behavior can be modeled (see Fig. 4.23).

The parameterization used for the drainage curve is:

$$p_c = A_2 \exp(B_2 S_w + C_2) + D_2\ (1 - S_w) + \frac{E_2}{S_w} \tag{4.20}$$

and the one for the imbibition curve given by:

$$p_c = A_1 \exp(B_1 S_w + C_1) + D_1\ (1 - S_w)\ . \tag{4.21}$$

4.6 Fluid-Structure Interaction and Deformation

Up to this point, we considered the porous media as rigid structures that influence the hydraulic behavior via constitutive relationships like the capillary pressure–saturation functions or the relative permeability–saturation functions. A deformation of the porous medium, for example, due to pressure variation or external loads was neglected. However, there are also multiphase flow problems in porous media where the deformation is an important process and needs to be accounted for in the conceptual model. Examples for such problems are consolidation problems or cohesive soils which show a characteristic swelling and shrinking behavior under water content variations.

There exist different approaches to include deformation into a multiphase flow model. They will be outlined in the following. However, we will keep this discussion short since a detailed analysis of coupled solid-fluid problems would go beyond the scope of this work.

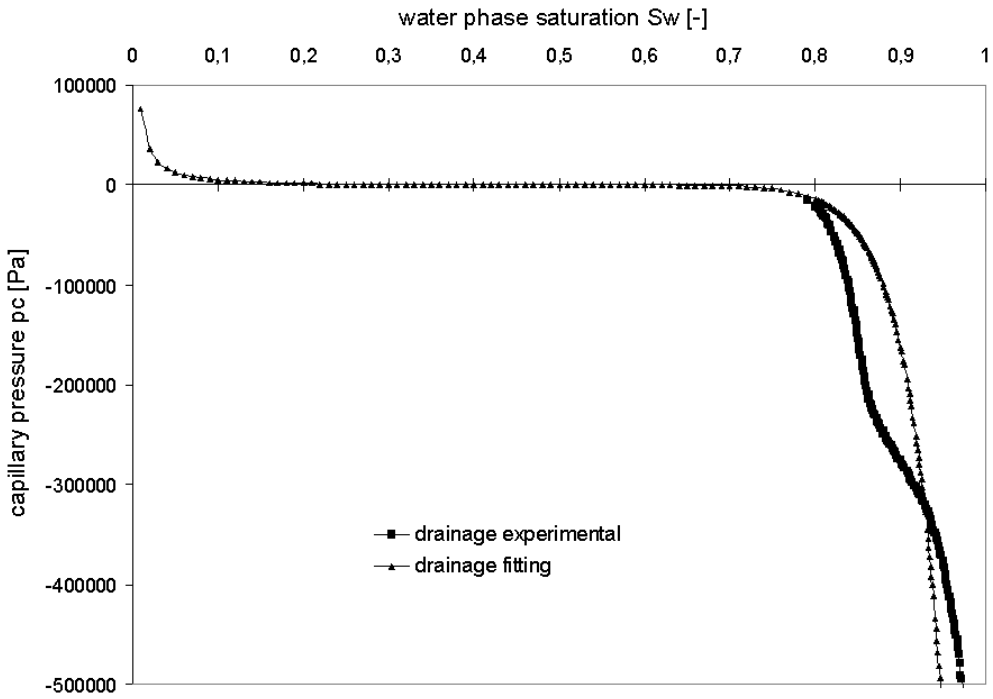

Figure 4.23: Capillary pressure–saturation data and a corresponding fitting curve for a *DS-ELAT* electrode [2].

4.6.1 Phenomenological Consideration of Structural Alterations

A *phenomenological approach* as proposed by *Freiboth* (2007) [66] includes structural alterations by considering their influence on the hydraulic properties. This presumes that the focus of the model is distinctly on the flow and transport processes since local displacement can not be quantified. A possible field of application would be the modelling of cohesive soils where changes in the water saturation lead to swelling and shrinking phenomena with varying porosity and permeability as a function of the water content.
Figure 4.24 illustrates the idea of a decoupled consideration of flow/transport and structural alteration. In a first step, the flow and transport processes are modeled with a conceptual model as, for example, presented in the previous sections. Then, in a second step, the influence of the variations in fluid saturations and water contents on the soil structure is evaluated. In case of a decreasing water content, the cohesive soil tends to shrink which results in a reduced porosity and permeability. Accordingly, also other parameters such as capillary pressure must be adapted. Therefore, it is necessary to balance the total water content in the REV which is obtained as the sum of the ”free” pore water and the immobile water that is bound to the soil matrix. Furthermore, a set of constitutive equations is required to account for the shrinkage factors, the porosity and permeability alterations, etc.

The advantage of such a phenomenological approach is its decoupled consideration of flow on

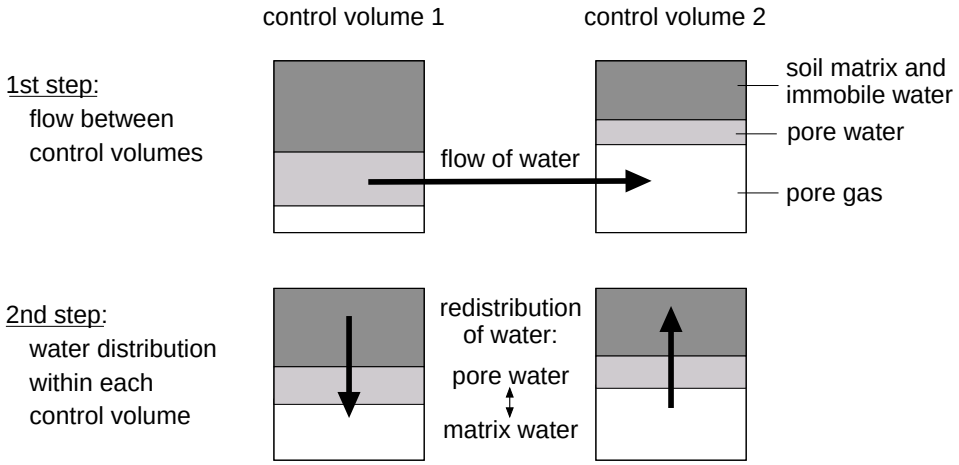

Figure 4.24: Decoupled phenomenological modelling of flow and structural alteration in cohesive soils [87].

the one hand and structural alteration on the other hand which reduces the computational complexity. However, it is clearly restricted in its applicability to weakly coupled solid-fluid problems and cannot explicitly account for local displacement.

A well-known simple example that fits also in the category of phenomenological considerations of structural deformation is the storage coefficient S_0 in the transient groundwater flow equation, which can be written as [24]:

$$S_0 \frac{\partial h}{\partial t} + \nabla \cdot \mathbf{v} - q = 0 \tag{4.22}$$

S_0 accounts for the variation of the storage capacity of the porous matrix with transient changes in the piezometric head h. This includes changes in the pore structure (changes in the porosity) and the compressibility of the grains and the water phase.

4.6.2 Coupled Solid-Fluid Problems

Depending on the degree of coupling between the flow processes through a porous medium and its deformation, a phenomenological description based on a decoupled consideration of these two aspects is not appropriate. Thus, a fully coupled model concept for both flow and deformation is required as, for example, given by the *Theory of Porous Media* (TPM), cf. *de Boer* (2000) [45], *Ehlers* (1996) [55].

Like all the multiphase flow concepts described in this work, the TPM is also based on an averaged macroscopic description of the porous medium and the fluids within a control volume. The TPM accounts for the different movement of the fluids and the deformable solid matrix. It incorporates the fields of the solid displacement $\mathbf{u}$, the fluid velocities $\mathbf{v}_\alpha$, and the pressure p into the model. Accordingly, balance equations for mass (including *Darcy's* law) and momentum are required. The TPM can also be extended to non-isothermal problems with mass transfer between the phases as presented, for example, for an elasto-viscoplastic material by *Graf & Ehlers* (2005) [71].

Chapter 5

Mathematical and Numerical Models

In Chapter 3 we presented conceptual models for different kinds of multiphase flow and transport problems. Based on that, we will discuss in the following the mathematical treatment of the arising systems of equations. Typically, they are mostly solved as coupled systems and it is a key issue to choose an appropriate formulation. In Sec. 5.1 this point is addressed in detail with a focus on a solution strategy for two-phase systems without non-isothermal effects. The concepts presented there are extended to more complex compositional problems in Sec. 5.3. The numerical treatment of the partial differential equations, particularly their discretization in time and space is the purpose of Sec. 5.2. After explaining the model concepts for systems of different complexity, we discuss in Sec. 5.4 the possibilities of coupling these concepts for special systems where the influence of certain characteristic processes changes with time. The aim of this is to reduce the computational costs and adapt them to the required complexity which may change during the whole simulation period. Minimizing the computational costs can be seen as the red line also through Sec. 5.5, 5.6, and 5.7. These sections deal with efficient multigrid solvers and preconditioners, the use of parallel computation, and numerical features for addressing specific problems with numerical robustness.

5.1 Solution of the General Multiphase Flow Equations

The general form of the multiphase flow equation for a phase α is given by:

$$\frac{\partial(\phi S_\alpha \rho_\alpha)}{\partial t} - \nabla \cdot (\rho_\alpha \lambda_\alpha \mathbf{K} \cdot (\nabla p_\alpha - \rho_\alpha \mathbf{g})) - \rho_\alpha q_\alpha = 0 \tag{5.1}$$

Depending on the number of phases, the supplementary constraints, and the constitutive relationships, Eq. (5.1) yields a fully-coupled system of partial differential equations. They are of mixed hyperbolic/parabolic character according to the influence of the capillary pressure relative to the advective flow of the phases. When extending these equations to compositional systems as it is done in Sec. 5.3 diffusive effects further shift the character of the equations towards parabolic. Such effects are molecular diffusion, dispersion, and heat conduction. The mathematical behavior of the general multiphase flow equations is discussed in more detail in *Helmig* (1997) [78] and *Bastian* (1999) [9].

For the case of an isothermal two-phase system, Eq. (5.1) stands for a set of two coupled partial differential equations representing the two-phase flow equations. One equation for the

wetting phase w (typically: water) and the other one for the non-wetting phase n (e.g.: NAPL, gas). The system of equations is closed by algebraic relations: the capillary pressure constraint (Eq. 3.61), the saturation constraint (Eq. 3.3), and constitutive relationships for $k_{r\alpha}(S)$, $p_c(S)$, $\rho(p,T)$, $\mu(p,T)$, etc. As will be explained in Sec. 5.3.1, according to the phase rule of Gibbs with the restriction to an isothermal system two independent primary variables are required in order to describe the system uniquely. The choice of the parameters allows some alternative formulations of the two-phase flow equations:

- pressure–pressure formulation
- pressure–saturation formulation
- global pressure formulation / fractional flow formulation

5.1.1 Formulations

5.1.1.1 Pressure–Pressure Formulation

Both phase pressures are primary variables in the solution vector. The saturations are then calculated by an inverse capillary pressure function

$$S_\alpha = g_\alpha(p_c) \qquad \text{with} \quad \alpha \in n, w \tag{5.2}$$

with the preconditions that p_c as a function of S_w (resp. S_n) behaves strictly monotonic. This allows formulating the partial differential equations as follows:

Wetting phase (index w):

$$\frac{\partial(\phi g_w \rho_w)}{\partial t} - \nabla \cdot \left(\lambda_w \rho_w \mathbf{K}(\nabla \underline{p_w} - \rho_w \mathbf{g})\right) - \rho_w q_w = 0 \tag{5.3}$$

Non-wetting phase (index n):

$$\frac{\partial(\phi g_n \rho_n)}{\partial t} - \nabla \cdot \left(\lambda_n \rho_n \mathbf{K}(\nabla \underline{p_n} - \rho_n \mathbf{g})\right) - \rho_n q_n = 0 \tag{5.4}$$

The primary variables are underlined herein. The numerical behavior of the pressure–pressure formulation depends strongly on the behavior of the capillary pressure function. If $\frac{dp_c}{dS_w}$ is too small, the determination of the saturation becomes unstable since small variations in p_c produce strong variations in S_w. This is probably the main reason why the pressure–pressure formulation is often not applied in favor of the pressure–saturation formulation.

5.1.1.2 Pressure–Saturation Formulation

One phase pressure and one saturation are primary variables. The decision which pressure resp. saturation is used may depend on several factors such as, e.g., the boundary conditions. For a detailed discussion of the type classification and applicability of the (p_w, S_n) and (p_n, S_w) formulations we refer to the work of *Bastian* (1999) [9]. Below, we take the p_w–S_n formulation, i.e.

the pressure of the wetting phase and the saturation of the non-wetting phase. The modifications of Eq. 5.1 are summarized by the algebraic relations

$$\nabla p_n = \nabla(p_w + p_c) \qquad \frac{\partial S_w}{\partial t} = \frac{\partial}{\partial t}(1 - S_n) = -\frac{\partial S_n}{\partial t} \quad , \tag{5.5}$$

which yields after inserting the system of partial differential equations:

Wetting phase:

$$-\frac{\partial(\phi \underline{S_n} \rho_w)}{\partial t} - \nabla \cdot \left(\lambda_w \rho_w \mathbf{K}(\nabla \underline{p_w} - \rho_w \mathbf{g})\right) - \rho_w q_w = 0 \tag{5.6}$$

Non-wetting phase:

$$\frac{\partial(\phi \underline{S_n} \rho_n)}{\partial t} - \nabla \cdot \left(\lambda_n \rho_n \mathbf{K}(\nabla \underline{p_w} + \nabla p_c - \rho_n \mathbf{g})\right) - \rho_n q_n = 0 \tag{5.7}$$

Since the pressure–saturation formulation includes one of the saturations in the vector of primary variables its numerical behavior is much less dependent on the steepness of the $p_c(S)$–curve.

5.1.1.3 Global Pressure–Saturation Formulation

The global pressure formulation is also known sometimes as fractional flow formulation. For a detailed derivation we refer to, e.g., *Chavent & Jaffre* (1978) [29] and *Bastian* (1999) [9].
The global pressure formulation is essentially based on mathematical constructs. One is the definition of the total velocity

$$\mathbf{v}_t = \mathbf{v}_w + \mathbf{v}_n \tag{5.8}$$

representing the sum of the two phase velocities. With this definition it is possible to transform the two-phase flow equations into

$$\frac{\partial \phi}{\partial t} + \frac{1}{\rho_w}\left(\phi S_w \frac{\partial \rho_w}{\partial t} + \nabla \rho_w \cdot \mathbf{v}_w\right) + \frac{1}{\rho_n}\left(\phi S_n \frac{\partial \rho_n}{\partial t} + \nabla \rho_n \cdot \mathbf{v}_n\right) + \nabla \cdot \mathbf{v}_t = q_w + q_n \, . \tag{5.9}$$

One can express the total velocity dependent on the non-wetting phase pressure p_n by using *Darcy's* Law and the capillary pressure relation $p_n - p_w = p_c$:

$$\mathbf{v}_t = -\lambda \mathbf{K}(\nabla p_n - f_w \nabla p_c - \mathbf{G}) \tag{5.10}$$

In Eq. (5.10) several abbreviations are used. $\lambda = \lambda_w + \lambda_n$ is the total mobility, $f_w = \lambda_w/\lambda$ is the fractional flow of the water phase, and $\mathbf{G} = \mathbf{g}(\lambda_w \rho_w + \lambda_n \rho_n)/\lambda$ is a modified gravity vector. The idea is to find a scalar function - the global pressure p - such that Eq. (5.10) looks similar to *Darcy's* Law. Thus, p must be chosen such that

$$\nabla p = \nabla p_n - f_w \nabla p_c \, . \tag{5.11}$$

It can be shown with this that for any S_w it is valid: $p_w \leq p \leq p_n$. Combining Eqs. (5.10) and (5.11) and inserting into Eq. (5.9) yields an equation for the global pressure p that is coupled to the saturation for low-compressible phases only via λ and $\mathbf{G}$ and not via the storage term as,

e.g., in Eq. (5.6). Thus, the set of equations for the global pressure–saturation formulation with the unknowns p and S_w is given by the pressure equation

$$\begin{aligned}\nabla \cdot \left(-\lambda \mathbf{K}(\nabla \underline{p} - \mathbf{G})\right) &= q_w + q_n - \frac{\partial \phi}{\partial t} \\ &\quad - \frac{1}{\rho_w}\left(\phi S_w \frac{\partial \rho_w}{\partial t} + \nabla \rho_w \cdot \mathbf{v}_w\right) - \frac{1}{\rho_n}\left(\phi S_n \frac{\partial \rho_n}{\partial t} + \nabla \rho_n \cdot \mathbf{v}_n\right) \end{aligned} \tag{5.12}$$

the saturation equation

$$\frac{\partial(\phi \rho_w \underline{S_w})}{\partial t} = \rho_w q_w - \nabla \cdot \{\rho_w \mathbf{v}_w\} \ , \tag{5.13}$$

and the equations for the phase velocities

$$\mathbf{v}_w = f_w \mathbf{v}_t + \lambda_n f_w \mathbf{K}(\nabla p_c + (\rho_w - \rho_n)\mathbf{g}) \tag{5.14}$$

$$\mathbf{v}_n = f_n \mathbf{v}_t - \lambda_n f_w \mathbf{K}(\nabla p_c + (\rho_w - \rho_n)\mathbf{g}) \ . \tag{5.15}$$

The weakly coupled equations (5.12) and (5.13) may be solved sequentially. The saturation equation is advection-dominated and often solved explicitly while the pressure equation is solved implicitly (IMPES method). However, since the global pressure p and the total velocity v_t are only mathematical constructs which are difficult to interpret physically, it may be a problem to experimentally determine the boundary conditions for a global pressure-saturation formulation.

Using some simplifying assumptions this formulation of two-phase flow systems is helpful to analytically investigate one-dimensional model problems. The complexity of the equations can be significantly reduced by assuming incompressibility of the fluids and the pore space, no sources/sinks and no gravity. Then the pressure equation is only

$$\frac{\partial}{\partial x}\left(-\lambda K \frac{\partial p}{\partial x}\right) = 0 \ . \tag{5.16}$$

If capillary pressure is zero, the saturation equation is purely hyperbolic and can be written as

$$\phi \frac{\partial S_w}{\partial t} + \mathbf{v}_t \frac{\partial}{\partial x} f_w(S_w) = 0 \ . \tag{5.17}$$

Eq. (5.17) is known as the *Buckley–Leverett* equation. The solution of this equation is extensively discussed in the literature, e.g., by *LeVeque* (1992) [107].

If capillary pressure is not neglected as in Eq. (5.17) the saturation equation reveals a parabolic behavior. We refer here again to the literature, e.g., the *McWhorther*–problem described by a quasi-analytical solution presented by *McWhorter & Sunada* (1990) [115].

5.1.2 Assignment of Boundary Conditions

The general balance equations for isothermal or non-isothermal multiphase systems form an initial and boundary value problem. Thus, solving the system of equations requires the assignment of boundary conditions to the complete boundary Γ of the solution domain. Different types of boundary conditions can be distinguished while they can be used also in combination to segments Γ^i of the subdivided boundary of the domain.

$$x = x^D(s,t) \quad \text{on } \Gamma^D \quad \textit{Dirichlet} \text{ boundary condition}$$

A *Dirichlet* boundary condition fixes the value of a primary variable x. A *Dirichlet* boundary value can be also a function of time t and location s.

$$C(s,t)\,\frac{\partial u}{\partial \mathbf{n}} = x^N(s,t) \quad \text{on } \Gamma^N \quad \textit{Neumann} \text{ boundary condition}$$

A *Neumann* boundary condition provides information about the derivative of the primary variable at the boundary. $\mathbf{n}$ is the normal vector at the boundary segment Γ^N. C can be some constant dependent on time and location. Dependent on $C\,x^N$ may express a flux across the boundary into or out of the domain. Thus, boundary conditions of type *Neumann* are also called flux boundary conditions.

$$C_1(s,t)\,\frac{\partial u}{\partial \mathbf{n}} + C_2 x = x^C(s,t) \quad \text{on } \Gamma^C \quad \textit{Cauchy} \text{ boundary condition}$$

A *Cauchy* boundary condition represents a more complex type that allows to specify informations both of the values of the primary variables and of their gradients. This is why they are also called mixed boundary conditions.

Boundary conditions of type *Cauchy* are commonly not applied for the kinds of multiphase flow systems that we consider in this work. *Cauchy* boundary conditions may be useful for describing the interaction between a groundwater system and a surface water system where the water flux across the system interface is determined by the water levels in both systems and the properties of the interface, for example, the permeability of the sediments in a river bed.

The assignment of boundary conditions is for many multiphase flow problems a rather non-trivial problem. It is not always practical to specify a *Dirichlet* or a *Neumann* condition at every segment of the model domain. This holds particularly for boundaries that represent an interface to another physical system which cannot be described with the same or similar partial differential equations, for example, interfaces between a porous and a non-porous medium where only the pressure can be fixed. This problem occurs in manifold variations like, for example, for the injection of a fluid into a laboratory sand-box with a free outflow to the atmosphere after the breakthrough [34]. There, the atmospheric pressure is known and can be assigned as a *Dirichlet* value to the interface between porous medium and environment which is the boundary of the solution domain. However, in general the phase saturations and the concentrations of components in the outflowing fluid phases is not known and neither their values can be fixed as *Dirichlet* conditions nor the phase/component fluxes are known a priori.
Dependent on the discretization method there are different options to deal with this problem. In case of a finite-volume discretization method one could assign a huge volume to an additional finite-volume next to the boundary of the solution domain, see for example the TOUGH2 simulator described by *Pruess* (1991) [142]. A huge volume keeps the conditions in the environment outside the solution domain constant independent of the fluxes out of the domain. If the domain description is based on a finite-element discretization this approach is not feasible. Instead, if the environment should be modeled with a large volume, one has to physically extend the model domain which may enlarge the mathematical problem and the solution effort significantly. Alternatively, we tested a so-called Freeflow boundary conditions where at least the pressure is

fixed at the boundary but all other variables may adapt values at the boundary according to the flow and transport of fluid phases and mass components across the boundary. However, this is strictly-speaking not a boundary condition and it requires to have a monotonic flux of the components or phases in outward direction which may be not always guaranteed.

While we will again take up the previous discussion for complex compositional models later in Sec. 5.3 and in Chapter 6, we comment in the following on the problem of boundary condition assignment for a two-phase system with a (p_w, S_n) formulation, cf. *Grass* (2005) [72]. In general, boundary conditions are assigned to all variables in the vector of unknowns. In case of the (p_w, S_n) formulation these are the wetting phase pressure p_w and the non-wetting phase saturation S_n. Dependent on the multiphase system to be numerically simulated it may be an unbearable limitation to have only these two variables available for the description of the boundary. For example, describing an atmospheric pressure condition demands to fix the non-wetting phase pressure p_n. This can be achieved by a recalculation of p_w via the capillary pressure function which in turn is a function of $S_w = 1 - S_n$. This yields the non-linear system $p_w - p_n + p_c(1 - S_n) = 0$ to be solved for p_w. Other combinations of secondary variables for the description of the boundary conditions can be found in a similar way. Since in some cases this requires iterative recalculation of the primary variables p_w and S_n this may lead to an inexact description of the boundary. Such problems could be avoided by adding more weight to the balance equations solved for the respective boundary node. This could be done, for example, by multiplying the balance equations at the boundary with large figures.

5.1.3 Linearization / Newton–Raphson Method

The multiphase flow differential equations are characterized by a high degree of nonlinearity predominantly caused by the relationships between the capillary pressure and the saturation as well as between the relative permeabilities and the saturation. Non-linear constitutive relations for fluid properties like density, viscosity, etc. further contribute to this. For multicomponent systems with mass transfer and energy exchange there are even more non-linear functional relations. For example, the specific enthalpy and the specific internal energy dependent on temperature and pressure, the saturation vapor pressure curve dependent on temperature, etc.

An iterative numerical non-linear solution of the coupled multiphase flow equations requires an appropriate linearization scheme. A commonly applied method in this context is the *Newton–Raphson* method which is explained in the following.

First, we write the system of multiphase flow differential equations given, for example, by Eqs. (5.6) and (5.7) in a simplified functional form:

$$\mathbf{F}(\mathbf{x}) = 0 \,, \tag{5.18}$$

where the vector $\mathbf{x}$ holds the primary variables p_w and S_n in case of the (p_w, S_n) formulation. Eq. (5.18) has to be solved for $\mathbf{x}$. A *Taylor* series expansion neglecting all terms higher than first order yields for the non-linear iteration step $m+1$ at time level $k+1$:

$$\mathbf{F}(\mathbf{x}^{k+1,m+1}) \approx \mathbf{F}(\mathbf{x}^{k+1,m}) + \left(\frac{\partial \mathbf{F}}{\partial \mathbf{x}}\right)_{k+1,m} \cdot (\mathbf{x}^{k+1,m+1} - \mathbf{x}^{k+1,m}) \tag{5.19}$$

As $\mathbf{F}(\mathbf{x}^{k+1,m+1})$ must become zero, we can transform Eq. (5.19) into

$$\mathbf{K}(\mathbf{x}^{k+1,m})\mathbf{u} = -\mathbf{F}(\mathbf{x}^{k+1,m}) \; . \tag{5.20}$$

Here, $\mathbf{K} = \partial\mathbf{F}/\partial\mathbf{x}$ represents the Jacobian matrix and $\mathbf{u} = \mathbf{x}^{k+1,m+1} - \mathbf{x}^{k+1,m}$ is the vector that holds the corrections of the primary variables. $\mathbf{F}(\mathbf{x}^{k+1,m})$ stands for the defect term at time level $k+1$ and non-linear iteration step m.

The Jacobian matrix can be computed exactly if the derivatives with respect to the primary variables can be found analytically. This is still feasible for the isothermal two-phase flow equations with constitutive relations derivable for the primary variables. However, with increasing complexity of the system equations this is no longer practicable. Instead, the Jacobian is computed by numerical differentiation. The coefficients K_{ij} are obtained by

$$\begin{aligned} K_{ij} &= \frac{\partial F_i^{k+1,m}}{\partial x_j^{k+1,m}} \\ &\approx \frac{F_i(...,x_{j-1},x_j+\Delta x_j,x_{j+1},...) - F_i(...,x_{j-1},x_j-\Delta x_j,x_{j+1},...)}{2\Delta x_j} \quad , \end{aligned} \tag{5.21}$$

where $\Delta x_j = \delta \cdot x_j$. Here, δ is a small increment, e.g. $\delta = 10^{-8}$.

We implemented the non-linear solution procedure with *Newton–Raphson* as follows:

Choose $x^{k+1,0}$; set $m = 0$;
while $((||F(x^{k+1,m})||_2 \,/\, ||F(x^{k+1,0})||_2 > \varepsilon_{nl}) \wedge (||F(x^{k+1,m})||_2 > abs_{nl}))$
{
  Solve $K(x^{k+1,m})u = -F(x^{k+1,m})$
    with accuracy ε_{lin} resp. abs_{lin};
  $x^{k+1,m+1} = x^{k+1,m} + \eta u$;
  $m = m + 1$;
}

In this algorithm, ε_{nl} and ε_{lin} are the accuracy criteria for defect reduction of the nonlinear and the linear solution respectively. abs_{nl} and abs_{lin} are stopping criteria for the nonlinear and linear solver if the defect term adopts smaller absolute values. Note that the defect term is scaled with the values of the primary variables since they may be of different orders of magnitude. The defect is a global measure; thus, the stopping criteria are applied uniformly to all the components of the primary variable vector. $||\cdot||$ is the Euclidean vector norm. The damping factor $\eta = (1/2)^q$ is chosen such that

$$||F(x^{k+1,m+1})||_2 \leq \left[1 - \frac{1}{4}\left(\frac{1}{2}\right)^q\right] ||F(x^{k+1,m})||_2 \tag{5.22}$$

is valid for the smallest possible $q \in \{0,1,...,n_{ls}\}$ with the maximum number of line search steps n_{ls} being between 4 and 6. A time-step reduction is applied if no such q can be found. For details, see *Bastian* (1999) [9].

$$Ku = f \tag{5.23}$$

is the Jacobian system to be solved by a linear solver. The numerical simulator MUFTE_UG, which is the basis of all our development work on multiphase flow models, includes a number of different direct and iterative linear solvers. We discuss the application of a multigrid preconditioner combined with an iterative BiCGStab solver later in Sec. 5.5.

5.2 Discretization

5.2.1 General Introduction and Overview

In this section, we want to focus on the discretization of the coupled non-linear multiphase flow equations. There is already a large number of methods available which were individually designed for dealing with distinct numerical difficulties occuring in the simulations. In general, the multiphase flow equations describe an advection-diffusion problem. Depending on the relevant physical processes, the characteristics of the equations can be shifted towards advection respectively diffusion. Diffusive effects are enhanced, for example, by capillary pressure, by concentration gradients, temperature gradients, etc.; advective problems are given typically during infiltration, displacement, and non-diffusive transport processes.

The hyperbolic character of *advection-dominated problems* is taken into account by the global pressure–saturation formulation (see Sec. 5.1.1.3). There, the equations are solved sequentially. First, the pressure equation is solved implicitly in time for the global pressure yielding a pressure and a velocity field. Given this, the saturation equation is solved explicitly in time yielding the new saturation distribution. However the explicit solution of the advection-dominated saturation equation is a challenging task. Standard finite-difference, finite-elements, and finite-volume methods reveal severe numerical problems like non-physical oscillations or strong sensitivity to the orientation of the grids. These problems could be reduced by higher-order time discretization schemes but going along with a lack of stability which in turn requires time-step restrictions.

Other methods are aimed at combining the temporal and spatial derivatives and obtaining a 'directional' derivative by considering the characteristics of the advective (hyperbolic part). There exist different schemes based on the *methods of characteristics*, for example, the *MMOC* (Modified Method Of Characteristics) [49] or the *ELLAM* scheme (Eulerian-Lagrangian Localized Adjoint Method) [148, 25, 123]. A recent publication [170] describes the application of a sequential operator splitting to advection-dominated and non-linear two-phase problems. There, a finite-volume method with slope limiter is used for the advective step while mixed hybrid finite-elements are applied to the elliptic global pressure equation and to the capillary diffusion term.

Another higher order scheme is the *discontiuous Galerkin method* [10]. This technique yields an accuracy comparable to a mixed finite-element method and shows a higher-order convergence behavior. It is applicable to unstructered meshes and is robust also to highly discontinuos coefficients. Like all higher order schemes, this method requires a slope limiter in order to obtain monotonicity. However, it seems that there is presently no experience with discontiuous Galerkin methods in the field of complex multiphase multicomponent systems.

For the problems we focus on in this work it is essential to use robust multi-dimensional discretization methods that cover a wide range of characteristic properties. In general, gas-liquid flow processes are also subject to strong non-linearities resulting from constitutive relations both for hydraulic and fluid properties as well as from compressibility effects. Thus, we prefer a fully coupled and fully implicit solution of the equations using mass-conservative finite-element based schemes derived from the principle of weighted residuals (see Sec. 5.2.3). The non-linearities are treated with a *Newton* method (see Sec. 5.1.3).

5.2.2 Time Discretization

In general, the system of multiphase multicomponent flow equations represents a transient problem which is parabolic in time. Thus, a time-stepping scheme forward in time is required to solve this. Different types of temporal discretization methods can be distinguished according to

- the approach in space and time:
  - Space-time finite-elements approximate the time-derivative of a variable

    $$\tilde{e}_i = \hat{e}_i N_i(\mathbf{x},t)$$

    at node i by

    $$\frac{\partial \tilde{e}_i(\mathbf{x},t)}{\partial t} = \frac{\partial(\hat{e}_i N_i(\mathbf{x},t))}{\partial t} = \hat{e}_i \frac{\partial N_i(\mathbf{x},t)}{\partial t} \tag{5.24}$$

    where $N(\mathbf{x},t)$ stands for a shape or weighting function in space and time that is multiplied with the discrete nodal values $\hat{e}$. Obviously, this requires a large system of equations to be solved which is a clear disadvantage of this method.
  - Semi-discrete methods discretize spatial and temporal derivatives separately. For example, the partial differential equations can be spatially discretized with a finite-element method while the occuring temporal derivatives are replaced by finite-differences:

    $$\frac{\partial \tilde{e}_i(\mathbf{x},t)}{\partial t} = \frac{\partial(\hat{e}_i N_i(\mathbf{x}))}{\partial t} = \frac{\hat{e}_i^{k+1} - \hat{e}_i^{k}}{\Delta t} N_i(\mathbf{x}) \tag{5.25}$$

    Here, the shape or weighting functions N are only spatial.
- the time-level on which the spatial derivatives are computed:
  - Implicit methods evaluate the a-priori unknown spatial derivatives on the new time-level. This results in general in an iterative procedure where a coupled system of equations must be solved. Implicit methods are unconditionally stable and have no stability-motivated restriction of time-step sizes.

    The transient flow equations can be formally written as

    $$\frac{\partial e}{\partial t} = A e\,, \tag{5.26}$$

where A stands for an operator containing the coefficient functions including the spatial derivatives. Then, an implicit scheme is given by

$$\frac{e^{k+1}-e^{k}}{\Delta t} = A^{k+1}e^{k+1}. \tag{5.27}$$

Here, A may contain coefficients which are dependent on the values of e on time-level $k+1$.

For the problems we address within the frame of this work Eq. (5.27) describes the applied fully implicit backward Euler method.

– Explicit methods take the already known solutions of the old time-level to compute the coefficients and spatial derivatives. Thus, the values on the new time-level can be obtained directly. For stability reasons, the time-step size is restricted according to the *Courant* criterion:

$$\mathrm{Cr} = \frac{|v|}{\Delta x/\Delta t} \leq 1 \quad \rightarrow \Delta t \leq \frac{\Delta x}{|v|} \tag{5.28}$$

Expressed in words, the *Courant* criterion means that there exists a true space-time domain of dependence in the real problem which must be completely within the numerical domain of dependence. Otherwise there exist points of which initial data would not effect the numerical solutions and a convergence to the true solution of the real problem is not possible.

Explicit schemes can be written as

$$\frac{e^{k+1}-e^{k}}{\Delta t} = A^{k}e^{k}. \tag{5.29}$$

LeVeque (1992) [107] gives a detailed overview of different explicit and implicit methods like, for example, backward Euler, Lax-Friedrichs, Lax-Wendroff, Leapfrog, etc., which can be distinguished by their stencils, i.e. the grid points that are involved in the computation of e^{k+1}.

– Mixed methods like, for example, the *Crank-Nicholson* method use both the new time-level and the old (known) level.

$$\frac{e^{k+1}-e^{k}}{\Delta t} = \theta A^{k+1}e^{k+1} + (1-\theta)A^{k}e^{k} \tag{5.30}$$

Here, θ is the *Crank-Nicholson* factor with values between 0 and 1. For $\theta = 0.5$ one obtains a scheme of second order according to the *Taylor* series expansion.

Other higher-order time-discretization methods use the solution of one or more time-levels and often also the new unknown level such that the advantages of stable implicit methods are combined with more accurate higher-order methods. However, these methods very often tend to produce oscillating solutions, and they are computationally costly and require more memory.

- the required steps to get from an old to a new time level:
  - Single-step methods do the computation of the solution on the new time-level in a single step. Both explicit and implicit methods can be single-step schemes as described above.
  - Multi-step methods split the computation of a new time-step into two or more steps. For a higher order of consistency multi-step methods often use more than only the solutions of one time-level to compute a new level.
    Also operator splitting methods as, for example, to consider advective and diffusive terms separately can be seen as multi-step methods [170].

5.2.3 Spatial Discretization with Finite-Volume Methods

In the following, we present two spatial discretization methods which both behave like finite-volume methods since they are based on updating grid cell averages dependent on fluxes through the boundary of the cells, cf., e.g. *Hirsch* (1988) [85]. We derive the BOX method and the Control-Volume-Finite-Element (CVFE) method using the two-phase flow equation (5.6) for the wetting phase.

5.2.3.1 The Weighted Residual Method

Basically, the weighted residual method assumes that the numerical solution of the partial differential equation can be expressed as

$$\tilde{\mathbf{x}} = \sum_{i=1}^{n_{no}} \hat{\mathbf{x}}_i N_i \,, \tag{5.31}$$

where N_i stands for a interpolation function (or: shape function) at a discrete nodal point i. n_{no} is the number of nodes in the discretized domain. Applying the assumption above to the (p_w, S_n) formulation of the two-phase flow equation yields

$$\tilde{p}_w = \sum_{i=1}^{n_{no}} \hat{p}_{w,i} N_i \,, \qquad \tilde{S}_n = \sum_{i=1}^{n_{no}} \hat{S}_{n,i} N_i \tag{5.32}$$

The order of the approximation is determined by the order of the shape functions. A common choice is the assumption of linear shape functions obeying the following conditions:

$$N_i(x_k) = \delta_{ik} = \begin{cases} 1 & \text{for } i = k \\ 0 & \text{for } i \neq k \end{cases} \,. \tag{5.33}$$

Here, n_{no} is the number of discrete nodal points (nodes) in the model domain and δ_{ik} stands for the *Kronecker* symbol. The above assumption for the shape functions defines that non-zero values only occur in the part of the domain that is confined by the set of neighboring nodes η_i to node i. With the choice of shape functions according to Eq. (5.33), we can interpret the discrete values $\hat{p}_{w,i}$ and $\hat{S}_{n,i}$ at node i as the *real* values of the pressures/saturations.

Inserting Eqs. (5.32) into the two-phase flow equation (5.6) leaves a global residual ε on the right-hand side:

$$\sum_{i=1}^{n_{no}} \frac{\partial(\phi \hat{S}_{n,i} N_i \rho_w)}{\partial t} - \nabla \cdot \left\{ \lambda_w \rho_w \mathbf{K} \cdot \left(\sum_{i=1}^{n_{no}} \hat{p}_{w,i} \nabla N_i - \rho_w \mathbf{g} \right) \right\} - \rho_w q_w = \varepsilon \tag{5.34}$$

Presuming that the vector of gravitation $\mathbf{g} = (0, 0, g)$ acts only in vertical direction (z-coordinate), a further modification of Eq. (5.34) can be written as:

$$\sum_{i=1}^{n_{no}} \frac{\partial(\phi \hat{S}_{n,i} N_i \rho_w)}{\partial t} - \nabla \cdot \left\{ \lambda_w \rho_w \mathbf{K} \cdot \left(\sum_{i=1}^{n_{no}} \hat{p}_{w,i} - \rho_w g \sum_{i=1}^{n_{no}} \hat{z}_i \right) \nabla N_i \right\} - \rho_w q_w = \varepsilon \tag{5.35}$$

Introducing the total potential

$$\hat{\Psi} := \hat{p} - \rho g \hat{z} \,, \tag{5.36}$$

where $\hat{z}$ is the geodetic height, we simplify this to

$$\sum_{i=1}^{n_{no}} \frac{\partial(\phi \hat{S}_{n,i} N_i \rho_w)}{\partial t} - \nabla \cdot \left\{ \lambda_w \rho_w \mathbf{K} \cdot \sum_{i=1}^{n_{no}} \hat{\Psi}_{w,i} \nabla N_i \right\} - \rho_w q_w = \varepsilon \tag{5.37}$$

The discrete values of the primary variables at the nodes have to be found such that the residual ε is minimized. In case of the exact solution ε becomes zero. For the weighted residual method the discrete nodal values $\hat{\mathbf{x}}$ are determined in such a way that a weighted local average of the residual vanishes. A number of different weighting methods can be found in the literature, an overview is given, for example, by *Bathe* (1982) [12].

- The *Galerkin method* introduces the shape functions N as weighting functions for the residual. Then, the solution in the (sub-)domain Ω associated with node i has to fullfill the condition that

$$\int_{\Omega} N_i \, \varepsilon \, d\Omega = 0 \qquad i = 1, 2, ..., n_{no} \,. \tag{5.38}$$

- The *least-squares method* minimizes the integral of the square of the residual ε with respect to the unknowns $\hat{\mathbf{x}}_j$:

$$\frac{\partial}{\partial \hat{\mathbf{x}}_j} \int_{\Omega} \varepsilon^2 \, d\Omega = 0 \qquad i = 1, 2, ..., n_{no} \,. \tag{5.39}$$

- The *point collocation method* sets the residual to zero at n_{no} points in the domain. This yields a system of equations to be solved for the unknowns $\hat{\mathbf{x}}_j$.

- The *subdomain collocation method* presumes a subdivision of the model domain. The integral of the residual in the subdomains is set to zero yielding a similar system of equations to be solved as in the point collocation method.

The BOX and the CVFE method that we derive below are based on a subdomain collocation resp. a modified Galerkin approach. Before we distinguish between both methods, we introduce the weighting function W in general and reformulate Eq. (5.38) to

$$\int_{\Omega} W_i \, \varepsilon \, d\Omega = 0 \qquad i = 1, 2, ..., n_{no} \,. \tag{5.40}$$

The weighting functions fulfill the general condition that the sum of all values of the weighting functions W_i at a node k equals 1. Typically, the weighting functions W_i have only very local influence (collocation), limited to the set of neighboring nodes of i. If W_i is chosen such that it equals 1 at node i and 0 at any neighboring node j, then the integrals need not to be evaluated in the entire domain, but only in a subdomain around i which is confined by the set of neighboring nodes $j \in \eta_i$.

Combining Eqs. (5.37) and (5.40) as well as applying an implicit time-discretization scheme according to Eq. (5.27) yields for each finite sub-space with node i in its center:

$$\begin{aligned}
&\frac{1}{\Delta t} \sum_{j \in \eta_i} \int_{\Omega_i} W_i N_j \, d\Omega_i \left[(\phi \hat{S}_n \rho_w)_j^{k+1} - (\phi \hat{S}_n \rho_w)_j^k \right] \\
&- \int_{\Omega_i} W_i \nabla \cdot \left\{ \lambda_w^{k+1} \rho_w^{k+1} \mathbf{K} \cdot \sum_{j \in \eta_i} \hat{\Psi}_{w,j}^{k+1} \nabla N_j \right\} d\Omega_i - \int_{\Omega_i} W_i (\rho_w q_w)^{k+1} = 0 \,, \quad \forall i
\end{aligned} \tag{5.41}$$

In the following, we apply a *mass-lumping technique* to the so-called mass matrix M_{ij} given by

$$M_{ij} := \int_{\Omega_i} W_i N_j \, d\Omega_i \,. \tag{5.42}$$

The mass-lumping allows a discretization in a finite volume form. All coefficients of a row in the mass matrix are lumped to the diagonal position of the matrix. Then, the lumped mass matrix can be written as

$$M_{ij}^{lump} = \begin{cases} \int_{\Omega_i} W_i \, d\Omega_i = \int_{\Omega_i} N_i \, d\Omega_i =: V_i & \text{for } i = j \\ 0 & \text{for } i \neq j \end{cases} \,. \tag{5.43}$$

Celia & Binning (1992) [26] mentioned that mass-lumping can reduce the occurence of non-physical oscillatory solutions. Analogously, this can be applied to the source/sink term, resulting in

$$\int_{\Omega_i} (W_i \rho_w q_w) \, d\Omega_i =: (V_i \rho_w q_w) \,. \tag{5.44}$$

With these modifications we can rewrite the discretized equation as follows:

$$\begin{aligned}
&\frac{V_i}{\Delta t} \left[(\phi \hat{S}_n \rho_w)_i^{k+1} - (\phi \hat{S}_n \rho_w)_i^k \right] \\
&- \int_{\Omega_i} W_i \nabla \cdot \left\{ \lambda_w^{k+1} \rho_w^{k+1} \mathbf{K} \cdot \sum_{j \in \eta_i} \hat{\Psi}_{w,j}^{k+1} \nabla N_j \right\} d\Omega_i - V_i (\rho_w q_w)^{k+1} = 0 \,, \quad \forall i
\end{aligned} \tag{5.45}$$

5.2.3.2 BOX method and CVFE method

The integral in Eq. (5.45) has to be numerically evaluated. Physically, this integral represents the flux term $\mathcal{F}$. The BOX method and the Control-Volume-Finite-Element method deal with that

in two different approaches which is explained below. For more details, we refer here to *Helmig & Huber* (1998) [80].

First, the *Green-Gauss* theorem is applied to the integral. Accordingly the transformations are given by

$$\begin{aligned}
&\int_{\Omega_i} W_i \nabla \cdot \left\{ \lambda_w^{k+1} \rho_w^{k+1} \mathbf{K} \cdot \sum_{j \in \eta_i} \hat{\Psi}_{w,j}^{k+1} \nabla N_j \right\} d\Omega_i \\
&= \int_{\Omega_i} \nabla \left\{ W_i \lambda_w^{k+1} \rho_w^{k+1} \mathbf{K} \cdot \sum_{j \in \eta_i} \hat{\Psi}_{w,j}^{k+1} \nabla N_j \right\} d\Omega_i - \int_{\Omega_i} \nabla W_i \left\{ \lambda_w^{k+1} \rho_w^{k+1} \mathbf{K} \cdot \sum_{j \in \eta_i} \hat{\Psi}_{w,j}^{k+1} \nabla N_j \right\} d\Omega_i \\
&= \int_{\Gamma_i} W_i \, \lambda_w^{k+1} \rho_w^{k+1} \mathbf{K} \cdot \sum_{j \in \eta_i} \hat{\Psi}_{w,j}^{k+1} \nabla N_j \cdot \mathbf{n}_{\Gamma_i} \, d\Gamma_i - \int_{\Omega_i} \nabla W_i \left\{ \lambda_w^{k+1} \rho_w^{k+1} \mathbf{K} \cdot \sum_{j \in \eta_i} \hat{\Psi}_{w,j}^{k+1} \nabla N_j \right\} d\Omega_i
\end{aligned} \tag{5.46}$$

The BOX and CVFE methods differ in the way the two integrals on the right-hand-side of Eq. (5.46) are treated.
For the BOX scheme, weighting functions being piecewise constant in the boxes (subdomain collocation) are chosen according to

$$W_i = \begin{cases} 1 & \text{in box } B_i \\ 0 & \text{else} \end{cases} \tag{5.47}$$

which leaves that $\nabla W_i = 0$ and the integral over the volume Ω_i vanishes. Thus, only the integral along the boundary Γ_i has to be considered further. Γ_i represents here the boundary ∂B_i of a box B_i. The construction of the boxes is illustrated in Fig. 5.1 for 2D elements. The extension to 3D is straightforward.

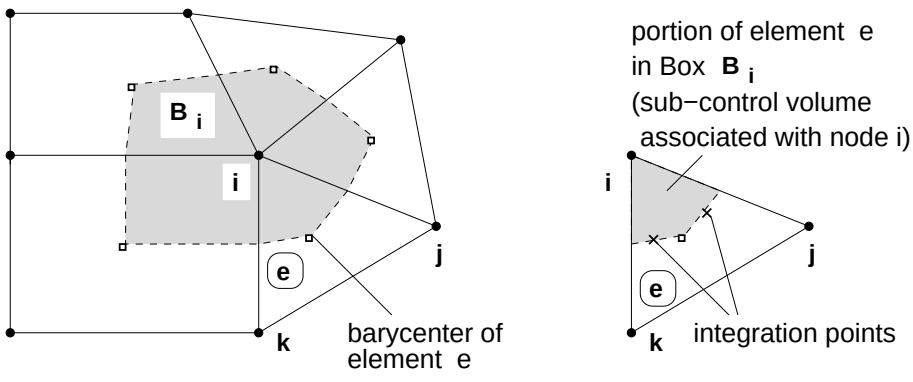

Figure 5.1: Box construction in a 2D finite-element mesh.

With $\nabla(\sum_j N_j) = 0$, it holds that

$$\nabla \left(\sum_j \hat{\mathbf{x}}_j N_j \right) = \sum_{j \neq i} (\hat{\mathbf{x}}_j - \hat{\mathbf{x}}_i) \nabla N_j \, . \tag{5.48}$$

Applying this to the boundary integral (flux term, here for the wetting/water phase) yields for the BOX method

$$\mathcal{F}_w^{\text{box}} := \sum_{j \in \eta_i} (\lambda_w \rho_w)^{k+1}_{\text{upw}(i,j)} \int\limits_{\partial B_i \cap \partial B_j} \mathbf{K} \cdot (\nabla N_j)_{\text{ip}} \cdot \mathbf{n}_{\partial B_i} \, dB_i \left(\hat{\Psi}^{k+1}_{w,j} - \hat{\Psi}^{k+1}_{w,i} \right) \tag{5.49}$$

Practically, the total flux from neighboring boxes j into box i is calculated as the sum of all fluxes between the subcontrol volumes associated with nodes j and i. As can be seen from Fig. 5.1, two nodes j and i have in general common interfaces between associated subcontrol volumes in more than one element.
The index $upw(i,j)$ indicates that the coefficients for the advective (hyperbolic) flux term are evaluated at the respective upstream node. This technique is commonly referred to as *Fully–Upwind method* (e.g. *Helmig*, 1997 [78]; *LeVeque*, 1992 [107]). In general, this produces more stable and non-oscillating solutions. However, sharp fronts tend to be smeared out (numerical diffusion).

The upwind node for phase α is identified by the following condition:

$$\text{upw}(i,j) = \begin{cases} i \text{ for } \gamma_{ij}(\hat{\Psi}_{\alpha,j} - \hat{\Psi}_{\alpha i}) \leq 0 \\ j \text{ for } \gamma_{ij}(\hat{\Psi}_{\alpha,j} - \hat{\Psi}_{\alpha i}) > 0 \end{cases} \tag{5.50}$$

with the transmissivity integral γ_{ij}, which is given for the BOX method by

$$\gamma_{ij}^{\text{box}} = \int\limits_{\partial B_i \cap \partial B_j} \mathbf{K} \cdot (\nabla N_j)_{\text{ip}} \cdot \mathbf{n}_{\partial B_i} \, dB_i \quad . \tag{5.51}$$

$(.)_{\text{ip}}$ indicates the evaluation at the integration points (see Fig. 5.1).

The Control-Volume-Finite-Element method (CVFE) employs a different approach for the weighting functions by using

$$W_i = N_i \qquad \forall i \, . \tag{5.52}$$

For the CVFE method, the remaining integral from the right-hand-side of Eq. (5.46) is the volume integral whereas the boundary integral equals zero due to local mass conservativity. Using further Eq. (5.48), we can rewrite the volume integral (flux term) as follows:

$$\mathcal{F}_w^{\text{cvfe}} := - \sum_{j \in \eta_i} (\lambda_w \rho_w)^{k+1}_{\text{upw}(i,j)} \int\limits_{\Omega_i} \nabla N_i \cdot \mathbf{K} \cdot \nabla N_j \, d\Omega_i \left(\hat{\Psi}^{k+1}_{w,j} - \hat{\Psi}^{k+1}_{w,i} \right) \tag{5.53}$$

The evaluation of upwind nodes occurs according to Eq. (5.50) while the transmissivity integral for the CVFE method is given by

$$\gamma_{ij}^{\text{cvfe}} = \int\limits_{\Omega_i} \nabla N_i \cdot \mathbf{K} \cdot \nabla N_j \, d\Omega_i \quad . \tag{5.54}$$

This CVFE method is described earlier by *Letniowski & Forsyth* (1991) [106]. They remark that the transmissivity integral can take negative values for unpropitous element geometries (side

length ratio). Since this produces numerical oscillation during the non-linear iteration process, they suggest to introduce a positive transmissibility condition, i.e. to avoid negative γ_{ij}. This is also mentioned by *Huber & Helmig* (2000) [90], *Helmig & Huber* (1998) [80], and *Helmig* (1997) [78].

Both for $\mathcal{F}_w^{\text{box}}$ and $\mathcal{F}_w^{\text{cvfe}}$ the permeability tensor $\mathbf{K}$ represents the harmonic mean of the two associated nodal permeability tensors.

For rectangular meshes, the CVFE method is characterized by its 9-point stencil which shows less grid orientation effects than the 5-point stencil of the BOX scheme. This was investigated for both a homogeneous and a heterogeneous porous medium in *Class* (2001) [30]. However, the BOX method as it is described above is not a pure 5-point scheme since the evaluation of velocities and shape functions is done at the integration points. Thus, an influence of all neighboring nodes is given.

5.3 Primary Variables for Compositional Models

As we discussed already in Sec. 5.1, the choice of appropriate primary variables for which the systems of partial differential equations are solved is a key issue for the solution process and the behavior of the solutions. While we focused then on mathematical aspects and the characteristic properties of the two-phase flow advection-diffusion equation, we will draw our attention now on compositional models with varying phase states. Here, we define a *phase state* as a distinct set of separate fluid phases within an *REV*. A phase state can locally change as a result of phase appearance or disappearance.

5.3.1 Degrees of Freedom according to the Gibbs Phase Rule

The thermodynamical state of a multiphase multicomponent can be uniquely described by a set of state variables. The number of required state variables is determined by the number of degrees of freedom which is given by the *phase rule* according to *Gibbs*, see Sec. 3.2.2.1, Eq. (3.78) and its modification for porous media flow above the REV-scale, Eq. (3.79).

The number of degrees of freedom then is $\mathrm{F} = \mathrm{C} - \mathrm{P} + 2$ which holds in general for non-isothermal multiphase multicomponent systems. Many multiphase models for flow in porous media assume isothermal conditions. This reduces the degrees of freedom by 1 and leaves F = C.

After determining the number of degrees of freedom F by the model assumptions, it is necessary to choose a set of F primary variables. The choice of the primary variables affects the numerical solution procedure. For the isothermal two-phase flow equations, this was already discussed in Sec. 5.1.1.

In the following we extend this discussion to non-isothermal multicomponent models where the choice of the primary variables is predominantly motivated by the local phase state and the

processes leading to appearance or disappearance of phases.

5.3.2 Primary Variable Substitution

Models for simulating non-isothermal processes, for example, in water-gas-NAPL systems should typically consider the disappearance and appearance of phases. In the majority of cases, these models are applied to NAPL recovery problems including thermally enhanced remediation. Thus, the disappearance of the NAPL phase after the clean-up and the re-condensation/appearance of NAPL in cooler regions is the main issue to be addressed. The disappearance of liquid water is relevant in regions where superheated steam is injected or where thermal wells with very high temperatures lead to a complete evaporation of the liquids. Different authors worked already on the development of switching criteria for primary variables concerning NAPL remediation problems, cf. [65, 89, 59]. Most of these models check after each Newton iteration step if the primary variables can still describe the thermodynamic state or if a change of the phase state occured somewhere in the solution domain. A principle of such an algorithm is illustrated in Fig. 5.2.

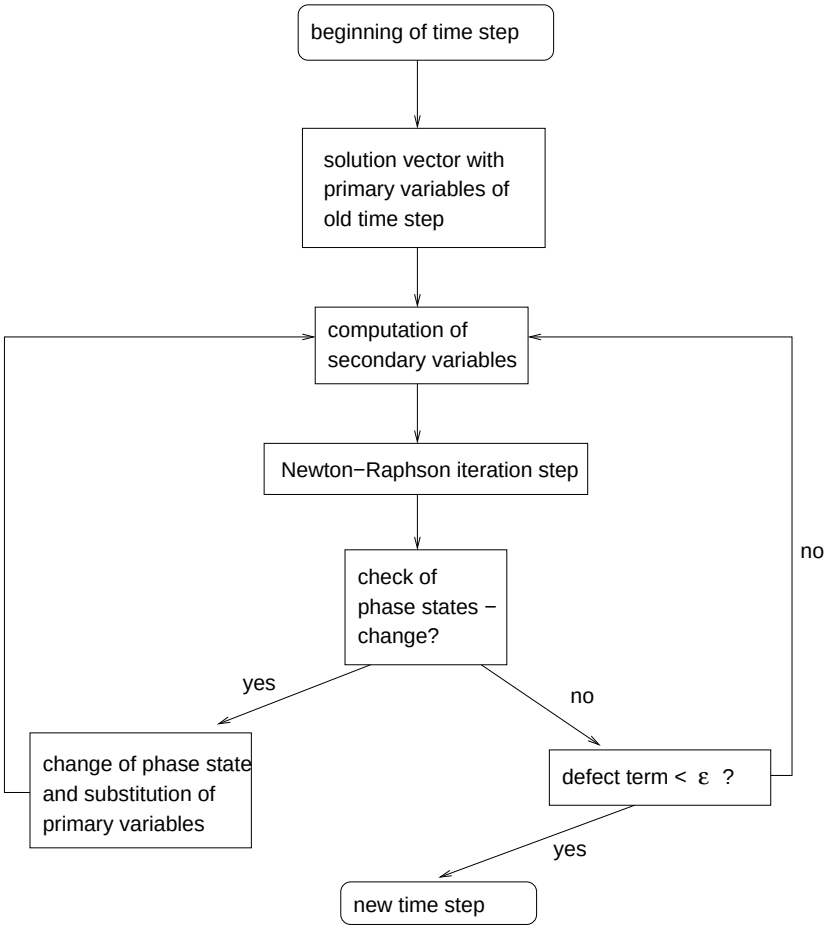

Figure 5.2: Algorithm for the substitution of the primary variables during the non-linear solution process.

A check of the phase states and primary variables after each Newton step ensures that the model

does not converge with a wrong phase state after a non-linear solution process. However, an overshooting and oscillations of the primary variables in an earlier stage of the iteration process before convergence is achieved may lead to a premature indication of a change of the phase state. In this case, this costs significant computation time since due to the premature substitution the ongoing iterations will lead to a resubstitution and a reduction of the time step size. This dilemma can be avoided when the substitution of the primary variables is done after achieved convergence in the Newton solver. The disadvantage of this method is the temporary acceptance of non-physical conditions during the non-linear solution process which are then corrected by the primary variable substitution. Also the conservation of mass is locally not assured when primary variables are substituted by others which have to be initialized with new unknown values.

A crucial issue concerning the robustness of a primary variable substitution algorithm is the definition of appropriate substitution criteria. For disappearing phases this can be easily indicated by negative values of the phase saturations whereas the appearance of phases requires a closer inspection of the physical processes behind. For example, the appearance of a liquid phase resulting from the condensation of the corresponding component can be indicated by comparing the partial pressure of the component in the gas phase with the saturation vapor pressure. If the partial pressure exceeds the saturation vapor pressure, then condensation occurs and a liquid phase is formed. Another typical case is the degassing of dissolved gas components, for example, due to pressure lowering. To indicate this in the algorithm one must compare the dissolved amount of an component with the maximum solubility.

5.3.3 Primary Variables for Non-Isothermal Water-Gas-NAPL Systems

Tab. 5.1 lists the primary variables that we choose for our non-isothermal three-phase three-component concept [35, 34, 30]. As already mentioned above, for typical scenarios in the context of thermally enhanced remediation of NAPL-contaminated soils it is important to model the disappearance and (re-)appearance of the NAPL phase. Thus, phase states NWG and WG (see Tab. 5.1) occur most frequently. For high-temperature techniques where also liquid water can fully evaporate it is further necessary to include state G with only the gas phase remaining. Temperatures beyond the boiling temperatures of the liquids can only occur in phase state G - only gas.

Table 5.1: Non-isothermal three-phase three-component model: phase states, corresponding primary variables, and criteria for the substitution in the case of phase appearance

phase state	present phases	primary variables	appearance of phase		
			water	NAPL	Gas
NWG	w,n,g	S_w, S_n, p_g, T	-	-	-
NG	n,g	S_n, x_g^w, p_g, T	$x_g^w p_g > p_{sat}^w$	-	-
G	g	x_g^c, x_g^w, p_g, T	$x_g^w p_g > p_{sat}^w$	$x_g^c p_g > p_{sat}^c$	-
WG	w,g	x_g^c, S_w, p_g, T	-	$x_g^c p_g > p_{sat}^c$	-

An example for a local change of the phase is illustrated in Fig. 5.3. The situation depicted

there could occur, for example, due to a steam-injection on the left-hand side of the quadrilateral element. Then a steam front would propagate through the system in x-direction. When the front reaches the element, the temperature increases. Since there is NAPL present in liquid phase, the temperature can only rise up to the boiling temperature of the water-NAPL mixture (see Sec. 4.1). In the following, the liquids evaporate and after some time ($t_0 + \Delta t$ the NAPL phase disappears (since we assume it to exist at a small initial saturation relative to water and/or the injected steam is not superheated). After the local disappearance of liquid NAPL, the temperature can increase further to the boiling temperature of pure water since now the vapor pressure is built-up only by the water component.
Applying the phase states and primary variables listed in Tab. 5.1, one can see that a change from NWG to WG occurs at the outer left corner of the element in Fig. 5.3. The NAPL saturation represents for $S_n = 0$ no independent variable, and must be replaced by the mole fraction of the NAPL component in one of the other phases (here: in the gas phase).

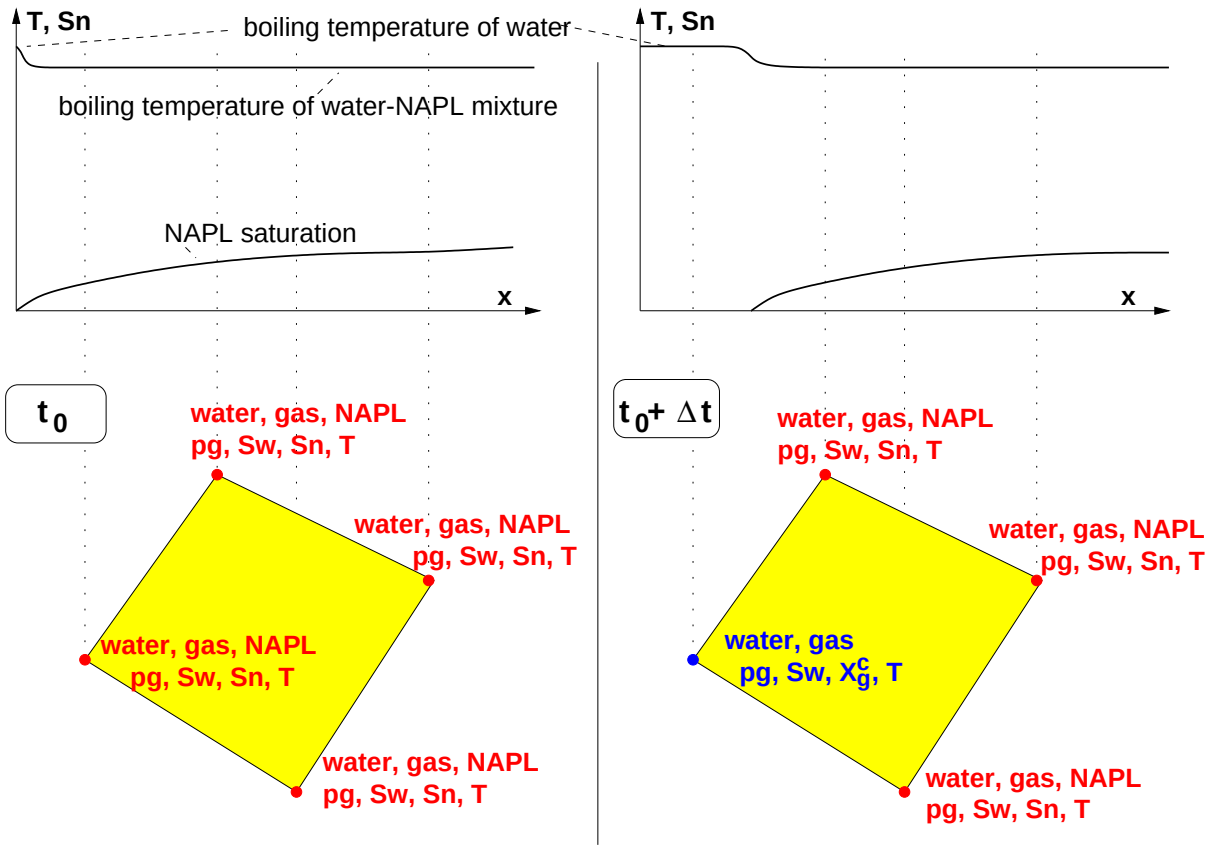

Figure 5.3: Process-adaptive substitution of primary variables after a local change of the phase state. Here, the NAPL phase disappeares at one node.

This concept works well and stable for processes in the unsaturated zone. If the saturated zone should be considered, for example, in case of a steam-injection below the water table, there appear some numerical difficulties which we will address in the following.

5.3.4 Primary Variables for modelling Steam-Injection in the Unsaturated and in the Saturated Zone

A special focus must be given to the mass balance of the air component when steam is injected into the saturated zone. Depending on the problem (initial and boundary conditions) it may occur that the component air disappears locally. We discussed this already in Sec. 4.2.2 and recall here the basic insights concerning the choice of the primary variables. If steam is injected or liquid water is boiling, the constitution of the gas phase approaches fully-steam conditions with the fraction of the air component going towards zero. If there is still a two-phase state with liquid water and gas (steam), the primary variables according to Tab. 5.1 are S_w, p_g, and T. Thus, the composition of the gas phase is calculated according to the saturation vapor pressure as a function of the temperature which leaves only very small values for the air mole fraction in the gas phase. Accordingly, using Henry's Law, the air mole fraction in the water phase is also very small. It is well-known, that if such small values for the air content in the phases are given in the domain, the numerical robustness can be affected by oscillations of the solution. This effect is described by *Ochs et al.* (2007) [131].
Another aspect in this context is that the primary variables p_g and T are practically not independent of each other if the air component disappears. Then p_g tends to equal the saturation vapor pressure and so becomes a function of the temperature. For problems that consider only steam-injection in the saturated zone, it is practical to neglect the air component and instead use a two-phase single-component model, cf. the work of *Ochs et al.* (2007) [131]. Then the following set of primary variables for the different phase states can be used:

Table 5.2: Non-isothermal two-phase single-component model for steam-injection in the saturated zone: phase states and corresponding primary variables

phase state	present phases	primary variables
W	w	p_w, T
G	g	p_g, T
WG	w,g	$p_g(T)$, S_w

If the unsaturated zone is included in the problem (see Fig. 4.8), we suggest to take the local displacement of the air component into account by switching off the mass balance equation in these zones. This can be achieved, for example, by setting the respective entries in the matrix and defect term in the equations to trivial values. However, this leaves the problem that a reappearance of air, for example, after the stop of the air-injection is difficult to indicate in the model.

5.3.5 Primary Variables for modelling CO_2-Sequestration

Dependent on the CO_2-sequestration scenario to be modeled, there are different characteristic phase state situations in a model domain. For example, it is typical for an injection scenario into a brine aquifer that initially the aquifer is fully saturated with the water phase (brine). Then, from the injection well a plume of CO_2 starts to grow and a two-phase region develops. The appearance of a CO_2 phase can be checked in the primary variable substitution algorithm by comparing

the amount of dissolved CO_2 in the brine (mass fraction $X_w^{CO_2}$) with the maximum solubility as a function of pressure, temperature, and salinity.

Bielinski (2006) [18] uses the primary variables and substitution criteria for phase appearance given in Tab. 5.3.

Table 5.3: two-phase two-component model for water and CO_2 including non-isothermal effects: phase states, primary variables, and substitution criteria

phase state	present phases	primary variables	water phase appears	CO_2 phase appears
Both phases	w, CO_2	S_w, p_{CO2}, T	–	–
Water phase	w	X_w^{CO2}, p_{CO2}, T	–	$X_w^{CO2} \geq (X_w^{CO2})_{\max}$
CO_2 phase	CO_2	X_{CO2}^w, p_{CO_2}, T	$X_{CO2}^w \geq (X_{CO2}^w)_{\max}$	–

There are obviously many questions and problems related to CO_2-sequestration in geologic formations that can be addressed by isothermal model concepts. In such cases, the temperature is not needed as a primary variable since the degrees of freedom are reduced by one according to *Gibbs* phase rule. However, for other issues the influence of thermal effects can be significant, for example, due to changes of fluid properties, in particular the variation of the CO_2 density according to temperature and pressure conditions (geothermal gradient, gas expansion).

5.3.6 Primary Variables for Systems with more than one Non-Condensible Gas Component

The multiphase multicomponent systems described above never included more than a single non-condensing component in the gas phase. At least, the air is not considered as a multicomponent species in the conceptual models. For such model concepts we can use the constraint that the sum of the mole fractions (or mass fractions) in each phase equals one (Eq. 3.62). If the other mole fractions in the gas phase, for the vapors of water and NAPL, can be calculated according to the saturation vapor pressure equilibrium as a function of temperature, then the gas mole fraction of air can be obtained by

$$x_g^a = 1 - x_g^w - x_g^c \,. \tag{5.55}$$

If the corresponding liquid phases are not present, the equilibrium assumption between liquids and vapor components is not applicable and the mole fractions x_g^w, x_g^c are chosen as primary variables (see Tab. 5.1) such that Eq. (5.55) still holds.

For compositional models with more than a single non-condensing component in the gas phase only one of the inert component mole fractions can be calculated analogously to Eq. (5.55). Thus, the other ones necessarily have to be treated as primary variables. Since these components do not form separate liquid phases, this concept agrees with the treatment of the condensible components in the gas phase. Their mole fractions are also taken as primary variables only

if their fraction is small enough that condensation and the existence of the corresponding liquid phase is not possible. In general, one can state that if n non-condensing components in the gas phase are given, then $n-1$ of their mole fractions need to be treated as primary variables. In cases, where locally the phase state W (only water) occurs, the respective mole fractions of these dissolved components in the water phase are taken as primary variables.

In Sec. 2.5 and 2.6, we already discussed the relevance to consider several inert components in the gas phase. While for the methane migration problems the air can still be treated as a pseudo-component, we need to distinguish between the air constituents oxygen and nitrogen for modelling the transport and consumption of oxygen in the gas-diffusion layer of a fuel-cell.

Table 5.4: Non-isothermal two-phase three-component model for modelling methane migration through unsaturated and saturated zones: phase states and corresponding primary variables

phase state	present phases	primary variables
W	w	x_w^a, x_w^m, p_w, T
G	g	x_g^w, x_g^m, p_g, T
WG	w,g	S_w, x_g^m, p_g, T

Tab. 5.4 lists a possible set of primary variables for a two-phase three-component system including the phase water and gas with the components water, air, and methane. In Tab. 5.5, we give the respective set for the fuel-cell problem, where also the two phases water and air including the components water, oxygen, and nitrogen are taken into account.

Table 5.5: Non-isothermal two-phase three-component model for modelling oxygen transport and consumption and the water management in the gas-diffusion layer of a fuel-cell: phase states and corresponding primary variables

phase state	present phases	primary variables
W	w	x_w^o, x_w^n, p_w, T
G	g	x_g^w, x_g^n, p_g, T
WG	w,g	S_w, x_g^o, p_g, T

We should note that the assumption of a gaseous component to be non-condensing is limited to a certain pressure range. If the pressure exceeds this range which obviously depends on the chemical species any gaseous component can reach the condensation pressure. In subsurface systems, the pressure typically increases with increasing depth. Thus, in deep formations we can observe, for example, CO_2 in its liquid or supercritical state, whereas at ambient environmental conditions one could assume it as a non-condensing gas.

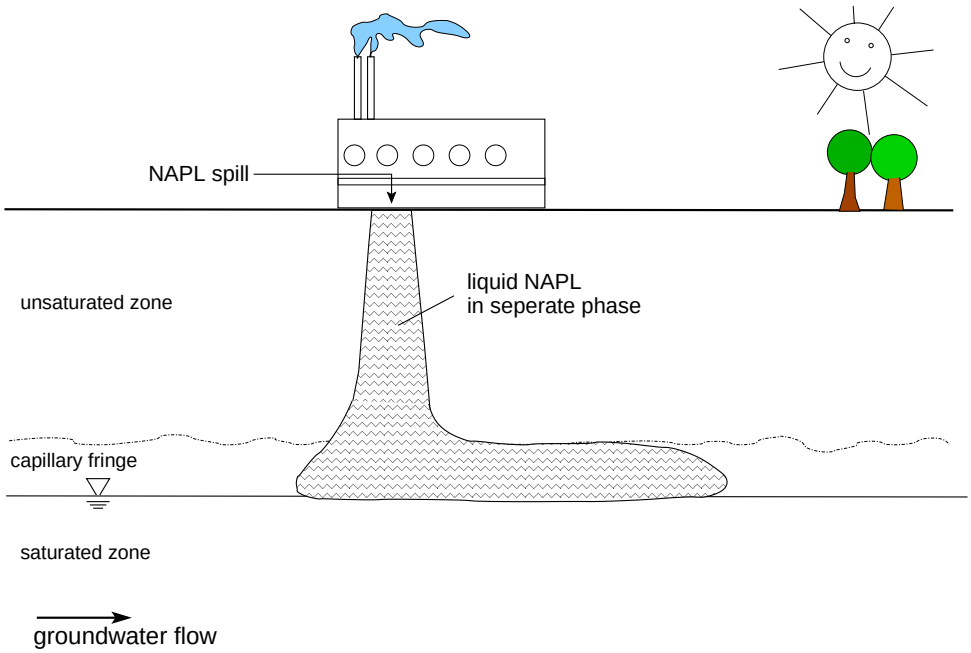

Figure 5.4: Multiphase system: spreading of liquid NAPL in the subsurface after a spill.

5.4 Modular Coupling of Model Concepts

In general, the development of model concepts is focused on certain types of problems. Thus, it is in the nature of a model that it is restricted in its applicability according to its underlying assumptions. For example, a multiphase model that does not take into account components as fractions of fluid phases is not able to reproduce compositional effects like dissolution, diffusive transport of components, etc. However, it may also be that a model concept is *over*sophisticated to be applied for relatively simple problems. An example therefore would be the infiltration and spreading of a very low miscible contaminant phase into the subsurface. Describing only the short-term phase spreading can be done without a compositional model if the long-term fate of the contaminant is out of interest. In the following, we use this example to motivate the coupling of an isothermal three-phase model (3p) with a non-isothermal three-phase three-component model (3p3cni). This will be illustrated in detail by the application example presented in Sec. 6.2. A comprehensive discussion of this coupling and the basic considerations about processes and their time-scales give *Class et al.* (2007) [36].

The 3p-model allows the simulation of a contaminant phase (NAPL) infiltration and the short-term phase spreading in the subsurface until the NAPL phase comes practically to rest. Such a situation is schematically depicted in Fig. 5.4. Here, a spill occured and NAPL seeps away into the subsurface. If the amount is limited the NAPL phase will come practically to rest after some time and stay in residual saturation. However the transport of the contaminant in the subsurface continues by diffusion of evaporated NAPL in the soil air and by advection/diffusion of dissolved NAPL in the groundwater. This is illustrated in Fig. 5.5. Although these processes occur on a larger time-scale than the spreading of the liquid NAPL phase before, they are nevertheless relevant to simulate the long-term impact of the NAPL contamination in the subsurface system for

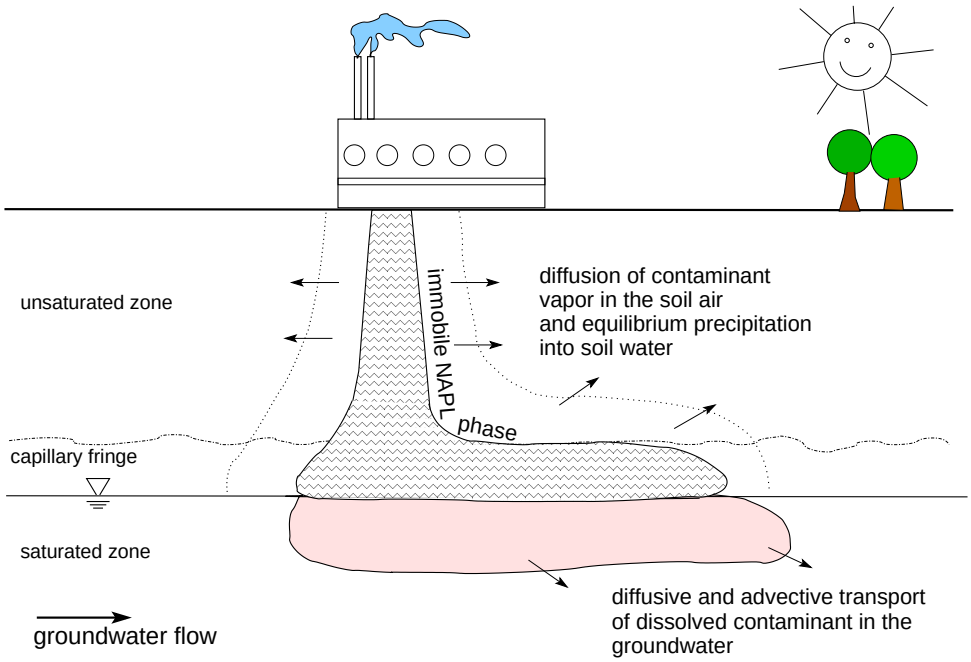

Figure 5.5: Multiphase multicomponent system: transport of evaporated and dissolved contaminant.

both the unsaturated and the saturated zones. Modelling these processes requires a multiphase multicomponent concept which is also necessary for the simulation of remediation scenarios. Thus, the 3p3cni-model can then be used to account for a thermally enhanced remediation with injection of steam, steam-air mixture, soil vapor extraction, or thermal wells.

The coupling algorithm concerns essentially the assignment of reasonable initial values to the primary variables of the 3p3cni-model after the restart from a previous 3p-simulation. It is assumed, that the primary variables in the 3p-model are given by

- the saturation of the water phase S_w,
- the saturation of the NAPL phase S_n,
- and the pressure of the gas phase p_g.

Note that there are obviously other possible choices of the primary variables in the 3p-model. However, the combination of two saturations and one pressure suggests itself. The primary variables of the 3p3cni-model are listed in Tab. 5.1. Since the 3p3cni-model distinguishes different phase states, it is further necessary to find criteria allowing the local assignement of phase states according to the results from the 3p-simulation. The algorithm applied for the primary variable transfer from the final 3p-result to the initial state of the 3p3cni-problem is given in the following pseudo-code (Page 136):

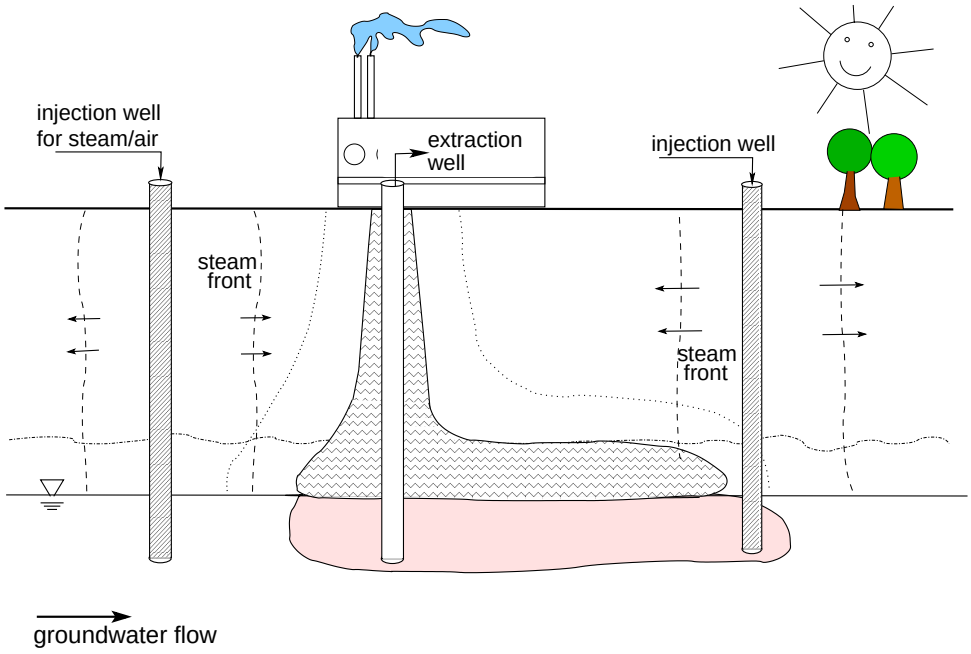

Figure 5.6: Non-isothermal multiphase multicomponent system: remediation scenarios, e.g., thermally enhanced soil vapor extraction.

set $T = T_{init} = const.$ in the whole model domain

if $(S_w > \varepsilon)$
{
  if $(S_n > \varepsilon)$
    $S_{n,new} = S_n$;
    state = NWG;
  else
  {
    $/*$ it is valid: $S_{n,new} = 0 */$
    $x_g^c = 1.E-10; /*$ arbitrary small value! $*/$
    state = WG;
  }
  $p_{g,new} = p_g$;
  $S_{w,new} = S_w$;
  if $(S_w == 1)$
  {
  $/*$ do not allow state W in 3p3cni-model $*/$
  $/*$ for the sake of robustness $*/$
  $S_{w,new} = 0.999$;
  }
}
else $/*$ only allow state G $*/$
{
  $p_{g,new} = p_g$;
    $x_g^w = 1.E-10; /*$ arbitrary small value! $*/$
    $x_g^c = 1.E-10; /*$ arbitrary small value! $*/$
  state = WG;
}

First, the temperature is set to an initial value which can not be derived from the isothermal 3p-results. Thus, we normally start the non-isothermal model with a constant temperature in the domain. Dependent on the saturations of the water and NAPL phases we then assign the saturations and phase states. However, for the sake of a more robust simulation we avoid phase states that are numerically not so stable. For example, if a phase state W was chosen, the time-step size becomes small due to premature switching trials of the primary variable substitution algorithm. For larger time-steps, the overshooting of the primary variable corrections during the

first non-linear iterations of a time-step triggers a switch of the phase state which actually should not yet occur.
Phase states with less than all three fluid phases have one or even two mole fractions in their set of primary variables. However, the assignment of values to the respective mole fraction is kind of arbitrary since no further information can be obtained from the given set of 3p primary variables.

Remark: The inconsistency of the primary variables is also a problem of the so-called *multi-scale modelling* where processes of varying complexity are considered in different parts of the model domain. *Niessner* (2006) [125] presents a concept to include local three-phase three-component processes in a subdomain, resolved on a finer scale and embedded by upscaling concepts into the larger scale two-phase problem. However, this concept requires that the mass conservation of the third component on the fine scale is not relevant on the larger scale where its mass can not be balanced.

5.5 Efficient Solvers Using Multigrid Methods

As we explained in Sec. 5.1.3, during the application of the iterative Newton–Raphson method one obtains a system of linearized equations (Eq. 5.23) to be solved by a direct or iterative linear solver. In general, the models that are presented in this work are rather complex which leads for realistic practical application very soon to a huge number of unknowns. Thus, it is essential to use fast and efficient solvers. For example, multigrid methods, c.f. [76], show an order of convergence, when applied to elliptic problems, independent of the discretization length. In other words, the costs for solving a system of linear equations increase proportional to the number of unknowns. *Bastian & Helmig* (1999) [11] showed, however without convergence proof, that also for the linearized fully-coupled two-phase flow equations a satisfactory performance of the multigrid method can be achieved. *Class et al.* (2002) [35] extended this to more complex multiphase flow equations including compositional effects and variable phase states. The following three subsections are a summary of the relevant explanations in that article.

5.5.1 Basic Multigrid Algorithm

Given by Eq. (5.23), the Jacobian system $Ku = f$ is to be solved. The hierarchy within the multigrid mesh structure leaves such a Jacobian system on each grid level l. The algorithm of a linear multigrid cycle requires mappings, so-called restriction R_l and prolongation P_l, for the interpolation between the grid levels. A V-cycle multigrid algorithm can then be written, for

example, as follows [9, 11, 35]:

mgc (l, u_l, f_l)
{
  if $(l == 0)\, u_0 = K_0^{-1} f_0$;
  else {
    Apply ν_1 smoothing iterations to $K_l u_l = f_l$;
    $d_{l-1} = R_l(f_l - K_l u_l)$;
    $e_{l-1} = 0$;
    mgc $(l-1, e_{l-1}, d_{l-1})$;
    $u_l = u_l + P_l e_{l-1}$;
    Apply ν_2 smoothing iterations to $K_l u_l = f_l$;
  }
}

For smoothing iterations, for example $\nu_1 = \nu_2 = 2$ ILU steps (incomplete decomposition, e.g. *Hackbusch* (1985) [76]) can be chosen.

5.5.2 Extended Prolongation Algorithm for Variable Phase States

Let e_{l-1}^m be the error, i.e. the deviation of u_{l-1}^m from the exact solution, on level $l-1$. Then, the coarse-grid correction can be written as an iteration of the form:

$$u_l^{m+1} = u_l^m + I_{l-1}^l e_{l-1}^m \,, \tag{5.56}$$

where matrix I_{l-1}^l describes the transfer (prolongation) between levels $l-1$ and l. For the prolongation of the coarse-grid corrections, it must be taken into account that different phase states mean different primary variables in the solution vectors. Thus, it may occur that the correction for a fine-grid node has to be interpolated from coarse-grid nodes with different phase states. Fig. 5.7 illustrates this case.
The figure shows a NAPL-contaminated subdomain, which is recovered by a steam/air injection. The subdomain is discretized with a coarse-grid element (1-2-3-4) or four fine-grid elements (I-II-III-IV; II-V-VI-III and so on). The NAPL-contaminated area represents a three-phase area and has phase state 1 (NWG). The area already cleaned up only contains the phases water and gas and therefore has phase state 6 (WG). Thus, the coarse-grid nodes 1, 2, and 4 have phase state WG, whereas node 3 still has NWG. We assume that the fine-grid node III has phase state WG. Then, the correction of the primary variables (p_g, S_w, x_g^c, T) can be interpolated directly from the coarse-grid nodes 1, 2, and 4. However, the vector of primary variables at node 3 contains x_g^c instead of S_n (phase state NWG). Thus, the correction value of coarse-grid node 3 for the primary variable S_n has to be transformed into a correction value for the primary variable x_g^c at fine-grid node III. This can be achieved by a linearization of the correction around the corresponding position in the solution vector in iteration m:

$$e^m|_{x_j} = f_{x_j}(u^m + e^m) - f_{x_j}(u^m) \,. \tag{5.57}$$

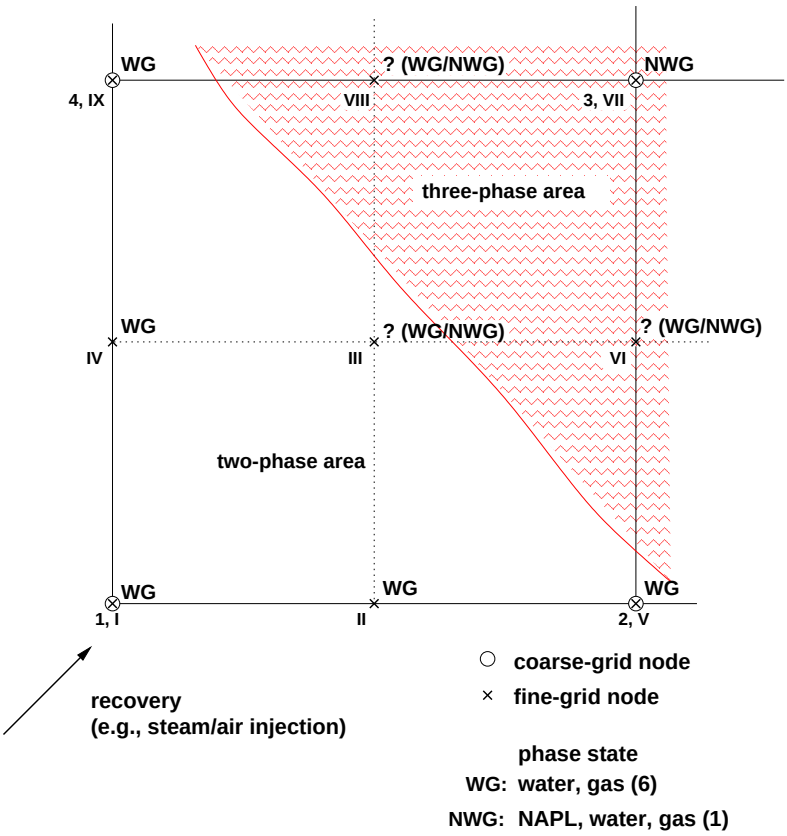

Figure 5.7: Prolongation dependent on the phase states.

$e^m|_{x_j}$ is the correction of variable x_j. f_{x_j} stands for the function or procedure by which x_j can be computed from the given primary variables. In the case of node III, $e^m|_{x_j}$ equals the correction value of variable x_g^c from the interpolation part of node 3. $e^m|_{x_g^c}$ at node 3 is computed using the functional $f_{x_g^c} = p_{sat}^c / p_g$.

The existence of a hierarchical grid system can be used for another efficient solution method. Applying *nested iterations* makes it possible to use approximate values for u_{l-1} from an iteration on grid level $l-1$ as starting values u_l for the iteration on grid level l. Thus, by improving the starting values, one obtains better iteration results, reducing the iteration steps necessary for a given accuracy. For large systems, this improved convergence behavior rapidly outweighs the apparently higher computational effort. Since a phase state must be assigned to every node, we need rules to determine the phase states of fine-grid nodes which are not part of the coarser grid. A look at Fig. 5.7 shows that fine-grid nodes I, V, VII, IX are identical with coarse-grid nodes 1, 2, 3, 4 and therefore inherit the respective phase states. For fine-grid nodes II, III, IV, VI, VIII, the phase states must be determined from the current state of the system. In a first approach, we evaluate the shape functions of the coarse-grid elements with respect to a given fine-grid node and take the phase state from the coarse-grid node with the highest shape function value. Doubt still remains as to whether the achieved determination of the respective coarse-grid node is unique (e.g. nodes III and VI in Fig. 5.7). Our next step in this context is to develop better criteria for assigning the phase states to fine-grid nodes, for example by evaluating the phase

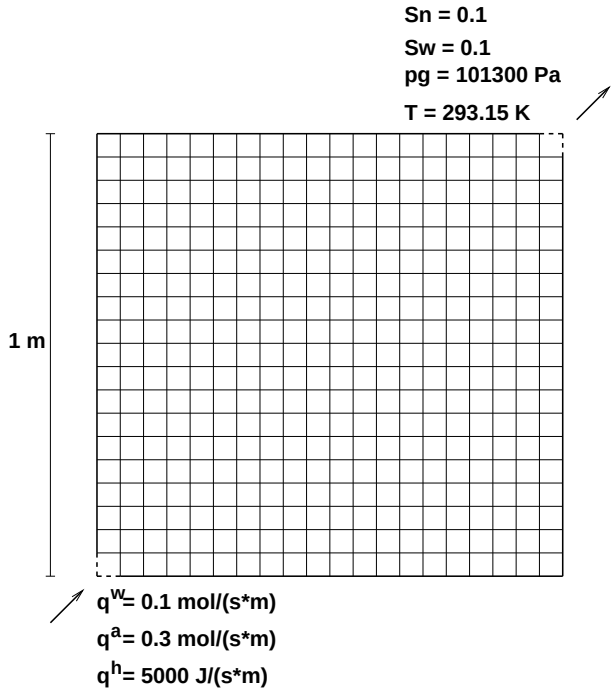

Figure 5.8: The fivespot problem (coarse grid: 400 elements)

velocities and transport rates around a node of interest.

5.5.3 Computational Performance Example

The multigrid method with the extensions for variable phase states, as explained above, was tested for a classical fivespot problem. It was applied as a preconditioner for an iterative BiCGStab solver and compared with a classical iteration method (ILU scheme).
Fig. 5.8 shows a two-dimensional horizontal (no gravity) model domain (1 m $\times$ 1 m). The coarsest grid used in the multigrid hierarchy is given with 400 quadratic elements. Any refinement of an element yields four quadratic elements on the next finer grid level (regular refinement [9]). The system is initially contaminated with NAPL in residual saturation. Furthermore, there is a water saturation slightly below residual saturation and atmospheric pressure at a temperature of 293.15 K. A steam/air mixture is injected (*Neumann* boundary condition) at the lower left-hand corner; at the upper right-hand corner, the system is open to the environment (*Dirichlet* boundary condition). The remaining boundary has no-flow properties, see Fig. 5.8. The initial conditions are the same as the *Dirichlet* conditions given in the upper right-hand corner (phase state 1: water, NAPL, and gas phases are present).

Fig. 5.9 shows the distribution of NAPL saturation and temperature after 3 hours of steam/air injection. One can see that the domain has been cleaned-up from the direction of the lower left-hand corner. The evaporated NAPL is transported within the gas phase towards the upper right-hand corner. When reaching the cooler regions, part of the NAPL vapor condenses such that the liquid NAPL phase accumulates, forming a peak of NAPL saturation. The temperature plot shows that in the subregion already cleaned-up an almost constant temperature of $\approx$330

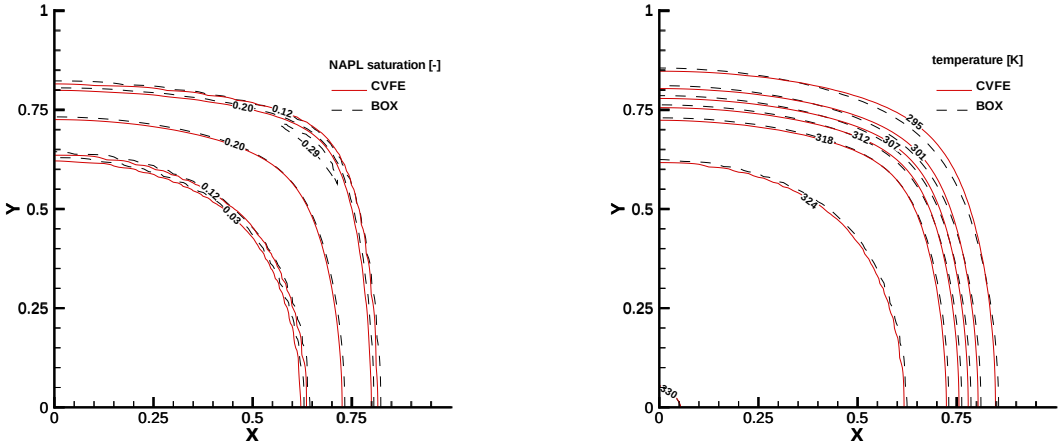

Figure 5.9: Isolines of NAPL saturation (left) and temperature (right) after 3 hours simulation time

K prevails, which is equal to the temperature of the injected steam/air mixture. A change of the phase state from NWG (1) to WG (6) occurs whenever the NAPL saturation disappears at a node.

The case study below investigates whether the application of the extended multigrid method to this complex non-isothermal three-phase three-component system yields a solution performance comparable with that known from the literature [76] for elliptic problems or for the isothermal two-phase flow system described by [11]. If so, one should observe a computing time which increases proportionally to the number of unknowns (number of grid nodes, when applying mesh refining). The following three combinations of iterative solvers for the linearized equations are compared:

1. Nested iteration, multigrid V-cycle preconditioner with $\nu_1 = \nu_2 = 2$ smoothing iterations (ILU), BiCGStab solver for the finest grid, direct solver as coarse-grid solver (for computation of the correction on the coarsest grid)

2. Same as Case 1, but nested iteration only for the computation of the first time step

3. ILU as preconditioner, BiCGStab solver for the finest grid, nested iteration only for the computation of the first time step

We applied a value of 10^{-4} for the criteria of linear and nonlinear accuracy (ε_{lin}, ε_{nl}). The simulations were done on different refinement levels. The coarsest grid contains 400 quadratic elements, the refinement levels 1, 2, 3, and 4 have 1600, 6400, 25600, and 102400 elements respectively. Each of the simulations ended at simulation time 14400 s (4 hours). In Tabs. 5.6, 5.7, and 5.8, some characteristic performance statistics are listed. The abbreviations used are explained briefly in the following:

SIZE	number of elements on the finest grid
avg. Δt	average time-step size [s]
EXECT	execution time [s]
NLIT	number of nonlinear iteration steps required
LIT	number of linear iteration steps required
AVG	= LIT/NLIT: average number of linear iteration steps per nonlinear iteration step
MAXLIT	maximum number of linear iteration steps during a nonlinear iteration step

In order to check the convergence behavior of the different cases with respect to the dependence on the refinement levels, we must compare the number of linear iteration steps (LIT) for the different cases. As we consider a nonlinear system of equations, it is necessary to refer LIT to the number of the nonlinear Newton iterations (NLIT). Note that NLIT is the same in Cases 2 and 3 for all refinement levels since the only difference between these two cases is the choice of the linear solver. If the convergence behavior of the multigrid solver is as in an elliptic problem, we would observe that the number of linear steps for each Newton step (AVG) is asymptotically constant. Since NLIT is approximately proportional to the number of unknowns on the different refinement levels (see Tabs. 5.6, 5.7, and 5.8), the same would be valid for the total computing effort in case of constant AVG.

Table 5.6: Simulation parameter Case 1

SIZE	avg. Δt	EXECT	NLIT	LIT	AVG	MAXLIT
1600	350	7561	317	582	1.84	4
6400	306.3	$3.48 \cdot 10^4$	615	1435	2.33	5
25600	248.9	$1.95 \cdot 10^5$	1172	3083	2.63	5
102400	181.2	$1.27 \cdot 10^6$	2277	6368	2.80	5

Table 5.7: Simulation parameter Case 2

SIZE	avg. Δt	EXECT	NLIT	LIT	AVG	MAXLIT
1600	254.8	8126	252	765	3.04	5
6400	121.3	$6.28 \cdot 10^4$	526	2072	3.94	6
25600	54.7	$5.16 \cdot 10^5$	1160	4781	4.12	6
102400	19.5	$5.25 \cdot 10^6$	3056	12265	4.01	7

Discussion of the results: With increasing refinement level, the average time-step size in Case 1 (nested iteration for all time steps) becomes significantly larger than in the other cases. The maximum time-step length was chosen at $\Delta t_{max} = 350$ s. An automatic time-step control is implemented in MUFTE_UG, which halves the time step if no convergence within the nonlinear Newton solver is achieved. Normally, a reduction of the space-discretization length is accompanied by a reduced time-step length. The use of nested iterations enables an improved starting value

Table 5.8: Simulation parameter Case 3

SIZE	avg. Δt	EXECT	NLIT	LIT	AVG	MAXLIT
1600	254.8	8288	252	12307	48.84	70
6400	121.3	$9.42 \cdot 10^4$	526	50505	96.02	141
25600	54.7	$1.18 \cdot 10^6$	1160	207033	178.48	318

for the iteration so that a better convergence behavior is obtained, permitting larger time-step sizes. The dependence of the computing effort on the refinement level is almost reached by the multigrid method in the manner expected for elliptic problems. Convergence should be achieved independently of the refinement level. The computing effort increases almost proportionally to the number of nodes (number of unknowns), i.e. the value of AVG seems to be nearly asymptotically constant. However, the ratio of linear to nonlinear iteration steps (AVG) is clearly better in Case 1 than in Case 2. The reason is probably that the starting values for the iterations on the finer grids obtained from the nested iterations are better. With increasing SIZE, this effect of better linear convergence has an important influence on the total execution time (EXECT). For 1600 elements, the computation time has the same order of magnitude for all three cases ($\approx$ 8000 s). The more grid levels are used within the multigrid preconditioner or even within nested iterations, the more computation time can be saved compared with the ILU scheme. The ILU/BiCGStab scheme (Case 3) confirms the expected convergence behavior ($\rho = 1 - O(h)$). The number of maximum linear iteration steps (MAXLIT) during a single Newton step roughly doubles with each refinement level, whereas it remains nearly constant for Cases 1 and 2. The computation effort for one multigrid step is larger by a factor of approximately 4 than for one ILU/BiCGStab step. But this is only a disadvantage for small refinement levels. Since the convergence behavior of the multigrid method was nearly textbook-like, it could outweigh this for higher levels of refinement and yield significant savings in computation time.

Note that we applied the multigrid preconditioner for a domain with homogeneous properties. Regarding heterogeneous porous media, this excellent convergence behavior of the method is limited to cases where the resolution of the coarsest grid allows the description of the heterogeneous structures. For heterogeneous permeability fields as applied in [34] the convergence behavior may be worse since some heterogeneities appear on smaller scales and are not accounted for on coarser grids.

5.6 Parallel Computations with the Simulator MUFTE_UG

For practically relevant problems on large scales it is essential to use parallel computing techniques in order to minimize computation time. Although it is not the focus of this work, we present in this section an application that shows the performance of the parallelized simulator considering as example a CO_2-injection benchmark problem. This benchmark was part of an international code intercomparison study [144] initiated in the early years of multiphase CO_2 model development in order to compare different existing multiphase codes with respect to their capabilities of simulating CO_2 injection, migration, and reaction processes in the subsurface.

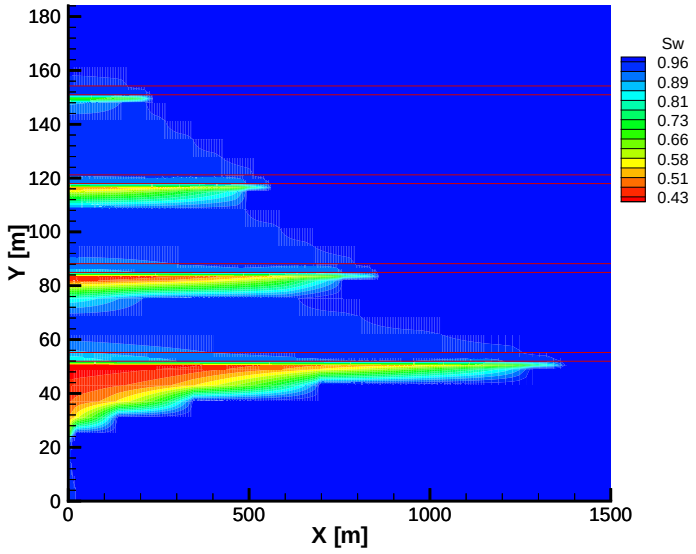

Figure 5.10: Benchmark problem: simulation of a CO_2–injection into a geological formation, cf. [144, 18]. The figure shows a plot of the CO_2 saturation after two years.

Fig. 5.10 shows the simulation results after two years of injection in a depth of 1000 m which corresponds to a y-coordinate of 30 m in Fig. 5.10. The model domain is chosen in such a way that the CO_2 remains in the super-critical state over the full height. The domain is initially fully water-saturated. Hydrostatic pressure conditions are given by *Dirichlet* boundary conditions at the top, bottom, and right-hand boundaries. The left-hand boundary is defined by *Neumann* conditions with the CO_2 influx at y=30 m and no-flux anywhere else. In the domain, there are four low-permeable layers where the CO_2 pools and spreads laterally before it reaches the entry pressure of a layer and penetrates through.

This system was simulated using a non-isothermal two-phase two-component model with constant fluid properties for CO_2 (super-critical) and water (brine). The simulation was performed on a Linux cluster with a varying number of processors. In total, the discretized problem contained 22500 nodes and accordingly 67500 unknowns. The BOX method and a fully implicit scheme were used. The problem was subdivided in time into 500 time-steps.

For details to the concepts of the parallelized multigrid method in the simulator based on the UG toolbox, we refer to [9]. The simulation runs were performed with a varying number of processors on the Linux cluster. Afterwards, the results were analyzed on the basis of runtimes (Fig. 5.11), speed-ups and efficiency (Fig. 5.12).

Fig. 5.11 shows the required runtime for the individual time-steps of the parallel simulation runs on 1, 2, 4, and 8 processors. It is obvious that the runtime per time-step decreases with increasing number of processors. The behavior of the simulation runs appears to be similar.

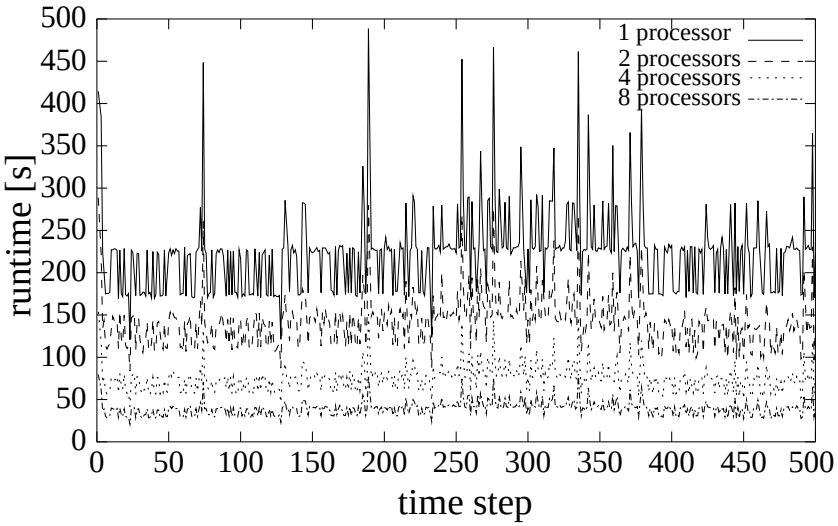

Figure 5.11: Runtime with 1, 2, 4, 8 processors

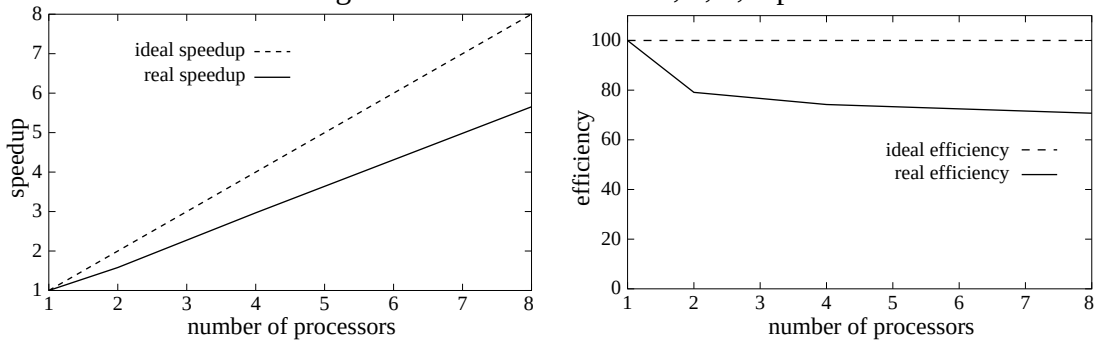

Figure 5.12: Speed-up and efficiency wuth 1, 2, 4, 8 processors

Peaks occur at the same positions as they do in the sequential run on 1 processor. Thus, it can be concluded that the parallelization produces no additional diffulties in the numerical procedure.

For a closer look at the relation between increasing number of processors and decreasing runtime, we can use the criteria speed-up and efficiency. The curve for those is plotted in Fig. 5.12. It can be seen that the speed-up is dampened if more processors are used. Thus, the efficiency is reduced. Using 8 processors a speed-up of almost 6 could be achieved. While the simulation run required about 32 hours on a single processor, this could be reduced to 6 hours with 8 CPUs. The efficiency is higher than 70% and is thus within an acceptable range. It can be expected that with increasing size of the problem (more nodes/unknowns) this value could be even improved. For a more detailed analysis also including the parameters of the multigrid method, we refer to [135].

5.7 Problem-Specific Improvements of Numerical Robustness

The spectrum of concepts introduced for the modelling of gas-liquid processes in porous media is rather broad. In Sec. 4, there has already been a discussion of the specific characteristics of

different physical systems. One of the features that is common for most of the presented kinds of problems is that phases can appear and disappear with the consequence that the set of primary variables has to be adapted locally during a simulation. The experience shows that in practice this can sometimes cause problems with the numerical robustness in terms of small time-step sizes or even failures of the simulations. In the following, we discuss some potential measures to improve the numerical robustness by taking into account the specific problems.

5.7.1 Alternative Primary Variable Switching Concepts

Figure 5.2 explains the basic procedure of the primary variable substitution algorithm. There, a check of the phase state is proposed after every non-linear *Newton-Raphson* iteration step. Alternatively, one could also reduce the number of checks within one time-step, or even evaluate the phase state only after the completed calculation of the time-step. The advantage of checking after every non-linear iteration step is that a convergence of the iteration onto a non-physical solution can be avoided. In other words, if the check - whether the current values of the primary variables fit into i a physically meaningful phase state or not - is done only after the completed time-step, it might, for example, occur that the solution vector contains a negative phase saturation. On the other hand, the check of the phase states after every *Newton-Raphson* iteration is susceptible for tedious numerical trouble. This depends on the initial defect in the non-linear solution procedure. If the initial guess of the primary variables is too bad, the *Newton-Raphson* iteration tends to overshoot into the other direction and to produce values in the vector of primary variables that lead to a premature change of the phase state. Given that this happens, there is no way to find a physically correct solution with the new (false) phase state. The time-step is then destined to fail and has to be re-initialized with a smaller time-step.
Thus, depending on the behavior of the individual problem it makes sense to adapt the number of checks of the phase state within the switching algorithm.

A general observation can be made with regard to the different processes and different model concepts explained in Chapter 3. Provided that the model concept considers diffusive processes, those have a positive influence on the numerical robustness. This, in turn, leads to the conclusion that advection-dominated displacement processes are more susceptible to the above described numerical troubles with premature phase switches. Such examples are the infiltration of a NAPL into the beforehand clean subsurface or the injection of CO_2 into a brine or oil reservoir. Phase switches could be avoided by initializing the phase states in the entire model domain with all possibly occuring phases, for example, by assigning a small number as initial value to the respective phase saturation. However, in this case, the compositional effects in the model concept are reproduced falsely. If, for example, the NAPL phase exists in the domain, this means that, even at very low saturations, the equilibrium between the liquid and gaseous component holds and the mole fraction of evaporated NAPL in the gas phase is equal to its saturation vapor pressure. Furthermore, the mole fraction of dissolved contaminant in the water phase is determined via *Henry's law*. It is accordingly not possible to model diffusive spreading of evaporated or dissolved contaminants since there are no concentration gradients possible.

modelling compositional effects in a model concept that neglects the appearance and disappearance of phases and uses all phases existing at all times, this requires a regularization of

the constitutive relationships. Of particular interest is the saturation vapor curve. It could be regularized in a way that the 'full' vapor pressure is calculated above a certain threshold value of the corresponding liquid phase saturation. Below that threshold, the vapor pressure could be linearly reduced and approaching zero if $S \rightarrow 0$. This would reduce also the partial pressure of the corresponding gaseous component and, if *Henry's law* is applied, also the amount of dissolved substance in the water phase.

Another method to deal with (dis)-appearing fluid phases and changing phase states was already introduced in Sec. 4.2.2 in the context of disappearing air component when steam is injected into the saturated zone. Note that this special problem implies not only the disappearance of a phase but even the disappearance of a component. In this case, it is no longer possible to formulate a numerically stable mass balance equation for the non-existing component. The problem is treated by completely dropping the respective balance equation.

5.7.2 Flash Calculations

A further concept to avoid numerically non-robust changes of the phase state and the primary variables is provided by so-called flash calculations. The term 'flash calculation' emanates from thermodynamics and originally denotes for a multi-component liquid the calculation of the amounts of flashed vapor and residual liquid in equilibrium with each other at a given temperature and pressure. This requires in general a trial-and-error iterative solution. Such a calculation is commonly referred to as an equilibrium flash calculation.

Transferred to the multiphase multicomponent gas-liquid problems, that this work deals with, this means that instead of saturations or mole/mass fractions, one uses global mole/mass fractions as primary variables. 'Global' means in this context the overall fractions of the involved components in a mixture regardless of the number of phases. Together with pressure and temperature, which complete the set of primary variables, this allows for the iterative calculation of an equilibrium state of fluid phases composed of the considered components. Examples are given, for example, by *Crone et al.* (2002) [42] for a two-phase two-component simulator for modelling thermal dewatering of brown coal and by *Stadler* (2005) [160] for a model to simulate alcohol flooding processes in DNAPL contaminated aquifers. Flash calculations are also applied for compositional models in the petroleum industry, cf., e.g. *Chang* (1990) [27]. They represent the physics more accurately than the black-oil simulators.

The disadvantage of flash calculation is the required computation time which increases strongly with the number of considered components, cf. [109]. This limits their widespread application for large detailed systems in reservoir engineering. Some authors therefore also describe non-iterative phase equilibria calculations, cf., e.g. [163] or simplified equilibria models with reduced equations.

Chapter 6

Applications

6.1 Steam-Injection into a NAPL-Contaminated Sand Column

The first example application in this chapter deals with the numerical simulation of a column experiment. The experiment was part of a series of laboratory investigations in the *VEGAS* [8] research facility at the Universität Stuttgart, cf. *Betz* (1997) [17], *Färber* (1996) [60]. The numerical simulation of this experiment aimed at investigating whether the model is able to reproduce the relevant physical processes, cf. *Class & Helmig* (2002) [34]. The identification of the processes by means of a comparison between the numerical model and a well-controlled experiment is considered essential for the validation of the model.

Problem Description

Figure 6.1 gives a schematic description of the experimental set-up and a photo of the sand-filled glass column having 30 cm in length and 10 cm in diameter. For minimizing heat losses, the column was insulated during the steam-injection experiment. The porosity was estimated by measuring the weight and density of the sand charge and the volume of the column.

First, the column was filled with air-dried sand so that the initial water saturation could be estimated to be less than 1%. Then, the sand in the column was saturated with xylene and the column was now allowed to drain for several hours until a state close to residual saturation of xylene in the column was reached. During the drainage, the bottom of the column was immersed in the outflowing liquid NAPL. Thus, the NAPL saturation at the bottom could be controlled ($S_n \approx 1$). The weight of the column before and after the drainage was measured and so the mass of xylene inside the column prior to the steam-injection could be calculated. A numerical simulation of the drainage using 'best-practice' guesses for the hydraulic parameters and a fitting of the remaining mass of xylene to the earlier determined value suggested how the xylene saturation was distributed over the height of the column. Then, after the drainage, steam was injected into the column from the top at a controlled rate. The steam quality could be estimated by observation of the condensate/steam ratio to be better than 90% steam.

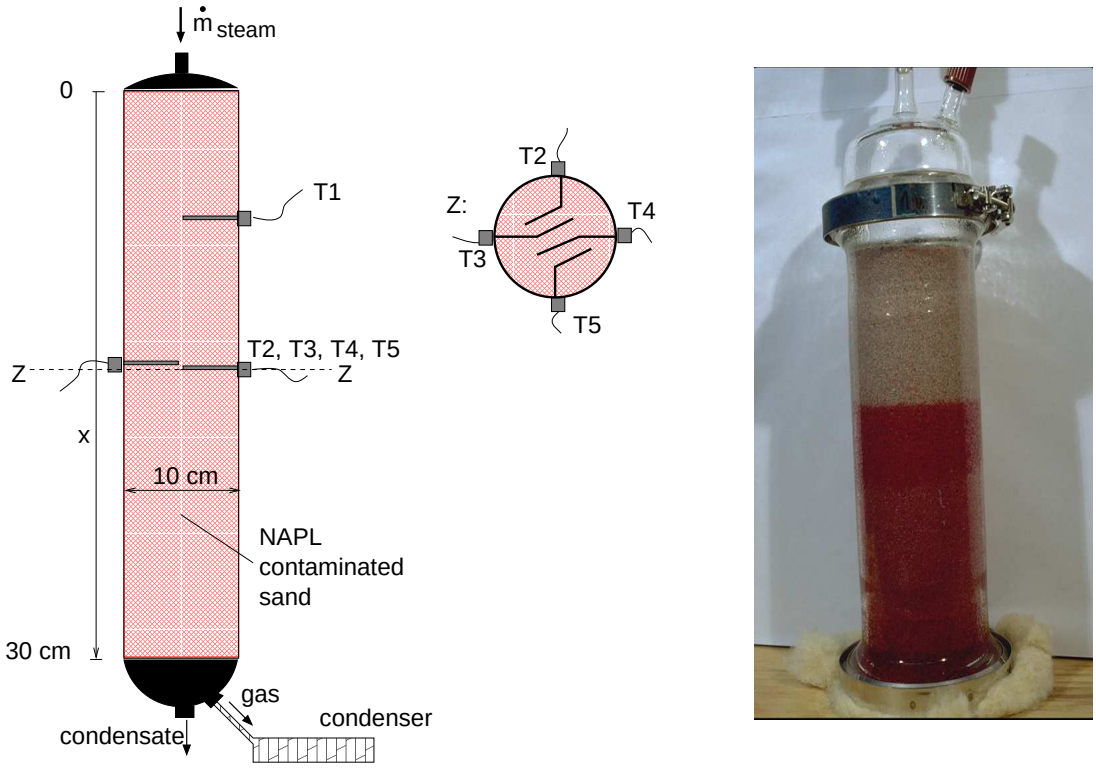

Figure 6.1: Configuration of the experiment

As already explained earlier in Sec. 2.2, it is characteristic for the developing steam front that it propagates steadily and stable through the porous medium, eventually breaking through at the bottom. There, the liquids water and xylene were separated in a liquid collector. The gaseous components first flowed through a condenser, after which they also reached the liquid collector. The temperature was measured by a number of sensors in the column to monitor the processes. The sensors were located 6.5 cm (T1, also called T_{upp}), 14.5 cm (T2, T3, T4, T5, collectively called T_{mid}) and 23 cm (T6) from the top of the column. Four sensors were placed on the same horizontal level to observe potential fingering effects.

The characteristics of the temperature curves were already explained in Sec. 2.2. As Tab. 4.1 suggests and can be observed in Fig. 6.2, the boiling temperature of the water-xylene mixture in the column is roughly 92 C. After passing through the temperature plateau, the temperature in all six sensors increased to the boiling temperature of pure water. This means that all NAPL disappeared from the column. The plateau of Sensor 1 was –as expected– significantly shorter than those of the sensors further downstream. The slope of the signal of Sensor 1 was not as steep as it was at Sensors 2 to 5. At the beginning of the injection, the steam has to heat the whole mass of the glass column head and the steam-supply pipe to operation temperature. During the first 400 s, only part of the injected energy could be transfered to the sand since the rest of the energy was lost in the column head. Thus, at this early stage of the injection the increased downward seeping of warm condensate caused an earlier but flatter temperature signal at Sensor 1.

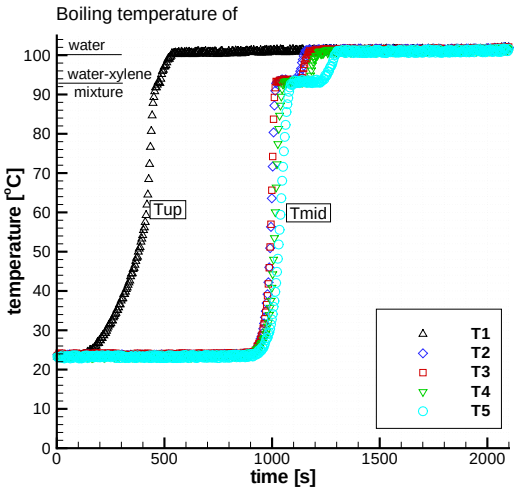

Figure 6.2: Measured data from the temperature sensors inside the column (cf. *Betz*, 1997 [17])

The slight time shift of the steam-front breakthroughs at Sensors 2, 3, 4, and 5 strengthened the assumption that the front did not propagate fully uniformly, but that some small fingering occurred as a result of small-scale heterogeneity. Nevertheless, these sensors showed a good agreement in the length of the temperature plateau.

Vaporized xylene is transported in the gas phase towards the condensation front, where it recondenses, increasing the xylene saturation at the front. An increased effective NAPL permeability allows more xylene to be displaced by pressure and gravitational forces, thus reducing the amount being evaporated behind the steam front. As a result, the length of the temperature plateau (see Fig. 6.2) critically depends on both the absolute permeability and the relative permeability of the free-phase xylene. This will be further discussed below when comparing with the numerical results (Fig. 6.4).

Boundary and Initial Conditions, Model Parameters

The choice of the model domain as well as the initial and boundary conditions for this specific problem is rather difficult as will be shortly explained in the following. The difficulties arise at describing the bottom of the column where the fluids in the experiment could break through into the environment at atmospheric pressure. Thus, the conditions at the bottom obviously change during the experiment and they can neither be described correctly by a *Neumann* (flux) boundary condition nor by a *Dirichlet* condition except for the pressure which is atmospheric. For that reason, the model domain is extended at the bottom by a factor of four (here: 1.2 m instead of 0.3 m) in order to simulate the environment. High storage properties (heat capacity, porosity) and high permeabilities (in order to prevent a pressure drop in the simulated environment) are assigned to the ambient part of the domain in order to guarantee that the bottom of the column (0.3 m from the top) is not affected by the *Dirichlet* conditions that are given at the extended bottom boundary.

The values assigned to the applied 2D-model are given in the following listings below.

Model domain:

width	0.1 m
height	1.2 m (height of column 0.3 m)

Boundary conditions:

top	*Neumann*	q_{steam} =0.396 mol/(s m) (corresponding to 0.21 kg/h) q_{enthalpy} =17455 J/(s m) (corresponding to $\approx$ 2590 kJ/kg or 96% steam/4% condensate)
bottom (extended)	*Dirichlet*	$S_w = 0.1$ $S_n = 0.1$ $T = 23$ C $p_g = 101300$ Pa
left and right	*Neumann*	no-flow conditions (heat losses neglected)

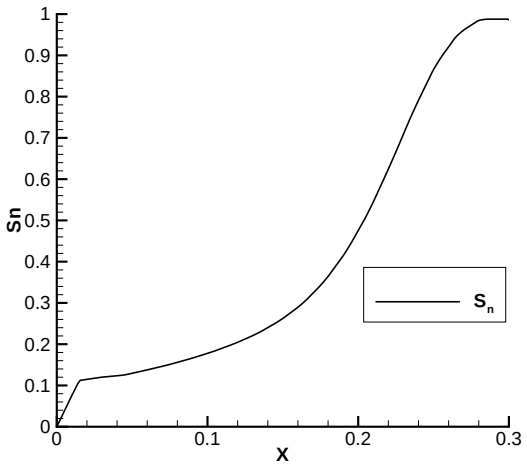

Figure 6.3: Initial distribution of the NAPL saturation in the column (without domain extension).

Initial conditions:

water saturation	S_w =0.005
NAPL saturation	S_n see Fig. 6.3 (in total: 315 g xylene) (in extended domain: S_n =0.0001)
temperature	$T = 23$ C
gas phase pressure	$p_g = 101300$ Pa

Other model input parameters:

porosity	$\phi = 0.46$
sand permeability	$K = 1.4 \cdot 10^{-11}$ m^2
sand grain density	$\rho_s = 2650$ kg/m^3
spec. heat capacity:	
sand	$c_{s,\text{sand}} = 840$ J/(kg K)
glass	$c_{s,\text{glass}} = 775$ J/(kg K)
heat conductivity:	
dry porous medium	$\lambda_{\text{sand}}^{S_g=1} = 0.35$ J/(m s K)
wet porous medium	$\lambda_{\text{sand}}^{S_w=1} = 1.60$ J/(m s K)
relative permeabilities:	
NAPL phase	*Parker* approach (Eq. 3.47), $n = 4.0$, $S_{wr} = 0.12$, $S_{nr} = 0.10$
water and gas phases	*van Genuchten* approach, $n = 4.0$
capillary pressures	*Parker & Lenhard* approach (Eq. 3.29)
	with $n = 4.0$, $\alpha = 0.0005$ Pa^{-1} (*van Genuchten* parameters)

Discretization

For the discretization in time, we used for all the examples in this chapter the fully-implicite *Euler* scheme as explained in Sec. 5.2.2.

The spatial discretization is done with the BOX method (see Sec. 5.2.3). Neglecting three-dimensional effects due to heat loss through the column walls or from small-scale heterogeneities, the problem is one-dimensional. However, we applied a 2D mesh since 1D elements were not available in the simulator. Anyway, this does not influence the one-dimensionality of the simulated problem except for an increased simulation time which is not a matter of concern in this rather small problem. The domain is discretized by 60 elements of $\Delta x = 0.5$ cm.

The heat capacities of column head, bottom, and walls are considered by an increased heat capacity for the respective elements. This yields an effective heat capacity

$$c_{\text{eff}} = c_{s,\text{sand}} + \frac{m_{\text{glass}}\, c_{s,\text{glass}}}{m_{\text{sand}}} \,. \tag{6.1}$$

For the standard elements (only considering the column walls), this yields an effective heat capacity of 970 J/(kg K); for the top and bottom elements accordingly 1125 J/(kg K).

Results and Discussion

Figure 6.4 gives a comparison of the numerical results with the measured curves (see also Fig. 6.2). Obviously, the propagation of the steam front is reproduced in good agreement with the measurements. The temperature increase due to the passing of the front at Sensor T_{upp} is clearly steeper in the numerical results. We believe that this is due to the boundary effects in the column head at the beginning of the steam injection which could not be reproduced exactly by

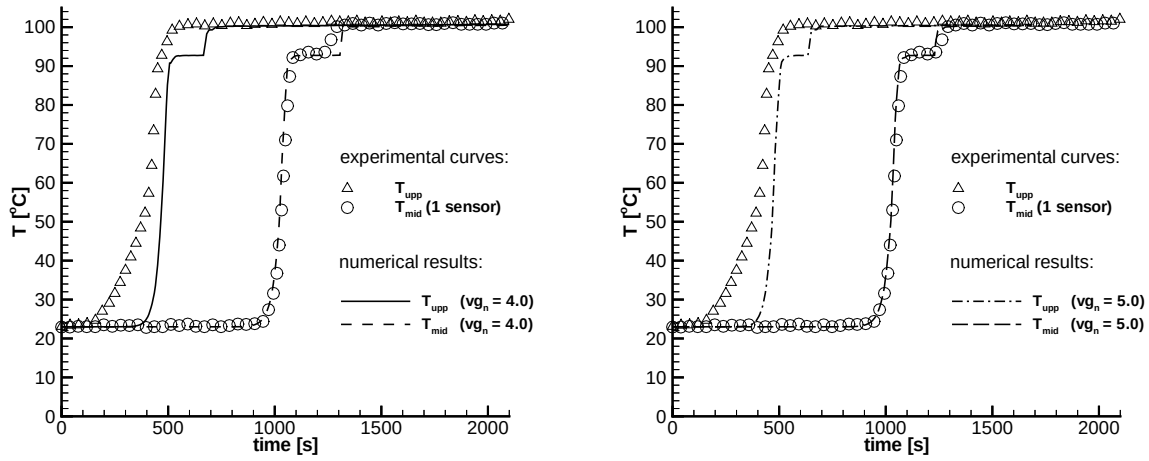

Figure 6.4: Comparison with the experimental curves: Numerical temperature curves at $x = 6.5$cm (T_{upp}) and $x = 14.5$cm (T_{mid}) for different n.

the model. The steepness of the temperature curve at the steam front could be matched well. Note that the steepness of the numerical front is dependent on the discretization length due to numerical diffusion. The temperature plateau at the water–xylene boiling point (see also Tab. 4.1) is reproduced exactly by the model, proving that the thermodynamic relations responsible for this, like vapor-pressure curves or Dalton's Law, are implemented correctly. In Fig. 6.4, one can see that the length of the temperature plateau is overestimated in the numerical simulation with the initial parameter set as described above, where $n = 4.0$ was used for the *van Genuchten* parameter. Again, we do not pay too much attention to the mismatch at Sensor T_{upp}. It is significant to note that the results of Fig. 6.4 are obtained without model calibration, except for a variation of the *van Genuchten* parameter which is explained below.

The length of the temperature plateau critically depends on several factors, so that it is difficult to calibrate the model. For example, a higher steam-injection rate leads to an increased evaporation rate of liquid xylene and thus to a shorter temperature plateau. A similar effect is achieved when the enthalpy of the injected steam is increased. Furthermore, the effective permeability of the porous medium, resulting from the interaction of the pore space with the flowing fluids, is important. In particular, it is extremely difficult to determine the relative permeability relationships in three-fluid-phase systems. When changing the van Genuchten parameter to $n = 5.0$, we get a better match of the plateau length. An increased n value yields a higher mobility of liquid xylene; thus, the re-condensed xylene at the front can be better displaced by gravity and less xylene has to be re-evaporated.

Effects of hysteresis should also be taken into consideration as a potential cause of the different lengths of the temperature plateau and the better results obtained with increased n values. Initially, the sand was saturated with xylene, which then started to drain in a downward direction. Thus, the pore space at the beginning of the steam injection is filled with NAPL and gas. Vaporized xylene from the hotter upper parts of the column re-condensed at the front, increasing

xylene saturation and thus xylene relative permeability. The flow of NAPL reversed from drainage to imbibition. Xylene is the wetting phase with respect to the gas phase and thus tended to flow through the smaller pores. However, gas entrapment (*Sheta*, 1999 [155]; *Lenhard et al.*, 1991 [104]) might result in an altered distribution of the pores available for xylene flow, allowing xylene to flow through larger pores. This causes an additional increase in the xylene relative permeability, which can be expressed by changing the value of n. In the case of imbibition, capillary forces counteracting the gravitational forces decreased, leading to the enhanced downward displacement of the wetting fluid (here: xylene). For relatively small saturations of the wetting phase, this changed behavior resulted in an increased value of n.

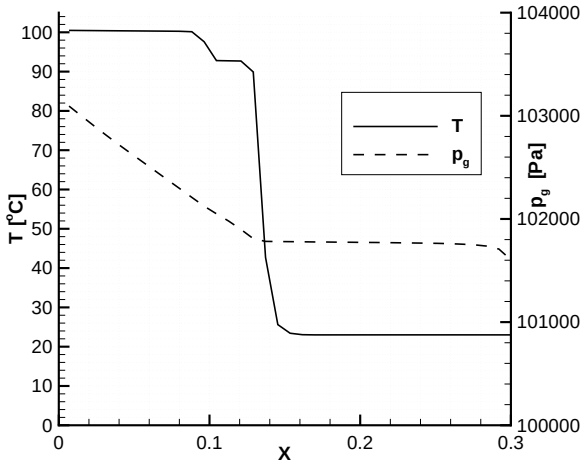

Figure 6.5: Profile of temperature and gas-phase pressure in the column obtained from the simulation at $t = 950$ s (top of the column corresponds to x=0).

Figs. 6.5 and 6.6 show the profiles of the variables temperature, gas-phase pressure, saturations and gas-phase mole fractions after 950 s simulation time. In Fig. 6.5, one can see the sharp temperature front with the plateau behind, where xylene evaporation still occurs. The gas-phase pressure gradient is high behind the front. At the front, all of the vapor condenses; thus, the pressure gradient before the front is much smaller. Fig. 6.6 illustrates some interesting effects. The non-monotone profile of the NAPL saturation illustrates the re-condensation of NAPL at the front. The hill of NAPL obviously corresponds to the front propagation. The mole fractions of steam and contaminant in the gas phase at the water-NAPL mixture boiling point can also be seen (Tab. 4.1).

The calibration of a numerical model describing such strongly coupled, nonlinear processes is hardly feasible by hand (trial-and-error method). Strong correlations between the model parameters and the large number of parameters exhibiting significant uncertainties reduce the reliability of quantitative predictions for real-life problems. Inverse modelling techniques can make helpful contributions to a more reliable parameter estimation, assuming that the measured data are of good quality and reliable (see e.g. *Finsterle*, 1999 [63]). A parameter estimation and sensitivity analysis for this experiment using the *ITOUGH2* code [63] is described in *Class* (2001) [30]. The

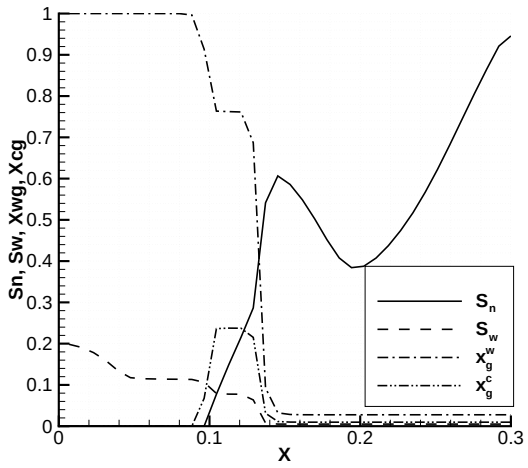

Figure 6.6: Profile of liquid saturations and gas-phase mole fractions of steam and contaminant in the column obtained from the simulation at $t = 950$ s (top of the column corresponds to x=0).

aim was to identify the essential parameters affecting the temperature behavior observed during steam flooding. The steam-injection rate proved to be a very sensitive quantity; it was included as a parameter to be estimated even though it was actually measured. The inverse modelling runs showed that it is difficult to match experimental data containing sharp fronts (here produced by the steam front passing a temperature sensor). These sharp fronts are likely to cause large differences between experimental and numerical data even for small deviations in the front-arrival time, thus leading the minimization algorithm to focus on matching the fronts. It turned out that the initial parameter set (as described above) is the most reliable one, apart from the fact that the n parameter deviated. This is consistent with what we obtained by trial-and-error matching. We failed in our attempt to determine the influence of possibly occurring heat loss by considering the heat capacity and the heat conductivity of the column wall and the insulation in the estimated parameter set. Analysis of these inversions made it clear that, with the available experimental data, these additional parameters (describing heat sinks) could not be reasonably estimated because of the strong correlation between them and the hydraulic parameters.

The results of the simulation of this column experiment show that key issues in the modelling of these complex processes are the determination of the hydraulic constitutive relationships and the quantification of temperature effects both for heat loss and for the influence of temperature on the system properties.

6.2 Simulation of NAPL-Infiltration and Remediation with Sequentially Coupled Models

In this section, we present a numerical study of a NAPL infiltration and subsequent remediation by thermally enhanced soil vapor extraction. The aim of this study is to show the applicability of

the coupling strategy introduced in Sec. 5.4 so that different model concepts can be sequentially applied to distinguishable sub-problems with respect to time. The study is further aimed at comparing the complexity of the model concepts and the computational efforts for solving the arising systems of partial differential equations. For further discussion it is referred to *Class et al.* (2007) [36].

General Description of Geometry, Problem Characteristics, and Model Parameters

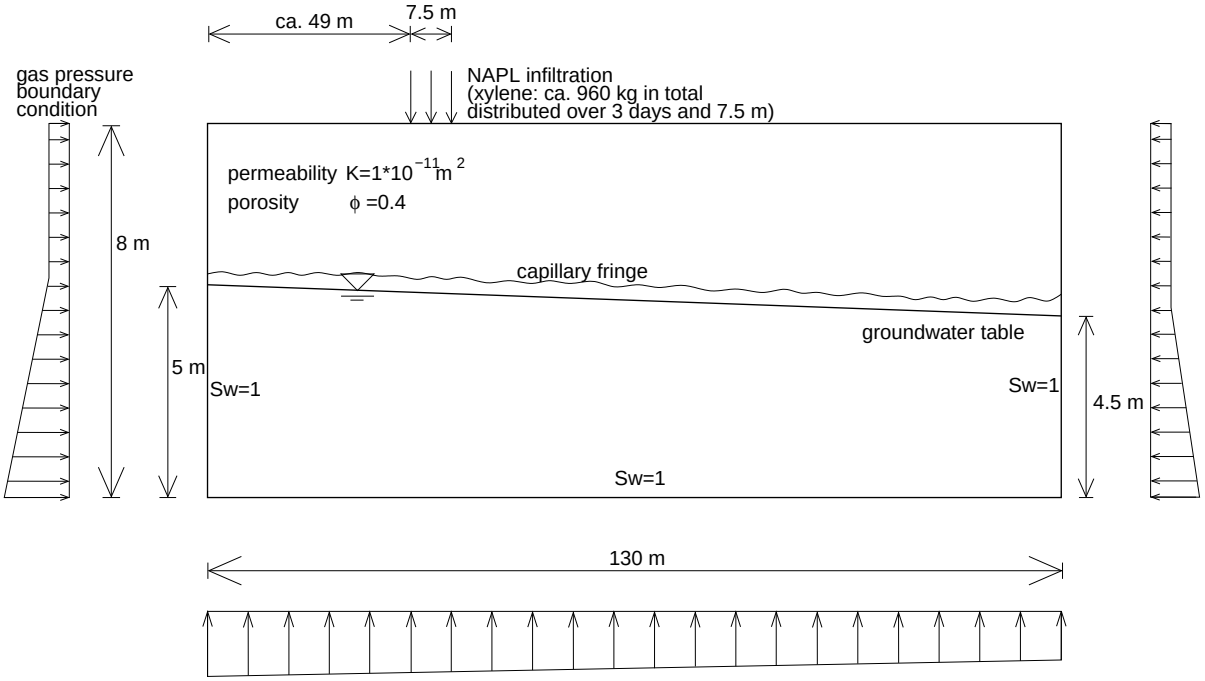

Figure 6.7: Schematic domain and set-up for the NAPL infiltration and spreading scenario.

The study is based on a two-dimensional model domain with 130 m length (x-direction) and 8 m height (y-direction); gravity acts in negative y-direction. The domain as illustrated in Fig. 6.7 consists of a saturated zone and an unsaturated zone with a capillary fringe according to the capillary pressure–saturation relationship (parameters see below). The groundwater table is inclined. It is at 5 m height at the left boundary and at 4.5 m at the right boundary of the domain.

NAPL (in this case: xylene, total amount: 960 kg)) infiltrates over a period of 3 days between 48 m $< x <$ 55 m at a constant rate from the top boundary into the unsaturated zone. After 3 days, the infiltration stops and the NAPL spreads further in the unsaturated zone and - since lighter then water (LNAPL) - on top of the groundwater table.

During the first phase of this example problem, which is the NAPL infiltration and spreading, the bottom, left, and right boundaries are described by *Dirichlet* conditions giving the hydrostatic pressure conditions and the water saturations. The top boundary is described by a *Neumann* no-flow condition except for the infiltration segment during the first 3 days where a constant flux

of xylene is given.

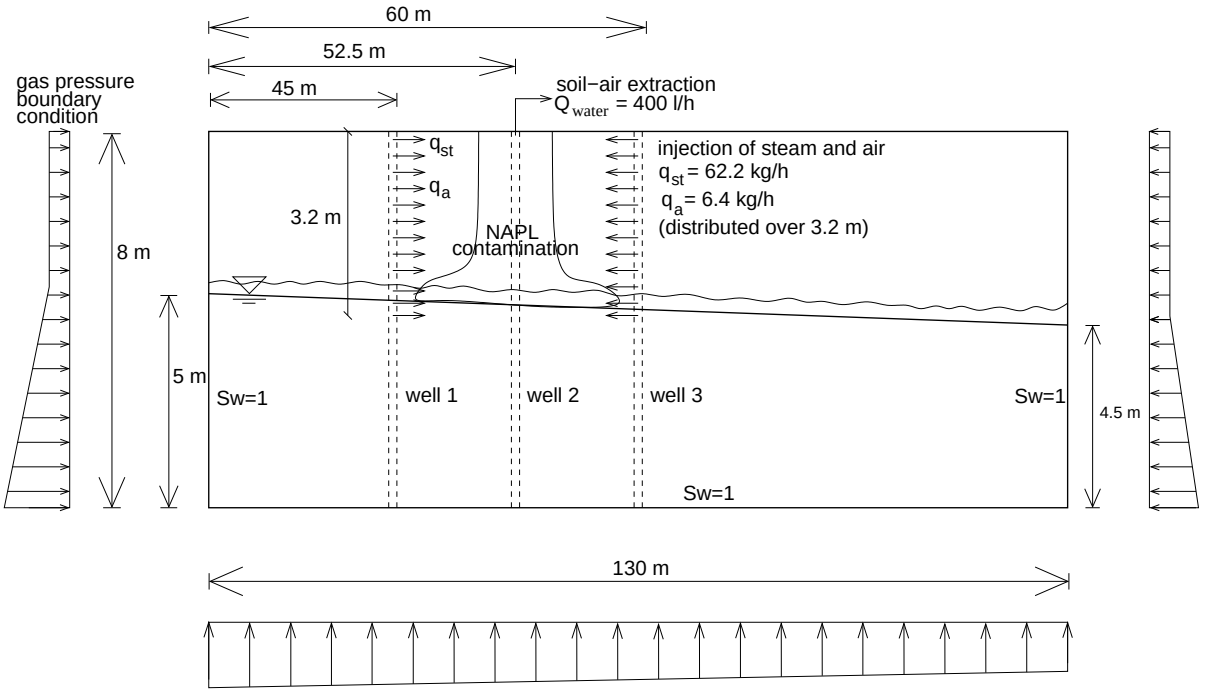

Figure 6.8: Schematic domain and set-up for the steam-injection plus soil-air extraction scenario.

The second phase of the problem is then characterized by the thermally enhanced remediation. Therefore, steam is injected in wells at x=45 m and x=60 m (see Fig. 6.8). This is achieved in the model by introducing inner vertical boundaries at these positions where *Neumann* flux conditions are used to define the injection rate for steam, air, and enthalpy. The injection occurs for y>4.8 m and thus mainly in the unsaturated zone. The interface between groundwater table and capillary fringe at the wells lies at 4.83 m at the x=45 m-well and at 4.77 m at the x=60 m-well. A third well is implemented at x=52.5 m in the center of the NAPL plume. This well is used for the extraction of the gas phase and the production of liquid water. Also in this case, an inner vertical boundary is applied with mixed *Neumann/Dirichlet* sections. For y>5.0 m the extraction of gas is modeled with *Dirichlet* conditions for pressure (1500 Pa below atmospheric pressure) and temperature (ambient temperature: 20 C). The water production is described by a *Neumann* flux at y=3.0 m.

The following model parameters are used for the simulations:

porosity	$\phi = 0.40$
sand permeability	$K = 1.0 \cdot 10^{-11}$ m^2
relative permeabilities:	
NAPL phase	*Parker* approach (Eq. 3.45), $n = 4.0$, $S_{wr} = 0.2$, $S_{nr} = 0.10$
water and gas phases	*van Genuchten* approach, $n = 4.0$, $S_{gr} = 0.05$, $S_{tr} = 0.25$
capillary pressures	*Parker & Lenhard* approach (Eq. 3.29)

with $n = 4.0$, $\alpha = 0.0005$ Pa^{-1} (*van Genuchten* parameters)

parameters only required for the non-isothermal three-phase three-component model:

sand grain density	$\rho_s = 2650$ kg/m^3
spec. heat capacity:	
sand	$c_{s,\text{sand}} = 850$ J/(kg K)
heat conductivity:	
dry porous medium	$\lambda_{\text{sand}}^{S_g=1} = 0.35$ J/(m s K)
wet porous medium	$\lambda_{\text{sand}}^{S_w=1} = 1.80$ J/(m s K)

A-Priori Estimation of the Time-Scales

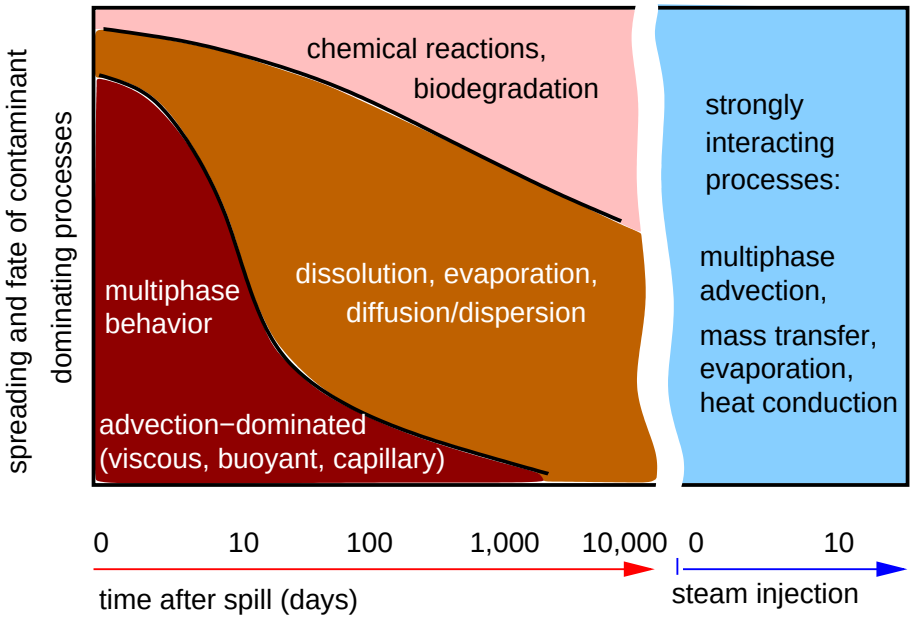

Figure 6.9: Dominating processes on different time-scales after a NAPL spill and subsequent steam-injection [36].

For a NAPL spill into the unsaturated zone, the spreading of the NAPL as a separate phase and as a component within other fluid phases, and a subsequent remediation of the site, it is possible to distinguish different characteristic processes according to the time-scale of interest (see Fig. 6.9).

- The NAPL infiltration occurs on a relatively short time-scale. Within this time, the liquid NAPL phase spreads and reaches a state of rest in residual saturation or is prevented from further propagation, for example, by heterogeneities. The relevant physical processes comprise the multiphase flow behavior of the liquid NAPL, liquid water, and the soil air in the vadose zone, and upon reaching the groundwater table, also in the saturated zone.

The extent of the liquid NAPL contamination can be modeled with an isothermal three-phase model without considering compositional effects.

- On a larger time-scale, the dissolution and evaporation of the NAPL component into the other phases (liquid water and soil air) can become the dominating process since by diffusive/dispersive spreading it may in this way collide with human interests, like drinking water wells or depreciation of building sites. Assessing these issues by numerical simulations requires compositional models.
- In the long-term the contaminants are diluted by the processes described above and they might be degraded by chemical or biological processes. However, for many sites, this process of natural attenuation takes too long and a technical remediation method needs to be applied. However, the modelling of these processes might be relevant for risk assessment.
- Finally, if a remediation is carried out on a NAPL-contaminated site by some thermally enhanced technique, like steam-injection or thermal wells, then the dominating processes change strongly. In this case, support by numerical simulations makes a non-isothermal compositional model inevitable.

Given that the time-scales of the processes that are described by different models can be identified, it is possible to derive estimates for the time to couple the models.

The first phase of the NAPL infiltration problem is dominated by **advective multiphase flow** mainly caused by **gravity-driven downward migration** of the NAPL phase through the unsaturated zone until it reaches the water table. This is superimposed by a **capillary-driven advection** since there is a gradient in the NAPL saturation. NAPL is the wetting phase with respect to gas.
Advective flow is described by the *Darcy* law given here in the form of Eq. (3.40). Considering only the gravitational downward-migration of the NAPL in the unsaturated zone, we have

$$\mathbf{v}_n = -\frac{k_{rn}}{\mu_n}\mathbf{K}\cdot(\underbrace{\nabla p_n}_{\approx 0} - \rho_n \mathbf{g})\,. \tag{6.2}$$

To estimate the velocity $\mathbf{v}_n$, we use the following values for the parameters in the *Darcy* law:

$$k_{rn} \approx 0.2, \quad \mu_n \approx 1\cdot 10^{-3}\ \text{Pa s}, \quad \rho_n = 900\ \text{kg/m}^3, \quad g_y = 9.81\ \text{m/s}^2, \quad K_y = 1\cdot 10^{-11}\ \text{m}^2 \tag{6.3}$$

While the orders of magnitude for the parameters μ, ρ, and g are constant and known well, this is different for the relative permeability due to variations in the saturation and in particular for the absolute permeability which can vary by several orders of magnitude. Using the values given above yields an estimated velocity $v_n \approx 1.5$ m/d. This means, that the NAPL phase is expected to reach the water table in 3.2 m depths **within a few days**. In this calculation we dropped ∇p_n assuming it to be zero. This is in general not true since there is capillarity acting in the unsaturated soil.
Capillary-driven advection is given if ∇p_n is non-zero. It superimposes the gravity-driven downward flow in the same order of magnitude for $\nabla p_n \approx 9.000$ Pa/m which is a realistic value for the parameters chosen above.

This estimation for the gravitational influence holds until the NAPL phase reaches the water table. Then, the inclinination of the water table determines the gravity component in the flow direction for further advective spreading. The capillary-driven advection reduces during the equilibration of the saturation.

The time-scale on which **diffusive spreading** occurs can also be estimated by using some rough assumptions. We could estimate a diffusive velocity in the gas phase as

$$v_{c,diff} \approx D^c_{pm} \nabla x^c_g \, . \tag{6.4}$$

Values for the diffusion coefficient D_{pm} in the porous medium and the concentration gradient x^c_g are chosen as

$$D^c_{pm} \approx 5 \cdot 10^{-7} \text{ m}^2/\text{s}, \qquad \nabla x^c_g = 1 \frac{1}{\text{m}} \tag{6.5}$$

For D^c_{pm} we assume a binary contaminant-air diffusion coefficient of $1 \cdot 10^{-6}$ which is reduced by the influence of the tortuosity, porosity, and saturation. This yields a diffusive velocity of $5 \cdot 10^{-7}$ m/s which is 4 cm per day. Note that ∇x^c_g rapidly decreases during the spreading of the contaminant component which further slows down the diffusion.
In the example, an amount of 960 kg of xylene is spilled which corresponds to a molar amount of $n_{xyl} \approx 9.000$ mole. The order of magnitude of the required time for the diffusive spreading of this amount in the gas phase can be estimated by

$$t = \frac{n_{xyl}}{v^c_{g,\text{diff}} \cdot \rho_{mol,g} \cdot A_{plume}} \tag{6.6}$$

The molar density of the gas phase is about $\rho_{mol,g} \approx 40$ mol/m^3. A_{plume} represents a characteristic surface area of the contamination plume which continuously grows. Inserting values between 10 and 100 m (two-dimensional case!) yields a diffusive spreading time of roughly **10 to 50 years** which is expected to be even exceeded since ∇x^c_g decreases strongly over time.
Diffusion in the water phase is approximately three orders of magnitude slower than in the gas phase due to the smaller diffusion coefficients.

We do not discuss here the time-scale of biological degradation or other chemical reactions since this would by beyond the scope of this study. This would depend strongly on kinetics and availabilities of reaction partners, conditions for bacterial growth, etc.

Summarizing, we can conclude that the NAPL movement through the unsaturated zone to the water table is expected to occur within a few days. Then, we expect an ongoing but slower advective spreading which is determined strongly by the slope of the water table. The diffusive spreading is in the order of a few centimeters per day and goes on for many years.

NAPL-Infiltration: Three-Phase Model versus Three-Phase Three-Component Model

Infiltration with the Three-Phase Model

The three-phase model (3p-model) uses constant values for densities and viscosities of the phases and does not account for mass transfer between the phases. Figure 6.10 shows the

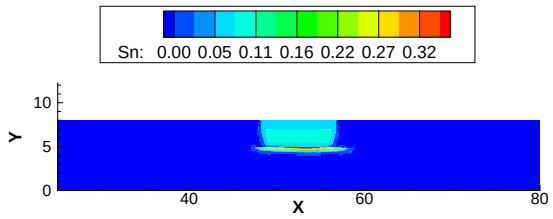

Figure 6.10: 3p-model: NAPL saturation after 50 days.

distribution of the NAPL saturation after 50 days simulation time in the region 25 m $\leq$ x $\leq$ 80 m. One can observe that, although the infiltration stopped 47 days before, there is a significant trace of residual NAPL in the unsaturated zone. This residual NAPL saturation is immobile and represents a long-term contamination source. The amount of the infiltrated NAPL was enough so that it could reach the saturated zone. NAPL pools upon the groundwater table and is slowly shifted in the direction of the inclined water table. However, this shifting of the plume with the flowing groundwater occurs very slowly and a continuation of the simulation would show only very small changes over long periods of time.

Infiltration with the Three-Phase Three-Component Model

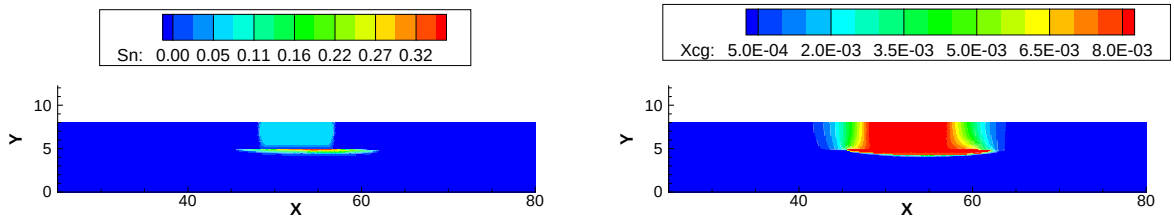

Figure 6.11: 3p3c-model: NAPL saturation (left) and contaminant mole fraction in the gas phase (right) after 50 days.

The same infiltration scenario as explained above for the 3p-model can be modeled with the more sophisticated and complex 3p3c-model. This model allows for compositional effects such as evaporation/volatilization (at constant temperature), dissolution, and diffusion. Thus, it is also possible to investigate how far the contaminant spreads after a transfer into the gas phase by volatilization and into the liquid water phase by dissolution. Figure 6.11 illustrates the distributions of the NAPL saturation and the contaminant mole fraction in the gas phase after 50 days simulation time. Comparing the NAPL saturations after 50 days obtained from the 3p-model (Fig. 6.10) and from the 3p3c-model (Fig. 6.11 left) shows that the principle behavior is the same in both cases and the results are in good agreement. However, it seems as if the NAPL lense on the groundwater table is flatter in the 3p3c-model and thus the lateral shift of the plume is slightly stronger than in the 3p-model. Concerning the influence of compositional effects in this comparison, one can observe in Fig. 6.11 (right) that the concentration of contaminant in the gas

phase is only significant directly within and ≈1 m around the zone of liquid NAPL contamination in the unsaturated zone where the diffusive spreading is higher by several orders of magnitude than in the groundwater. Since the mole fraction of dissolved contaminant in the liquid water corresponds to the contaminant concentration in the gas phase via *Henry's* law [35], its spatial distribution is the same, however with different values.

It could be shown that both models agree on the shape of the NAPL plume extent which leads to the conclusion that the use of the simpler 3p-model is preferable. A model run with the non-isothermal 3p3cni-model yielded the same results as the isothermal 3p3c-model, however at further increased computational costs.

Comparison of the Numerical Performance

In the following, we compare the performances of the model runs of the 3p, the 3p3c, and the 3p3cni-model without going into too much detail of absolute numbers. One must be aware that the required computing time for the simulated 50 days in all three models depends not only on the different number of unknowns but also on the number and complexity of the implemented constitutive relationships and auxiliary calculations. Furthermore, absolute values for computing times, obviously depend on the hardware, particularly the processor.

All simulations used a multigrid preconditioner with an iterative BiCG-Stab solver [11, 35]. The finest grid contained 36864 rectangular 2D-elements (37505 nodes). The coarsest grid had 2304 elements (2465 nodes). Thus, the multigrid cycle included three levels. The parameters for the linear and non-linear solvers used in all simulations were the same and are listed below.

non-linear defect reduction	ε_{nl}	$= 1 \cdot 10^{-4}$
stopping criterion non-linear defect	abs_{nl}	$= 1 \cdot 10^{-4}$
linear accuracy criterion	ε_{lin}	$= 1 \cdot 10^{-6}$
stopping criterion linear solver	abs_{lin}	$= 1 \cdot 10^{-8}$

The 50 days-simulations for all three models were carried out on a parallel cluster on 8 processors. The maximum allowed time-step size was 1 h in both cases. This yielded then a computation time of roughly 24 hours for the 3p-model, 4 days for the 3p3c-model, and 6 days for the 3p3cni-model. Although the 3p-model and the 3p3c-model have the same number of unknowns, the computational effort for the 3p3c-simulation is significantly increased by the evaluation of constitutive functions, for example, for calculations of density and viscosity dependent on pressure and temperature instead of constant values in the 3p-model. Our version of the 3p3c-model considers initial temperatures to remain constant. Nevertheless, the temperature is an input parameter to constitutive functions. More computation time is consumed for the calculation of compositional quantities like *Henry's* constants and the diffusion coefficients. The 3p3cni-model requires additional relationships for the specific enthalpy, the specific internal energy, and the heat conductivities which are related to the non-isothermal capabilites.
Table 6.1 lists some characteristic performance parameters of the model runs. Comparing the average time step size, the number of non-linear and linear iterations, their average ratio, and the

Table 6.1: Comparison of selected parameters of the 3p, 3p3c, and 3p3cni model runs for the simulation of the first 25 days of the NAPL-infiltration scenario.

Model	avg. Δt	non-lin. iter.	lin. iter.	avg lin./non-lin.	max. lin.
3p	3529 s	2835	18215	6.4	16
3p3c	3042 s	3152	15337	4.9	86
3p3cni	3064 s	3109	15483	4.8	13

maximum occuring number of linear iterations per one non-linear step reveals no significant differences in the convergence behavior of the three models. It is remarkable that the performance behavior of the 3p3cni-model appears to be slightly better than the that of the 3p3c-model. A possible explanation for this could be that the additional inclusion of the heat balance into the system of coupled partial differential equations in this case - since actually isothermal - reduces the weight that the other equations contribute to the overall global defect [9]. Anyway, the increase in computation time for the 3p3c-simulation in comparison with the 3p-simulation by a factor of 4 is mainly due to the increased complexity of the 3p3c-model. The same holds for the 3p3cni-simulation which took by a factor of more than 6 longer than the 3p-simulation.

Concluding remarks:
We could show above - by comparing the results of both models regarding the extent of the NAPL plume - that the application of the more complex 3p3c model gives no further details regarding the plume evolution after the infiltration. Thus, it is not recommendable to use this model for this scenario. However, one must be aware that the 3p-model cannot account for compositional effects which might gain influence on a larger time-scale where evaporation and dissolution of the contaminant become processes of increased interest.

What should also be mentioned is that the model concepts applied here could be even better adapted to the complexity of the problem. For the phase spreading in the unsaturated zone, it would be possible to use a model based on the *Richards* equation which assumes that the soil air is infinitely mobile so that its flow does not have to be considered in the equations. However, this does not change the basic ramification out of this study: adapting the model complexity to the complexity of the governing processes saves computation time and thus enables modelers to make predictions for complex flow and transport scenarios over longer time spans.

Coupling the Three-Phase Model with the Three-Phase Three-Component Model after the NAPL Plume is almost at Rest

After having applied the 3p-model for the infiltration and phase spreading scenario for 50 days (see above, Fig. 6.10), we are now interested in the phase transition processes of the contaminant into the gas phase (by evaporation) and into the liquid water phase (by dissolution). From Fig. 6.11 we can already conclude that diffusion has practically no influence in the water phase since the extent of the NAPL phase corresponds directly with the zone of high dissolved concentration in the saturated zone. Above, in the unsaturated zone, a distinct diffusive spreading

of evaporated contaminant away from the zone of liquid NAPL can be observed. However, this process slows down rapidly since the concentration gradient of x_g^c decreases.

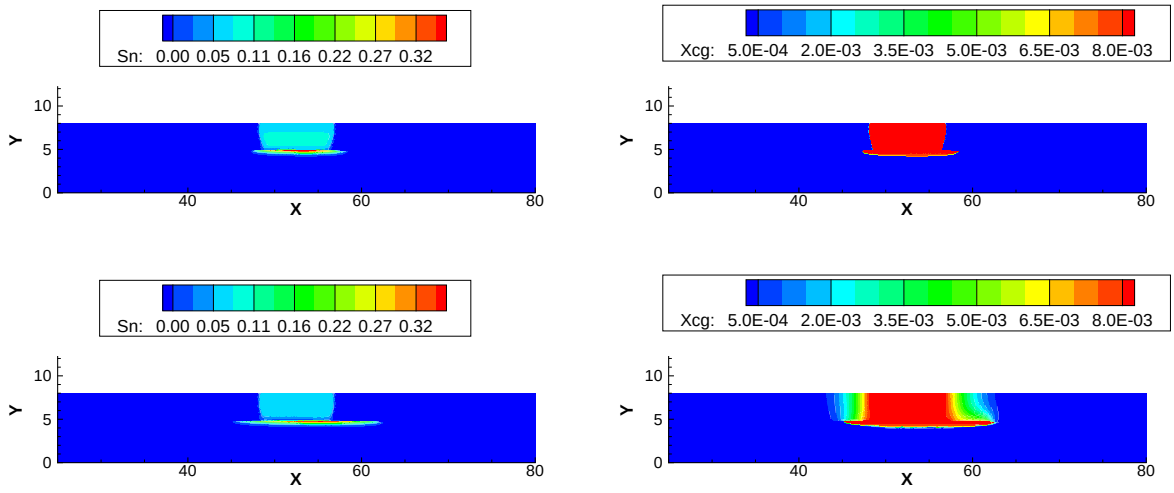

Figure 6.12: Coupling 3p with 3p3cni-model after 50 days: NAPL saturation at 50 days (time of coupling - top left) and 75 days (25 days after coupling - bottom left) and corresponding mole fractions of the contaminant component in the gas phase.

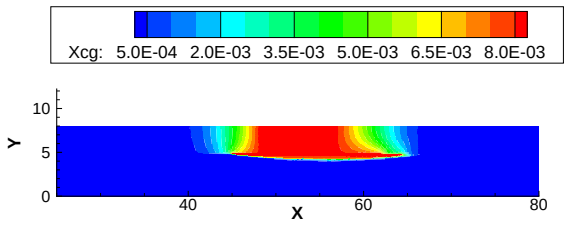

Figure 6.13: 3p3c-model: mole fraction of the contaminant component in the gas phase after 75 days without coupling.

Figure 6.12 shows the results of the 3p3c-model immediatly after the coupling with the results of the 3p-model after 50 days. This means that the plots in the upper half of Fig. 6.12 reflect the result of the transfer algorithm given in Sec. 5.4 applied to the primary variable vector of the 3p-model after 50 days and hence represent the initial conditions for the 3p3c model run. Thus, the contaminant mole fraction in the gas phase is only non-zero (larger than 10^{-10}) at those nodes which have an existing NAPL phase. Yet, we see that already after 75 days (this corresponds to 25 days simulated by the 3p3c-model) the x_g^c–distribution is already in good agreement with that in Fig. 6.13 which shows the x_g^c–distribution obtained from the '3p3c-from-the-beginning' scenario. Over larger time spans, the differences between the results of the '3p3c-from-the-beginning' scenario and the coupling-scenario further diminish and are no longer visually distinguishable.

Remediation: Steam-Injection and Soil Vapor Extraction

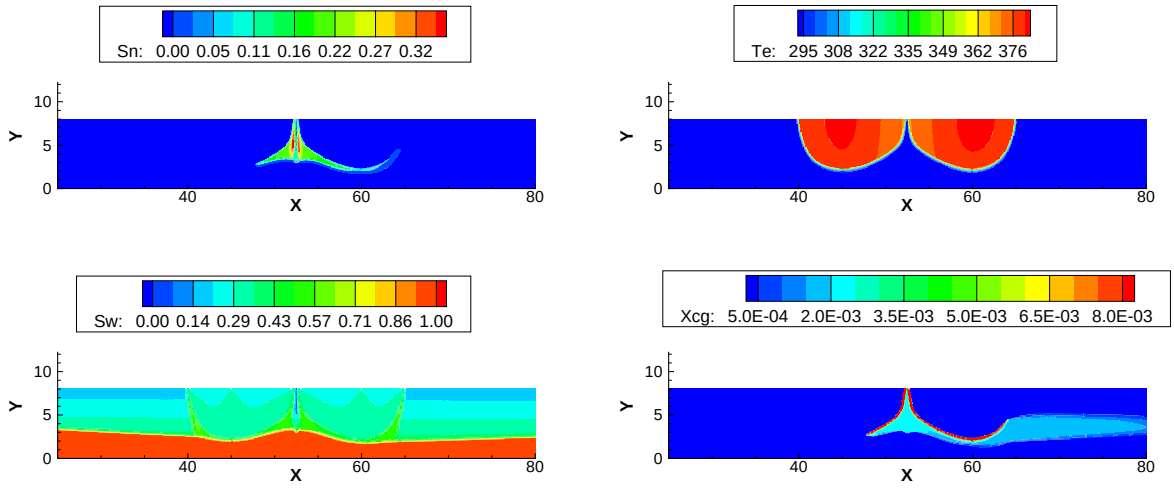

Figure 6.14: Steam-injection and soil-vapor extraction after 30 hours: NAPL-saturation (upper left), temperature (upper right), water saturation (lower left) contaminant mole fraction in the gas phase (lower right).

After 75 days of the NAPL spreading scenario, a steam-injection is started in two wells as sketched in Fig. 6.8. The results after injecting 30 hours with a soil-air extraction in the center of the plume are given in Fig. 6.14. The NAPL saturation in the upper left plot shows the same behavior as already explained in previously in the column experiment (Sec. 6.1). Liquid NAPL accumulates at the steam/condensation front. The position of the front can be seen from the temperature distribution in the upper right plot. One can also reckognize the plateau of the water-xylene boiling temperature close to the extraction well, where liquid xylene is still present. The lower plots of the water saturation (left) and the contaminant mole fraction in the gas phase (right) show the distributions over the full range of the domain. The water saturation plot shows how the water table is lowered by the water production. Eye-catching in the x_g^c-plot is that obviously some contaminant could escape in downstream direction after the steam-injection. The reason why this could happen is simply that the injection well was placed not far enough away from the plume to catch it as a hole. The downstream injection well is located at x=60 m while Fig. 6.12 shows that the NAPL plume extends to almost 65 m.

6.3 Steam-Injection in the Saturated Zone: A Field Case

The following example deals with a practical problem of a real contaminated site in Durlach (city of Karlsruhe/Germany). Engineers of the *VEGAS* facility at the *Universität Stuttgart* worked on a pilot-study for a remediation in the year 2005. Numerical modelling was used to support the planning of the site set-up, for example, concerning the number of required wells. The detailed description of the applied model, the simulations, and an additional planning guideline based on a dimensional analysis are given by *Ochs* (2007) [132, 130].

Description of the Problem and the Field Site

The field site under a former dry-cleaning facility exhibited a contamination in the saturated zone with chlorinated solvents. A former pump-and-treat remediation failed and regulators suggested to test the capability of a steam-injection technique by means of a pilot installation. The aim of the pilot study was (i) to investigate the thermal radius of influence of the steam front, which depends mainly on the permeability distribution and the rate of injection, and (ii) to collect field data for the planning and layout of the actual remediation. This was supported by numerical modelling in order to minimize the required costs, for example, for wells, temperature sensors, energy, and labor. For the simulations, a two-phase single-component model (see Sec. 4.2.2) was applied to model the spreading of the steam front in the saturated zone and to determine the thermal radius of influence. The thermal radius of influence is a measure that determines the number of required wells for the remediation. The higher the permeability and the lower the steam-injection rate, the smaller is the thermal radius of influence. However, the injection rate is in general limited to some upper value of the injecting pressure. Thus, the thermal radius of influence is also restricted for a given permeability.

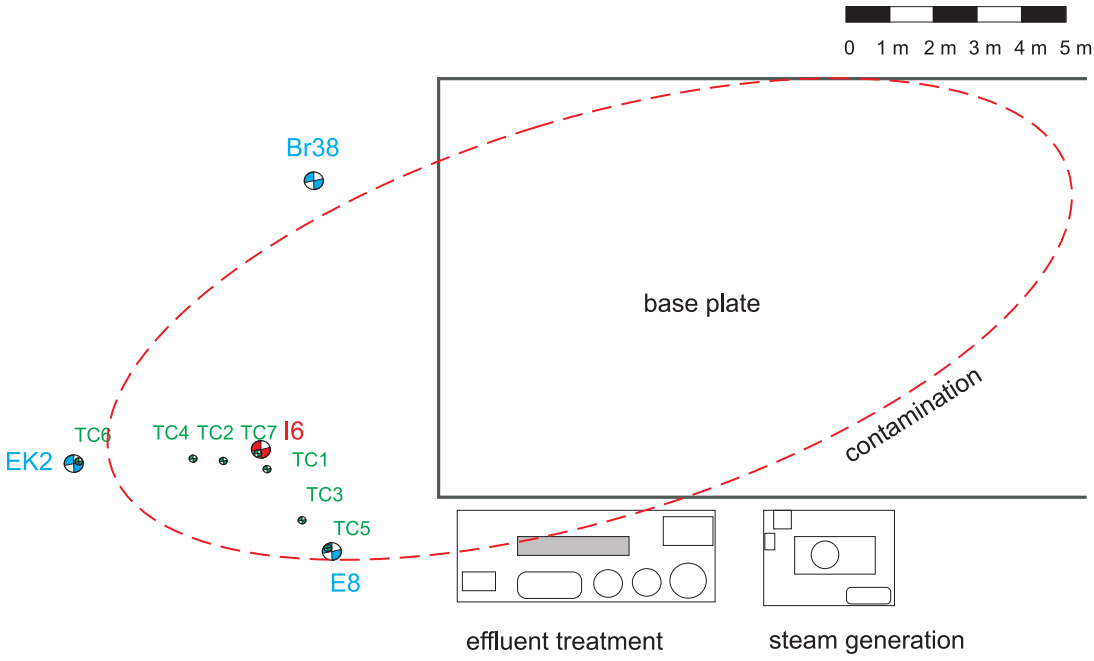

Figure 6.15: Site-plan with contamination, wells, and thermo-couples [130].

Figure 6.15 shows a sketch of the site with the extent of the contamination and the infrastructure of the pilot study. The available informations of the site indicated that the main zone of the contamination is below the builiding and in its near vicinity as shown in the figure. The contamination extends in vertical direction into a depth of 5-7 m below ground surface (bgs) and thus into the saturated zone. The groundwater table is less than 3 m bgs (see Fig. 6.16). Well I6 was used as an injection well, while three wells (Br38, E8, EK2) were installed for extraction. Two rows of thermocouples were placed between I6-E8 and I6-EK2 in order to monitor the steam propagation. The thermocouples consisted of several Pt100 sensors at different depths to allow a 3D

tracking of the steam front.

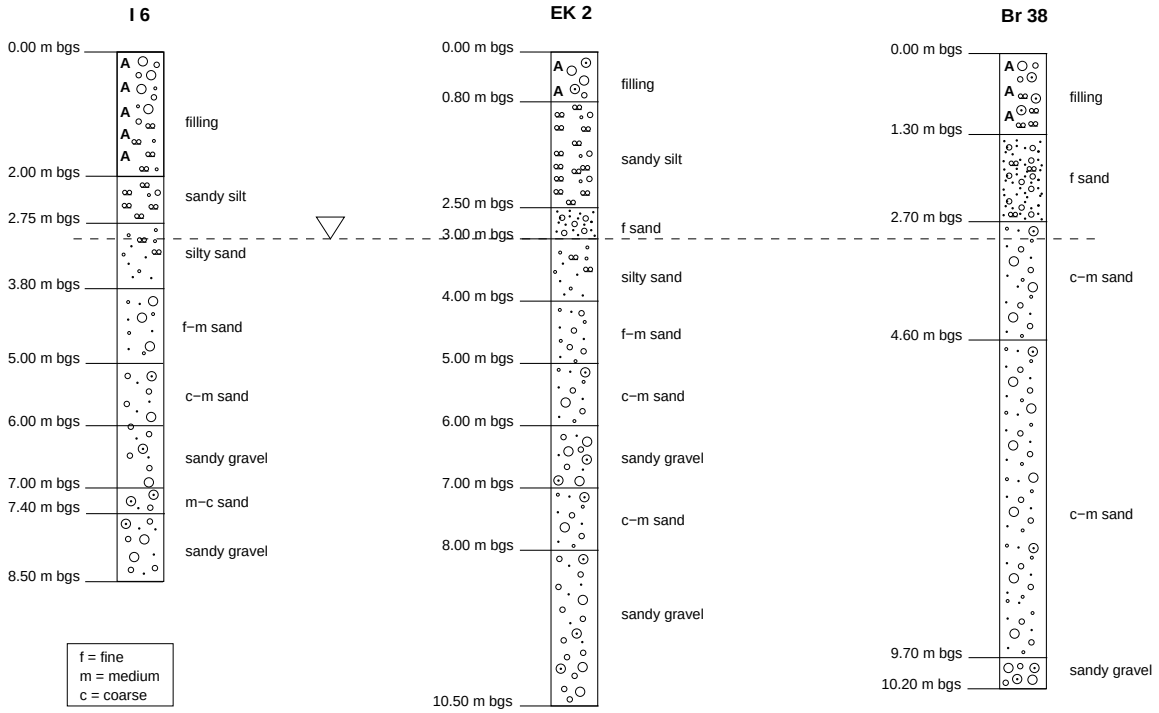

Figure 6.16: Geological profiles of drilling cores from wells I6, EK2, and Br38 [130].

Figure 6.16 gives an overview of geological profiles recovered from cores at wells I6, Ek2, and Br38. From these, it can be seen that the soil body contains some distinct units. First, an artificial filling up to 2 m thickness, below that a sandy silt and a silty fine sand. Below a depth of roughly 4 m bgs, there is a series of fine and medium sand sediments until $\approx$7 m bgs. Medium and coarse sands with some gravel inclusions are located between 7-10 m bgs. The water table at the site is at roughly 3 m bgs.

Model Parameters and Boundary Conditions

As the drilling cores indicate, the heterogeneity of the soil is supposed to play an important role for the spreading of the steam in the saturated zone. Thus, the permeability is a key parameter for the predictive modelling. The cores were evaluated by permeameter tests. Furthermore, on-site borehole tests with a flowmeter have been conducted that allowed the measurement of the vertical flow in the wells at different depths. From these informations, the permeability profiles given by Fig. 6.17 could be elaborated.

It is evident from Fig. 6.17 that distinction of different geological units over the depth is less detailed for well Br38 than for I6 and EK2. *Ochs* (2007) showed with a series of numerical simulations that the thermal radius of influence for well Br38 is by a factor of two smaller than for the other two wells. This is a result of the higher permeability in the depth between 4 and 8 m bgs.

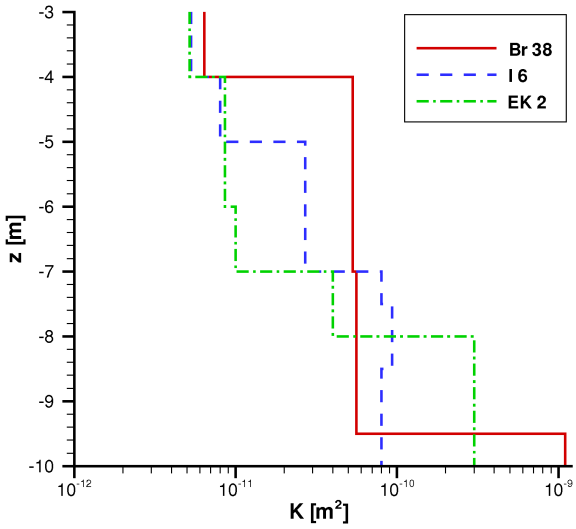

Figure 6.17: Permeability profiles for wells I6, EK2, and Br38 [130].

Further model input parameters are listed in Tab. 6.2. They are taken from the literature due to a lack of data.

Table 6.2: Model parameters for the simulations

parameter	symbol	value	reference
soil grain density	ρ_s	2650 kg/m^3	[30]
porosity	ϕ	0.4	[133]
residual water saturation	S_{wr}	0.1	[133]
residual gas saturation	S_{gr}	0.0	by definition
van Genuchten parameter	α	0.0028 Pa^{-1}	[133]
van Genuchten parameter	n	2.0	[133]
heat conductivity dry sand	$\lambda_{s,dry}$	0.582 W/(m K)	[156]
heat conductivity wet sand	$\lambda_{s,wet}$	1.13 W/(m K)	[156]

Since the aim of the simulations was to predict the spreading of the steam front in the saturated zone, the unsaturated zone was not included into the model domain here. This can be justified by the low permeable silty zone in which the water table resides (see Figs. 6.16 and 6.17).

Steam is injected in well I6 at a depth between 7 and 8 m bgs. Since the steam front is strongly driven upward by buoyancy, the lower border of the model domain which is chosen at 10 m bgs is assumed not to be influenced by the injection. Assuming a radial and symmetric spreading of the steam front around the well, the model domain could be simplified as, for example, shown in Fig. 6.18.

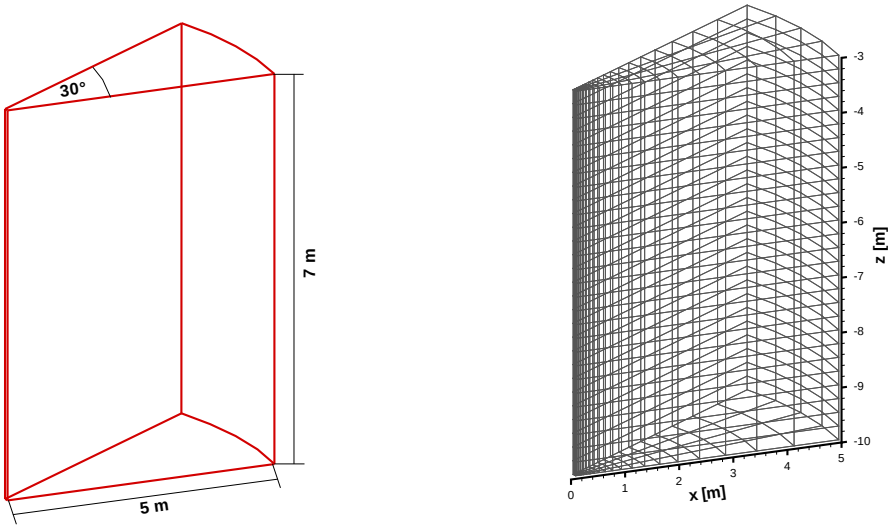

Figure 6.18: Model domain and mesh for the numerical simulations [132].

The mesh consists of 2240 three-dimensional elements of variable size. The mesh resolution decreases in outward direction away from the injection well.

Boundary conditions:
The boundary surfaces representing the cut-out of the cylinder-segment are *symmetry-boundaries*. Therefore, they are modelled with a *Neumann* no-flow boundary condition for the mass flux of water and the thermal energy flux (spec. enthalpy). The same holdes for the *bottom* boundary. To the *outer* boundary (5 m from the injection well) is assigned a *Dirichlet* condition with a fixed temperature of 283.15 K and hydrostatic pressure. For the *top* a *Dirichlet* boundary condition with a constant temperature of 283.15 K and an atmospheric gas phase pressure is applied. The *inner* boundary represents the well. It is modelled also with a *Neumann* no-flow boundary condition except for the regions between 7 and 8 m bgs. There, a *Neumann* condition representing a steam injection rate of 180 kg/h is given.

For the predictive simulation of the steam zone spreading, it was assumed that the permeability profile of well I6 is representative for the whole domain. This is also justified by the fact that this profile will have the major influence on the spreading since the injection occurs in this well. A factor of anisotropy for the permeability ($K_{xx}/K_{yy} = 3$) has been chosen based on expert knowledge. Since the model domain is chosen based on a symmetry assumption, the geological layers are set horizontally.

Simulation Results

Fig. 6.19 shows the spreading of the steam front by a visualization of the temperature distribution at four selected times. They indicate a thermal radius of influence of approximately 3 m. Then, the buoyancy forces dominate and drive the steam front further into upward-vertical direction. The thermal radius of influence corresponds to the zone that can be efficiently heated-up to steam temperature with this single well. In this region, the contamination is reached by the front.

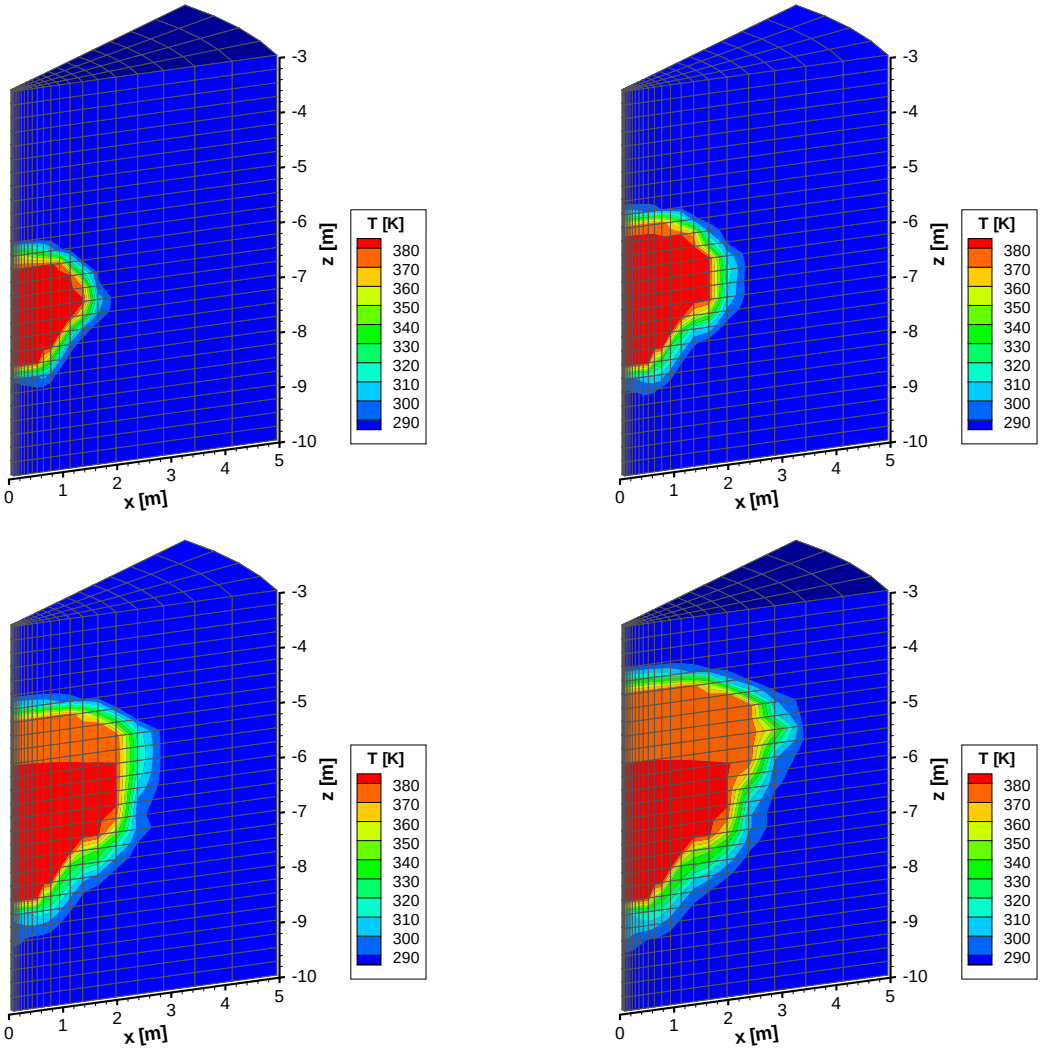

Figure 6.19: Prediction for the pilot steam-injection: simulation results after 6 h, 12 h, 24 h, and 36 h.

For the contaminants beyond the thermal radius of influence further injection wells are needed. Minimizing the number of wells required for the actual remediation is the key issue for saving costs. Thus, this simulation provides very important information for the planning engineers.

The simulation results can also be compared with the temperature measurements by the Pt100 sensors in the thermocouples. The two rows of thermocouples are shown in the overview sketch of Fig. 6.15. Their distances from the injection well and the depth of the Pt100 sensors are summarized in Tab. 6.3.

The two clusters of thermocouples are differently oriented, one in south-eastern, the other one in western direction. However, since the model domain is assumed to be radially symmetric, the simulation results don't take the direction into account but they depend only on the distance from the well and the depth of the sensors. Thus, any deviation of the real permeability distribution from the assumed radially symmetric distribution is expected to influence the temporal develop-

Table 6.3: Distance of thermocouples from well I6 and depth of the included Pt100 sensors

name	distance from I6 [m]	depth of sensors [m]
TC1	0.50	-3, -4, -5, -6, -7, -8
TC2	0.90	-3, -4, -5, -6, -7, -8
TC3	2.05	-3, -4, -5, -6, -7, -8
TC4	1.55	-3, -4, -5, -6, -7, -8
TC5	2.90	-3, -4, -5
TC6	4.25	-3, -4, -5
TC7	0.10	-3, -4, -5, -6, -7, -8

ment of the steam zone in the field.

Figures 6.20 and 6.21 give for different times the comparisons of numerical temperature profiles and the measurements at the Pt100 sensors. In cluster 1, one can observe a good match of the temperature profiles for the TC7 and TC1 sensors near to the injection well. They only disagree significantly between 3 and 4 m bgs which is obviously due to the *Dirichlet* boundary condition of 283.15 K at a depth of 3 m bgs since this represents the upper boundary of the model domain. The measurements of TC2 after 12 h indicate that the temperature front (steam front) is ahead of the simulated front. Thus, the permeability in a depth between 6 and 7 m bgs is likely to be too low in the model.

The comparison between the measurements of cluster 2 and the simulations shows similar behavior as for cluster 1. The thermocouples in the direct vicinity of the injection well (TC7 and TC2) are in good agreement with the simulation results. The other thermocouples indicate here a slightly slower front movement than predicted by the simulation. It is supposed that this hints again to a not exactly reproduced permeability distribution.

Concluding remarks:
The simulation of this field application showed that the model can be validated under the precondition of reliable measurement data. A key model parameter is the distribution of the permeability in the subsurface. Of particular interest for the efficiency of steam injection into the saturated zone is the thermal radius of influence. It depends (i) on the pressure gradient induced by the injection, which drives the front radially away from the injection well, and (ii) on the buoyancy forces, which force the steam upward. Buoyancy can not be influenced and the applicable pressure gradient is higher if low permeabilities are given, however, there will always be an upper limit of the injection pressure.

Having a reliable predictive numerical model, this can be applied to support pilot tests in the run-up of a steam injection and may at least partly replace costly experiments.

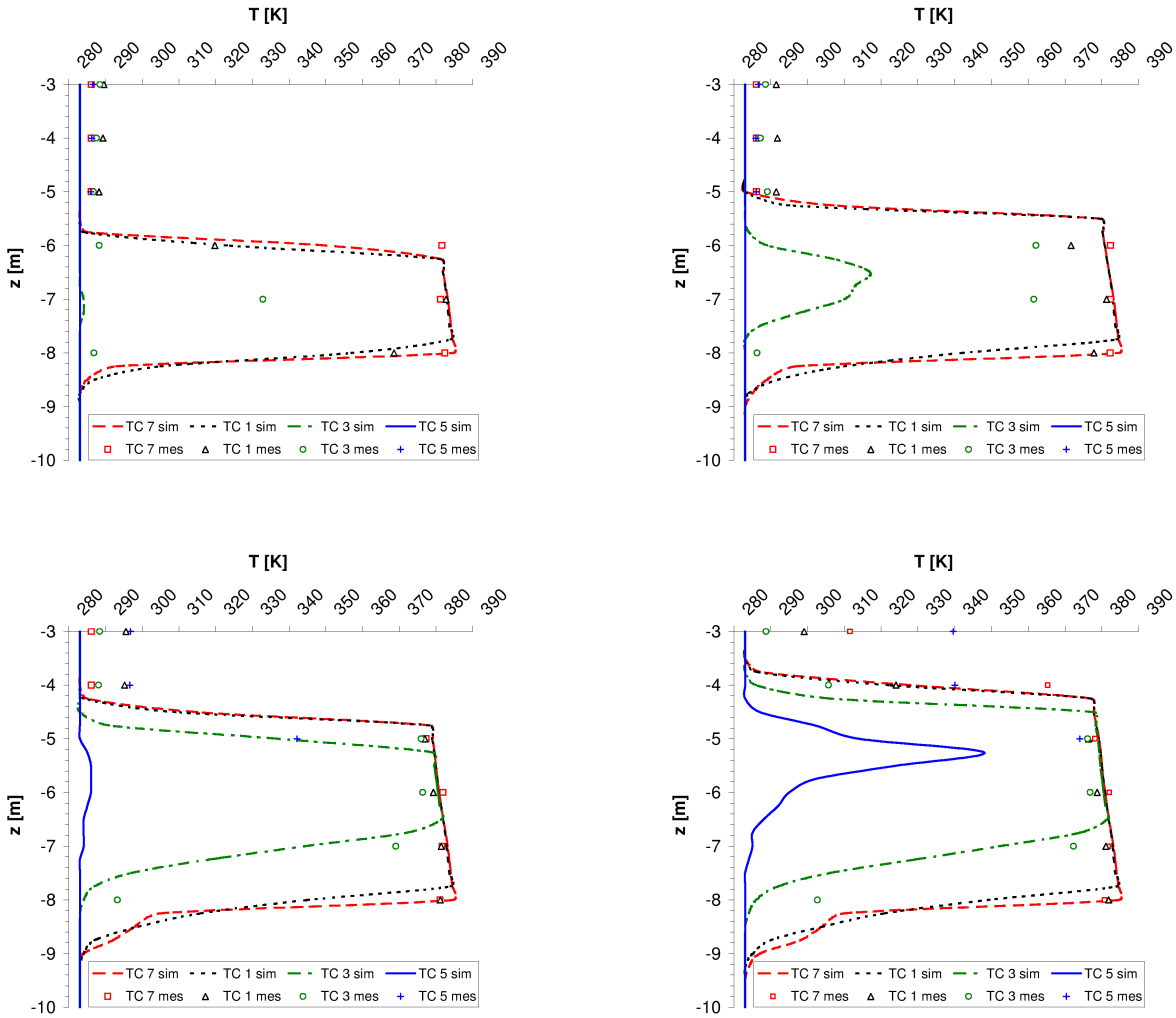

Figure 6.20: Comparison between the thermocouple measurements of cluster 1 (TC7-TC1-TC3-TC5) and the simulation results after 6 h, 12 h, 24 h, and 36 h.

6.4 Long-Term CO_2 Storage in a Saline Aquifer

As was already explained in Sec. 2.4, the processes during an injection of CO_2 in a saline aquifer are manifold. The degree of coupling has to be considered with respect to the time-scale of interest (see Fig. 2.7). In this example [18], we focus on the 'medium' time-scale up to 100 years. On this time-scale, phase transfer processes are expected to play an important role while the influence of multiphase processes declines, provided that the injection had stopped before.

Problem Description

The sample problem is set up in 2D and its model domain, dimensions, and boundary conditions are illustrated in Fig. 6.22. The domain extends over 3000 m in horizontal and 1000 m in ver-

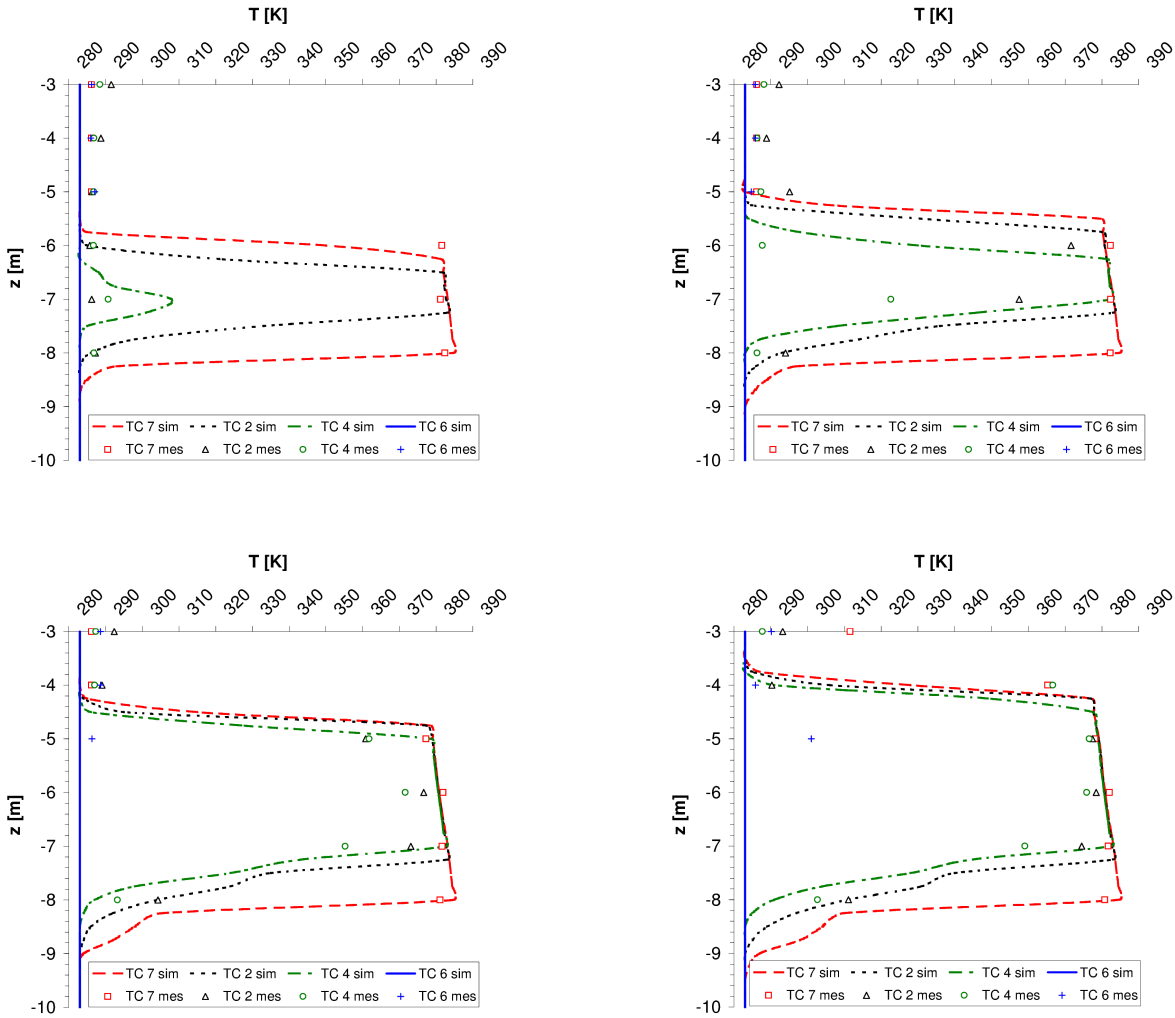

Figure 6.21: Comparison between the thermocouple measurements of cluster 2 (TC7-TC2-TC4-TC6) and the simulation results after 6 h, 12 h, 24 h, and 36 h.

tical direction. It consists of three sub-domains, where the lower and upper sub-domains have equal 'high-permeability' property (Ω_1) and the middle sub-domain (Ω_2) constitutes a hydraulic barrier due to its much lower permeability and higher capillary entry pressure. The lower Ω_1 sub-domain represents a reservoir which is aimed at storing CO_2 which is injected at the bottom of the domain over a 200 m broad segment.

CO_2 is injected in the middle part of the bottom boundary over a short time-span of only 40 days. This amount of CO_2 is enough to reach the barrier Ω_2 as a seperate fluid phase. In the following, the plume of CO_2 in phase redistributes until a state of rest in quasi-residual saturation is reached. Then, the multiphase flow processes cease and the remaining further ongoing processes are dissolution, diffusion, and a density-driven flow of heavier CO_2-rich brine into deeper regions towards the bottom of the reservoir. The fate of the injected CO_2 is modeled over a time-span of 100 years after the stop of the injection.

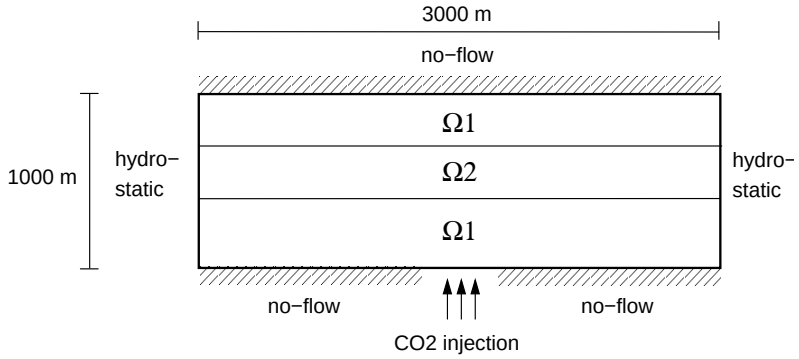

Figure 6.22: Model setup for the CO_2 storage scenario.

The injection strategy and the model parameters given below are not necessarily realistic. The main goal of this sample problem is to identify the different processes, in this case (i) the advective multiphase behavior on the time-scale of the injection and (ii) the influence of compositional effects like mutual dissolution, diffusion, and density-driven brine flow on a larger time-scale up to hundreds of years.

Boundary and Initial Conditions, Model Parameters

A principal sketch of the boundary value problem is given by Fig. 6.22. The values of the initial and boundary conditions are given in the thesis of *Bielinski* (2006) [18] and listed in the following. It should be noted that the list of model parameters considers only those which are decisive for the behavior of the processes that are in the focus of this study. Other parameters are used as described in Sec. 4.3.

Initial conditions:

phase state	only water phase ($S_w = 0.0$)
CO_2 mass fraction in brine	$X_b^{CO_2} = 1.0 \cdot 10^{-9}$
gas phase pressure	$p_{CO_2} = p_{atm} + 5.0 \cdot 10^6 + \rho_b g z$ Pa
temperature	$T = 25 + 0.03 \cdot z$ C

Boundary conditions:

top, bottom	*Neumann*	no-flow
(except for injection segment)		$q_w = q_{CO_2} = q_h = 0$
injection segment (bottom)	*Neumann*	$q_w = 0.0$
(only for $t < 40$ days)		$q_{CO_2} = -0.02$ kg/(m^{2}s)
		$q_h = -3560.0$ kg/(m^{2}s)
left, right	*Dirichlet*	$X_b^{CO_2} = 1.0 \cdot 10^{-9}$
		$p_{CO_2} = p_{atm} + 5.0 \cdot 10^6 + \rho_b g z$ Pa
		$T = 25 + 0.03 \cdot z$ C

Table 6.4: Model parameters for the CO_2 injection problem

parameter	symbol	Ω_1	Ω_2
porosity	ϕ	0.2	0.2
permeability	K	$1 \cdot 10^{-12}$ m^2	$1 \cdot 10^{-14}$ m^2
residual water saturation	S_{wr}	0.2	0.2
residual CO_2 saturation	S_{gr}	0.05	0.05
Brooks-Corey parameter	p_d	1000 Pa	10000 Pa
Brooks-Corey parameter	λ	2.0	2.0
salinity	S	0.25 kg/kg	0.25 kg/kg
diffusion coefficient	D_b^{CO2}	$2 \cdot 10^{-9}$ m^2/s	$2 \cdot 10^{-9}$ m^2/s

Results and Discussion

Figures 6.23, 6.24, 6.25, and 6.26 show the results of the numerical simulation after 1, 10, 50, and 100 years by plots of the distributions of both CO_2 saturation S_{CO2} and CO_2 mass fraction X_b^{CO2} in the brine. Note that X_b^{CO2} represents the mass ratio of dissolved CO_2 to its solvent brine and is only to a limited extent suitable for the estimation of the total dissolved amounts which are then effectively stored. The dissolved amounts (in kg) require further information about local saturation and porosity. Anyway, as will be discussed in the following, the variation of the distribution of X_b^{CO2} over time is an indicator for a complex interaction of coupled processes including the dissolution of CO_2 into water (brine), the following increase of the brine's density, and a gravity-induced convection of the brine.

Since the injection process stops early after 40 days, the first set of plots after 1 year in Fig. 6.23 shows already a state, where the CO_2 phase is almost at rest. The CO_2, entering the domain in the injection segment at the bottom, driven by buoyancy migrates upwards until it reaches the layer Ω_2 which has a lower permeability and therefore acts as a barrier. While some CO_2 can penetrate into this layer, the barrier Ω_2 causes a lateral spreading of the CO_2 phase. Eventually, owing to a lack of replenishment, this multiphase processes reaches a state of rest. The trace of CO_2 in residual saturation shows the areas which had come into contact with CO_2 in phase. This is of particular interest for the storage mechanism *residual trapping* (see Sec. 2). We should notice that particularly for the residual trapping the effects of hysteresis can play an important role, cf. [98], yet these are not taken into account in this sample problem. The distribution of X_b^{CO2} Fig. 6.23 (bottom) shows already after 1 year a high concentration of X_b^{CO2} near to the bottom inside the area that had contact with the CO_2 phase. However, the process that is responsible for this effect occurs not in the CO_2 phase but in the water (brine) phase. The CO_2-rich brine has an increased density, thus it tends to sink down. This prevents dissolved CO_2 to move upwards with the CO_2 phase. Instead, once dissolved, it tends to move into deeper regions of the reservoir.

Figure 6.24 shows that after 10 years the redistribution of the mobile CO_2 phase into a non-mobile residual phase appears to be completed. At the same time, one can observe, that on the bottom segment a pool of the heavier CO_2-rich brine develops which starts spreading laterally.

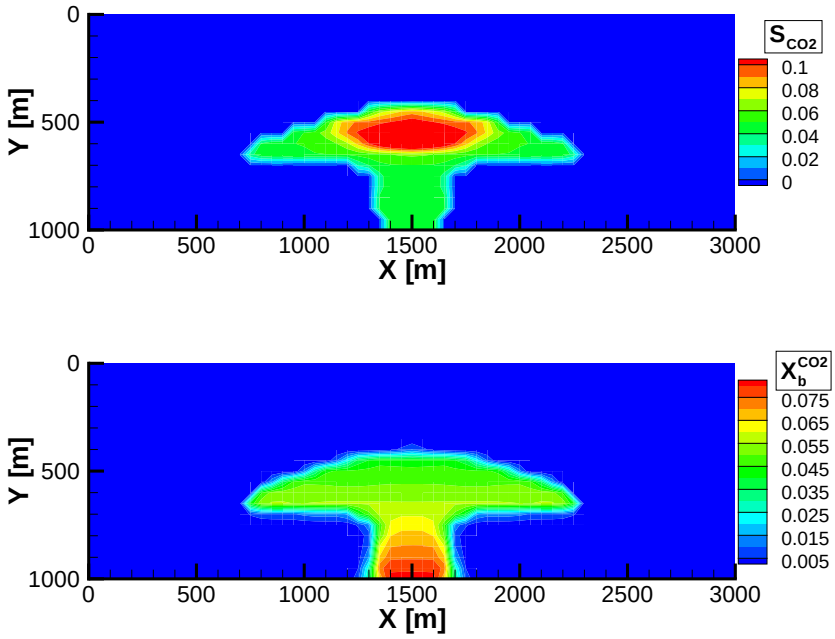

Figure 6.23: Long-term CO_2 storage: CO_2 saturation after 1 year (upper) and corresponding CO_2 mass fraction in brine..

The dissolution of CO_2 into brine and an initiating convection in the brine can also be observed at the lateral edges of the pool of CO_2 in phase below the Ω_2 layer. These processes now dominate over the multiphase processes which have ceased (compare with the time-scales given by Fig. 2.7). In the following, the ratio of CO_2 in phase to dissolved CO_2 is continuously shifted towards the latter (see Figs. 6.25 and 6.26) until eventually the CO_2 phase may completely disappear. As notably can be seen in Fig. 6.25, the downward convection of the CO_2 enriched brine occurs in fingers. These fingers develop due to the unstable layering of the heavier CO_2-rich brine above the lighter ambient brine without dissolved CO_2. In this case of blockwise homogeneous domain properties the number of fingers depends on the discretization length. The fingers are triggered by perturbations which are given in natural systems by small-scale heterogeneities. However, in the numerical simulation of a homogeneous domain they are induced by numerical perturbations which can only occur at the discrete points of the mesh. *Bielinski* (2006) [18] discussed the influence of the discretization length on the development of these fingers. Furthermore, the development of gravity-induced fingers is a known phenomenon in the literature , for example, in saltwater-freshwater instabilities when heavier saltwater is layered above the lighter freshwater, cf. e.g. [96]. The forming of these fingers affects the dissolution rate of CO_2 into the brine since they increase the surface of the CO_2-enriched water body. Thus, they are of great interest for the storage mechanism *solubility trapping*. A large contact area between CO_2-rich brine and ambient brine results in a faster dissolution process. Once a finger is triggered, there are two main processes that determine its further development and its shape and maximum extent. First, this is the gravity-driven convection, which is mainly dependent on the density-difference and the permeability, and which is the triggering process itself. Second, there is the diffusion of

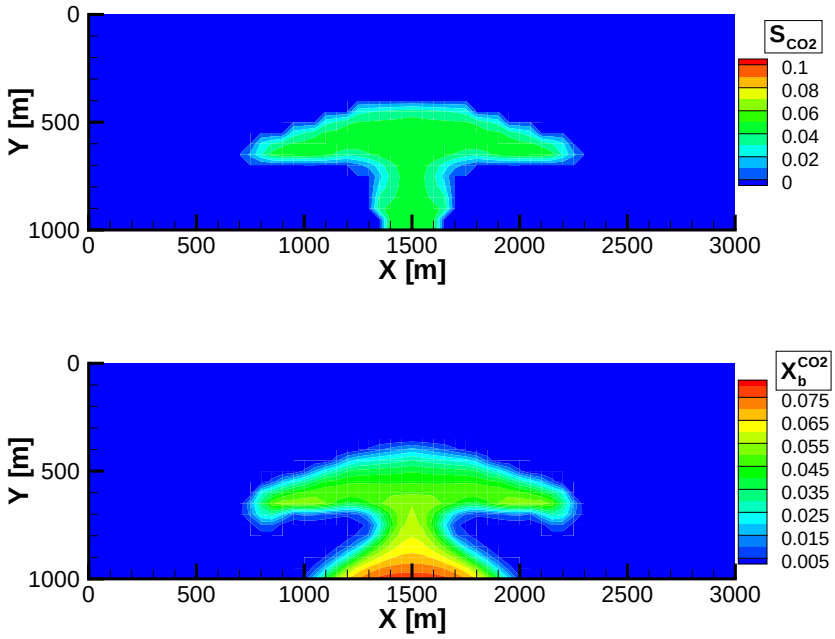

Figure 6.24: Long-term CO_2 storage: CO_2 saturation after 10 years (upper) and corresponding CO_2 mass fraction in brine..

CO_2 in the brine which tends to smooth out the arising concentration gradients so that also the density-differences diminish.

Concluding remarks:
This sample problem demonstrates the occurence of different physical processes on different time-scales. The injected amount of CO_2 was chosen to be rather low when compared to a efficient usage of such a reservoir for the purpose of CO_2 storage. This was chosen in order to better illustrate the time after which the multiphase processes cease and the dissolution of CO_2 into brine, the diffusion, and the gravity-induced convection begin to dominate the system, which in this case is at approximately 10 to 50 years. *Residual trapping* as the result of the advective multiphase flow processes and *solubility trapping* due to the dissolution into brine and its subsequent downward migration are both important trapping mechanisms, however on different time-scales. The phenomenon of gravity-induced finger development on the dissolution rate is a topic that deserves further research where analogies to saltwater-freshwater instabilities are clearly at hand.

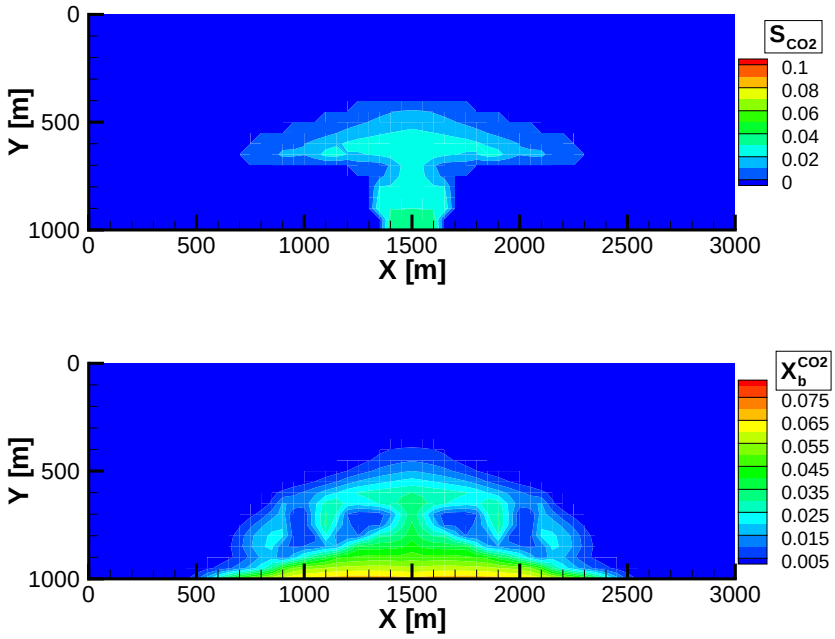

Figure 6.25: Long-term CO_2 storage: CO_2 saturation after 50 years (upper) and corresponding CO_2 mass fraction in brine..

6.5 Enhanced Gas Recovery - A Five-Spot Benchmark Example

This example deals with another storage option for carbon dioxide. The primary goal of enhanced gas recovery (EGR), however, is the production of methane as an energy source (see Sec. 2.4). The motivation for this sample problem was given by the paper of *Seo & Mamora* (2005) who used it as a computational example for the methane recovery rates that can be achieved in a depleted gas reservoir by enhancing the production by injecting CO_2. A similar numerical study is described by *Oldenburg & Benson* (2002) [134]. Enhanced gas recovery is also applied in unmineable coal seams, e.g. at the Weyburn site in Alberta/Canada. Coal, however, is not considered here. The processes in coal would additionally involve a strong influence of competitive carbon dioxide adsorption to the coal and methane desorption from the coal.

Problem Description

The sample problem includes the injection and storage of CO_2 in a depleted gas (methane) reservoir with a symmetric (five-spot) arrangement of injection well and production wells. The processes are modeled with an approach as explained in Sec. 4.3.3. Two phases are considered, a residual brine phase and the gas phase, which contains the components methane, carbon dioxide, and water vapor. The reservoir pressure is initially at 50 bar in a depth of more than 2 km, which is supposed to represent a reservoir approaching its depletion. The gas in the

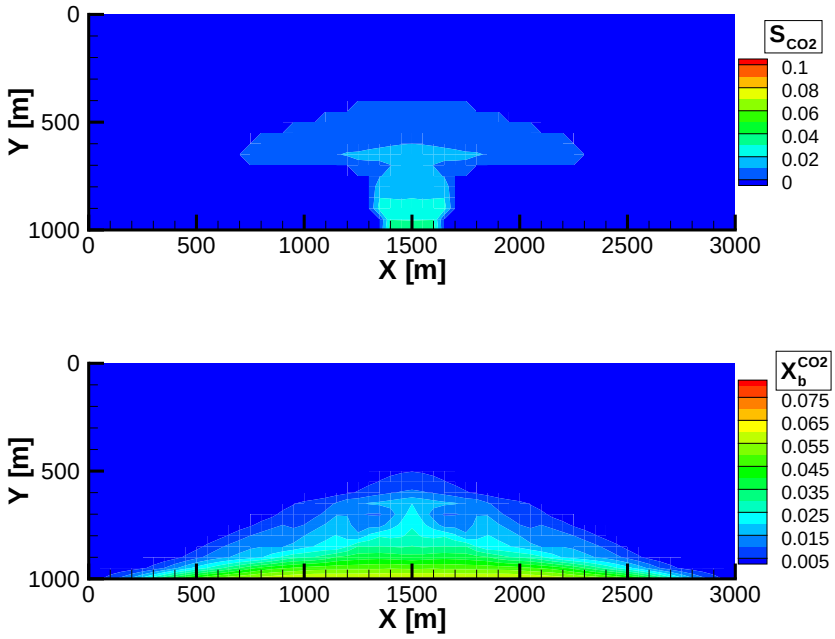

Figure 6.26: Long-term CO_2 storage: CO_2 saturation after 100 years (upper) and corresponding CO_2 mass fraction in brine.

reservoir contains initially 10% by mass CO_2 and is dry (corresponding to a CO_2 mole fraction in the gas phase of $x_g^c = 0.0388$). CO_2 is the heavier gaseous component and is injected at the bottom part of the reservoir at a constant rate. The production of the CH_4 at the production well is run by keeping the pressure constant there. The injection in the lower part of the injection well and the production in the upper part of the production well follow a strategy to minimize mixing effects. The methane production is stopped when the produced gas in the production well contains up to 50% by mass CO_2. The injection of CO_2 for the purpose of storing a larger amount of it in the reservoir could continue until the pressure in the reservoir reaches the original pressure before the gas production began (here: 209.9 bar).

Model Parameters, Mesh and Boundary Conditions

The properties of the reservoir are listed in Tab. 6.5. Note, that here we assume homogeneous conditions (see the discussion below). While the thickness of the reservoir is 45.72 m, the CO_2 injection occurs at the lower 22.86 m of the reservoir at the injection well, and the production at the upper 4.57 m at the production well. Mechanical dispersion is neglected and the mixing of the components occurs solely due to molecular diffusion. The binary diffusion coefficients for CO_2/CH_4 are $4.7 \cdot 10^{-7}$ m^2/s in the gas phase and $5.5 \cdot 10^{-9}$ m^2/s in the brine phase.

The domain is meshed with 10125 hexahedra. The elements near the wells are smaller than elsewhere. This can be seen in Fig. 6.28. The CO_2 injection well is at the left edge of the domain while the production occurs at the right edge. The boundary conditions are no-flow (*Neumann*)

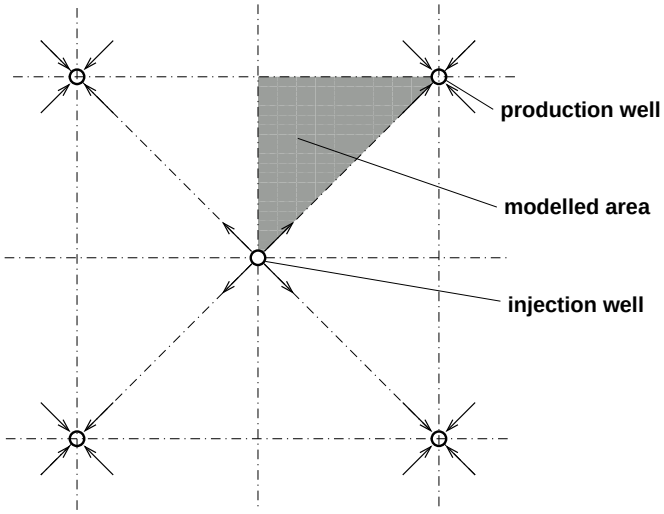

Figure 6.27: Five-spot pattern showing the CO_2 injection well at the center and the production wells at the corners [32]. The shaded area is the part of this symmetric pattern which is modelled.

Table 6.5: Reservoir properties (taken from [153]).

Property	Value
One-eighth five-spot area	20237.91 m^2
Reservoir thickness	45.72 m
Porosity	0.23
Horizontal permeability	$50 \cdot 10^{-15}$ m^2
Vertical permeablity	$5 \cdot 10^{-15}$ m^2
Initial brine saturation	0
Reservoir temperature	66.7 C
Original reservoir pressure	209.9 bar

except at the wells. At the right edge (x$=285.52$ m), which represents the production well, the boundary conditions at the top 4.572 m are constant (*Dirichlet*) and equal to the initial conditions (given below). The rest of the edge is a no-flow boundary. Similarly, CO_2 is injected over the lower half 22.86 m of the left edge (x$=0$ m) and the rest of the edge is also a no-flow boundary.

Initial conditions:

Depleted reservoir pressure	50 bar
Mole fraction of CO_2 in gas phase, x_g^c	0.0388
(corresponding to a mass fraction of 10 %)	

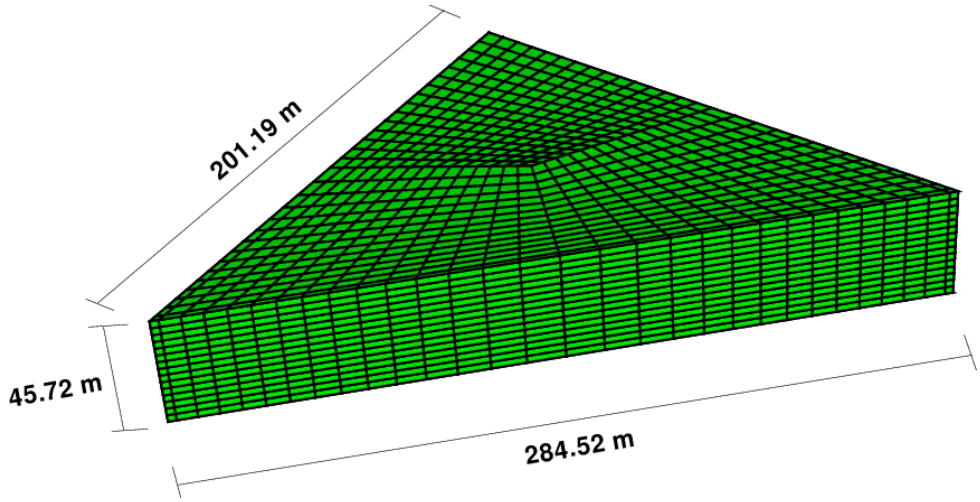

Figure 6.28: Model domain and mesh of the five-spot EGR example.

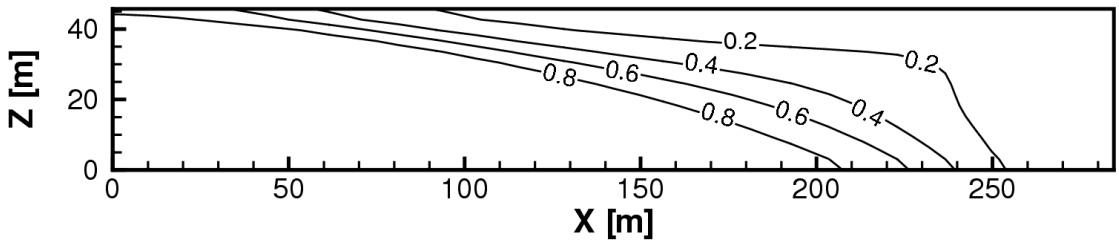

Figure 6.29: Simulation result at $t = 800$ days: CO_2 mass fraction in the gas phase between the injection and the production well.

Simulation Results

The injected (heavier) CO_2 displaces the CH_4 towards the production well while simultaneously mixing with it at the front. Isolines of the CO_2 mass fractions after 800 days of injection are shown in Fig. 6.29. The plot represents the slice between the wells. The wedge-shaped displacement of the methane by the carbon dioxide can be observed. The width of the front, i.e. the transition zone from high CO_2 concentrations to high CH_4 concentrations, depends strongly on the influence of diffusive/dispersive effects.

Figure 6.30 gives the simulated mass fluxes of CO_2 and CH_4 at the production well. The gas production is stopped upon reaching a CO_2 mass fraction of 30% in the produced gas. This occurs after 1210 days in this example. By that time, 56% by mass of the methane in the domain before the start of the injection is recovered.

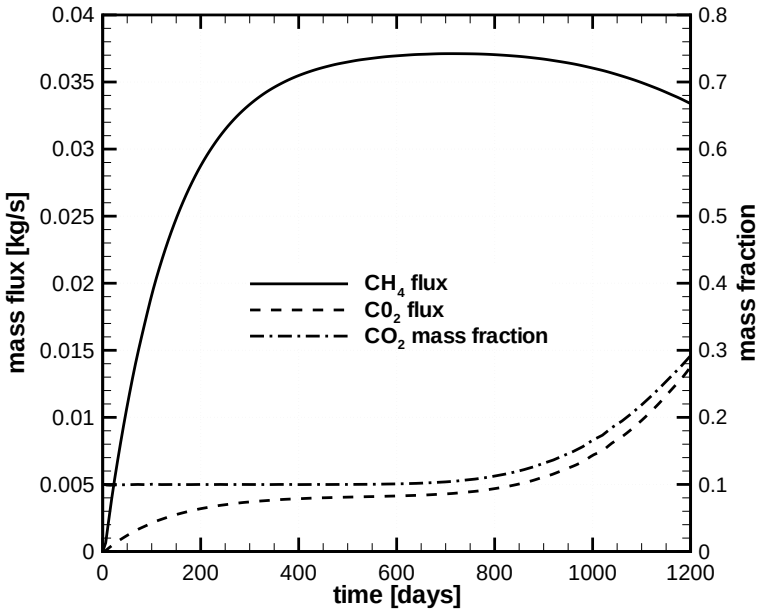

Figure 6.30: Gas production rate for the one-eighth five-spot problem.

Discussion

The assumption of homogeneous domain properties can be hardly held in practice. Heterogeneities will always affect the flow field in a gas reservoir. In this case, one would expect that heterogeneities enhance the dispersive mixing of the gaseous components. The basic mechanisms of dispersive processes were explained earlier in Sec. 3.2.1.1 and illustrated in Fig. 3.13. Eq. (3.66) gives the mathematical approach to model diffusive and dispersive spreading. The more heterogeneous the distribution of permeability and porosity in the reservoir is, the larger are the values for the longitudinal and transversal dispersivities α_l and α_t. This effect is neglected in the five-spot example. The recovery rate is affected by the diffusive/dispersive mixing in the reservoir. A strong mixing causes a broader transition zone (compare with Fig. 6.29) and thus an earlier breakthrough of the injected CO_2 at the production well. This means, that in the present example the recovery rate is likely to be overestimated with the given assumption of a homogeneous reservoir and the neglection of dispersion. For a more detailed analysis of the influence of diffusion/dispersion on the processes during an EGR-scenario we refer to [32].

6.6 Water and Gas Flux in a PEM Fuel-Cell

This example application was described and simulated in cooperation with the *Institut für Chemische Verfahrenstechnik* at the *Universität Stuttgart*. More details and explanations can be found in *Acosta et al.* (2006) [2].

Problem Description

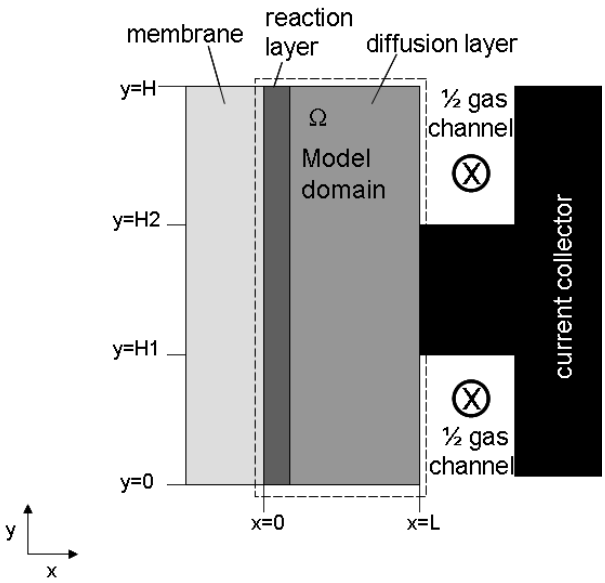

Figure 6.31: Characteristic 2D model domain of a gas diffusion layer as part of the membrane-electrode assembly in a fuel-cell [2].

The principle problem is depicted in Fig. 6.31. It shows a characteristic section through the membrane-electrode assembly. The gas distributor plate on the right supplies the cathode diffusion layer (left) with oxygen or air. The oxygen is then transported through the diffusion layer to the reaction layer where it is consumed by the reaction (Eq. 4.15) under production of water (Eq. 4.16) and heat (Eq. 4.18). An additional water source at the reaction layer is due to electro-osmotic drag through the membrane as given by Eq. (4.17). The water is transported in opposite direction to the gas channels which is supported by the hydrophobic property of the diffusion layer. The channels of the gas distributors are considered in this simulation as representing the boundary conditions for the model domain sketched in Fig. 6.31. Depending on the type of gas distributor (conventional or interdigitated, see Fig. 2.12), different kinds of flow fields develop in the diffusion layer with consequences for the performance of the fuel-cell. This is described and explained below by two simulations, one for the conventional flow field, the other one for the interdigitated flow field.

Model Parameters and Boundary Conditions

Table 6.6 lists the geometrical data of the model domain and the gas distributors. The model domain represents a characteristic section through the membrane-electrode assembly. The shoulder of the gas distributor is in the center of the domain. Due to symmetry it is sufficient to include two half-channels above and below the shoulder into the domain.
The model input parameters concerning the hydraulic behavior of the electrode are listed in Tab. 6.7. Note that the electrode consists mainly of the diffusion layer with the thin reaction layer attached at the left. The parameters for the capillary pressure–saturation relationship are given

Table 6.6: Geometrical and gas distributor parameters

Geometrical parameters [2]	
Length x (L)	0.05 cm
Length y (H)	0.2 cm
Gas distributor parameters	
Channel width (half)	0.05 cm
Shoulder width	0.1 cm
Thermal conductivity, $\lambda^{\text{shoulder}}$	14.7 W K^{-1} m^{-1}
Flow field plate thickness, δ^{shoulder}	0.3 cm
ΔT for cooling	2 K

Table 6.7: Electrode parameters [2]

Diffusion layer parameters	
Diffusion layer thickness	0.045 cm
Porosity, ϕ	0.78
Absolute permeability, **K**	5.20×10^{-11} m^2
Residual water saturation for imbibition process, S_{wr}	0.10
Residual water saturation for drainage process, S_{wr}	0.41
Contact angle water, θ_{water}	143°
Contact angle mercury, θ_{Hg}	141°
Surface tension of water, γ_{water}	0.0625 N m^{-1}
Surface tension of mercury, γ_{Hg}	0.480 N m^{-1}
Constants used in capillary pressure-saturation	
A_1, B_1, C_1, D_1 (Eq. 4.21)	-1168.75, 8.5, -0.2, -700
A_2, B_2, C_2, D_2, E_2 (Eq. 4.20)	-600, 25, -16, -3300, 800
Tortuosity, τ	3
Thermal conductivity, λ	15.6 W K^{-1} m^{-1}
Heat capacity, c_p	710 J kg^{-1} K^{-1}
Reaction layer parameters	
Reaction layer thickness	0.005 cm
Porosity, ϕ	0.07
Tortuosity, τ	5

for both imbibition and drainage process although only the imbibition curves are used in the following examples.

For the relative permeability–saturation functions of the two fluid phases an approach after Bur-

dine [22] is used.

$$k_{rw} = \left[\frac{S_w - S_{wr}}{1 - S_{wr}}\right]^2 \frac{\int_0^{S_w} \frac{dS_w}{p_c^2}}{\int_0^1 \frac{dS_w}{p_c^2}}, \tag{6.7}$$

$$k_{rg} = \left[1 - \frac{S_w - S_{wr}}{1 - S_{wr}}\right]^2 \frac{\int_{S_w}^1 \frac{dS_w}{p_c^2}}{\int_0^1 \frac{dS_w}{p_c^2}}. \tag{6.8}$$

This approach allows a derivation of the relative permeabilities from the shape of the capillary pressure curves.

Table 6.8: Parameters for the electro-chemical reaction [2]

Reversible voltage at $T = 70\ ^\circ$C, U_{rev}	1.191 V
Thermoneutral voltage at $T = 70\ ^\circ$C, U_{th}	1.4836 V
Free activation enthalpy, $\Delta G_0^{\neq}$	73.0×10^3 J mol^{-1}
Cell voltage	0.5 V
Exchange current density ORR i_o^{ref}	1.87×10^{-8} A cm^{-2}
Reference temperature	353.15 K
Reference partial pressure of O_2	5.0×10^5 Pa
Transfer coefficient for oxygen reduction, α	0.5
Surface increasing factor, f_v	60
Electro-osmotic drag coefficient, t_{H_2O}	0.2327
MEA specific resistance R_{spec}	0.25 Ω m^2
Membrane thermal conductivity, λ^M	0.43 W K^{-1} m^{-1}
Membrane thickness, δ^M	87.5 μm

The parameters for the electro-chemical reaction during the fuel-cell operation are given by Tab. 6.8. For more details concerning the electro-chemical processes, we refer to *Acosta et al.* [2]. Here, we will consider them as given and concentrate our attention on the non-isothermal multi-phase multicomponent system in the diffusion layer.
The operational conditions summarized by Tab. 6.9 are of great importance for the flow and transport processes. They will therefore be discussed in context with the boundary conditions below.

Boundary conditions:
The *top* and *bottom* boundaries of the model domain are chosen due to symmetry reasons.

Table 6.9: Operational conditions [2]

Inlet gas pressure	2.013×10^5 Pa
Inlet gas temperature	70 °C
Inlet oxygen mole fraction	0.1775
Inlet water vapor mole fraction	0.1546
Inlet liquid water saturation	0.01
Inlet stream relative humidity	100%

Therefore, they are modeled with *Neumann* no-flow conditions for both mass and heat.

The *left* boundary represents the interface between the membrane and the reaction layer. Since we assume that the electro-chemical reaction occurs completely within the reaction layer, we take this into account by source/sink terms to include the production of water and heat and the consumption of oxygen. The same holds for the sake of simplicity also for the electro-osmotic drag flow of water. Then, the *left* boundary can also be modeled with *Neumann* no-flow conditions.

The *right* boundary is characterized by three distinct segments. The segment in the center of the *right* boundary is the contact surface between the diffusion layer and the shoulder of the current collector. Since this is an impermeable barrier for the fluids, *Neumann* no-flow conditions for the mass components are valid. However, there is a flux of heat across this boundary segment which can be modeled by the following heat flux which is assumed to be constant.

$$q^{\text{shoulder}} = \frac{\lambda^{\text{shoulder}}}{\delta^{\text{shoulder}}}(\Delta T_{\text{cooling}}), \tag{6.9}$$

$\lambda^{\text{shoulder}}$ and δ^{shoulder} are the thermal conductivity and the thickness of the shoulder respectively. Values for both and also for $\Delta T_{\text{cooling}}$, which is assumed to be constant here, are found in Tab. 6.6.

Conventional Flow Field

For $H2 \leq y \leq H$ and $0 \leq y \leq H1$ (i.e. at the inlet of the reacting gases) *Dirichlet* boundary conditions for the oxygen concentration in the gas phase, the liquid water saturation, the total gas pressure, and the temperature are set (see Tab. 6.9).

$$x_g^{\text{O}_2} = x_g^{\text{O}_2,\text{inlet}}, \quad S_w = 0, \quad p_g = p_g^{\text{inlet}}, \quad T = T^{\text{inlet}} \tag{6.10}$$

Since dealing with hydrophobic materials it is assumed for simplicity that the liquid water saturation at the interface between the gas channel and the diffusion layer is near to zero. However, we are aware that during the real operation of the fuel-cell, the liquid water saturation at the interface depends on the actual wettability of the gas diffusion material and on the water vapor content

of the gas stream. Accordingly, a saturation value will establish. One approach to estimate this saturation at the interface could be obtained from a local equilibrium assumption, based on experimentally determined phase distributions for these materials under different operating conditions of water vapor content in the gas phase. Another possibility would be to include the gas flow and the vapor transport in the gas channels into the model. However, this requires an extension of the *Darcy* flow concept to a pipe-flow model in the channels.

Interdigitated Flow Field

For $H2 \leq y \leq H$ and $x = L$ (flow inlet) *Neumann* fluxes of all mass components are set. The ratio of the fluxes is chosen so that the values of the mole fractions given in Tab. 6.9 are obtained at the boundary. For the energy equation a *Dirichlet* condition for the inlet temperature is used.

For $0 \leq y \leq H1$ and $x = L$ (flow outlet) the fluid phases can break through into the gas channel at the fixed outlet pressure p_g^{outlet} (Tab. 6.9). This segment of the boundary rises problems for the choice of appropriate boundary conditions since neither *Dirichlet* conditions for the saturation and the oxygen mole fraction nor the respective fluxes can be determined a-priori since they change during the simulation. Therefore, we extended the domain at the lower segment to $x = 2L$ below the shoulder so that an L-shaped model domain is obtained. This allows to quasi-simulate the ambient region in the gas-channel. The top and bottom of the domain extension are modeled with *Neumann* no-flow conditions while at the right boundary, a *Dirichlet* liquid water saturation of zero is assigned. The extended domain was given a very high permeability in order to reduce the influence of this *Dirichlet* condition on the saturation values in the diffusion layer (no pressure gradient in the domain extension). It is further assumed that the gas is completely mixed in the outlet channel at the interface with the gas diffusion layer. At the outlet of the extended portion the diffusion term is eliminated, to make sure that back-diffusion has no influence on the real model domain. For the energy equation, a free boundary for the enthalpy flow is chosen, so that the heat flux is allowed out of the domain as it occurs due to the respective gradient given at the boundary.

For improving the description of the boundary conditions in the case of an interdigitated flow field, the same considerations as for the conventional flow field are valid (see above).

Initial conditions:
The initial conditions in the model domain for the primary variables are:

$$x_g^{\mathrm{O}_2} = x_g^{\mathrm{O}_2,\text{inlet}}, \quad S_w = 0.25, \quad p_g = p_g^{\text{inlet}}, \quad T = T^{\text{inlet}} \tag{6.11}$$

The model input parameters introduced in this section are used for the simulation of the two different flow fields, where for both cases we present in the following only the results that we obtained from the imbibition curves of capillary pressure and the relative permeabilities derived thereof.

Conventional Flow Field: Results

The steady-state distributions of the oxygen mole fraction in the gas phase, the liquid water saturation, and the temperature are shown in Fig. 6.32. Figure 6.33 gives the local current density profile along the electrode at the interface between the membrane and the reaction layer (this corresponds to the left boundary of the model domain). In the conventional flow field scenario, the gas stream in the channels flows parallel to the diffusion layer. Thus, the oxygen transport into the electrode is predominantly by diffusion since no pressure gradients within the fluid phases can establish due to the boundary conditions. The oxygen is consumed by the reaction on the very left of the domain. This causes a decrease of x_g^o in this region which in turn keeps the diffusive transport upright by establishing a concentration gradient. The liquid water that is produced by the reaction plus the electro-osmotic drag flow of water accumulates and increases the liquid water saturation. The removal of this water from the diffusion layer occurs in reality mainly due to two mechanisms - capillary expulsion, since the medium is hydrophobic, and evaporation. However, in this simulation, the gas stream is assumed to be saturated with water vapor and has therefore no capacity to vaporize additional water.

In Fig. 6.32 one can observe that the water saturation in the reactive region under the shoulder is slightly higher than in the reactive regions under the channels. This effect is clearly caused by the larger distance over which the accumulated water has to be transported to the gas channel. Note that this effect overrides the fact that in this region less water is generated due to the reduced oxygen supply. This is also indicated by the lower current density under the shoulder in Figure 6.33 which corresponds to the distribution of the oxygen concentration in the reaction layer (Fig. 6.32). The current density depends directly on the performance of the reaction and thus on the oxygen availability.

The temperature distribution given in Fig. 6.32 shows slightly higher values in the regions of high current densities and lower values near the shoulder which indicates the cooling effect due to heat conduction in the current collector. The absolute values of the temperature variation within the gas diffusion layer depend on the heat conductivity of the material.

Interdigitated Flow Field: Results

The big difference between the interdigitated flow field and the conventional flow field is that there is now a pressure drop between the inlet and the outlet channels of the gas distributor plates. Thus, the gas flow is forced through the gas diffusion layer which can be seen from the pressure distribution and velocity vectors in Fig. 6.34. The benefit from this flow field is that the advective gas flow enhances the oxygen availability at the reaction layer and utilizes the region under shoulder more efficiently. Further, the removal of the water produced by the reaction and the electro-osmotic drag is enhanced.

The results of the simulations for the interdigitated flow field are shown in Fig. 6.35 (distributions of x_g^c, S_w, T) and in Fig. 6.36 (current density distribution).
The highest oxygen concentration occurs in the inlet region (above the shoulder). From there on, a more or less continuous decrease of x_g^c along the flow-path through the diffusion layer can

be observed due to the consumption at the reaction layer. This corresponds to the curve of the current density profile along the interface to the catalyst reaction layer shown in Fig. 6.36. The current density profile has a different shape than in the conventional flow field (Fig. 6.33) with the lower values at the bottom under the outlet channel. One can further see that here the interdigitated flow field causes an increased average current density compared to the conventional case.

The temperature distribution in the interdigitated case (Fig. 6.35c) differs also from that in the conventional case. Two observations can be made. First, the temperature increases along the flow path of the gas stream from the inlet to the outlet channel and has no distinct cooler region near the shoulder of the current collector. Second, the absolute values of the temperature are higher than in the conventional flow field. The reason for both is supposedly that the conductive cooling flow across the shoulder - which is assumed to be constant, see Eq. (6.9) - is not large enough to compensate the higher heat production rate due to the increased reaction rate (current density).

Summarizing Discussion of the Results

The simulations of the conventional and the interdigitated flow field showed that the model concept is principally appropriate to model the basic multiphase multicomponent transport in the gas diffusion layer of a fuel-cell. However, the comparison with experimental data, as discussed, for example, in *Acosta et al.* (2006) [2], reveals some severe problems of the model that need to be further investigated in the future. The most important problems are:

- The porous material of the gas diffusion layer has mixed hydrophobic/hydrophilic properties. This conclusion can be drawn from experimental observations. Particular at high current densities (low cell voltage), the performance of the fuel-cells deteriorates due to accumulations of liquid water. It could further be observed that the capillary pressure–saturation curves differ significantly for imbibition and drainage (see Figs. 4.22 and 4.23). Thus, the hysteretic behavior of the water-gas system in the gas diffusion layer has a huge impact on the liquid water management in the cell and thus dominates the cell performance. The most important parameter is thereby the residual water saturation.
  The investigation of this behavior still requires thorough fundamental experimental research.

- The description of the boundary conditions at the interface between the gas diffusion layer and the gas channels is based on strong simplifying assumptions in the examples presented above. For the conventional flow field, we assumed to know the liquid water saturation at the interface and the water vapor content in the gas stream. In the interdigitated case, we tried to take the ambient gas channel at the outlet into account by an extension of the model domain. In both cases, we neglected that both parameters can vary along the interface since a state of quasi-equilibrium will establish along the gas channels. While the gas stream enters the gas channel almost dry, it takes up water vapor along the channel and after a certain distance will be saturated with water vapor. In this region, the gas stream is not able to further evaporate liquid water at the interface with the gas diffusion layer and thus, the water accumulates which in turn limits the oxygen transport and the cell performance.

Taking this effect into account by the model concept requires first, that the membrane-electrode assembly is considered three-dimensional. It is further necessary to model the water vapor transport in the gas channel.

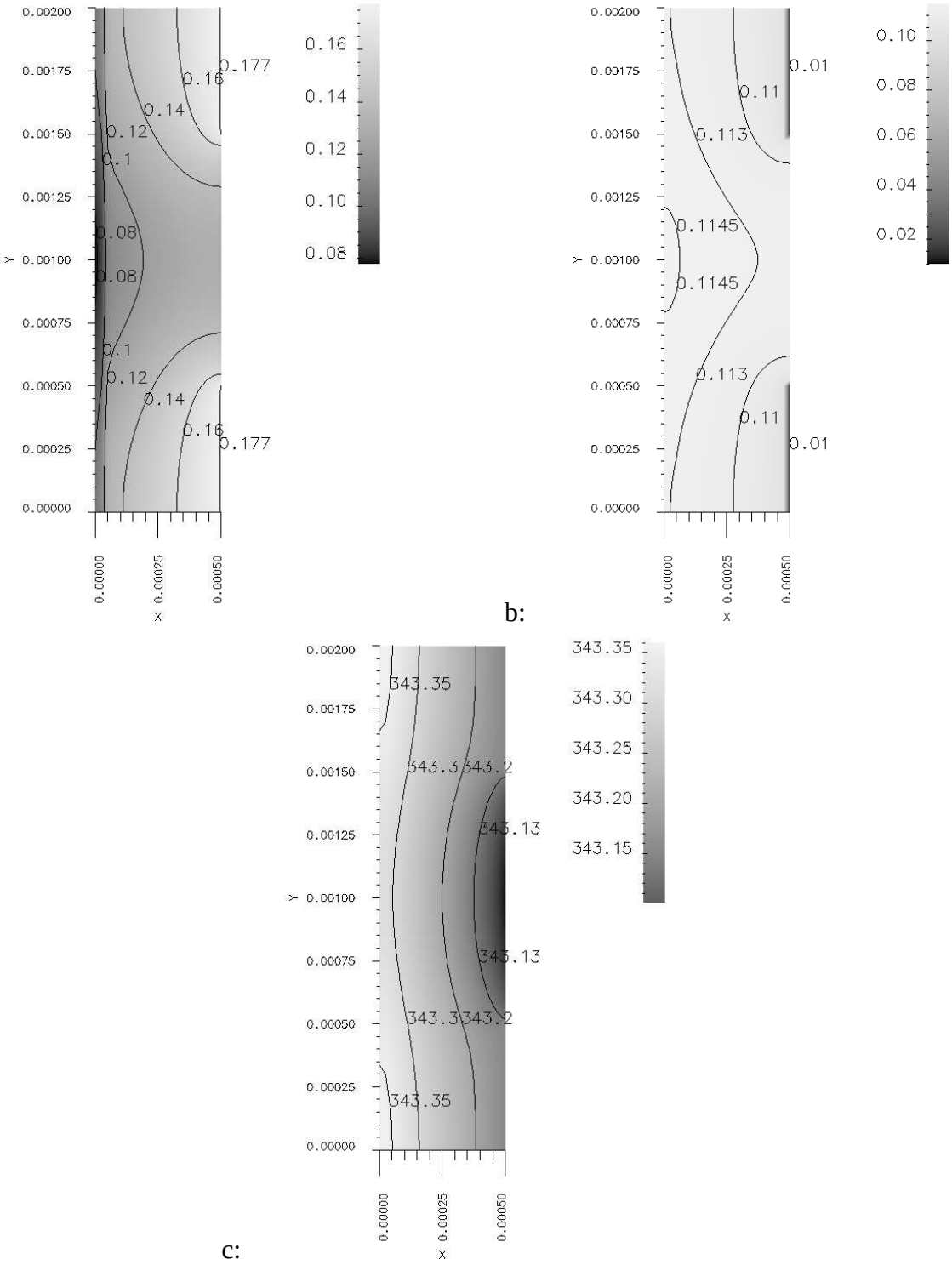

Figure 6.32: Steady-state oxygen concentration (a), liquid water saturation (b) and temperature (c) distribution in the electrode for the imbibition curve - conventional gas distributor (X, electrode thickness and Y, electrode height).

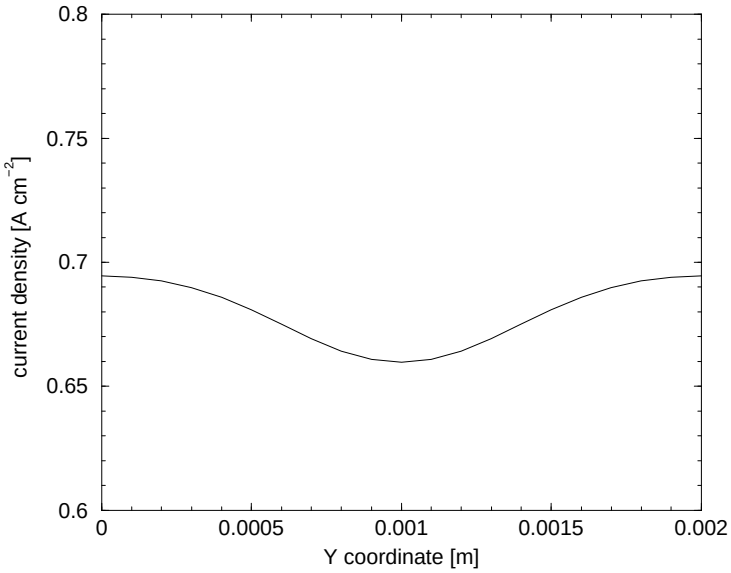

Figure 6.33: Current density distribution at the catalyst layer-membrane interface for the imbibition curve - conventional gas distributor.

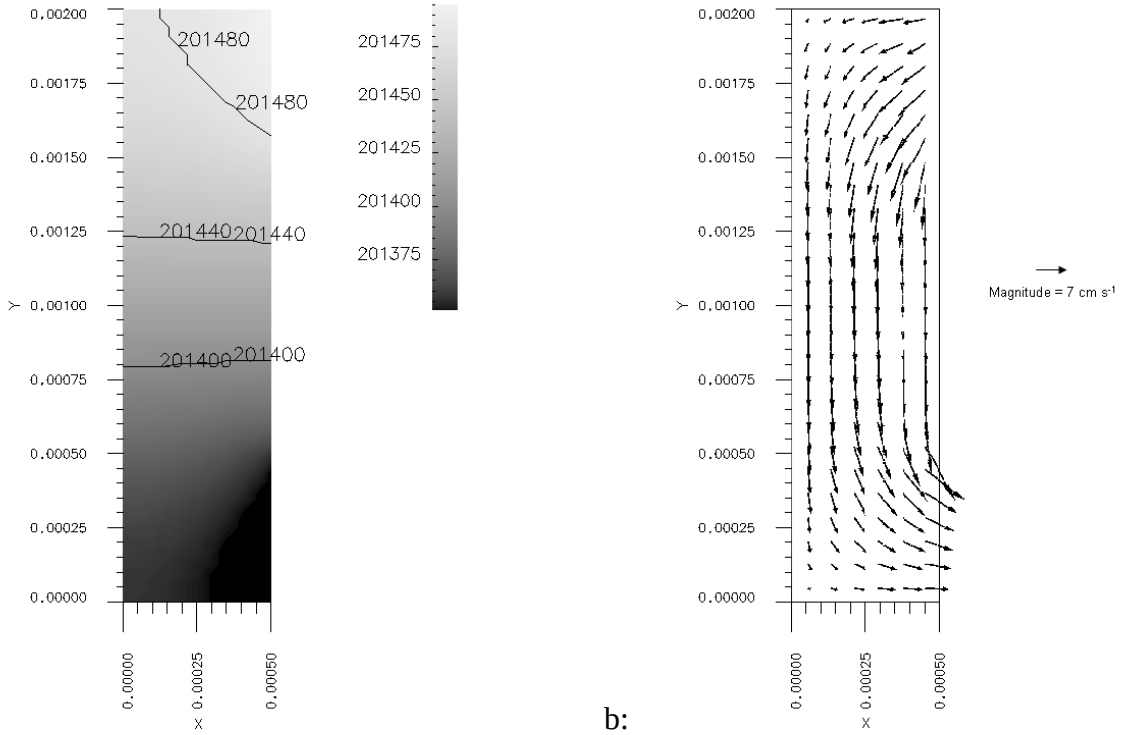

a: b:

Figure 6.34: Steady-state gas pressure distribution and vector plot of the gas velocity in the electrode for the imbibition curve - interdigitated gas distributor (X, electrode thickness and Y, electrode height).

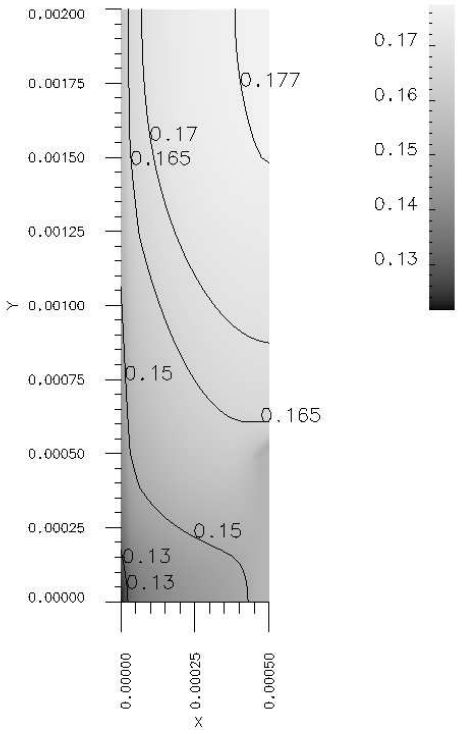

a:

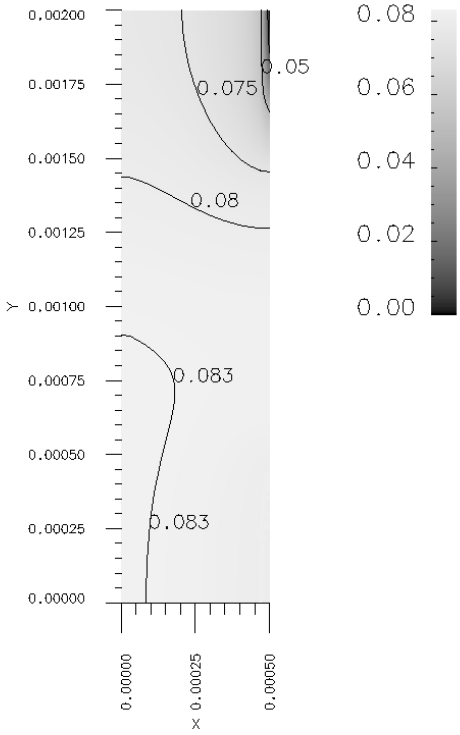

b:

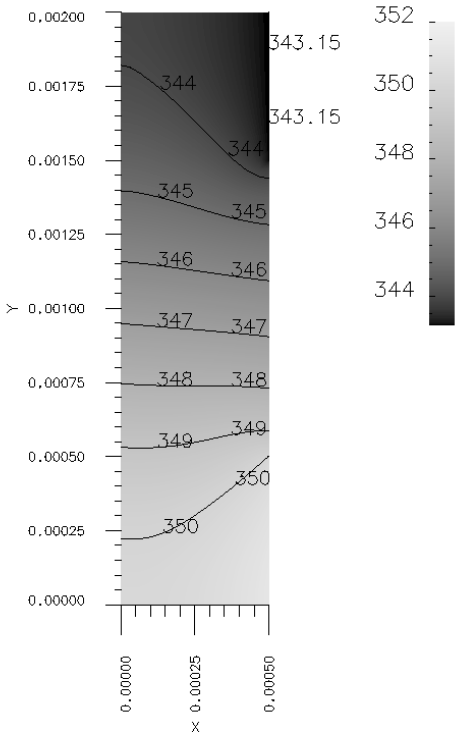

c:

Figure 6.35: Steady-state oxygen concentration (a), liquid water saturation (b) and temperature (c) distribution in the electrode for the imbibition curve - interdigitated gas distributor (X, electrode thickness and Y, electrode height).

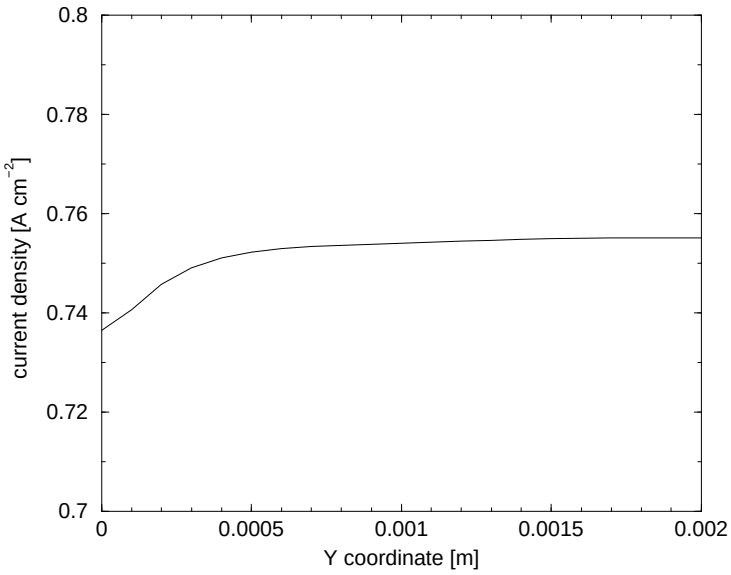

Figure 6.36: Current density distribution at the catalyst layer-membrane interface for the imbibition curve - interdigitated gas distributor.

Chapter 7

Summary and Future Perspectives

7.1 Summary

- Chapter 1 gives a comprehensive introduction and sets the frame and scope of the thesis. The chapter focuses on discussing the different types of porous media, in which the non-isothermal compositional gas-liquid problems, that are addressed by this thesis, are located. While the majority of problems are in the natural subsurface, the fuel-cell represents a technical porous medium. Furthermore, the distinctiveness of gas-liquid processes in comparison to other multiphase systems is explained. This concerns the large differences in the fluid properties between gases and liquids, the involvement of vapors and condensates coupled with heat exchange, the particular influence of the gas phase composition on the fluid properties, and the compressibility of the gas phase.

  At the end of the first chapter, the structure of the thesis and the treatment of the various topics within the following chapters are explained and supported by a graphical illustration.

- Chapter 2 introduces the characteristics of the gas-liquid multiphase flow topics that are addressed in the frame of this thesis. The topics are:

  – Contaminant spreading and retention mechanisms in the unsaturated and saturated zone with a special focus on non-aqueous phase liquids (NAPLs) and a distinction between LNAPLs (lighter than water) and DNAPLs (denser than water).

  – Thermally enhanced remediation techniques for NAPL-contaminated sites including the application in the unsaturated and in the saturated zone, where the dominating processes strongly differ, mainly resulting from the strongly increased influence of buoyant forces in relation to viscous forces in the saturated zone.

  – CO_2 injection into geological formations for the purpose of long-term storage and the mitigation of the greenhouse effect, thereby considering the different target formations that are currently discussed in the scientific community as well as the trapping and potential leakage mechanisms in the target reservoirs.

  – Methane migration in abandoned coal mines, which is a serious problem in the German Ruhr area, where many mines are shut down and the uncontrolled release of

methane from unmined coal seams and its buoyancy-driven migration towards the ground surface poses a threat the urban areas.

– Complex water-gas flow and transport in porous gas diffusion layers of PEM fuel-cells.

– Some brief comments on the deformation of porous media and its influence on the hydraulic properties.

Chapter 2 explains the specific open questions for which numerical models are aimed to contribute. The chapter also discusses the challenges and key issues that are to be considered for the development of appropriate model concepts.

- Chapter 3 first introduces the general concepts of models for multiphase flow in porous media. The basic definitions of the vocabulary are given, the different scales are explained on which the governing processes can be viewed, and the representative elementary volume is introduced which is related to the scale on which the model concept is developed. The fluid properties and hydraulic properties and their description on the REV-scale are explained in detail before the general balance equations for mass and energy are derived using, for example, the *Reynolds transport theorem* and *Darcy's law*.
  The second part of Chapter 3 extends these concepts to compositional and also to non-isothermal processes. A strong focus is thereby on the transfer of mass components between gaseous and liquid phases and the equilibrium conditions that are assumed for the computation of the phase compositions.

- The aim of Chapter 4 is to emphasize the specifically required model adaptations for the different problems and their particular issues that were presented earlier in Chapter 2. All the adaptations are based on the general concepts derived in Chapter 3. The main points are briefly summarized in the following:

  – A three-phase three-component water-air-NAPL concept is required for the modelling of thermally enhanced remediation of NAPL-contaminated sites, for example, by steam injection and simultaneous soil air extraction. One of the difficulties thereby is the description of the very low mutual mixing of the water and NAPL phases and the resulting boiling behavior at a characteristic boiling temperature which is reduced in comparison to the boiling temperatures of the pure fluids.
    Other distinct features are the tertiary diffusion in the three-component system which requires an extension of the binary diffusion approaches and also the consideration of potentially occuring adsorption of components to the solid matrix.

  – Special adaptations are required when numerically simulating an injection of steam into the saturated zone in order to deal with appearing numerical problems. This concerns first of all the blocking of unphysical water back-fluxes due to pressure fluctuations that produce a large pressure peak whenever a discrete volume changes from single-phase water conditions to two-phase water-steam conditions. Secondly, the disappearance of the air component in the saturated zone requires an adaptation of the primary variables since in such cases the primary variables pressure and temperature are coupled via the saturation vapor pressure curve and therefore not

independent of each other. This problem is solved by dropping the mass balance equation for the air component in the regions where the concentration of air becomes less than a certain threshold value.

- The modelling of CO_2 injection for storage in geological formations has to consider the high pressure conditions in the great depths of the reservoirs, including sub- and supercritical conditions for the CO_2 phase. This puts high demands to the constitutive relationships, for example, for the fluid properties density, viscosity, and enthalpy dependent on pressure, temperature, and composition (including salinity). There are only a few approaches available in the literature. They are rather complex and commonly restricted to the properties of pure CO_2 without impurities from other flue gas components. The same difficulties are faced when describing the mutual dissolution behavior of water and CO_2.
- For the modelling of the gas-water processes in gas diffusion layers of PEM fuel-cells, a two-phase three-component model is presented with the components water, nitrogen, and oxygen, where oxygen is consumed by the overall reaction and its transport to the reaction layer is limiting for the performance of the cell. It is therefore important to distinguish between oxygen and nitrogen as the main components of air instead of treating air as a pseudo component with averaged properties. Furthermore, in this section, some first approaches for describing the hydrophobic properties of the porous diffusion layers are introduced.
- At the end of Chapter 4, a brief discussion of fluid-structure interaction problems and deformation processes is given. This basically comprises phenomenological models on the one hand, which consider the influence of structural alteration by simply adapting the hydraulic properties according. On the other hand, fully coupled concepts involving the detailed description of solid displacement and fluid movement, for example, by the theory of porous media, are capable of modelling also strong matrix deformations.

- Chapter 5 gives an overview of the mathematical and numerical methods which are required to solve the non-linear systems of partial differential equations (PDE) that arise from the model concepts of Chapters 3 and 4. At first, the general solution strategy for the multiphase flow equations is presented. Thereby the different formulations, for example, pressure-pressure formulations or pressure-saturation formulations as well as the implementation of boundary conditions is discussed. Furthermore, Chapter 5 addresses the linearization of the set of PDE and the explains the therefore applied *Newton-Raphson* method. Time discretization and spatial discretization is outlined with a closer look at the finite-volume schemes BOX and CVFE, both based on the weighted residuals method.
  It is shown that the choice of the primary variables depends on the local phase state which may change due to phase appearance or disappearance. Therefore, an adaptive substitution algorithm for the switching of primary variables is developed and adopted to the requirements of the specific problems.
  The coupling of different models requires rules for transferring the primary variables (solution vectors) from one model to another one and - if necessary - algorithms that ensure the compatibility of different models by adopting the primary variables or choosing certain assumption for the initialization.

The application and required extension of a multigrid method for the complex non-elliptic problems, as given in this work, is explained before the chapter closes with some investigations of numerical performance, also involving parallel computations and some comments on problems with numerical robustness.

- Chapter 6 presents a number of sample problems which are aimed to demonstrate the application of the different gas-liquid model concepts. The assignment of initial and boundary conditions, as well as the choice of the model domain, the model input parameters, the mesh, etc. are discussed with respect to the individual specific problems. The sample problems include:
  - a steam-injection into a laboratory sand column with a residual NAPL contamination,
  - a study of sequentially coupled models for simulating the infiltration and spreading of a LNAPL spill in the subsurface followed by a thermally enhances soil remediation,
  - a field case example for steam-injection in the saturated zone aiming, for example, at the determination of the thermal radius of influence,
  - a principle study of CO_2 injection into a saline aquifer and the long-term effects of dissolution and fluid transport,
  - a five-spot EGR example aiming at illustrating the effects of CO_2-CH_4 mixing in the gas phase and the thereby influenced recovery rate during an injection of CO_2 into a gas reservoir for enhanced gas recovery, and
  - a comparison and discussion of the modelling results obtained from simulating the water-gas management in the diffusion layer of a PEM fuel-cell, where the oxygen supply is given by either a interdigitated or a conventional flow field.
- This Chapter 7 summarizes the contents and - below - closes the thesis with some final remarks on the demand for further research work in the future and a general concluding discussion.

For an overview of the structure and the topics of this thesis, we refer also to Fig. 1.6.

7.2 Final Remarks

7.2.1 Demand for Further Work

The topics that are covered by this thesis are manifold. So for comprehensivly embracing the demand for future work and research activties, we can distinguish between the individual problem-specific (or: topic-specific) open questions and modelling tasks on the one hand and the general demand for model improvements and further developments on the other hand. The problem-specific open questions were already largely raised earlier in this thesis and we will recollect and extend them below for getting a better overview, which is necessary to detect potential overlaps and to generalize certain issues.

Model Coupling

Regarding the topic of NAPL contaminations and remediation techniques, we already discussed the issue of model adaptation to varying dominating processes. It could be shown that in certain cases the dominating processes change over the time and that an adaptation of the model complexity yields computational benefits. This issue is not exclusive to the NAPL/remediation problems but it occurs as well during CO_2 storage in geological formations, where the relevant processes for the different trapping mechanisms change strongly over time (see Fig. 2.7). It is for the modelling of both problems a key issue to identify the time of a potential sequential model coupling based on a thorough analysis of the relevant processes as for example done in 6.2. If this kind of distinct variation of the processes is not given and an overlap of the time-scales forbids a sequential coupling of different models, then it is necessary to think about other coupling strategies. We belive that in the future the coupling of different models for solving complex problems will gain increasing attention since, regardless of continuously growing hardware capabilities, an efficient usage of computational resources will still be of great importance. Model coupling is not only limited to processes that change over time. It is also an issue for problems that have different subregions of a model domain. An example for this is the coupling of the ”free” gas flow in the gas distribution plate in a fuel-cell with the multiphase ”Darcy” flow in the porous gas diffusion layer. Without considering the strong coupling of these two flow systems it is for both systems hardly possible to take the respective other one into account by boundary conditions [2]. A very similar problem occurs in coal mines when modelling the release of methane from unmined coal seams. While most of the methane is ”drained” by the road and shaft system, part of it migrated through the rock matrix.

Such kinds of multi-physics approaches in a single model domain can also be required on different scales, for example, when a locally restricted complex sub-problem is embedded into a larger domain, in which relatively simple processes dominate. A model with the full complexity of the sub-scale problem would be computationally inefficient and one is endeavoring after a strategy to the less complex global model. A first approach of a multi-scale model coupling is described by *Niessner & Helmig* (2007) [126].
Generally speaking, the art of model coupling comprises the identification of different complexities in space and time and the choice of appropriate ”tools” like implicit or explicit solution of equations, the definition of spatial and temporal scales on which the sub-problems are described and solved, and the mutual consideration of the sub-problems by coupling conditions or boundary conditions.

Model Validation and Verification

Basically, the issue of model validation amd verification is clearly structured for problems where analytical mathematical solutions and well-controlled experimental or field measurement data are available for comparisons with the model results. Yet, the more complex the process, the less at hand are those requirements. In the field of CO_2 storage in geological formations it is even worse since the pressure conditions, at which the storage is typically operated, are very high. This poses high demands on the experimental apparatus and restricts laboratory experiments to very small scales.

In the field, the monitoring of the fate of the injected CO_2 in a formation is of high interest, for example, in the CO_2SINK project in Ketzin (State of Brandenburg/ Germany) [39]. Nevertheless, the remaining uncertainties due to the only course resolution of measurements prevent that such data are sufficient for thorough model validations. Therefore, one has to find other ways for improving the confidence in the mathematical and numerical models.
One option, of which we believe that it is most pragmatical, is an extensive intercomparison of different model approaches by means of appropriate benchmark problems [33]. Comparisons between numerical studies and analytical analyses as well as intercomparisons of different codes are essential (i) to improve the understanding of the complex coupled processes taking place in the formations and (ii) to explore the accuracy and reliability of the models. The benchmark problems that are defined in the frame of the research project *Numerical Investigations of CO2 Sequestration in Geological Formations - Problem-Oriented Benchmarks* funded by the German GEOTECHNOLOGIEN [70] program are specific to certain key issues of a large-scale implementation of underground CO_2 storage. They address, for example, the expected leakage rates from CO_2 disposals through fault zones (abandoned wells or fractures), the mechanisms and processes in enhanced gas recovery systems, or the estimation of storage capacities and the different trapping mechanisms like hydrodynamic trapping and solubility trapping.
Benchmarks can help on the one hand to detect wrong numerical implementations by comparing model results that use the same exactly prescribed equations and input parameters. On the other hand, a rather loose presetting of the model parameters like fluid properties or phase interaction parameters for a certain given problem can show the bandwidth of implementations in different codes and of interpretations and estimations done by the responsible modellers. Both will help to better assess the reliability of numerical simulation results in the addressed fields of application.

Fluid Properties, Hydraulic Properties, and Related Uncertainties

The reliability of numerical simulation results depends crucially on the accuracy of the model input parameters. This concerns in particular the properties of the fluids depending on pressure, temperature, and composition as well as the hydraulic properties which determine the relation between fluxes and their driving forces.
Generally, fluid properties are apparently better (or more reliably) available than hydraulic properties. Properties of pure fluids are commonly found in the literature for a wide range of pressure and temperature conditions. The determination of the properties of a fluid phase that consists of more than one component is more complex. In the case of only very diluted concentrations, the influence of a dissolved component may be negligible, for example, in the water-NAPL-air systems described in this work, where dissolved NAPL and air in the water phase have no significant effect on density, viscosity, enthalpy, and internal energy. However, for example, the gas phase properties are in most cases a strong function of the phase composition. Also, in CO_2-water systems the influence of mutual mass transfer (dissolution, evaporation) as well as the presence of other constituents like salt cannot be neglected for an accurate description of the fluid phase properties. Therefore, it is an important task to provide reliable equations of state that are capable of taking the influence of pressure, temperature, and composition into account. In the CO_2 sequestration business, this problem is likely to become even more challenging in the future. While recently most modellers assumed the injection of pure CO_2 in their simulation

studies of CO_2 injection and storage scenarios, there remains the task to quantify the influence of impurities on the fluid properties. The concentration of CO_2 in the injected gas is aimed to be near to 100%. However, depending on the capturing technology in the power plants, there will always be impurities due to other flue gas components like nitrogen or sulfur compounds. Depending on the mass fractions in the injected gas, this can alter the properties of the CO_2 phase, for example, a shift of the critical point towards higher pressures so that the density of the injected gas in a certain depth is increased in comparison to pure CO_2 injection. Presently, there are practically no thorough approaches available which consider the effects of impurities on the CO_2 phase properties quantitatively. Therefore, we consider this to be one of the most-needed fields of research in order to improve the reliability of numerical simulators for injection and storage scenarios.

Another great source of uncertainties in the numerical simulation results is the quantitative description of the hydraulic properties, in particular the intrinsic permeabilities, porosities, and the relationships between phase saturations, relative permeabilities, and capillary pressure. The determination of the intrinsic permeabilities and porosities is mainly a sub-task of the site exploration and depends, for example, on the availability of drilling cores, seismic data, etc., whereas the parameterizations for relative permeability–saturation and capillary pressure–saturation relationships cannot be directly measured in the field. The relative permeability and capillary pressure functions depend on the soil type, which in turn is characterized by intrinsic permeability and porosity, and of course also by other factors like grain size distribution, chemical composition, etc. In any case, for field problems the degree of knowledge about the distribution of the soil types in the model is also decisive for the reliability of the applied parameterizations for relative permeabilities and capillary pressures. The problem aggravates when we become aware that the parameterizations of these hydraulic properties themselves reveal significant uncertainties and non-uniquenesses, for example, caused by hysteretic or dynamic effects.
While most soils are typically hydrophilic, we discussed in this work that this holds not for the gas diffusion layer in PEM fuel-cells. These layers are hydrophobized in order to make the water repellent and to prevent performance-limiting accumulations of water that is produced by the reaction or by electro-osmotic drag. In particular for such systems on very small scales there exist almost no measurement data for capillary pressure–saturation relationships. There is even a strong demand for first developing appropriate measurement techniques.

Flow Instabilities

The development of flow instabilities in porous media flow system has been discussed only at the margin of this work. Fingering effects occur when a less-viscous fluid displaces a more-viscous resident fluid. In porous media, the decisive quantity is rather the ratio of the mobilities than the ratio of the viscosities. This also takes the relative permeabilities as functions of the saturations into account. Fingering is also observed, when a fluid phase of higher density is layered above a less dense fluid. We discussed this for CO_2-enriched brine which has a higher density than the ambient brine so that CO_2-rich fingers evolve in downward vertical direction. The length and number of fingers in the simulations was dependent on the discretization length for homogeneous conditions. For heterogeneous porous media it is expected that the permeability distribution in the subsurface strongly affects the triggering and the number and size of develop-

ing fingers. Although there exists already a considerable amount of literature on flow instabilities, it is still necessary to extend theoretical approaches and analyses and to make them applicable for quantitative estimations in practically relevant scenarios.

7.2.2 General Concluding Discussion

This thesis presented a number of different topics which are characterized by non-isothermal compositional gas-liquid processes in a porous medium. It could be shown that the governing processes reveal significant similarities and that the general approach for modelling them can be adopted to many specific problems and applications.

The model concepts were implemented into the numerical simulator MUFTE-UG within a number of research projects, hence a powerful tool could be provided for dealing with a variety of engineering problems and open questions in current research. One could mention, for example, the sample problem of Sec. 6.3. There, we showed that the application of the numerical model within a pilot-study for the remediation of a NAPL-contaminated subsurface zone essentially supported the decision about the number of required wells for steam-injection and extraction. This helped to minimize the costs for the wells and other infrastructure on the remediation site.

While the application of numerical simulation capabilities for contaminant spreading and remediation or natural attenuation processes may become common engineering practice in the near future, this does not yet hold for the field of CO_2 storage in geological formations. Nevertheless, CO_2 sequestration is of utmost societal importance which is evidenced by the overall international initiatives of politics and science to develop methods for the mitigation of the climate change by reducing the concentration of greenhouse gases in the atmosphere. This recently also evoked great efforts on further developing the existing model capabilities in environmental and petroleum engineering to model the processes of CO_2-injection into deep geological formations including the different trapping and leakage mechanisms. Such models are urgently needed for improving the understanding of the strongly coupled thermal, hydraulic, chemical, and mechanical processes on the different time-scales, see also Secs. 6.4 and 6.5. Numerical models are also inevitable for risk assessment and studies of feasibility, for example, with regard to technical or economical issues.

A similarly important current research field is the development of fuel-cells as an alternative to fossil-fired engines. Here are numerical gas-liquid flow models in the complex structures of the gas diffusion layer and the neighboring gas distribution channels also needed. Recently there is intensive research on the improvement of the models, in particular with respect to the coupling of the porous media gas-liquid flow systems in the diffusion layer and the free gas flow in the gas channels.

This thesis is aimed at giving a contribution to the understanding of the complex interacting processes in non-isothermal compositional gas-liquid flow systems in porous media. The discussions of the different open questions and the specific research topics were intended to outline the challenges of upcoming work in the near future. One of the major challenges is undoubtedly the validation and verification of mathematical or numerical models. By the time of finishing this

work, the author and his colleagues prepare an international workshop on numerical models for carbon dioxide storage in geological formations [33]. The main goal of this workshop is to evaluate the reliability of mathematical and numerical simulators by an extensive benchmark study related to specific current problems and questions. The author is also a member of the Dutch-German research training group *NUPUS* (Non-linearities and UPscaling in PoroUS media) [129]. There, gas-liquid processes play an important role in several projects related to CO_2 storage or fuel-cells. This also shows the relevance of the models and provides the motivation to further improve them.

Bibliography

[1] M. Aalto and K.I. Keskinen. Liquid Densities at High Pressures. *Fluid Phase Equilibria*, 29:183–205, 1999.

[2] M. Acosta, C. Merten, G. Eigenberger, H. Class, R. Helmig, B. Thoben, and H. Müller-Steinhagen. Modeling non-isothermal two-phase multicomponent flow in the cathode of PEM fuel cells. *Journal of Power Sources*, 9:1123–1141, 2006.

[3] A.W. Adamson. *Physical Chemistry of Surface*. Wiley, New York, 4. edition, 1982.

[4] T. Adrian, M. Wendland, H. Hasse, and G. Maurer. High-pressure multiphase behaviour of ternary systems carbon dioxide-water-polar solvent: review and modeling with the Peng-Robinson equation of state. *Journal of Supercritical Fluids*, 12:185–221, 1998.

[5] A. Assteerawatt, P. Bastian, A. Bielinski, T. Breiting, H. Class, A. Ebigbo, H. Eichel, S. Freiboth, R. Helmig, A. Kopp, J. Niessner, S. O. Ochs, A. Papafotiou, M. Paul, H. Sheta, D. Werner, and U. Ölmann. MUFTE-UG: Structure, Applications and Numerical Methods. *Newsletter, International Groundwater Modeling Centre, Colorado School of Mines*, 23(2), 10/2005.

[6] P.W. Atkins. *Physikalische Chemie*. VCH, Weinheim, 2. edition, 1996.

[7] K. Aziz and A. Settari. *Petroleum Reservoir Simulation*. Applied Science Publishers, London, 1979.

[8] B. Barczewski and H.-P. Koschitzky. The VEGAS Research Facility. Technical equipment and research projects. In H. Kobus, B. Barczewski, and H.-P. Koschitzky, editors, *Groundwater and Subsurface Remediation*, pages 129–157. Springer Verlag, Berlin Heidelberg, 1996.

[9] P. Bastian. Numerical Computation of Multiphase Flows in Porous Media. Habilitation, Technische Fakultät, Christian–Albrechts–Universität Kiel, 1999.

[10] P. Bastian. Higher order discontinuous galerkin methods for flow and transport in porous media. In E. Bänsch, editor, *Challenges in Scientific Computing - CISC 2002.*, volume 35, pages 1–22. 2003.

[11] P. Bastian and R. Helmig. Efficient Fully-Coupled Solution Techniques for Two Phase Flow in Porous Media. Parallel Multigrid Solution and Large Scale Computations. *Adv. Water Resour.*, 23:199–216, 1999.

[12] K.-J. Bathe. *Finite Element Procedures in Engineering Analysis*. Prentice-Hall, Inc., Englewood Cliffs, New Jersey, 1982.

[13] A. Battistelli, C. Calore, and K. Pruess. The Simulator TOUGH2/EWASG for Modelling Geothermal Reservoirs with Brines and Non-condensible Gas. *Geothermics*, 26,4:437–464, 1997.

[14] M. Batzle and Z. Wang. Seismic Properties of Pore Fluids. *Geophysics*, 57:1396–1408, 1992.

[15] J. Bear. *Dynamics of Fluids in Porous Media*. Elsevier, New York, 1972.

[16] J. Bear and Y. Bachmat. *Introduction to Modeling of Transport Phenomena in Porous Media*. Kluwer Academic Publishers, The Netherlands, 1990.

[17] C. Betz. *Wasserdampfdestillation von Schadstoffen im porösen Medium: Entwicklung einer thermischen in-situ Sanierungstechnologie*. PhD thesis, Mitteilungsheft 97, Institut für Wasserbau, Universität Stuttgart, 1997.

[18] A. Bielinski. *Numerical Simulation of CO_2 Sequestration in Geological Formations*. PhD thesis, Institut für Wasserbau, Universität Stuttgart, 2006.

[19] T. Breiting, R. Hinkelmann, H. Sheta, and R. Helmig. Coupling of hydroinformatic methods and techniques for the simulation of gas-water flow processes in the subsurface. In J. Ganoulis and P. Prinos, editors, *30th IAHR Congress: Water Engineering and Research in a Learning Society, August 2003, Thessaloniki, Greece*, pages 263–270, 2003.

[20] A.N. Brooks and A.T. Corey. Hydraulic Properties of Porous Media. In *Hydrol. Pap.* Fort Collins, Colorado State University, 1964.

[21] E. Buckingham. Studies on the movement of soil moisture. *USDA Bureau of Soils, Washington, DC*, Bulletin 38, 1907.

[22] N.T. Burdine. Relative permeability calculations from pore–size distribution data. Technical report, Petroleum Transactions, Aime, 1953.

[23] A. Busch, Y. Gensterblum, B.M. Krooss, and N. Siemons. Investigation of High-Pressure Selective Adsorption/Desorption Behaviour of CO2 and CH4 on Coals: An Experimental Study. *International Journal of Coal Geology*, 66:53–68, 2006.

[24] K.F. Busch, L. Luckner, and K. Tiemer. *Lehrbuch der Hydrogeologie, Band 3: Geohydraulik*. Gebrüder Borntraeger, Berlin, Stuttgart, 3. edition, 1993.

[25] M. Celia, T. Russel, I. Herrera, and R. Ewing. An eulerian-lagrangian localized adjoint method for the advection-diffusion equation. *Adv. Water Resour.*, 13(4):187–206, 1990.

[26] M.A. Celia and P. Binning. A Mass Conservative Numerical Solution for Two–Phase Flow in Porous Media With Application to Unsaturated Flow. *Water Resour. Res.*, 28:2819–2828, 1992.

[27] Y.B. Chang. *Development and Application of an Equation of State Compositional Simulator.* PhD thesis, University of Texas at Austin, 1990.

[28] I. Chatzis and F.A. Dullien. Dynamic immiscible displacement mechanisms in pore doublets: theory versus experiment. *J. of Colloid and Interface Science*, 91(1):199–222, 1983.

[29] G. Chavent and J. Jaffre. *Mathematical Models and Finite Elements for Reservoir Simulation*. North-Holland, 1978.

[30] H. Class. *Theorie und numerische Modellierung nichtisothermer Mehrphasenprozesse in NAPL–kontaminierten porösen Medien*. PhD thesis, Mitteilungsheft 105, Institut für Wasserbau, Universität Stuttgart, 2001.

[31] H. Class, A. Bielinski, R. Helmig, A. Kopp, and A. Ebigbo. Numerische simulation der speicherung von co$_2$ in geologischen formationen. In W. Arlt and G. Kreysa, editors, *Chemie Ingenieur Technik - Themenheft: Kohlendioxid und Klimaschutz*, volume 78, pages 445–452. Wiley-VCH, Weinheim, 2006.

[32] H. Class, A. Ebigbo, and R. Helmig. Benchmark problems on enhanced methane recovery in combination with carbon dioxide storage in depleted gas reservoirs. *to be submitted to International Journal of Greenhouse Gas Control*, 2007.

[33] H. Class, A. Ebigbo, A. Kopp, R. Helmig, M. Darcis, H. Dahle, J. Nordbotten, and M. Celia. Workshop on Numerical Models for Carbon Dioxide Storage in Geological Formations, Stuttgart, April 2.-4. 2008. `http://www.iws.uni-stuttgart.de/co2-workshop/`.

[34] H. Class and R. Helmig. Numerical Simulation of Nonisothermal Multiphase Multicomponent Processes in Porous Media - 2. Applications for the Injection of Steam and Air. *Adv. Water Resourc.*, 25:551–564, 2002.

[35] H. Class, R. Helmig, and P. Bastian. Numerical Simulation of Nonisothermal Multiphase Multicomponent Processes in Porous Media - 1. An Efficient Solution Technique. *Adv. Water Resourc.*, 25:533–550, 2002.

[36] H. Class, R. Helmig, and I. Neuweiler. Sequential coupling of models for contaminant spreading in the vadose zone. *submitted to Vadose Zone Journal*, 2007.

[37] C. Clauser. *Numerical Simulation of Reactive Flow in Hot Aquifers, SHEMAT and Processing SHEMAT*. Springer, 2003.

[38] CMWR XVI - Computational Methods in Water Resources, Copenhagen, Denmark, June 19-22, 2006. *Numerical Modeling of CO_2 Sequestration in Geologic Formations - Recent Results and Open Challenges.*, 2006.

[39] CO_2SINK consortium. CO_2SINK - CO_2 Storage by Injection into a Saline Aquifer at Ketzin. `http://www.co2sink.org`.

[40] K.H. Coats. Simulation of steamflooding with distillation and solution gas. *Society of Petroleum Engineers Journal*, October 1976.

[41] K.H. Coats, W.D.G. Chieh Chu, and B.E. Marcum. Three–dimensional simulation of steamflooding. *Society of Petroleum Engineers Journal*, December 1974.

[42] S. Crone, C. Bergins, and K. Strauss. Multiphase flow in homogeneous porous media with phase change. part i: Numerical modeling. *Transport in Porous Media*, 49:291–312, 2002.

[43] H. Darcy. *Les fontaines de la ville de Dijon*. Dalmont, Paris, 1856.

[44] T. E. Daubert and R. P. Danner. *Physical and thermodynamic properties of pure chemicals: data compilation*. Design Institute for Physical Property Data, 1989.

[45] R. de Boer. *Theory of Porous Media*. Springer-Verlag, 2000.

[46] DELPHIN4. Simulation program for coupled Heat, Air, Moisture and Salt transport in capillary porous building materials. `http://http://bauklimatik-dresden.de/delphin/delphin_description.html`.

[47] E. Ditterich. Wirbel um den Bodenschutz. *Umweltmagazin Nr. 4*, April 1996. Vogel Verlag, Würzburg.

[48] J. Divisek, J. Fuhrmann, K. Gärtner, and R. Jung. Performance modeling of a direct methanol fuel cell. *Journal of The Electrochemical Society*, 150(6):A811–A825, 2003.

[49] J. Douglas Jr and T. Russel. Numerical methods for convection dominated diffusion problems based on combining the method of characteristics with finite element or finite difference procedures. *SIAM J. Numer. Anal.*, 19(5):871–885, 1982.

[50] Z. Duan, N. Møller, and J.H. Weare. An equation of state for the CH_4-CO_2-H_2O system: I. Pure systems from 0 to 1000°C and 0 to 8000 bar. *Geochemica et Cosmochimica Acta*, 56:2605–2617, 1992.

[51] Z. Duan, N. Møller, and J.H. Weare. An equation of state for the CH_4-CO_2-H_2O system: II. Mixtures from 50 to 1000°C and 0 to 1000 bar. *Geochemica et Cosmochimica Acta*, 56:2619–2631, 1992.

[52] Z. Duan and R. Sun. An Improved Model Calculating CO_2 Solubility in Pure Water and Aqueous NaCl Solutions from 273 to 533 K and from 0 to 2000 bar. *Chem. Geol.*, 193:257–271, 2003.

[53] A. Ebigbo. Thermal Effects of Carbon Dioxide Sequestration in the Subsurface. Master's thesis, Institut für Wasserbau, Universität Stuttgart, 2005.

[54] A. Ebigbo, H. Class, and R. Helmig. CO2 Leakage through an Abandoned Well: Problem-Oriented Benchmarks. *Computional Geosciences*, 11(2):103–115, 2006.

[55] W. Ehlers. Grundlegende Konzepte in der Theorie poröser Medien. *Technische Mechanik*, 16:63–76, 1996.

[56] H. Eichel, R. Helmig, I. Neuweiler, and O.A. Cirpka. Upscaling of two-phase flow processes in porous media. In D.B. Das and S.M. Hassanizadeh, editors, *Upscaling Multiphase Flow in Porous Media.* Springer Verlag, 2005.

[57] M. Emmert. *Numerische Simulation von isothermen/ nichtisothermen Mehrphasenprozessen unter Berücksichtigung der Veränderung der Fluideigenschaften*. PhD thesis, Institut für Wasserbau, Universität Stuttgart, 1997.

[58] R. Falta. Numerical modeling of kinetic interphase mass transfer during air sparging using a dual-media approach. *Water Resour. Res.*, 36(12), 2000.

[59] R.W. Falta, K. Pruess, I. Javandel, and P.A. Witherspoon. Numerical Modeling of Steam Injection for the Removal of Nonaqueous Phase Liquids From the Subsurface. 1. Numerical Formulation. *Water Resour. Res.*, 28,2:433–449, 1992.

[60] A. Färber. *Wärmetransport in der ungesättigten Bodenzone: Entwicklung einer thermischen in-situ Sanierungstechnologie*. PhD thesis, Mitteilungsheft 96, Institut für Wasserbau, Universität Stuttgart, 1997.

[61] A. Fenghour, W.A. Wakeham, and V. Vesovic. The Viscosity of Carbon Dioxide. *J. Phys. Chem. Ref. Data*, 27(1):31–44, 1998.

[62] C.W. Fetter. *Contaminant Hydrogeology*. Prentice-Hall, Inc., New Jersey, 2. edition, 1998.

[63] S. Finsterle. iTOUGH2 User's Guide. Technical report, Lawrence Berkeley National Laboratory, University of California, 1999. LBNL-40040.

[64] P.A. Forsyth. Three dimensional modeling of steam flush for DNAPL site remediation. Technical report, Dep. of Computer Science, University of Waterloo, 1993. CS-93-56.

[65] P.A. Forsyth and B.Y. Shao. Numerical simulation of gas venting for NAPL site remediation. *Adv. Water Resour.*, 14:354–367, 1991.

[66] S. Freiboth, H. Class, R. Helmig, T. Graf, W. Ehlers, and V. Schwarz. A model for multiphase flow and transport in porous media including a phenomenological approach to account for deformation. *to be submitted to Computational Goesciences*, 2007.

[67] J. Garcia. Density of Aqueous Solutions of CO_2. Technical report, LBNL Report 49023, Lawrence Berkeley National Laboratory, Berkeley, CA, U.S.A., 2001.

[68] J. Garcia and K. Pruess. Flow Instabilities During Injection of CO_2 into Saline Aquifers. In *Proceedings, TOUGH Symposium 2003*. Lawrence Berkeley National Laboratory, 2003.

[69] S.E. Gasda, S. Bachu, and M.A. Celia. Spatial characterization of the location of potentially leaky wells penetrating a deep saline aquifer in a mature sedimentary basin. *Environmental Geology*, 46:707–720, 2004.

[70] GEOTECHNOLOGIEN - A geoscientific research and development programme funded by the Federal Ministry of Education and Research (BMBF) and the German Research Foundation (DFG). CO_2SINK - CO_2 Storage by Injection into a Saline Aquifer at Ketzin. `http://www.geotechnologien.de`.

[71] T. Graf and W. Ehlers. Modelling of multiphase flow phenomena in deformable porous materials under consideration of thermal effects. *PAMM*, 5:395–396, 2005.

[72] C. Grass. Untersuchung von Randbedingungen bei der numerischen Simulation von Zweiphasenströmungen in porösen Medien (Investigation of boundary conditions for the numerical simulation of two-phase flow in porous media). Master's thesis, Institut für Wasserbau, Universität Stuttgart, 2005.

[73] J. Grunewald. *Diffusiver und konvektiver Stoff- und Energietransport in kapillarporösen Baustoffen.* Verlag TU Dresden, 1997.

[74] J. Gudbjerg, O. Trötschler, A. Färber, T.O. Sonnenborg, and K.H. Jensen. On spurious water flow during numerical simulation of steam injection into water-saturated soil. *Journal of Contaminant Hydrology*, 75:297–318, 2004.

[75] W.D. Gunter, E.H. Perkins, and T.J. McCann. Aquifer disposal of CO2-rich gases: reaction design for added capacity. *Energy Conversion and Management*, 34:941–948, 1993.

[76] W. Hackbusch. *Multi–grid methods and applications*. Springer Verlag, Berlin, 1985.

[77] S.M. Hassanizadeh, M.A. Celia, and H.K. Dahle. Dynamic effect in the capillary pressure - saturation relationship and its impact on the unsaturated flow. *Vadose Zone Hydrology*, 1:38–57, 2002.

[78] R. Helmig. *Multiphase Flow and Transport Processes in the Subsurface - A Contribution to the Modeling of Hydrosystems*. Springer Verlag, 1997.

[79] R. Helmig, H. Class, R. Huber, H. Sheta, R. Ewing, R. Hinkelmann, H. Jakobs, and P. Bastian. Architecture of the Modular Program System MUFTE-UG for Simulating Multiphase Flow and Transport Processes in Heterogeneous Porous Media. *Mathematische Geologie*, 2:123–131, 1998.

[80] R. Helmig and R. Huber. Comparison of Galerkin-type discretization techniques for two-phase flow in heterogeneous porous media. *Adv. Water Resour.*, 21,8:697–711, 1998.

[81] R. Helmig, H. Sheta, H. Meiners, and E. Kunz. Numerische Simulation von Gasströmen im Grubengebäude und im Gebirge. *Glückauf*, 142:37–44, 2006.

[82] R. Hilfer and R. Helmig. Dimensional analysis and upscaling of two-phase flow in porous media with piecewise constant heterogeneities. *Adv. Water Resour.*, 27(10):1033–1040, 2004.

[83] M. Hilpert, R. Glantz, and C.T. Miller. Calibration of a pore-network model by a pore-morphological analysis. *Transport in Porous Media*, 51(3):267–285, 2003.

[84] R. Hinkelmann, T. Breiting, K. Kobayashi, R. Helmig, and H. Sheta. Application of hydroinformatic methods and techniques for complex systems - quantification of methane migration processes from abandoned coal mines. In S.Y. Liong, K.K. Phoon, and V. Babovic, editors, *6th International Conference on Hydroinformatics, June 21-24, 2004*, volume 1, pages 222–229. World Scientific Publishing Company, 2004.

[85] C. Hirsch. *Numerical Computation of Internal and External Flow. Volume 1: Fundamentals of Numerical Discretization*. John Wiley & Sons, 1988.

[86] J.O. Hirschfelder, C.F. Curtiss, and R.B. Bird. *Molecular theory of gases and liquids*. John Wiley & Sons, New York, 1954.

[87] S. Hölzemann, H. Class, and R. Helmig. A new concept for the numerical simulation and parameter identification of multiphase flow and transport processes in cohesive soils. In *Unsaturated Soils: Numerical and Theoretical Approaches. Proceedings of the International Conference 'From Experimental Evidence towards Numerical Modeling of Unsaturated Soils', Weimar, Germany, September 18-19, 2003*, volume 2, 2005. Springer Verlag Berlin-Heidelberg.

[88] G.M. Homsy. Viscous fingering in porous media. *Ann. Rev. Fluid Mech.*, 19:271–311, 1987.

[89] R. Huber. *Immiscible and Compositional Multiphase Flow and Transport in Heterogeneous Porous Media: Modelling, Formulation, and Numerical Simulation*. PhD thesis, Institut für ComputerAnwendungen im Bauingenieurwesen, TU Braunschweig, 1999.

[90] R. Huber and R. Helmig. Node–centered finite volume discretizations for the numerical simulation of multiphase flow in heterogeneous porous media. *Journal of Computational Geosciences*, 4(2):141–164, 2000.

[91] M.-J. Huron and J. Vidal. New Mixing Rules in Simple Equations of State for Representing Vapour-Liquid Equilibria of Strongly Non-Ideal Mixtures. *Fluid Phase Equil.*, 3:255–271, 1979.

[92] P.S. Huyakorn and G.F. Pinder. *Computational Methods in Subsurface Flow*. Academic Press, London, 1983.

[93] International Formulation Committee. A formulation of the thermodynamic properties of ordinary water substance. Technical report, IFC Sekretariat, Düsseldorf, Germany, 1967.

[94] IAPWS (The International Association for the Properties of Water and Steam). Revised Release on the IAPS Formulation 1985 for the Viscosity of Ordinary Water Substance. http://www.iapws.org/, 2003.

[95] IPCC. Special Report on Carbon Dioxide Capture and Storage. Technical report, Intergovernmental Panel on Climate Change (IPCC), prepared by Working Group III (Metz, B., O. Davidson, H.C. de Conink, M. Loos, and L.A. Meyer (eds), Cambridge University Press, Cambridge, United Kingdom and New York, NY, USA, 2005.

[96] K. Johannsen, S. Oswald, R. Held, and W. Kinzelbach. Numerical simulation of threedimensional saltwater-freshwater fingering instabilities observed in a porous medium. *Adv. Water Resour.*, 29,11:1690–1704, 2006.

[97] R. Juanes, H.S. Al-Shuraiqi, A.H. Muggeridge, C.A. Grattoni, and M.J. Blunt. Experimental and numerical validation of an analytical model of viscous fingering in two-phase three-component flow. *submitted Journal of Fluid Mechanics.*, 2005. available as preprint at http://web.mit.edu/juanes/www/papers/preprints/jfm-visc.pdf.

[98] R. Juanes, E.J. Spiteri, F.M. Orr, and M.J. Blunt. Impact of relative permeability hysteresis on geological co_2 storage. *Water Resour. Res.*, 42, 2006.

[99] H. Kobus and U. De Haar. Perspektiven der Wasserforschung. Technical report, Deutsche Forschungsgemeinschaft, 1995.

[100] O. Kolditz, W. Wang, J. de Jonge, M. Xie, and S. Bauer. A process-oriented approach to compute thm problems in porous media - part 1: Theoretical and informatics background - part 2: Numerical applications. *Springer Proceedings in Physics 94*, 2:53–65, 2004.

[101] L.W. Lake. *Enhanced Oil Recovery*. Prentice-Hall, Inc., Englewood Cliffs, New Jersey, 1989.

[102] C.S. Land. Calculation of imbibition relative permeabilities for two- and three-phase flow from rock properties. *Soc. Pet. Eng. J.*, 243:149–156, 1968.

[103] R.J. Lenhard. Scaling fluid content–pressure relations of different fluid systems in porous media. In H.J. Morel-Seytoux, editor, *14th Annual American Geophysical Union Hydrology Days*, volume CA:223–235, Atherton, 1994. Hydrology Days Publ.

[104] R.J. Lenhard, J.C. Parker, and J.J. Kaluarachchi. Comparing simulated and experimental hysteretic two-phase transient fluid flow phenomena. *Water Resour. Res.*, 27(8):2113–2124, 1991.

[105] R.J. Lenhard, J.C. Parker, and S. Mishra. On the correspondence between Brooks–Corey and Van Genuchten models. *Journal of Irrigation and Drainage Engineering*, 115(4):744–751, 1989.

[106] F.W. Letniowski and P.A. Forsyth. A control volume finite element method for three-dimensional napl groundwater contamination. *Int. J. Num. Meth. Fluids*, 13:955–970, 1991.

[107] R. J. LeVeque. *Numerical Methods for Conservation Laws*. Birkhäuser, 1992.

[108] M.C. Leverett. *Capillary Behavior in Porous Solids*, volume 142. AIME Transactions, 1941.

[109] Y. Li and R.T. Johns. Rapid Flash Calculations for Compositional Simulation. *SPE Reservoir Evaluation & Engineering*, 9(5):521–529, 2006. 95732-PA.

[110] D.R. Lide. *CRC Handbook of Chemistry and Physics*. CRC Press, Boca Raton, 1995.

[111] D.R. Lide and H.V. Kehiaian. *CRC Handbook of Thermophysical and Thermochemical Data*. CRC Press, Boca Raton, 1994.

[112] B.B. Looney and R.W. Falta. *Vadose Zone*. Battelle Press, Columbus, OH, 2000.

[113] S. Manthey. *Two-Phase Flow Processes with Dynamic Effects in Porous Media - Parameter Estimation and Simulation*. PhD thesis, Institut für Wasserbau, Universität Stuttgart, 2006.

[114] S. Manthey, S.M. Hassanizadeh, and R. Helmig. Macro-scale dynamic effects in homogeneous and heterogeneous porous media. *Transport in Porous Media*, 58:121–145, 2005.

[115] D. McWhorter and D. Sunada. Exact integral solutions for two-phase flow. *Water Resour. Res.*, 26(3):399–413, 1990.

[116] G. A. Melhem, R. Saini, and B. M. Goodwin. A Modified Peng-Robinson Equation of State. *Fluid Phase Equil.*, 47:189–237, 1989.

[117] J. Middendorf. *Zur Beschreibung des kapillaren Flüssigkeitstransports in Papier.* PhD thesis, Fakultät für Maschinenbau und Verfahrenstechnik, Technische Universität Chemnitz, 2000.

[118] A. Mikelic, V.M. Devigne, and C.J.van Duijn. Rigorous upscaling of a reactive flow through a pore, under dominant Peclet and Damkohler numbers. *SIAM Journal on Mathematical Analysis*, 38(4):1262–1287, 2006.

[119] E.E. Miller and R.D. Miller. Physical theory for capillary flow phenomena. *Journal of Applied Physics*, 27(4):324–332, 1956.

[120] R.J. Millington and J.P. Quirk. Permeability of porous solids. *Trans. Faraday Soc.*, 57:1200–1207, 1961.

[121] Y. Mualem. A new model for predicting the hydraulic conductivity of unsaturated porous media. *Water Resour. Res.*, 12:513–522, 1976.

[122] J. H. Nam and M. Kaviany. Effective diffusivity and water-saturation distribution in single- and two-layer PEMFC diffusion medium. *Int. J. Heat and Mass Transfer*, 46:4595–4611, 2003.

[123] T. Neubauer and P. Bastian. On a monotonicity preserving Eulerian-Lagrangian localized adjoint method for advection-diffusion equations. *Adv. Water Resour.*, 28(12):1292–1309, 2005.

[124] I. Neuweiler and H. Eichel. Effective parameter functions for Richards equations in layered porous media. *Vadose Zone Journal*, 5:963–977, 2006.

[125] J. Niessner. *Multi-Scale Modeling of Multi-Phase - Multi-Component Processes in Heterogeneous Porous Media.* PhD thesis, Mitteilungsheft 151, Institut für Wasserbau, Universität Stuttgart, 2006.

[126] J. Niessner and R. Helmig. Multi-scale modeling of multi-phase-multi-component processes in heterogeneous porous media. *Adv. Water Resour.*, 2007. accepted for publication.

[127] J. Niessner, R. Helmig, H. Jakobs, and J. Roberts. Interface Condition and Linearization Schemes in the Newton Iterations for Two-Phase Flow in Heterogeneous Porous Media. *Adv. Water Resour.*, 28(7):671–687, 2005.

[128] J.M. Nordbotten, M.A. Celia, and S. Bachu. Injection and Storage of CO_2 in Deep Saline Aquifers: Analytical Solution for CO_2 Plume Evolution During Injection. *Transport in Porous Media*, 58(3):339–360, 2005.

[129] NUPUS. International Research Training Group - Nonlinearities and Upscaling in Porous Media. `http://www.nupus.uni-stuttgart.de/`.

[130] S. Ochs. *Steam injection into saturated porous media - process analysis including experimental and numerical investigations.* PhD thesis, Mitteilungsheft 159, Institut für Wasserbau, Universität Stuttgart, 2007.

[131] S. Ochs, H. Class, and R. Helmig. Steam injection into groundwater systems. 1. An improved robust numerical model concept. *submitted to Water Resources Research*, 2007.

[132] S. Ochs, A. Färber, H. Class, and R. Helmig. Steam injection into groundwater systems. 2. Experimental and theoretical process analysis. *submitted to Water Resources Research*, 2007.

[133] S.O. Ochs, R.A. Hodges, R.W. Falta, T.F. Kmetz, J.J. Kupar, N.N. Brown, and D.L. Parkinson. Predicted heating patterns during steam flooding of coastal plain sediments at Savannah River Site. *Environmental and Engineering Geoscience*, 9(1):51–69, 2003.

[134] C.M. Oldenburg and S.M. Benson. CO_2 Injection for Enhanced Gas Production and Carbon Sequestration. *Society of Petroleum Engineers*, SPE 74367, 2002.

[135] U. Ölmann, R. Hinkelmann, and R. Helmig. Parallel Two-Phase Flow Simulations in Porous Media. In E. Krause and W. Jäger, editors, *High Performance Computing in Science and Engineering '02*, pages 347–353, Berlin, Heidelberg, 2002. Springer Verlag, in cooperation with High Performance Computing Center (HLRS) Universität Stuttgart.

[136] S. Panday, P.A. Forsyth, R.W. Falta, Y. Wu, and P.S. Huyakorn. Considerations for robust compositional simulations of subsurface nonaqueous phase liquid contamination and remediation. *Water Resour. Res.*, 31(5):1273–1289, 1995.

[137] J.C. Parker and R.J. Lenhard. A Model for Hysteretic Constitutive Relations Governing Multiphase Flow, 1. Saturation–Pressure Relations. *Water Resour. Res.*, 23(12):2187–2196, 1987.

[138] J.C. Parker, R.J. Lenhard, and T. Kuppusami. A Parametric Model for Constitutive Properties Governing Multiphase Flow in Porous Media. *Water Resour. Res.*, 23(4):618–624, 1987.

[139] U. Pasaogullari and C.Y. Wang. Liquid Water Transport in Gas Diffusion Layer of Polymer Electrolyte Fuel Cells. *J. Electrochem. Soc.*, 151(3):A399–A406, 2004.

[140] J.C. Pashin, R.H. Groshong, Jr., and R.E. Carroll. Enhanced coalbed methane recovery through sequestration of carbon dioxide: potential for a market-based environmental solution in the black warrior basin of alabama. In *National Energy Technology Laboratory, First National Conference on Carbon Sequestration*, 2001. http://www.netl.doe.gov/publications/proceedings/01/carbon_seq/3a2.pdf.

[141] B.E. Poling, J.M. Prausnitz, and J.P. O'Connel. *The Properties of Gases and Liquids*. McGraw-Hill, Inc., 2001.

[142] K. Pruess. TOUGH2 - A General–Purpose Numerical Simulator for Multiphase Fluid and Heat Flow. Technical report, Lawrence Berkeley Laboratory, University of California, 1991. LBL-29400.

[143] K. Pruess. Thermal Effects During CO2 Leakage from a Geologic Storage Reservoir. *Lawrence Berkeley National Laboratory Report LBNL-55913*, 2004.

[144] K. Pruess, A. Bielinski, J. Ennis-King, R. Fabriol, Y. Le Gallo, J. Garcia, K. Jessen, T. Kovscek, D.H.-S. Law, P. Lichtner, C. Oldenburg, R. Pawar, J. Rutqvist, C. Steefel, B. Travis, C.-F. Tsang, S. White, and T. Xu. Code Intercomparison Builds Confidence in Numerical Models for Geologic Disposal of CO2. In *Gale, J. and Kaya, Y. (Editors): GHGT-6 Conference Proceedings: Greenhouse Gas Control Technologies*, pages 463–470, 2003.

[145] W. R. Purcell. Capillary pressures - Their measurement using Mercury and the calculation of permeability therefrom. *Petroleum Transactions, AIME*, T.P. 2544:39–46, 1949.

[146] R.C. Reid, J.M. Prausnitz, and B.E. Poling. *The Properties of Gases and Liquids*. McGraw-Hill, Inc., 1987.

[147] L.A. Richards. *Capillary conduction of liquids through porous mediums.* PhD thesis, Cornell University, 1931.

[148] Thomas F. Russell and Michael A. Celia. An overview of research on Eulerian-Lagrangian localized adjoint methods (ELLAM). *Adv. Water Resour.*, 25(8-12):1215–1231, 2002.

[149] A.E. Scheidegger. General Theory of Dispersion in Porous Media. *Journal of Geophysical Research*, 66:3273–3278, 1961.

[150] A.E. Scheidegger. *The Physics of Flow through Porous Media*. University of Toronto Press, Toronto, 3. edition, 1974.

[151] R. Schmidt. *Wasserdampf- und Heissluftinjektion zur thermischen Sanierung kontaminierter Standorte*. PhD thesis, Mitteilungsheft 106, Institut für Wasserbau, Universität Stuttgart, 2001.

[152] H. Schubert. *Kapillarität in porösen Feststoffsystemen*. Springer-Verlag, 1982.

[153] J.G. Seo and D.D. Mamora. Experimental and Simulation Studies of Sequestration of Supercritical Carbon Dioxide in Depleted Gas Reservoirs. *Energy and Resources Technology*, 127, 2005.

[154] H.Y. She and B.E. Sleep. The effect of temperature on capillary pressure-saturation relationships for air-water and perchloroethylene-water systems. *Water Resour. Res.*, 34(10):2587–2597, 1998.

[155] H. Sheta. *Simulation von Mehrphasenvorgängen in porösen Medien unter Einbeziehung von Hysterese–Effekten*. PhD thesis, Mitteilungsheft 100, Institut für Wasserbau, Universität Stuttgart, 1999.

[156] W.H. Somerton, A.H. El-Shaarani, and S.M. Mobarak. High temperature behaviour of rocks associated with geothermal type reservoirs. *Society of Petroleum Engineers*, Paper SPE-4897 presented at 48th Annual California Regional Meeting of the Society of Petroleum Engineers, 1974.

[157] R. Span and N. Flacke. Kohlendioxid - Besonderheiten und Einsatzchancen als Kältemittel (Kap. 3.1 Thermophysikalische Eigenschaften von CO2, pp. 14 - 45). Technical report, DKV, 2004. Statusbericht Nr. 20.

[158] R. Span and W. Wagner. A New Equation of State for Carbon Dioxide Covering the Fluid Region from the Triple–Point Temperature to 1100 K at Pressures up to 800 MPa. *J. Phys. Chem. Ref. Data*, 25(6):1509–1596, 1996.

[159] N. Spycher, K. Pruess, and J. Ennis-King. CO_2-H_2O Mixtures in the Geological Sequestration of CO_2. I. Assessment and Calculation of Mutual Solubilities from 12 to 100°C and Up to 600 Bar. *Geochim. et Cosmochim. Acta*, 67(16):3015–3031, 2003.

[160] L. Stadler. Entwicklung und Implementierung eines numerischen Modellkonzepts zur Simulation von Alkoholspülungsprozessen in DNAPL-kontaminierten Grundwasserleitern. Master's thesis, Institut für Wasserbau, Universität Stuttgart, 2005.

[161] F. Stauffer. *Einfluss der kapillaren Zone auf instationäre Drainagevorgänge.* PhD thesis, Eidgenössische Technische Hochschule Zürich, Switzerland, 1977.

[162] F. Stauffer. Time dependence of the relations between capillary pressure, water content and conductivity during drainage of porous media. In *On scale effects in porous media*, Thessaloniki, Greece, 1978. IAHR.

[163] E.H. Stenby and P. Wang. Non-iterative Phase Equilibrium Calculation in Compositional Reservoir Simulation. *Society of Petroleum Engineers*, Paper SEP-9316 presented at the 1993 SPE Annual Technical Conference and Exhibition, 1993.

[164] L. Stroink (editor). GEOTECHNOLOGIEN Science Report - Investigation and Protection of the Underground. Technical Report 6, ISSN 1619-7399, Koordinierungsbüro GEOTECHNOLOGIEN, Potsdam, 2005.

[165] G.H. Thomson, K.R. Brobst, and R.W. Hankinson. An Improved Correlation for Densities of Compressed Liquids and Liquid Mixtures. *AIChE Journal*, 28:671–676, 1982.

[166] M.Th. Van Genuchten. A closed-form equation for predicting the hydraulic conductivity of unsaturated soils. *Soil Sci. Soc. Am. J.*, 44:892–898, 1980.

[167] J. Van Lookeren. Calculation Methods for Linear and Radial Steam Flow in Oil Reservoirs. *SPE*, pages 427–439, 1983.

[168] N.B. Vargaftik. *Tables on the thermophysical properties of liquids and gases*. John Wiley & Sons, New York, 2. edition, 1975.

[169] A.K. Verma. *Effects of phase transformation of steam–water relative permeabilities*. PhD thesis, Lawrence Berkeley National Laboratory report No. LBL-20594, University of California, 1986.

[170] E. Wendland and D. Flensberg. Numerical solution of two-phase flow for the advection-dominated and non-linear case. *Adv. Water Resour.*, 28:643–660, 2005.

[171] S. Whitaker. *The Method of Volume Averaging*. Kluwer Academic Publishers, The Netherlands, 1999.

[172] Wikipedia. The Free Encyclopedia. `http://en.wikipedia.org/`.

[173] A. Winkler. *Prozesse des Wärme- und Stofftransports bei der In-situ-Sanierung mit festen Wärmequellen*. PhD thesis, Mitteilungsheft 115, Institut für Wasserbau, Universität Stuttgart, 2003.

Appendix A

Deutsch-sprachige Zusammenfassung

Modelle für nichtisotherme Mehrkomponenten-Gas-Flüssigkeits-Strömungs- und -Transportprozesse in porösen Medien

Holger Class

A.1 Einleitung und Motivation

Mehrphasenströmungen in porösen Medien sind für eine Vielzahl von umweltrelevanten und technischen Fragestellungen von Bedeutung. Im Rahmen dieser Arbeit bezeichnet der Begriff Mehrphasensystem das gleichzeitige Vorhandensein von mehr als einer Fluidphase in einem Materialpunkt bzw. lokalen Kontrollraum. Insbesondere im natürlichen Untergrund gibt es sehr viele unterschiedliche ingenieurpraktische Probleme, deren Bearbeitung ein solides Verständnis von Mehrphasenströmungen erfordert. Dazu gehören z.B. Ausbreitungsvorgänge von wasserunlöslichen bzw. schwach löslichen Substanzen, in-situ Techniken zur thermisch unterstützten Sanierung von kontaminierten Standorten, bestimmte Maßnahmen zur tertiären Öl- und Gasförderung oder auch die jüngst intensiv diskutierte Speicherung des Treibhausgases Kohlendioxid (CO_2) in tiefen geologischen Formationen. Strömungs- und Transportvorgänge in Systemen aus mehreren Fluidphasen treten auch in technischen bzw. künstlich hergestellten porösen Medien wie Papier, Filtern und Brennstoffzellen auf.
Die Beschreibung der den Mehrphasenvorgängen zu Grunde liegenden Strömungs- und Transportprozesse durch prozessgenaue Modellkonzepte gewann vor allem in den 1970er Jahren für tertiäre Fördermaßnahmen in der Öl- und Gasindustrie an Bedeutung. Diese Modellkonzepte konnten nachfolgend auch für umwelt- und technisch relevante Fragestellungen angepasst und erweitert werden.

Viele Mehrphasenprobleme in porösen Medien sind durch äußerst komplex gekoppelte, nichtlineare und oftmals nichtisotherme Prozesse charakterisiert, wobei zwischen den beteiligten Fluidphasen ein Massentransfer von Komponenten stattfinden kann. Im Rahmen dieser Arbeit werden besonders solche Mehrphasensysteme behandelt, die aus einer oder mehreren flüssigen

Phasen sowie einer Gasphase bestehen.

Diese Systeme weisen typische Besonderheiten auf, z.B. große Unterschiede in den Fluideigenschaften. Dynamische Viskosität und Dichte von Gasen sind in der Regel um zwei bzw. drei Größenordnungen geringer als bei Flüssigkeiten. Dies kann zu Stabilitätsproblemen und der Ausbildung von *Fingering*–Effekten führen. Weiterhin ist für Gas-Flüssigkeits-Systeme der Massenübergang in Form von Verdampfung und Kondensation gekoppelt mit einem Austausch thermischer Energie. Bei gasförmigen Phasen ist der starke Einfluss der Zusammensetzung auf die Eigenschaften der Fluidphase besonders zu beobachten. Nicht zuletzt handelt es sich bei Gasen um kompressible Fluide, was für die mathematisch-numerische Modellbildung eine Schwierigkeit darstellt, da viele vereinfachende Ansätze auf der Annahme von Inkompressibilität der beteiligten Fluid basieren.

Die vorliegende Arbeit beinhaltet neben Fragen zur Modellbildung die numerische Umsetzung und die Applikation für ausgewählte Problemstellungen.

A.2 Themen und Problemstellungen

In der Arbeit werden verschiedene Gas-Flüssigkeits-Probleme detailliert diskutiert. Es werden dabei zunächst die charakteristischen Besonderheiten der jeweiligen Problemstellung vorgestellt. Im Einzelnen sind folgende Themen Gegenstand einer näheren Untersuchung:

- **Schadstoffausbreitung und thermisch-unterstützte Bodensanierung.**
  Die Ausbreitung von Schadstoffen, die in den Untergrund eindringen, erfolgt auf vielfältige Weise. Die dabei auftretenden Prozesse sind beispielsweise abhängig von der Art des Schadstoffs und speziell von seiner Mischbarkeit mit Wasser. Eine besonders in den Industrieländern vorhandene Problematik stellen nicht bzw. schwach mischbare flüssige Schadstoffe (NAPL - Non-Aqueous Phase Liquids, z.B. chlorierte Kohlenwasserstoffe) dar, die durch Unfälle oder Leckagen in die ungesättigte Bodenzone eindringen, dort als residuale (immobile) Phase verbleiben, oder auch, bei entsprechend großer Menge, den Grundwasserspiegel erreichen können. In der ungesättigten Bodenzone können so kontinuierlich geringe Mengen über lange Zeiträume hinweg ausgewaschen und ins Grundwasser eingetragen werden, wo sie auf Grund ihrer Toxizität eine erhebliche Gefahr für das Trinkwasser darstellen. Noch schwieriger stellt es sich dar, wenn die Schadstoffmenge genügend groß ist, um als eigene Phase den Wasserspiegel zu erreichen. In diesem Fall hängt das weitere Ausbreitungsverhalten von der Dichte des Schadstoffs im Vergleich zur Dichte des Wassers ab. Ein besonders komplexes nichtisothermes Dreiphasensystem bestehend aus einer gasförmigen und bis zu zwei flüssigen Phasen entsteht, wenn z.B. mit Hilfe einer Injektion von Dampf eine thermisch-unterstützte Bodenluftabsaugung betrieben wird. Zur Beschreibung der dabei ablaufenden physikalischen Prozesse ist ein sehr komplexes und stark gekoppeltes nichtlineares System aus partiellen Differentialgleichungen erforderlich, welches unter anderem die Massenbilanzen der einzelnen beteiligten Komponenten sowie eine Bilanzgleichung für die thermische Energie beinhaltet.

- **CO_2-Speicherung in geologischen Formationen und tertiäre Gasförderung.**

Die Speicherung von CO_2 in tiefen geologischen Formationen wird derzeit intensiv diskutiert und als eine von mehreren Optionen in Betracht gezogen, um die Emission von klimarelevanten Treibhausgasen zu minimieren. Die sogenannte *Carbon Capture and Storage* (CCS) Technologie zielt darauf ab, CO_2 bei großen punktförmigen Emittenten, wie z.B. bei Kraftwerken, abzutrennen und anschließend unter hohem Druck in tiefen Lagerstätten oder salinaren Aquiferen zu verpressen. Die Speichermechanismen, die dafür sorgen sollen, dass das CO_2 nachhaltig im Untergrund verbleibt, sind vielfältig und variieren über die Zeit sehr stark. Während anfänglich (während bzw. kurz nach Abschalten der Injektion) vor allem Mehrphasenströmungs- bzw. Verdrängungsprozesse dominieren, spielen mit zunehmender Zeitdauer nach dem Abschalten der Injektion auch andere Prozesse eine wichtiger werdende Rolle. Dazu gehört die Lösung des CO_2 im Formationswasser, oder auch die chemische Reaktion mit dem umliegenden Gesteinsmaterial. Aus Sicht der Modellierung stellt vor allem die thermodynamische Beschreibung der Fluideigenschaften eine große Herausforderung dar, da sich das CO_2 typischerweise in Tiefen ab ca. 700 m in überkritischem Zustand befindet. Der überkritische Zustand wird auf Grund der dann zu erzielenden hohen Dichte des CO_2 zur Injektion bevorzugt. Dies setzt voraus, dass eine geeignete Formationen eine entsprechende Tiefe haben muss, um die erforderlichen Druck- und Temperaturbedingungen zu gewährleisten.Im Falle einer Injektion in eine Erdgaslagerstätte zur tertiären Methangewinnung und gleichzeitigen Speicherung von CO_2 wird die Beschreibung der Eigenschaften, vor allem in der Gasphase, nochmals komplexer.

- **Methanmigration in stillgelegten Kohlebergwerken.**
  Die Freisetzung von Methan aus nicht abgebauten Kohleflözen ist ein bekanntes Problem, z.B. im Ruhrgebiet, da ein unkontrolliertes zu Tage treten des Gases in besiedelten Gebieten eine erhebliche Gefahr darstellt. Es ist deshalb von großem Interesse, die Gasflüsse bzw. die Migrationswege des Gases im Untergrund möglichst genau zu kennen, um geeignete Maßnahmen, wie beispielsweise die gezielte Abteufung von Bohrungen, durchführen zu können.

- **Strömung und Transport von Wasser und Gas in Brennstoffzellen.**
  Die Gasdiffusionsschichten von PEM- (Polymer-Elektrolyt-Membran)-Brennstoffzellen bestehen in der Regel aus einem dünnschichtigen porösen Material. Durch eine Oberflächenbeschichtung wird die Struktur hydrophobiert, sodass Wasser in diesem Fall das nicht-benetzende Fluid darstellt. Die Gasdiffusionsschicht dient dazu, einerseits das bei der Reaktion entstehende Wasser zu den Gaskanälen hin abzuleiten, was durch die hydrophobe Eigenschaft begünstigt wird. Andererseits muss gleichzeitig der für die Reaktion benötigte Sauerstoff von den Gaskanälen durch die Diffusionsschicht hindurch zur Reaktionsschicht transportiert werden. Für eine gezielte Optimierung des Betriebs der Brennstoffzelle ist daher eine Kenntnis des auftretenden Gas-Wasser-Systems und der dabei im Einzelnen beteiligten Prozesse und Parameter unbedingt erforderlich.

A.3 Modellbildung

Die physikalisch-mathematische Modellbildung hat zum Ziel, zunächst die relevanten physikalischen Prozesse für eine spezifische Problemstellung zu identifizieren, um diese dann durch geeignete mathematische Formulierungen zu beschreiben. Dies resultiert in einem mathematischen Modell, welches je nach Komplexität und Kopplungsgrad der Modellgleichungen (gekoppelte partielle Differentialgleichungen und algebraische Schließbedingungen) analytisch oder durch geeignete numerische Methoden und Algorithmen gelöst werden muss. Die in dieser Arbeit untersuchten Problemstellungen resultieren in allen Fällen in derart komplexen Gleichungssystemen, dass lediglich eine numerische Lösung für praktisch relevante Szenarien in Frage kommt.

Im Rahmen der Arbeit werden zunächst die allgemeinen Bilanzgleichungen für Masse, Impuls (Darcy) und Energie hergeleitet und anschließend schrittweise für die spezifischen Problemstellungen erweitert bzw. angepasst. Vor der Herleitung der allgemeinen Mehrphasen-Strömungs-Differentialgleichung erfolgt eine Definition und Einordnung der hierbei angewendeten Betrachtungsskala. Auf dieser Skala wird ein repräsentatives Elementarvolumen (REV) eingeführt, um daran eine Betrachtung des physikalischen Systems auf der Grundlage der Kontinuumsmechanik vorzunehmen. Im Zuge dessen werden die Fluideigenschaften Dichte und Viskosität diskutiert, aber auch die effektiven, durch Mittelung über das REV erhaltenen, Größen wie z.B. Porosität und Sättigung definiert. Die Ursachen der Kapillarität im porösen Medium werden sowohl mit Hilfe der mikroskalig relevanten Systemgrößen erläutert, als auch hinsichtlich ihrer Beschreibung durch effektive Parameter mit Hilfe der stark nichtlinearen Kapillardruck-Sättigungs-Beziehung auf der Skala des REV. Des Weiteren ist die Permeabilität eine Größe, die mit Hilfe des Fließgesetzes nach *Darcy* das hydraulische Verhalten der advektiven Strömungen maßgeblich bestimmt. In Mehrphasensystemen ist zusätzlich die relative Permeabilität-Sättigungsbeziehung zu berücksichtigen. Mit dieser kann auf der REV-Skala beschrieben werden, wie sich das Vorhandensein mehrerer Fluidphasen innerhalb eines REV durch eine gegenseitige Behinderung im Strömungsverhalten bemerkbar macht. Auch für die relativen Permeabilitäten ergibt sich im Allgemeinen eine stark nichtlineare Funktion, die von den Phasensättigungen abhängig ist. Mit diesen Systemgrößen ist nun eine Beschreibung von allgemeinen isothermen Mehrphasensystemen ohne Phasenübergang möglich, was im Wesentlichen advektive Flüsse der jeweiligen Phasen, kapillare Diffusion sowie einen Speicherterm und einen Quell-/Senkenterm beinhaltet.

Um den Einfluss zusätzlicher Prozesse, die durch eine Mehrkomponenten-Betrachtung innerhalb der Fluidphasen relevant werden, in das Modellkonzept zu integrieren, wird das zuvor hergeleitete allgemeine Modellkonzept in der Arbeit schrittweise erweitert. Es werden zunächst die für die Beschreibung einer aus mehreren Komponenten bestehenden Fluidphase erforderlichen Molenbrüche bzw. Massenbrüche eingeführt. Diese quantifizieren den jeweiligen Anteil der Komponenten innerhalb der Fluidphasen. Damit und mit Hilfe des *Fick'*schen Gesetzes kann dann der diffusive bzw. dispersive Transport von Komponenten auf Grund von Konzentrationsgradienten innerhalb der Phase abgebildet werden. Um Massentransferprozesse durch Verdampfung und Kondensation bzw. durch Lösung und Ausgasung zu beschreiben, wird hier die Annahme lokalen thermodynamischen Gleichgewichts getroffen, wobei die Berechnung der

Molen- bzw. Massenbrüche in den Fluidphasen mit Hilfe der Modelle von *Dalton*, *Henry* bzw. *Raoult* vorgenommen wird. Dabei wird vereinfachend vorausgesetzt, dass sich alle Komponenten in der Gasphase wie ideale Gase verhalten, was für Drücke, die deutlich unterhalb des kritischen Drucks liegen, eine gute Näherung darstellt. Für nichtisotherme Systeme muss zusätzlich eine Bilanz der thermischen Energie erfolgen. Hierfür werden kalorische Zustandsvariablen benötigt. Dazu zählen die spezifische Enthalpie und die spezifische innere Energie der Fluidphasen sowie die Wärmekapazitäten. Des Weiteren spielen die Wärmeleitfähigkeiten des Korngerüsts und der Fluidphasen eine wichtige Rolle, um konduktive Wärmeflüsse zu beschreiben. Wird dabei lokales thermisches Gleichgewicht vorausgesetzt, so genügt es, eine einzige Wärmebilanzgleichung für das fluidgefüllte poröse Medium aufzustellen und die Wärmeleitfähigkeiten anteilig über die jeweiligen Volumenanteil innerhalb eines REV zu mitteln. Andernfalls müssen die Wärmebilanzen jeder Phase sowie entsprechende Wärmeübergangskoeffizienten zwischen den Phasen formuliert werden.

Einen zentralen Baustein der Arbeit stellen die in den darauf folgenden Kapiteln diskutierten Anpassungen des Modellkonzepts für die eingangs erwähnten Problemstellungen dar.
Am Beispiel eines Wasser-NAPL-Gemischs wird das Siedeverhalten zweier nicht bzw. nur schwach mischbarer Substanzen erklärt. Eine Besonderheit dabei ist beispielsweise, dass die Siedetemperatur des Zweiphasengemischs gegenüber den Siedetemperaturen beider Reinstoffe reduziert ist. Dadurch kann sich bei der thermisch-unterstützten Sanierung NAPL-kontaminierter Böden ein charakteristisches Siedetemperaturplateau einstellen, mit Hilfe dessen allein durch Messung der lokalen Temperatur eine Aussage über das Verschwinden des NAPLs als Phase getroffen werden kann. Während sich bei der Dampfinjektion in der ungesättigten Bodenzone eine stabile Dampffront ausbreiten kann, deren Reichweite lediglich durch thermische Verluste limitiert ist, gilt dies für die Dampfinjektion in der gesättigten Zone keineswegs. Dort bestimmt im Wesentlichen das Verhältnis zwischen viskosen Kräften und Auftriebskräften, wie weit sich eine Dampffront ausgehend vom Injektionsbrunnen ausbreiten kann, bevor der Dampf auf Grund des Auftriebs nach oben durchbricht. Bei der numerischen Modellierung von Dampfinjektionsprozessen in der gesättigten Zone treten typischerweise zweierlei numerische Schwierigkeiten auf. Zum Einen ergeben sich beim Fortschreiten der Dampffront Fluktuationen des Drucks, deren Frequenz und Amplitude von der Diskretisierungsweite abhängen. Die Ursache der Druckoszillationen und deren Beeinträchtigung der numerischen Robustheit werden in der Arbeit detailliert erklärt, und es wird eine Methode vorgeschlagen, um die Robustheit des numerischen Algorithmus zu verbessern. Eine zweite Schwierigkeit ist darin begründet, dass die Massenkomponente Luft mit zunehmendem Anteil des Wasserdampfs aus dem System verschwindet und dadurch die Massenbilanzgleichung für die Luft nicht mehr stabil gelöst werden kann. Es wird daher eine Reduktion des Modellkonzepts bzw. des Gleichungssystems vorgeschlagen, sodass im speziellen Fall einer Dampfinjektion in ein wassergesättigtes System lediglich noch die Komponente Wasser berücksichtigt wird, wobei sich diese allerdings auf zwei verschiedene Phasen - gasförmig und flüssig - verteilen kann.

Die Anpassung des physikalisch-mathematischen Modellkonzepts zur Simulation von CO_2-Injektionsvorgängen in tiefen geologischen Formationen erfordert grundlegende thermodynamische Kenntnisse, um die stark mit Druck und Temperatur variierenden Fluideigenschaften, vor allem des Kohlendioxids, im Modell wiedergeben zu können. Es existieren in der Literatur einige

wenige Ansätze, die den gesamten Druck- und Temperaturbereich abdecken, in welchem Dichte, Viskosität und spezifische Enthalpie berechnet werden müssen. Besondere Komplexität besteht im Bereich des kritischen Drucks von CO_2, der bei 73.8 bar and 30.95 °C liegt. Für die quantitative Beschreibung von Massentransferprozessen zwischen den Fluidphasen werden des Weiteren Ansätze zur Beschreibung der entsprechenden Gleichgewichtsbedingungen benötigt. Hierbei hat z.B. die Zusammensetzung des Formationswassers, insbesondere auch die Salinität, einen großen Einfluss auf die Löslichkeit von CO_2. Weiterhin ist zu berücksichtigen, dass Wasser mit hohen Konzentrationen an gelöstem CO_2 eine höhere Dichte hat, was zur Folge hat, dass dadurch schwerkraftbedingte Konvektionsströmungen in Gang gesetzt werden. Im Rahmen der Ausführungen zur physikalisch-mathematischen Modellbildung wird in der Arbeit ebenfalls noch die Anpassung des Konzepts für die Simulation von *Enhanced Gas Recovery* (EGR)-Maßnahmen und Methanmigrationsprozessen in stillgelegten Kohlebergwerken diskutiert.

Im Anschluss daran werden grundlegende mathematische Formulierungen und Lösungsstrategien der aus der physikalischen Modellbildung hervorgegangenen Systeme gekoppelter partieller Differentialgleichungen vorgestellt. Es werden dabei kurz die Vorteile und Nachteile der Druck-Sättigungs-, Druck-Druck- sowie der fraktionalen Fluss-Formulierung diskutiert. Es wird gezeigt, dass der Auswahl geeigneter Primärvariablen eine wichtige Rolle zukommt, da hiermit eine numerisch robuste Berechnung sämtlicher weiterer (sekundärer) Variablen gewährleistet werden muss. Eine Besonderheit der in dieser Arbeit vorgestellten Konzepte ist, dass die Wahl der Primärvariablen in Abhängigkeit der lokal im REV vorliegenden Fluidphasen getroffen werden muss. Je nach dem kann es notwendig sein, dass einzelne Primärvariablen ausgetauscht werden, beispielsweise wenn eine als Primärvariable ausgewählte Phasensättigung beim Verschwinden dieser Phase ihre Eigenschaft einer unabhängigen Größe verliert und den trivialen Wert Null annimmt. In diesem Fall muss diese Phasensättigung dann durch eine andere Primärvariable ersetzt werden, z.B. durch einen Molenbruch der als Phase verschwundenen Komponente in einer anderen noch existierenden Phase. Für den Fall, dass eine Komponente vollständig aus dem System verschwindet, kann es sogar erforderlich sein, die entsprechende Massenbilanzgleichung aus dem Gleichungssystem in einem REV zu eliminieren. Die Wahl der Primärvariablen hängt unmittelbar mit der Zuweisung von Rand- und Anfangsbedingungen zusammen. Für die hier verwendeten Modelle stehen dabei Randbedingungen vom Typ *Dirichlet* (entspricht einem bekannten Wert der Primärvariable) oder vom Typ *Neumann* (entspricht in diesem Fall dem Massen-/Molen-Fluss einer Komponente bzw. einem Enthalpiefluss über den Rand).

Die Linearisierung des gekoppelten nichtlinearen Gleichungssystems erfolgt mit Hilfe der *Newton-Raphson*-Methode, wobei zur Berechnung der *Jacobi*-Matrix eine numerische Differentiation der Gleichungen nach den Primärvariablen verwendet wird, da die Herleitung analytischer Ableitungen des numerischen Defekts nach den Primärvariablen einen nicht zu realisierenden Aufwand darstellt.
Es werden dann verschiedene Methoden zur zeitlichen und räumlichen Diskretisierung vorgestellt, wobei eine Betonung auf den in dieser Arbeit verwendeten Finite-Volumen-Methoden liegt. Ausgehend vom Prinzip der gewichteten Residuen werden detailliert die BOX- und die CVFE-Methode erklärt.

Die Komplexität der gekoppelten Prozesse, die im zeitlichen Verlauf oder auch in verschiedenen Regionen des Modellgebiets auftreten, kann so sehr variieren, dass es nicht sinnvoll ist, während der ganzen Simulationsdauer bzw. im gesamten Gebiet dasselbe Modellkonzept anzuwenden. Die zeitliche oder räumliche Kopplung unterschiedlicher Modellkonzepte erscheint daher zur Simulation solcher großer Systeme eine vielversprechende Methode zur Begrenzung der benötigten Rechenzeiten. Hierzu ist es wichtig, die Interaktion der im Gesamtsystem integrierten unterschiedlichen Modelle zu gewährleisten. Am Beispiel einer NAPL-Infiltration und Ausbreitung mit anschließender Bodensanierung durch Dampfinjektion und Bodenluftextraktion wird die sequentielle Kopplung unterschiedlich komplexer Modelle diskutiert. Es wird ein Algorithmus vorgestellt, der dazu dient, den Transfer der Primärvariablen zwischen den Modellen bzw. deren Initialisierung während der Kopplung durchzuführen.

Die Lösung der durch Diskretisierung und Linearisierung erhaltenen linearen Gleichungssysteme erfordert schnelle, effiziente und robuste Methoden. Dazu kann einerseits die lineare Lösungsstrategie selbst optimiert werden, z.B. durch den Einsatz einer Mehrgittermethode. Andererseits ist die Parallelisierung der Lösungsverfahren unverzichtbar, um großskalige Systeme von praktischer Relevanz überhaupt lösen zu können. Die Robustheit der Lösungsmethoden ist für großskalige Systeme von ebenso großer Bedeutung. Es werden verschiedene Probleme hinsichtlich der numerischen Robustheit diskutiert, z.B. der Einsatz sogenannter *Flash Calculations* und die Verwendung globaler Molenbrüche anstatt der für die Robustheit problematischen adaptiven Substitution der Primärvariablen bei wechselnden Phasenzuständen.

A.4 Anwendungen

Die in dieser Arbeit ausführlich dokumentierten Beispielanwendungen greifen die Komplexität der Prozesse auf und veranschaulichen diese. In allen Fällen werden dabei die Anwendung des Modellkonzepts, die Zuweisung der Rand- und Anfangsbedingungen, sowie die jeweiligen Besonderheiten der einzelnen Fragestellungen, welche die Motivation für den Einsatz des numerischen Modells liefern, detailliert beschrieben.

- Das erste Anwendungsbeispiel behandelt einen Vergleich zwischen einem in der Versuchseinrichtung für Grundwasser- und Altlastensanierung (VEGAS) durchgeführten eindimensionalen Säulenexperiment und numerischen Simulationen. Das Experiment war Teil einer Labortestserie, die der technologischen Optimierung von thermisch-unterstützter Bodenluftabsaugung durch Injektion von Dampf bzw. eines Dampf-Luft Gemischs diente. Ziel der begleitenden numerischen Studie war dabei zum Einen die Validierung des Modellkonzepts anhand von unter kontrollierten Bedingungen gewonnenen Messdaten, zum Anderen die Verbesserung des Prozessverständnisses durch eine Identifikation der dominierenden Prozesse und Parameter. Die vertikal ausgerichtete Säule wurde im Experiment zunächst mit einem luftgetrockneten Sand befüllt und anschließend mit dem NAPL Xylol gesättigt. Daraufhin wurde der Auslass am unteren Rand geöffnet, sodass eine Drainage des NAPLs bis zum Erreichen der NAPL-Restsättigung erfolgen konnte. Die Reinigung der Säule wurde mit Hilfe einer Dampfinjektion vom Kopf her erzielt, wobei

am unteren Rand freier Ausfluss der Fluidphasen gewährleistet war. Es wurde an verschiedenen Stellen innerhalb der Säule der zeitliche Verlauf der Temperatur gemessen, was als Grundlage für den Vergleich mit den aus der numerischen Simulationen erhaltenen Ergebnisse diente. Die Temperaturverläufe zeigen einen steilen Anstieg, der die Ankunft der Dampffront indiziert, daran anschließend eine Plateautemperatur auf dem Niveau der Siedetemperatur des NAPL-Wasser-Gemischs bevor nach dem lokalen Verschwinden des NAPLs als eigene Phase der weitere Temperaturanstieg auf die Siedetemperatur des Wassers erfolgt. Vom numerischen Modell kann dieses Verhalten gut wiedergegeben. Die Steilheit der Front und der Wert der Platautemperatur werden quantitativ sehr exakt reproduziert. Eine Diskrepanz ist jedoch hinsichtlich der zeitlichen Dauer des Temperaturplateaus zu beobachten. Die dafür potentiell verantwortlichen Abweichungen zwischen Modell und Experiment bzw. die vereinfachenden Modellannahmen, insbesondere die Vernachlässigung von Hystereseeffekten der relativen Permeabilität und des Kapillardruck, werden an dieser Stelle im Detail diskutiert.

- Die zweite Anwendung beschäftigt sich ebenso mit der Injektion von Dampf, wobei in diesem Fall die Injektion in der gesättigten Bodenzone stattfindet. Die Motivation zu dieser Studie lieferte eine Feldanwendung in Karlsruhe, für welche VEGAS-Ingenieure eine Pilotstudie durchführten, um die Sanierung des Untergrunds im Bereich einer ehemaligen chemischen Reinigung vorzubereiten. Dazu wurden ein Injektionsbrunnen und einige Messpegel installiert, in denen die Ankunft des Dampfdurchbruchs durch Temperaturmonitoring beobachtet wurde. Die begleitenden dreidimensionalen numerischen Untersuchungen hatten unter anderem zum Ziel, die thermische Reichweite der Brunnen zu bestimmen, und daraus die für die Sanierung erforderliche Anzahl an Injektionsbrunnen abzuschätzen. Die thermische Reichweite eines Brunnens wird maßgeblich durch das Verhältnis zwischen viskosen Kräften und Auftriebskräften bestimmt. Während die Auftriebskräfte durch das Dichteverhältnis zwischen Wasser und Dampf bereits festgelegt sind, können die viskosen Kräften stark variieren. Hohe Injektionsraten oder geringe Permeabilitäten sind verantwortlich für hohe viskose Kräfte und damit für eine eher zylindrische Entwicklung der Dampfzone bzw. für eine größere thermische Reichweite. Der Vergleich zwischen Temperaturmessungen in den Beobachtungsbrunnen und den Ergebnissen der numerischen Simulationen zeigt gute Übereinstimmungen. Die auftretenden Abweichungen sind vor allem auf mangelnde Information über die hydraulischen Eigenschaften (Permeabilität, Porosität) des Untergrunds zwischen den Brunnen zurückzuführen.

- Das dritte Beispielproblem thematisiert die Speicherung von Kohlendioxid in einem salinaren Aquifer. Es handelt sich in diesem Fall um eine numerische Prinzipstudie, in der die unterschiedlichen Zeitskalen und Prozesse während und nach einer Injektion von CO_2 in der Formation anschaulich gemacht werden. In einem zweidimensionalen, 3000 m$\times$1000 m, großen Modellgebiet wird eine horizontal geschichtete Struktur abgebildet mit zwei verhältnismäßig gut durchlässigen Schichten, die in der Mitte von einer geringer durchlässigen hydraulischen Barriere (*Caprock*) unterbrochen werden. Eine begrenzte Menge an CO_2 wird während eines Zeitraums von 40 Tagen vom unteren Rand in die untere höher durchlässige Schicht injiziert. Dort steigt es in zwar überkritischem Zustand, aber dennoch mit einer geringen Dichte als das umgebende Wasser, in Richtung der geringer durchlässigen Schicht auf, wo es zu einem Aufstau und demzufolge zu einer lateralen Ausbreitung

kommt. In den Bereichen, die von CO_2 durchflossen werden, bleibt eine Restsättigung als immobile Phase zurück. Nach dem Abschalten der Injektion, kommt das Mehrphasensystem CO_2-Wasser allmählich zur Ruhe, da das CO_2 entweder hydrodynamisch am *Caprock* oder residuell zurückgehalten wird (*trapping*). Gleichzeitig löst sich aber das CO_2 in der Wasserphase, woraufhin deren Dichte zunimmt und CO_2-reiches Wasser schwerkraftbedingt nach unten absinkt. Dadurch wird einerseits die weitere Lösung von CO_2 begünstigt, andererseits auch eine nachhaltige Speicherfalle (*solubility trapping*) für das gelöste CO_2 bewirkt. Die Zeitskala des Lösungsvorgangs und der dadurch erzeugten dichteinduzierten Wasserkonvektion liegt in der Größenordnung von mehreren Jahrzehnten bis Jahrhunderten und damit deutlich über der Zeitskala des hydraulischen Ausbreitungsverhaltens der CO_2-Phase nach der Injektion. Das Absinken des CO_2-reichen Wassers geschieht charakteristischerweise in sogenannten Fingern, da es sich um eine instabile Schichtung des schwereren CO_2-reichen Wassers oberhalb des leichteren CO_2-armen Wassers handelt.

- Das vierte Anwendungsbeispiel behandelt eine Injektion von CO_2 in eine Erdgaslagerstätte zum Zweck einer verbesserten Förderung von CH_4 (Methan). Die Motivation für dieses dreidimensionale Beispielproblem entstammt einer in der Literatur vorgefundenen Studie, welche die durch eine CO_2-Injektion noch erreichbare Ausbeute des in der bereits erschöpften Lagerstätte verbliebenen Methans diskutiert. Da Kohlendioxid schwerer ist als Methan, wird ersteres in einem tief verfilterten Injektionsbrunnen in die Lagerstätte eingebracht, während das produzierte Gas im Förderbrunnen in einer höher gelegenen Verfilterung entnommen wird. Durch die Injektion steigt der Druck in der Formation wieder an. Gleichzeitig verdrängt das schwerere Kohlendioxid das Methangas in Richtung des Förderbrunnens. Dieser advektive Verdrängungsvorgang wird jedoch durch diffusive bzw. dispersive Vermischung der Gaskomponenten überlagert, sodass mit der Zeit das CO_2 am Förderbrunnen durchbricht. Mit zunehmender Dauer steigt nun der CO_2-Anteil im produzierten Gas an und die weitere Gasproduktion wird schließlich unwirtschaftlich. Mit der Hilfe numerischer Simulationsmodelle kann der Einfluss unterschiedlicher Faktoren, wie z.B. die Verteilung struktureller Inhomogenitäten in der Lagerstätte auf die Durchbruchskurven des CO_2 am Förderbrunnen untersucht und bewertet werden.

- Die fünfte und letzte Problemstellung beinhaltet die Strömungs- und Transportvorgänge in der Diffusionsschicht einer PEM-Brennstoffzelle. In einem vereinfachten zweidimensionalen Schnitt werden die grundlegenden Prozesse mit Hilfe einer numerischen Studie anschaulich dargestellt. Dabei werden zwei grundsätzlich unterschiedliche Strömungs- bzw. Transportbedingungen durch verschiedene Anordnungen der Gaskanäle in den Gasverteilerplatten erzeugt. Während im Fall einer konventionellen Anordnung der Gaskanäle der Transport des Sauerstoffs durch die Diffusionsschicht hindurch hauptsächlich durch Diffusion erfolgt, wird im Fall des sogenannten *interdigitated* Strömungsfeldes ein advektiver Gasstrom durch die Diffusionsschicht hindurch erzwungen. In diesem Fall stellt die Zuweisung geeigneter Randbedingungen an der Grenzschicht zwischen Diffusionsschicht und Gaskanal eine besondere Schwierigkeit dar, die ohne die explizite Modellierung der Strömung im Gaskanal kaum zu überwinden ist. Der hierfür erforderliche weitere Forschungsbedarf wird ausführlich diskutiert. Im Beispiel wird ebenfalls die Integration der elektrochemischen Reaktion durch Quell-/Senkenterme sowie die Implementierung einer

Kapillardruck-Sättigungs-Beziehung für die hier vorliegende hydrophobe poröse Struktur behandelt.

A.5 Schlussbemerkungen

Die Arbeit behandelt eine Reihe von unterschiedlichen Fragestellungen, die durch nichtisotherme Gas-Flüssigkeits-Vorgänge mit Phasenübergang charakterisiert werden. Es kann gezeigt werden, dass die dominierenden Prozesse signifikante Ähnlichkeiten aufweisen, und dass die hier entwickelten und vorgestellten generellen Modellkonzepte auf viele spezifische Probleme und Anwendungen übertragen bzw. angepasst oder weiterentwickelt werden können.

Die Modellkonzepte wurden im Rahmen einer ganzen Anzahl verschiedener Forschungsprojekte in der numerischen Simulationsplattform MUFTE-UG implementiert, sodass ein leistungsfähiges Werkzeug zur Verfügung steht, mit welchem sehr verschiedene sowohl ingenieurpraktische Fragestellungen als auch offene Fragen aktueller Forschungsthemen beantwortet werden können. Am Ende der Arbeit wird der künftige Forschungsbedarf zur weiteren Verbesserung der Modelle diskutiert. Ein stets aktuelles Gebiet für künftige Arbeiten betrifft die Validierung und Verifizierung von numerischen Modellen. Die Entwicklung von analytischen mathematischen Lösungen ist für die in dieser Arbeit behandelten komplexen Fragestellungen meist nicht bzw. nur unter stark vereinfachenden Annahmen möglich. Ebenso fehlen insbesondere auf dem Gebiet der CO_2-Injektionsprozesse in tiefen geologischen Formationen kontrollierte Messdaten, um einen tragfähigen Vergleich mit den numerischen Simulationsergebnissen herzustellen. Im Rahmen der CO_2-Problematik gibt es darüber hinaus noch weiteren Forschungsbedarf, um die Beschreibung der Fluideigenschaften zu verbessern. Vor allem beim CO_2 ist für praktisch relevante Injektionsszenarien zu erwarten, dass Verunreinigungen aus den Verbrennungsgasen zu einer Veränderung der Eigenschaften im Vergleich zu reinem CO_2 führen, wofür bislang aber keine Ansätze in der Literatur vorliegen. Die Beschreibung der hydraulischen Eigenschaften eines porösen Mediums basiert in sehr vielen Fällen auf der vereinfachenden Annahme, dass Hysterese-Effekte vernachlässigbar sind. Dies erfolgt jedoch meist nur deshalb, weil zum Einen die Parametrisierungen für eine quantitativ richtige Approximation nicht vorliegen und zum Anderen, weil die Berücksichtigung von Hysterese die benötigten Rechenzeiten weiter sehr stark vergrößern würde. Ein in dieser Arbeit nur am Rande behandelter Aspekt betrifft die auch in Gas-Flüssigkeits-Strömungen auftretenden Dichte-Instabilitäten und viskosen Fingering-Effekte. Obgleich hierzu in der Literatur bereits einige grundlegende Arbeiten vorliegen, ist dennoch erheblicher Forschungsbedarf vorhanden, um die theoretischen Ansätze und Untersuchungen auf praktisch relevante Szenarien zu übertragen und den Einfluss von heterogenen Strukturen auf die Fingerbildung besser zu verstehen.
Ein Thema, welches für künftige Arbeiten von übergreifender Relevanz sein wird, betrifft die Weiterentwicklung von Strategien für zeitliche und räumliche Kopplungen unterschiedlicher Modelle. Ein Schlüsselproblem stellt dabei der Transfer von Informationen durch Austausch geeigneter das jeweilige System charakterisierender Parameter über die Modellgrenzen hinweg dar.